GEOTECHNICAL RECONNAISSANCE OF THE 2016 M_w7.8 KAIKOURA, NEW ZEALAND EARTHQUAKE

Version 1.0: 10 JUNE 2017

EDITORS

Misko Cubrinovski – QuakeCoRE (NZ) Lead; University of Canterbury, Christchurch, New Zealand
Jonathan D. Bray – GEER (US) Lead; University of California, Berkeley, CA, USA

CONTRIBUTING AUTHORS (alphabetical order)

Sarah Bastin – QuakeCoRE, NZ
Brendon A. Bradley – University of Canterbury, Christchurch, NZ
Jonathan D. Bray – University of California, Berkeley, CA, USA
Claudio Cappellaro – University of Canterbury, Christchurch, NZ
Misko Cubrinovski – University of Canterbury, Christchurch, New Zealand
Christopher de la Torre – University of Canterbury, Christchurch, NZ
Russell A. Green – Virginia Tech, Blacksburg, VA, USA
Christopher R. McGann – University of Canterbury, Christchurch, NZ
Michael Olsen – Oregon State University, OR, USA
Alessandro Palermo – University of Canterbury, Christchurch, NZ
Mark Stringer – University of Canterbury, Christchurch, NZ
Liam Wotherspoon – University of Auckland, Auckland, NZ

OTHER CONTRIBUTORS (alphabetical order)

Jason Aricheta – University of Auckland, Auckland, NZ
Adda Athanasopoulos-Zekkos – University of Michigan, USA
Xavier Bellagamba – University of Canterbury, Christchurch, NZ
Gabriele Chiaro – University of Canterbury, Christchurch, NZ
Richard Cole – Tonkin+Taylor, Wellington, NZ
Ross Davis – Davidson Group, Blenheim, NZ
Kevin Foster – University of Canterbury, Christchurch, NZ
Sally Hargraves – Terra Firma Engineering, Blenheim, NZ
Laurie Johnson – Laurie Johnson Consulting | Research, CA, USA
Maya El Kortbawi – Virginia Tech, Blacksburg, VA, USA
Royce Liu – University of Canterbury, Christchurch, NZ
John Manousakis – Elxis Group, GREECE
Leigh McGlynn – Davidson Group, Blenheim, NZ
Rebecca McMahon – University of Auckland, Auckland, NZ
Matthew O'Banion – Oregon State University, OR, USA
Rolando Orense – University of Auckland, Auckland, NZ
Jarg Pettinga – University of Canterbury, Christchurch, NZ
Emilia Stocks – Tonkin+Taylor, Wellington, NZ
Sjoerd Van Ballegooy – Tonkin + Taylor, Auckland, NZ

TABLE OF CONTENTS

ACKNOWLEDGEMENTS

The NZ team was principally supported by the EQC Capability Grant at the University of Canterbury, and MBIE support provided for the 2016 Kaikoura Earthquake Reconnaissance. The US Geotechnical Extreme Events Reconnaissance (GEER) Association team members were supported by the National Science Foundation (NSF) through Grants CMMI-1266418 and CMMI-1724866. Any opinions, findings, and conclusions or recommendations expressed in this material are those of the authors and do not necessarily reflect the views of the NSF, EQC or MBIE. For more information about GEER visit: www.geerassociation.org.

We would like to acknowledge the collaboration provided by the CentrePort Ltd. especially for allowing access to our team and making special arrangements for our multiple visits. We would also like to acknowledge the great support and collaboration from Stuart Palmer, Richard Cole, Mike Jacka, and Sjoerd van Ballegooy, from Tonkin + Taylor, who as engineers for the CentrePort provided critical input and support in various phases of these efforts. Site access assistance through Hugh Cowan of the Earthquake Commission is sincerely appreciated. Use of results from aerial survey of Thorndon Reclamation and Wharf performed by Cardno is gratefully acknowledged.

We also acknowledge the efforts of Tonkin + Taylor for developing a geospatial resource to combine the observations of the reconnaissance teams, for sharing their data and information relating to the Canterbury region, and for arranging access to the town of Kaikoura for members of the reconnaissance team. We acknowledge the Marlborough District Council for site access and allowing geotechnical information from sites within Blenheim to be shared with the reconnaissance teams.

We additionally acknowledge the support of John Wood; Michael Cowan, Jeremy Waldin and Mark Jeffries from Opus International Consultants Ltd.; and John Reynolds from NZTA for assistance, information, and insights in regard to the South Island bridges, as well as Simon Cox (GNS) for constructive feedback and comments that have been incorporated into the discussion of geotechnical aspects to the damage on the South Island.

Finally, we would like to acknowledge the collaboration of GNS Science and EERI in the coordination of the reconnaissance efforts and information sharing.

This is QuakeCoRE publication number 0187, and GEER Report Number: GEER-053.

1. INTRODUCTION

On November 14, 2016 at 12:02 am local time, the M_w7.8 Kaikoura earthquake occurred along the east coast of the upper South Island, New Zealand. The fault rupture initiated in the Waiau plains in North Canterbury and then progressed northeast. The rupture involved multiple fault segments in the region of Kaikoura and north of it. The earthquake generated intense ground shaking in the near-source region, and it caused numerous surface fault ruptures, landslides, as well as other forms of ground distress and failures, including liquefaction and lateral spreading. The earthquake affected a relatively large area along the Waiau (North Canterbury) – Kaikoura – Blenheim (Marlborough) stretch of the South Island. It also caused considerable distress in Wellington, the capitol of New Zealand at the southern tip of the North Island. In the South Island, the most significant impacts were to a few smaller townships and rural settlements in the North Canterbury, Kaikoura, and South Marlborough regions, including residential and commercial buildings, and particularly the horizontal infrastructure in the region. In Wellington, the earthquake affected several buildings in its Central Business District (CBD) and caused liquefaction in the reclamations of port of Wellington (CentrePort), which affected wharves and buildings at the port.

Because of the large area affected by the earthquake and the different effects it produced, the geologic and geotechnical effects of the Kaikoura earthquake were documented through several independent teams who collaborated at the interfaces between their focus areas. A GNS-UC-GEER team of researchers mapped and documented surface fault ruptures and its effects, and another GNS-GEER-UC team of researchers documented the occurrence and effects of landslides. Comprehensive reconnaissance efforts were carried out by these GNS-lead efforts on surface fault rupture and landslides. The results of their reconnaissance efforts are published elsewhere.

The primary geotechnical engineering reconnaissance effort in response to the Kaikoura earthquake was conducted by a joint QuakeCoRE-GEER (NZ-US) team of researchers and engineers. The QuakeCoRE-GEER team focused on earthquake ground motions and site effects, geotechnical effects of the earthquake in Wellington (with a focus on liquefaction effects at the port of Wellington), general geotechnical effects in the South Island, geotechnical impacts on bridges and infrastructure in the South Island, and societal impacts and emergency response. The results of these geotechnical reconnaissance efforts are documented in this report.

The initial reconnaissance was performed in the period of 15 to 19 November 2016, and covered the Waiau and Blenheim areas (but not Kaikoura itself), as well as the initial inspection of CentrePort in Wellington. Follow-on efforts from 20 November to mid-December were then organized through four teams focussing on the Waiau area, Marlborough, Kaikoura, and CentrePort (Wellington). The majority of the observations presented in this report resulted from these reconnaissance efforts in the second half of November and early December in 2016.

The QuakeCoRE-GEER team included the following members:

Misko Cubrinovski – QuakeCore (NZ) Lead; University of Canterbury, Christchurch, New Zealand
Jonathan D. Bray – GEER (US) Lead; University of California, Berkeley, CA, USA
Sarah Bastin – QuakeCoRE, NZ
Brendon A. Bradley – University of Canterbury, Christchurch, NZ
Christopher de la Torre – University of Canterbury, Christchurch, NZ
Russell A. Green – Virginia Tech, Blacksburg, VA, USA
Christopher R. McGann – University of Canterbury, Christchurch, NZ
Michael Olsen – Oregon State University, OR, USA
Alessandro Palermo – University of Canterbury, Christchurch, NZ
Mark Stringer – University of Canterbury, Christchurch, NZ
Liam Wotherspoon – University of Auckland, Auckland, NZ
Jason Aricheta – University of Auckland, Auckland, NZ
Dan Ashfield – Tonkin + Taylor, Christchurch, NZ
Adda Athanasopoulos-Zekkos – University of Michigan, USA
Xavier Bellagamba– University of Canterbury, Christchurch, NZ
Claudio Cappellaro – University of Canterbury, Christchurch, NZ
Gabriele Chiaro – University of Canterbury, Christchurch, NZ
Ross Davis – Davidson Group, Blenheim, NZ
Kevin Foster – University of Canterbury, Christchurch, NZ
Sally Hargraves – Terra Firma Engineering, NZ
Carlo Lai – University of Pavia, Italy
Robin Lee – University of Canterbury, Christchurch, NZ
Nikolaos Ntritsos – University of Canterbury, Christchurch, NZ
Laurie Johnson – Laurie Johnson Consulting | Research, CA, USA
Maya El Kortbawi – Virginia Tech, Blacksburg, VA, USA
John Manousakis – Elxis Group, GREECE
Leigh McGlynn – Davidson Group, Blenheim, NZ
Rebecca McMahon – University of Auckland, Auckland, NZ
Matthew O'Banion – Oregon State University, OR, USA
Rolando Orense – University of Auckland, Auckland, NZ
Emilia Stocks – Tonkin+Taylor, Wellington, NZ
Jarg Pettinga – University of Canterbury, Christchurch, NZ
Sjoerd Van Ballegooy – Tonkin + Taylor, Auckland, NZ
Richard Cole – Tonkin+Taylor, Wellington, NZ
Abdul Baki – University of Canterbury, Christchurch, NZ
Royce Liu – University of Canterbury, Christchurch, NZ
Adnan Rais – University of Canterbury, Christchurch, NZ
Brandon McHaffie – University of Canterbury, Christchurch, NZ
Kaveh Andisheh – University of Canterbury, Christchurch, NZ
Roberto Gentile – University of Canterbury, Christchurch, NZ
Iolanda Nuzzo – University of Canterbury, Christchurch, NZ
Mario Granerio – University of Canterbury, Christchurch, NZ
Giuseppe Loporcaro – University of Canterbury, Christchurch, NZ

The QuakeCoRE and GEER team members worked collaboratively and shared resources, information, and logistics to conduct a thorough and efficient reconnaissance covering a large area over a limited period of time. This report summarises the key evidence and findings from the reconnaissance efforts. Any opinions, findings, and conclusions or recommendations expressed in this report are those of the authors and do not necessarily reflect the views of the associated organizations and funding agencies. Online versions of this report are available at the QuakeCoRE and GEER websites.

The report is organized in five chapters in addition to this introductory chapter. Chapter 2 provides the geological context for the Kaikoura Earthquake, including geologic setting, geomorphology, causative faults, and rupture characteristics of the earthquake. Chapter 3 summarizes strong ground motion observations at representative strong motion stations, and it also discusses the characteristics of the ground motions through comparisons with design spectra and empirical and physics-based ground motion models. Chapter 4 covers the geotechnical impacts of the Kaikoura Earthquake on the South Island of New Zealand, and presents key observations in three separate sections for the affected regions of Waiau, Kaikoura, and Marlborough, respectively. Chapter 5 summarizes key observations on the performance of reclamations, wharves and buildings at the Wellington port during the Kaikoura Earthquake. Finally, Chapter 6 is focused specifically on the effects of ground shaking and ground deformation on the South Island bridges and infrastructure.

2. GEOLOGICAL SETTING

2.1. Summary

The moment magnitude M_w7.8 Kaikoura Earthquake occurred on the 14 November 2016 at 12:02 am NZ Standard Time (11:02:56 UTC). The rupture initiated beneath the Waiau Plains in North Canterbury and propagated over 150 km north-eastward progressively stepping over segments of at least twelve faults within the region. The complex sequence involving ruptures on multiple faults resulted in the cumulative M_w7.8 earthquake with a bracketed shaking duration of approximately two minutes. The earthquake was felt throughout much of New Zealand and resulted in widespread damage to land and infrastructure in the northern South Island and lower North Island. Efforts to characterize the distribution of ground deformation and associated rupture traces are on-going due to the remoteness of much of the area and complex nature of the ground surface rupture traces including accommodation of strain on many different tectonic structures. This chapter summarizes the basic geological context of the earthquake and affected regions which are discussed further in this report.

2.2. Geological context for the Kaikoura Earthquake

The South Island of New Zealand straddles the tectonic plate boundary between the Australian and Pacific Plates (Figure 2.1). The plate boundary transitions from oblique continent-to-continent collision between the Pacific plate and the Australian plate across the central South Island, to subduction of the thick oceanic crust of the Hikurangi Plateau beneath the Australian Plate in the NE. Subduction extends northward from Kaikoura in NE South Island along the Hikurangi Trough off the east coast of the North Island (Figure 2.1).

The Australian and Pacific plates converge obliquely at rates of 39-48 mm/yr within New Zealand resulting in a wider zone of collisional deformation marked by a distributed zone of active faulting (Figure 2.1). The Alpine Fault accommodates ~70-75% of the total relative plate boundary motion of the oblique continental collision zone within the central South Island and results in the uplift of the Southern Alps (Figure 2.1) (Norris & Cooper, 2001). The remaining ~30% of plate boundary deformation across South Island is accommodated largely by slip on a series of faults throughout the Southern Alps, eastern foothills, and the adjoining Canterbury Plains, as exemplified by the 2010 Darfield (Canterbury) Earthquake rupture of the Greendale Fault (Cubrinovski et al., 2010; GEER, 2010). In the northern South Island, the Alpine Fault splays into a series of north-east trending transpressional strike-slip faults, comprising the Marlborough Fault Zone (MFZ). The MFZ marks the transition zone of the plate boundary from continental convergence onshore into the Hikurangi subduction zone offshore with the southernmost interface of the subduction zone underlying the MFZ at depths of 20-60 km (Little & Jones, 1998; Reyners & Robertson, 2004). The Kaikoura Earthquake initiated approximately 20 km south of the southern strand of the MFZ and propagated north-eastward, rupturing multiple segments of the major mapped faults within the region, along with several previously unmapped faults.

The MFZ accommodates 70-100% of the oblique plate-boundary convergence in the NE South Island resulting in a complex region of active earth deformation extending over 200 km in width (Figure 2.2). Plate motion is accommodated primarily through the four major NE trending transpressive dextral strike-slip faults spaced approximately 30 km apart, including the Wairau, Awatere, Clarence, and Hope faults.

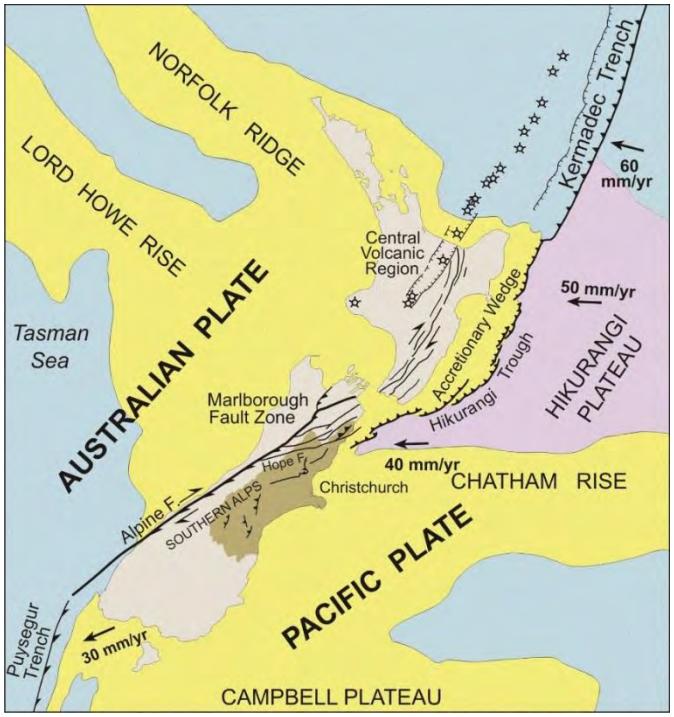

Figure 2.1: The Australian-Pacific plate boundary within New Zealand and associated relative convergence rates (from Pettinga et al. 1998).

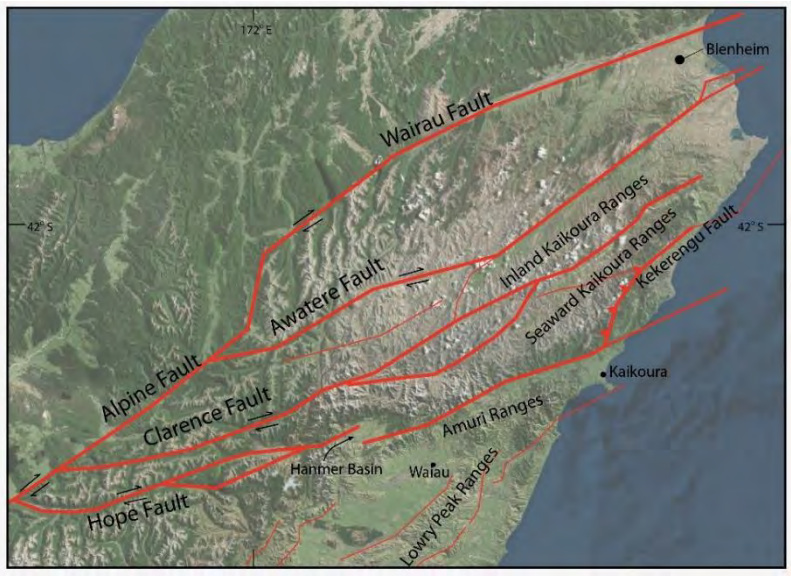

Figure 2.2: Location of active faults and uplifted mountain ranges within the Marlborough Fault Zone (MFZ) in Marlborough and North Canterbury as derived from the New Zealand active faults database (Litchfield et al., 2014).

Slip rates on these faults are well constrained from displaced geomorphic features with Quaternary slip rates on the Wairau, Awatere, and Clarence faults ranging from 4-8 mm/yr (Benson et al., 2001; Nicol & van Dissen, 2002; Zachariasen et al., 2006), while the NE Conway segment of the Hope fault carries approximately 23+/-4 mm/yr of slip (Langridge et al., 2003). Activity within the MFZ has propagated southwards over time as the collisional zone of the Chatham Rise has migrated south (Little & Jones, 1998). A zone of active faulting and folding continues to the south of the Hope Fault and includes the Hundalee Fault and Humps Fault Zone, both of which ruptured during the Kaikoura Earthquake (Figure 2.2) (Pettinga et al. 2001). N-S to NE-SW trending valley and range topography extends south of the MFZ into North Canterbury and is characterised by a set of geologically young and complex faults and related folds associated with the Quaternary widening of the plate boundary zone (Nicol et al., 1995; Pettinga et al. 2001). Smaller mapped and unmapped faults are present throughout the MFZ region and accommodate the remainder of the plate boundary motion.

2.3. The Kaikoura Earthquake

The epicentre of the M_w 7.8 earthquake was located approximately 15 km northeast of the town of Culverden with a focal depth of ~15 km (Figure 2.3). The earthquake rupture initiated on a strand of the Humps Fault Zone beneath north Culverden Basin, and it propagated over 150 km north-eastward, progressively rupturing several mapped and unmapped faults, including the North and South Leader, Hundelee, Jordan Thrust, Papatea and Kekerengu Faults (Figure 2.3). The rupture then transitioned offshore onto the Needles Fault near Ward, and continued for approximately 34 km before the rupture terminated near Cape Campbell off the NE coast of the South Island (Figure 2.3). The rupture of multiple faults within the MFZ during the Kaikoura Earthquake indicates that these structures are most likely connected at depth, possibly in association with the subduction interface. Prior to the Kaikoura Earthquake, the New Zealand Seismic Hazard Model accounted for several rupture scenarios within the MFZ involving ruptures of single faults, as well as combinations of fault ruptures, however, did not account for the complexity or number of faults that ruptured during the Kaikoura Earthquake (Stirling et al., 2012).

The surface rupture traces appear to be discontinuous and segmented with step-overs up to 1 km observed along single faults traces, while jumps in the rupture traces are observed between the ruptured faults. The surface displacement patterns and associated deformation is shown to vary along the length of the rupture traces and between the faults that ruptured (Figure 2.3). Oblique dextral strike-slip displacements of varying magnitudes are typically observed and reported, although localized sinistral displacements are observed (e.g., the Papatea and Stone Jug faults). Maximum horizontal displacements of ~2 m and vertical displacements of up to 2 m were recorded in the epicentral area near Waiau (Figure 2.3), while vertical displacements of up to 4-5 m are reported on the oblique thrust North Leader fault, ~20km NE of Waiau township. Displacements as small as 1-2 centimetres were measured near the epicentre from offset anthropogenic features in farmland including crop-rows, farm tracks, and fence lines. Displacement magnitudes increased as the rupture

propagated northward, with up to 10 m of horizontal slip and 7-8 m of vertical displacement recorded on the Kekerengu Fault (Figure 2.3). Offshore seismic surveys conducted by NIWA in the days after the earthquake revealed vertical displacements in the seafloor along the Needles Fault (Figure 2.3).

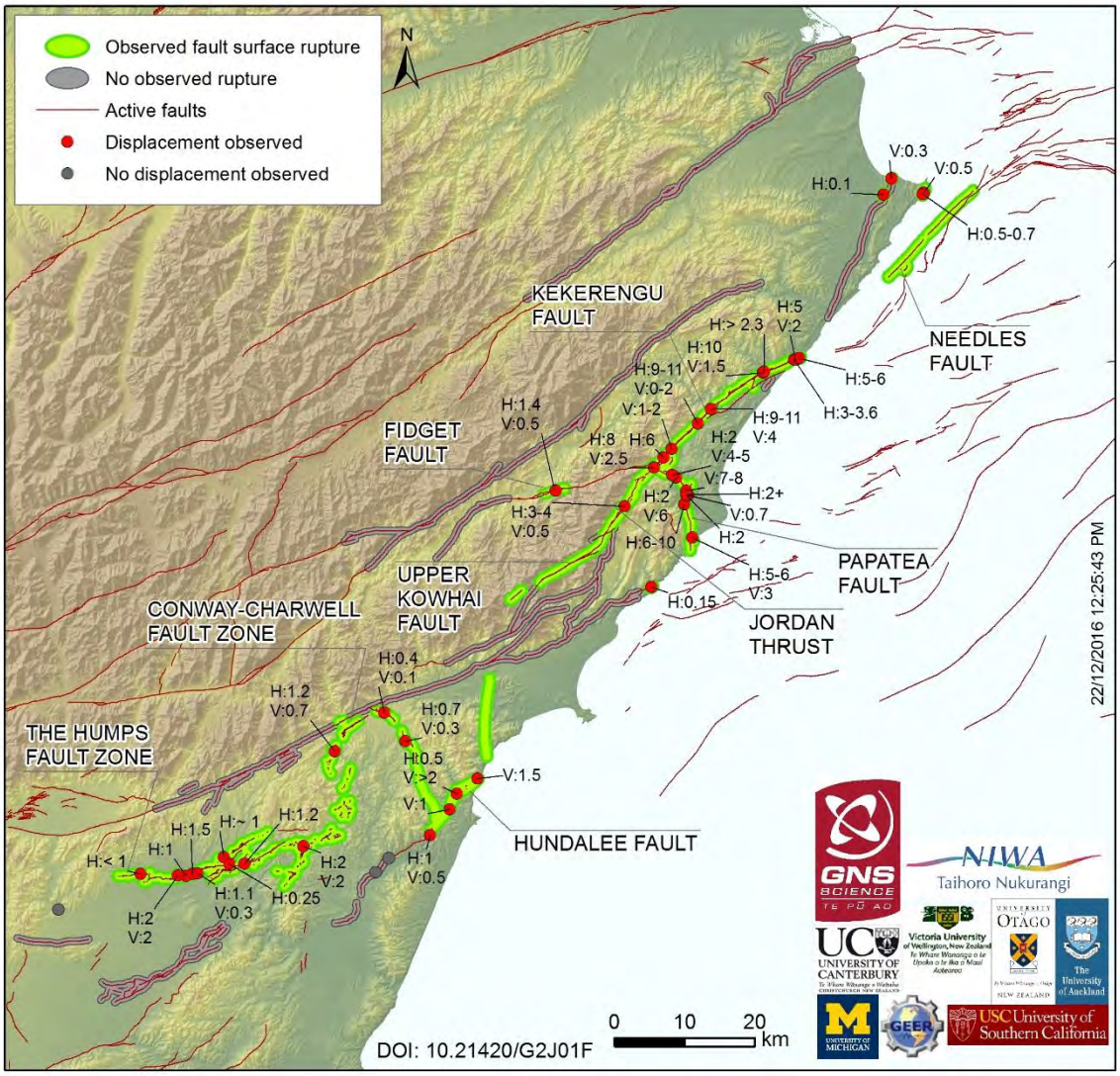

Figure 2.3: Observed and documented fault ruptures as at 22 December 2016 from the 2016 M_w7.8 Kaikoura Earthquake and associated displacements, as measured in the field by scientists from GNS Science, Victoria University of Wellington, University of Canterbury, University of Otago, NIWA, and GEER, among others.

Coastal uplift is observed in the area north of where the Hundalee Fault intersects the coast, and appears broadly controlled by the locations of surface ruptures at the coast (Figure 2.3). Approximately 1 m of coastal uplift is observed proximal to the Hundalee Fault and at the Kaikoura Peninsula (Figure 2.3). The maximum observed coastal uplift occurs where two strands of the Papatea Fault intersect the coast, resulting in the intervening block between the two strands being uplifted by up to ~6 m. Coastal uplift of approximately 2 m continues to the north to the where rupture transitioned offshore onto the Needles Fault (Figure 2.3).

The distribution of aftershocks from the Kaikoura Earthquake generally occur throughout a broad region trending parallel to the rupture traces between North Canterbury and Cook Strait (Figure 2.4). A high proportion of the initial aftershock distribution was concentrated at the northernmost terminus of the surface rupture near Cape Campbell and proximal to the Wellington region in the lower North Island (Figure 2.4). In the two months following the main shock, the region experienced 53 aftershocks of M5-5.9 and four of M6-6.9, which is below that expected for a M_w7.8 earthquake.

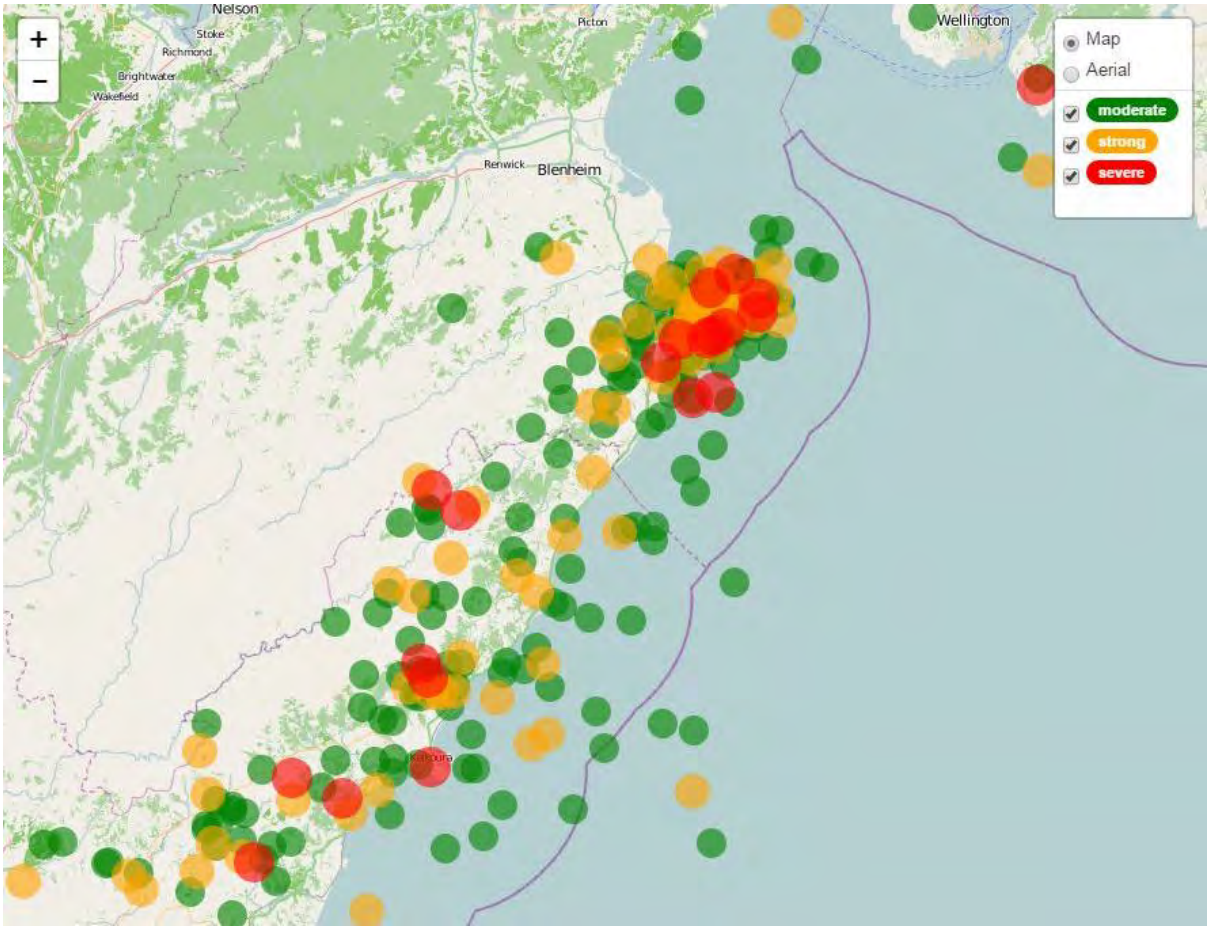

Figure 2.4: Map of aftershock locations in the 24 hours following the M_w7.8 Kaikoura Earthquake as compiled by GeoNET.

2.4. Historic and Pre-historic seismicity within the Marlborough Fault Zone

The MFZ is one of the most tectonically active regions of New Zealand with many shallow earthquakes recorded in the region since initial European settlement and subsequent instrumental monitoring began (Figure 2.5). Two large earthquakes with magnitudes greater than 7.0, and six shallow earthquakes with magnitudes 6.0-6.9 have been recorded in the MFZ post-settlement in ~1840, and prior to the 2016 Kaikoura Earthquake (Grapes et al., 1998). The 1848 ~M7.5 Marlborough Earthquake ruptured approximately 100-110 km of the Awatere Fault extending inland from the coast. Mean dextral co-seismic displacements of 5.3

+/- 1.6 m were derived for this event from later studies by Grapes et al. (1998) and Mason & Little (2006). The earthquake caused extensive regional shaking and damage to buildings, with shaking intensities of MM9-10 inferred in the Wairau and Awatere valleys. Liquefaction was reported close to rivers within the Wairau, Awatere, and Clarence valleys (Grapes et al., 1998). Three deaths were reported within Wellington city (Grapes et al. 1998). Paleo-seismic studies provide evidence for 9-10 surface-rupturing earthquakes on the eastern section of the Awatere Fault between 1848 and 8330-8610 years before present (BP). A mean recurrence interval of 820-920 years has been derived for the fault, however, intervals between individual events are non-uniform (Mason et al. 2006).

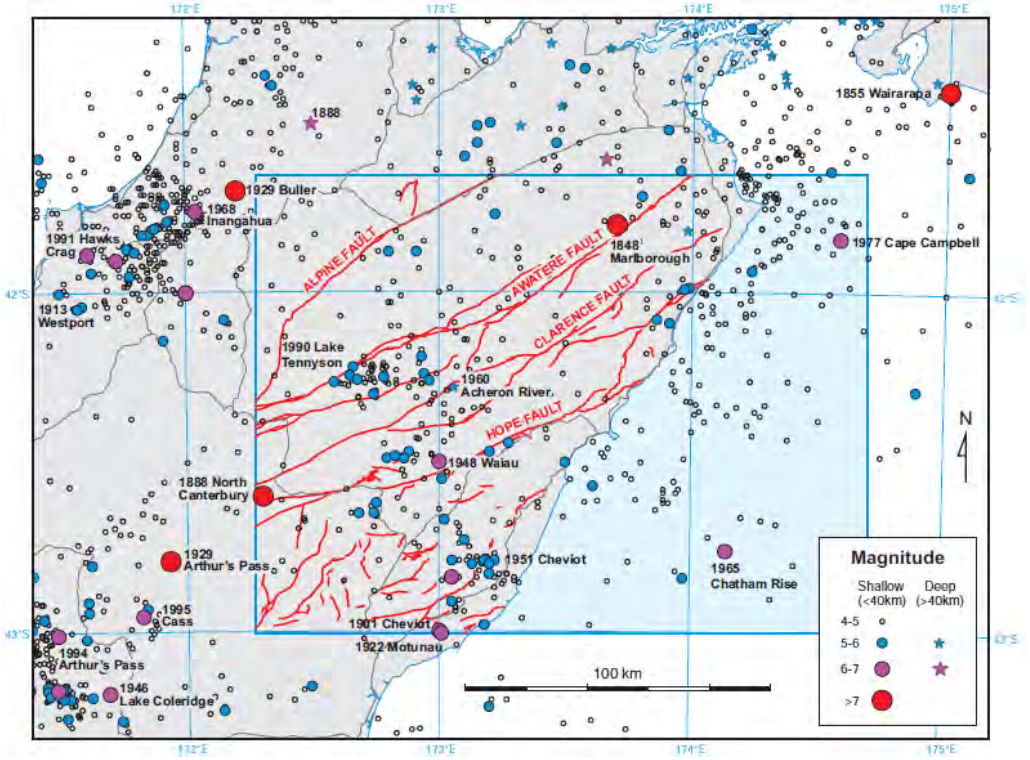

Figure 2.5: Historic earthquakes within the northern South Island of New Zealand (Rattenbury et al., 2006).

The 1888 the M7.0–7.3 North Canterbury Earthquake ruptured a 30 ± 5 km segment of the Hope Fault to the west of Hanmer Springs. Maximum dextral displacements of up to 2.6 m were recorded along the rupture from offset features such as farm fences (Cowan, 1991). The earthquake resulted in a narrow zone of extensive building damage running parallel to the rupture trace, and caused widespread contents damage within the central South Island (Cowan, 1991).

Other damaging earthquakes within the MFZ include the 1901 M6.9 Cheviot Earthquake, and the 1922 M6.4 Motunau Earthquake, both of which caused widespread damage within northern Canterbury (Downes & Yetton, 1995). The 1948 M6.4 Waiau Earthquake also caused minor structural damage in Hanmer and Waiau (Downes & Yetton, 1995). More recently the 2013 M_w6.5 Cook Strait Earthquake, centred 25 kilometres east of Seddon, and the M_w6.6 Lake Grassmere Earthquake, located 30 kilometres SE of Blenheim, caused

moderate damage to land and infrastructure near the source region, including triggering liquefaction within the township of Blenheim (Morris et al., 2013).

2.5. Geologic setting and geomorphology of the Marlborough Fault Zone

The geomorphology of the Marlborough region is dominated by NE trending mountain ranges associated with transpressional uplift along the major dextral strike-slip Wairau, Awatere, Clarence and Hope faults of the Marlborough Fault Zone (MFZ) (Figure 2.2). The faults have controlled the formation of long straight NE trending valleys adjoining the range-front location of the active faults, with corresponding rivers approximately aligned with the active fault traces (Figure 2.2). The river courses have been strongly influenced by movements on the corresponding fault segments and associated uplift (Figure 2.2). The mountain ranges generally comprise indurated sandstone and argillite assigned to the Torlesse greywacke basement sequence with local igneous intrusions. Remnants of the Cretaceous-Pliocene covering sequence are preserved in fault-angle depressions on the south-eastern sides of the faults within the major valleys (Rattenbury et al., 2006). Landforms within the valleys reflect alternating glaciations and inter-glacial cycles throughout the Pleistocene with many glaciated landforms offset and deformed by activity and uplift along the faults within the valleys.

The ~220 km long Hope Fault is segmented into three strands as it traverses across South Island and is topographically defined by alignment of major valleys coincident with these major fault splays. At the eastern tip of the central Hope River segment a 7 km wide releasing bend/step-over between this segment and the SE Conway segment (Figure 2.2) has resulted in the formation of the Hanmer pull-apart basin which extends approximately 15 km length (Wood et al., 1994). The North Canterbury region to the south of Hope Fault is comprised of NE-SW to N-S trending ranges, such as the Lowry Peak Ranges, which are significantly lower in altitude to those in the MFZ to the north, and are separated by thrust fault controlled valleys and depressions such as Culverden and Cheviot basins (Figure 2.2) (Nicol et al., 1995; Pettinga et al. 2001). The Culverden and Cheviot basins are partly rimmed by Cretaceous-Miocene sedimentary rocks including Paleogene limestones, and are infilled with Plio-Pleistocene sediments eroded from the surrounding ranges along with Torlesse greywacke-derived sandstone from the exposed and eroding cores of the local thrust propagated anticlinal folds as well as the more distal source regions of the Southern Alps. The fold and thrust driven valley and range topography is transected by the Waiau and Hurunui Rivers which flow eastwards from their upper catchments in the ranges of the Southern Alps. Several antecedent gorges are present along the Waiau and Hurunui Rivers reflecting active and continuing uplift and deformation along the mountain ranges of northern Canterbury.

The rapid and continuing uplift of the mountain ranges within the MFZ, and consequent erosion, provided sediment that infilled the valley floors and intervening basins. Much of the

Quaternary fill within the valleys originated as glacial outwash deposits. Sediments have subsequently been re-worked by the rivers within the valleys. Flights of aggradational terraces comprising gravel with sand and silt lenses are present above the active river floodplains; older terraces are preserved at progressively higher elevations above valley floors. The terrace surfaces are commonly tilted and warped as a result of uplift and fault-driven deformation along the mountain range-fronts. Floodplain deposits in the valleys typically comprise gravel with sand and silt lenses, average clast size and sediment grading decreases towards the coast and with increasing distance from the source. Compositions generally comprise basement Torlesse derived sandstone that outcrops within the mountain ranges. Alluvial fan and scree deposits are widespread along the flanks of mountain ranges and often merge into the aggradation surfaces.

Tectonic activity along the faults within the MFZ has uplifted much of the coastline between North Canterbury and the Kekerengu fault (Figure 2.2). Steep slopes and sea cliffs are present along much of the coastline and are comprised of Torlesse greywacke sandstone, and Paleogene limestones capped by flights of uplifted marine terraces (Rattenbury et al., 2006). The peninsula at Kaikoura comprises uplifted flights of marine terraces underlain by of Late Cretaceous-Paleogene limestone and siltstones as well as upper Tertiary siltstones, and reflects continued uplift of the region throughout the Quaternary (Rattenbury et al., 2006). Poorly preserved and tilted raised shorelines comprising marine sand and gravel are present as narrow benches and terraces along the flanks of the coastal ranges and reflect tectonic uplift rather than actual interglacial sea levels. The coastline north of the Kekerengu Fault generally exhibits low-profile beaches comprised of sand and gravel and commonly fringed by sand dunes. At the mouths of the Waiau and Awatere valleys successions of paleo-dunes indicate coastline progradation and marine regression following the 6,500 year before present sea-level highstand. Offshore, the seafloor morphology is dominated by the continental shelf, the continental slope, the Hikurangi Trough, and the Chatham Rise.

The interface of floodplain alluvium and coastal marine deposits at the mouths of the Wairau and Awatere rivers has resulted in sediments that display significant spatial variability. Swamp deposits are observed in the inter-dune hollows between the paleo-dune ridges present between the Blenheim township and the coast, and reflect water pooling in these areas following flood-events. Active and paleo-channels are present in the area surrounding Blenheim and reflect the migration of the Wairau River and associated tributary streams across the alluvial plains. The distribution of liquefaction and associated lateral spreading proximal to Blenheim appears to be strongly influenced by the position of the present and paleo-streams along with the inter-dune swamp deposits.

References

Benson, A.M., Little, T.A., van Dissen, R.J., Hill, N., Townsend, D.B. (2001). Late Quaternary paleoseismic history and surface rupture characteristics of the eastern Awatere strike-slip fault, New Zealand, *Geological Society of America Bulletin*, 113(8): 1079-1091.

Cowan, H.A. (1991). The North Canterbury earthquake of September 1, 1888, *Journal of the Royal Society of New Zealand*, 21(1): 1-12.

Cubrinovski, M., Green, R., Allen, J., Ashford, S., Bowman, E., Bradley, B., Cox, B., Huthinson, T., Kavazanjian, E., Orense, R., Pender, M., Quigley, M., Wotherspoon, L. (2010). Geotechnical reconnaissance of the 2010 Darfield (Canterbury) earthquake, *Bulletin of the New Zealand Society for Earthquake Engineering*, 43(4): 243-320.

Downes, G. and Yetton, M. (2012). Pre-2010 historical seismicity near Christchurch, New Zealand: The 1869 Mw 4.7-4.9 Christchurch and 1870 Mw 5.6-5.8 Lake Ellesmere earthquakes, *New Zealand Journal of Geology and Geophysics*, 55(3): 199-205.

GEER, 2010. Geotechnical Reconnaissance of the 2010 Darfield (New Zealand) Earthquake. Version 1: November 14, 2010, Report of the National Science Foundation – Sponsored Geotechnical Extreme Events Reconnaissance (GEER) Team.

Grapes R.H., Little, T.A., Downes, G.L. (1998). Rupturing of the Awatere Fault during the 1848 October 16 Marlborough earthquake, New Zealand: historical and present day evidence. *New Zealand Journal of Geology and Geophysics*, 41: 387-399.

Langridge, R. M.; Campbell, J.K.; Hill, N.; Pere, V.; Pope, J.; Pettinga, J.R.; Estrada, B.; Berryman, K.R. (2003): Paleoseismology and slip rate of the Conway segment of the Hope Fault at Greenburn Stream, South Island, New Zealand. *Journal annals of Geopyhsics, Special Issue "Ten years of Paleoseismology in the ILP: progress and Prospects"*; Volume 46; Number 5: 1119-1139.

Litchfield, N.J., Van Dissen, R., Sutherland, R., Barnes, P.M., Cox, S.C., Norris, R., Beavan, R.J., Langridge, R., Villamor, P., Berryman, K., Stirling, M., Nicol, A., Nodder, S., Lamarche, G., Barrell, D., Pettinga, J.R., Little, T., Pondard, N., Mountjoy J.J., Clark, K. (2014). A model of active faulting in New Zealand, *New Zealand Journal of Geology and Geophysics,* 57(1): 32-56.

Little, T.A. and Jones, A. (1998). Seven million years of strike-slip and related off-fault deformation, north-eastern Marlborough fault system, South Island, New Zealand, *Tectonics*, 17(2): 285-302.

Mason, D. P. M. and Little, T. A. (2006). Refined slip distribution and moment magnitude of the 1848 Marlborough earthquake, Awatere Fault, New Zealand, *New Zealand Journal of Geology and Geophysics*, 49: 375-382.

Mason, D. P. M., Little, T. A., van Dissen, R.J. (2006). Refinements to the paleoseismic chronology of the eastern Awatere Fault from trenches near Upcot Saddle, Marlborough, New Zealand, *New Zealand Journal of Geology & Geophysics*, 49: 383-397.

Morris, G.J., Bradley, B.A., Walker, A., Matuschka, T. (2013). Ground motions and damage observations in the Marlborough region from the 2013 Lake Grassmere earthquake, *Bulletin of the New Zealand Society for Earthquake Engineering*, 46(4): 169-187.

Nicol, A., Cowan, H., Campbell, J.K., Pettinga, J. (1995) Folding and the development of small sedimentary basins along the New Zealand Plate Boundary, *Tectonophysics*, 241: 47-54.

Nicol, A., and van Dissen, R. (2002). Up-dip partitioning of displacement components on the oblique-slip Clarence Fault, New Zealand, *Journal of Structural Geology*, 24(9):1521-1535.

Norris, R.J. and Cooper, A.F. (2001). Late Quaternary slip rates and slip partitioning on the Alpine Fault, New Zealand, *Journal of Structural Geology*, 23, 507– 520.

Pettinga, J.R., Chamberlain, C.G., Yetton, M.D., Van Dissen, R.J., Downes, G. (1998): Earthquake Source Identification and Characterisation: Stage 1 (Part A) Earthquake Hazard and risk Assessment Study, Canterbury Regional Council CRC Publication No. U98/10: 121pages and 6 Appendices.

Pettinga, J.R., Yetton, M.D., Van Dissen, R.J., Downes, G. (2001): Earthquake Source Identification and Characterisation for the Canterbury Region, South Island, New Zealand. *NZ Society for Earthquake Engineering Bulletin* 34: 282-317.

Rattenbury, M.S., Townsend, D.B., Johnston, M.R. (compilers) 2006: Geology of the Kaikoura area. Institute of Geological & Nuclear Sciences 1:250 000 geological map 13. 1 sheet + 70p. Lower Hutt, New Zealand. GNS Science.

Reyners, M. and Robertson, E. (2004). Intermediate depth earthquakes beneath Nelson, New Zealand, and the southwestern termination of the subducted Pacific plate, *Geophysical Research Letters*, 31: L04607.

Stirling, M., McVerry, G., Gerstenberger, M., Litchfield, N., Dissen, R. V., Berryman, K., Barnes, P., Wallace, L., Villamor, P., Langridge, R., Lamarche, G., Nodder, S., Reyners, M., Bradley, B., Rhoades, D., Smith, W., Nicol, A., Pettinga, J., Clark, K., and Jacobs, K. (2012). National seismic hazard model for New Zealand: 2010 update. *Bulletin of the Seismological Society of America*, 102(4): 1514-1542.

Wood, R.A., Pettinga, J.R., Bannister, S., Lamarche, G., Morran, T.J. (1994): Structure of the Hanmer Strike-slip Basin, Hope Fault, New Zealand. *Bulletin of the Geological Society of America* 106: 1459-1473.

Zachariasen, J., Berryman, K., Langridge, R., Prentice, C., Rymer, M., Stirling, M., Villamor, P. (2006). Timing of late Holocene surface rupture of the Wairau Fault, Marlborough, New Zealand, *New Zealand Journal of Geology and Geophysics*, 49: 159-174.

3 STRONG GROUND MOTION OBSERVATIONS

This chapter discusses observed strong ground motions from the 14 November 2016 $M_w7.8$ Kaikoura earthquake. Specific attention is given to the near-source region where ground motions exceeding 1.0 g horizontal were recorded, as well as up to 2.7 g in the vertical direction at one location. Ground motion response spectra in the near-source, North Canterbury, Marlborough and Wellington regions are examined and compared with design levels. Observed spectral amplitudes are also compared with predictions from empirical and physics-based ground motion modelling.

3.1 Tectonic setting and inferred causative rupture

Observations and multiple geophysical and geodetic methods highlight the source complexity of this earthquake with numerous fault segments rupturing (Litchfield et al., 2016; Stirling et al., 2017). Figure 3.1 illustrates the rupture segment geometries of the causative faults presented by Bradley et al. (2017b), and adopted here for ground motion observation and modelling interpretations. For reference, the surface trace of fault segments that are considered in the InSAR+GPS inversion of Hamling (2016), significant aftershocks, and mapped active faults are also shown.

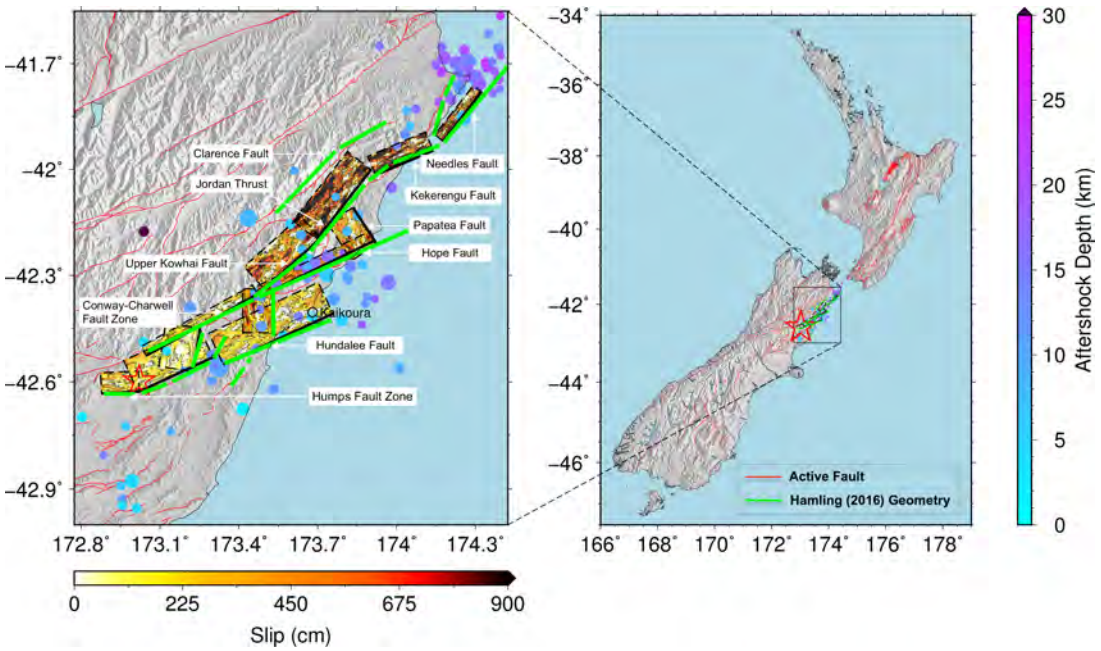

Figure 3.1: Location of the $M_w7.8$ Kaikoura earthquake and causative faults on the east coast of the South Island, New Zealand. Hypocentre is marked with a red star. Surface trace of the source inversion of Hamling (2016) shown in green, and adopted kinematic rupture model faults shown as planes coloured by slip amplitude and contoured by rupture time. $M_w > 4.5$ GeoNet CMT aftershocks till 15 Dec 2016 also illustrated as a function of centroid depth (after Bradley et al. (2017b)).

Litchfield et al. (2016) have so far identified at least nine fault segments (The Humps, Hundelee, Conway-Charwell, Upper Kowai, Fidget, Jordan Thrust, Papatea, Kekerengu, and Needles Faults) that have evidence of surface fault rupture. Eight of these faults are located onshore

with displacements obtained principally from direct field measurement of identifiable features; while rupture of the Needles Fault, located offshore at the northern end of the ruptured faults, has been identified from seabed uplift (NIWA, 2016). Most notably, essentially no surface rupture of the Hope Fault, the major fault identified $apriori$ in the region (Stirling et al., 2012), has been mapped to date (Litchfield et al., 2016).

3.2 Ground motion observations

3.2.1 A regional view

A total of 224 Volume 1 (i.e. unprocessed) ground motion records were obtained from GeoNet, and processed to obtain realistic spectral ordinates over the vibration period range of T=0.01-10 s, as discussed in Bradley et al. (2017b). Figure 3.2 illustrates the three component velocity time series of the GeoNet ground motion station recordings and their location relative to the causative rupture, which have a range in source-to-site distances of R_{rup}=0-216 km. As would be expected, the highest velocities are evident in the near-source region. However, the nature of the waveforms vary significantly at similar R_{rup} values depending on the back-azimuth from the site to the rupture - those stations in proximity to the southern end of the rupture in North Canterbury (e.g., stations WTMC, WIGC, CULC, HSES, CECS) exhibit high-amplitude short-duration ground motions, while those at the north end of the rupture in northern Marlborough (e.g., SEDS, BWRS) and Wellington (e.g., FKPS, NEWS) have substantially longer duration and also well-defined multiple wave packets indicating delayed' rupture initiation of several segments. Central South Island stations, such as in Molesworth (MOLS) and Wairau Valley (WVFS), also exhibit two clear velocity wave packets.

Figure 3.3 illustrates the distribution of recorded geometric mean[1] peak ground acceleration, PGA. In total, 47, 16, and 5 ground motions were observed with $PGA > 0.1$ g, 0.2 g, and 0.5 g, respectively, and will contribute substantially to the existing database of NZ strong motion records (e.g. Van Houtte et al., 2017). The subsequent sections discuss specific aspects of observed ground motions in regions of particular interest.

3.2.2 Accelerations in the near-fault region

Figure 3.4 illustrates four strong motion stations that are located in the immediate region of the causative faults. Station WTMC is located immediately near the inferred epicenter in Waiau; KIKS in Kaikoura, approximately halfway along the north-south extent of the rupturing faults; and KEKS and WDFS are located in Kekerengu and Ward, respectively, at the northern end of the rupturing faults.

Because of its location near the epicenter (see Figure 3.1), the ground motion observed at WTMC (Figure 3.4a) indicates a short strong motion duration relative to the other three near-fault stations. The ground motion accelerations at WTMC exceed 1.0 g in both horizontal directions, and notably the acceleration in the vertical direction reaches 2.7 g (with a 100 Hz

[1] Geometric mean metrics are used throughout unless noted.

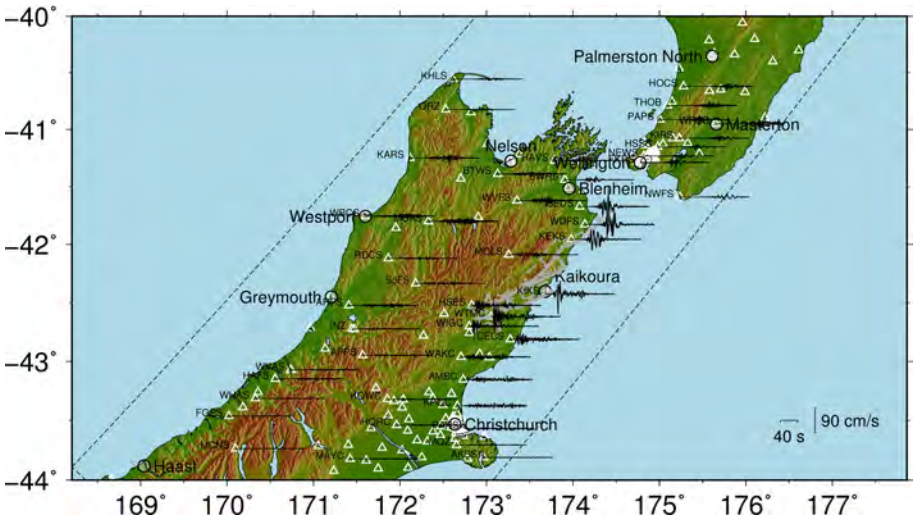

(a) 000

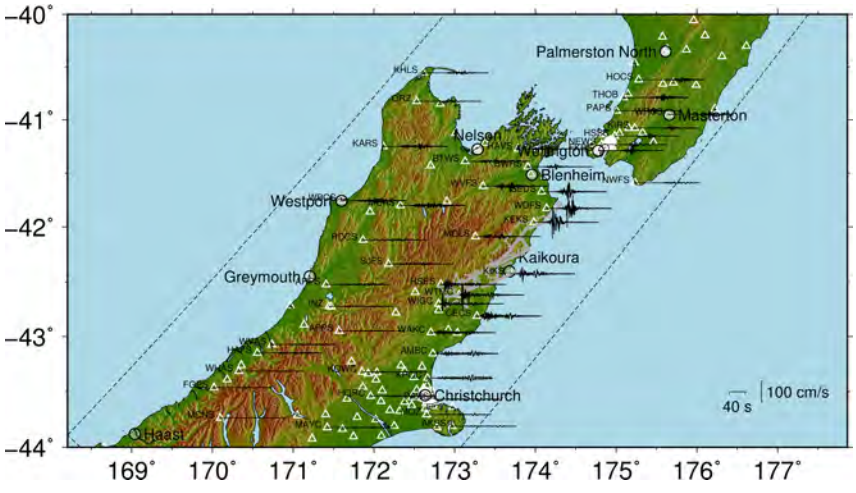

(b) 090

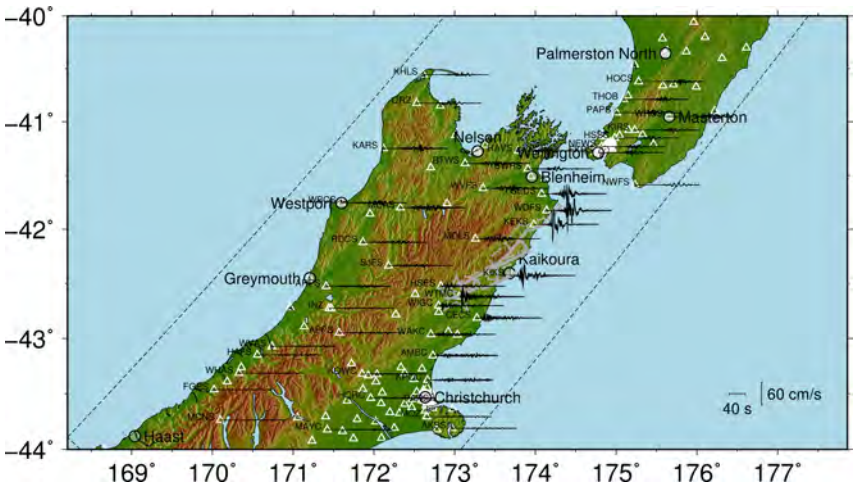

(c) vertical

Figure 3.2: Spatial illustration of the variation in observed ground motion accelerations at selected strong motion stations for: (a) north-south (000); (b) east-west (090); and (c) vertical components.

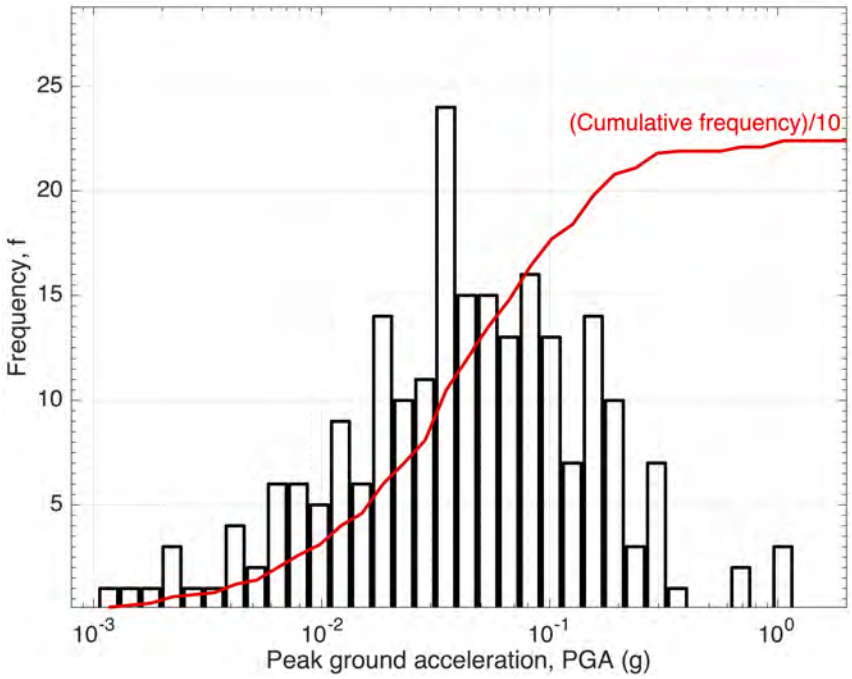

Figure 3.3: Distribution of geometric mean horizontal peak ground acceleration, PGA, recorded by strong motion stations (after Bradley et al. (2017b)).

high-cut filter). It is worth noting that the vertical accelerations exhibit strong asymmetry toward higher amplitudes in the positive direction (e.g., two exceedances of +2.0 g, while negative accelerations are limited to a little over -1.0 g). This phenomena has been documented in several ground motions from past earthquakes such as the 2011 Christchurch, New Zealand (Bradley and Cubrinovski, 2011; Fry et al., 2011), and the 2008 Iwate-Miyagi, Japan (Aoi et al., 2008; Yamada et al., 2009; Tobita et al., 2010) earthquakes. As demonstrated by Tobita et al. (2010) and Jeong and Bradley (2016), such asymmetry results from the varying near surface soil shear strength during induced compression and dilation. Furthermore, independent evidence of the extreme vertical accelerations in the vicinity of the WTMC site were seen in the form of bearing pads significantly moving (and, in one case, coming out from) between bridge abutment and girders at two bridges on Inland Road (SH70), within 2km from the WTMC station. Further information on this observed bridge damage is discussed in Chapter 6 of this report.

The KIKS station recorded relatively small levels of ground motion acceleration, given its location on a peninsula near the north-south mid-point of the rupturing fault segments, with horizontal and vertical peak accelerations of approximately 0.22 g and 0.27 g, respectively. The horizontal peak velocities are also a similarly small PGV=41-45 cm/s, as compared to the other three stations in Figure 3.4 which generally have PGV >80 cm/s (velocity time series at all four stations are shown in Figure 3.2).

Figure 3.4c and 3.4d illustrate the recorded ground motion accelerations at Kekerengu (KEKS) and Ward (WDFS) stations, which are located near the northern end of the rupturing faults, and are themselves located 16km apart. Both of these stations clearly illustrate acceleration records which are dominated by two predominant wave packets, one near $t = 60s$, and the other near

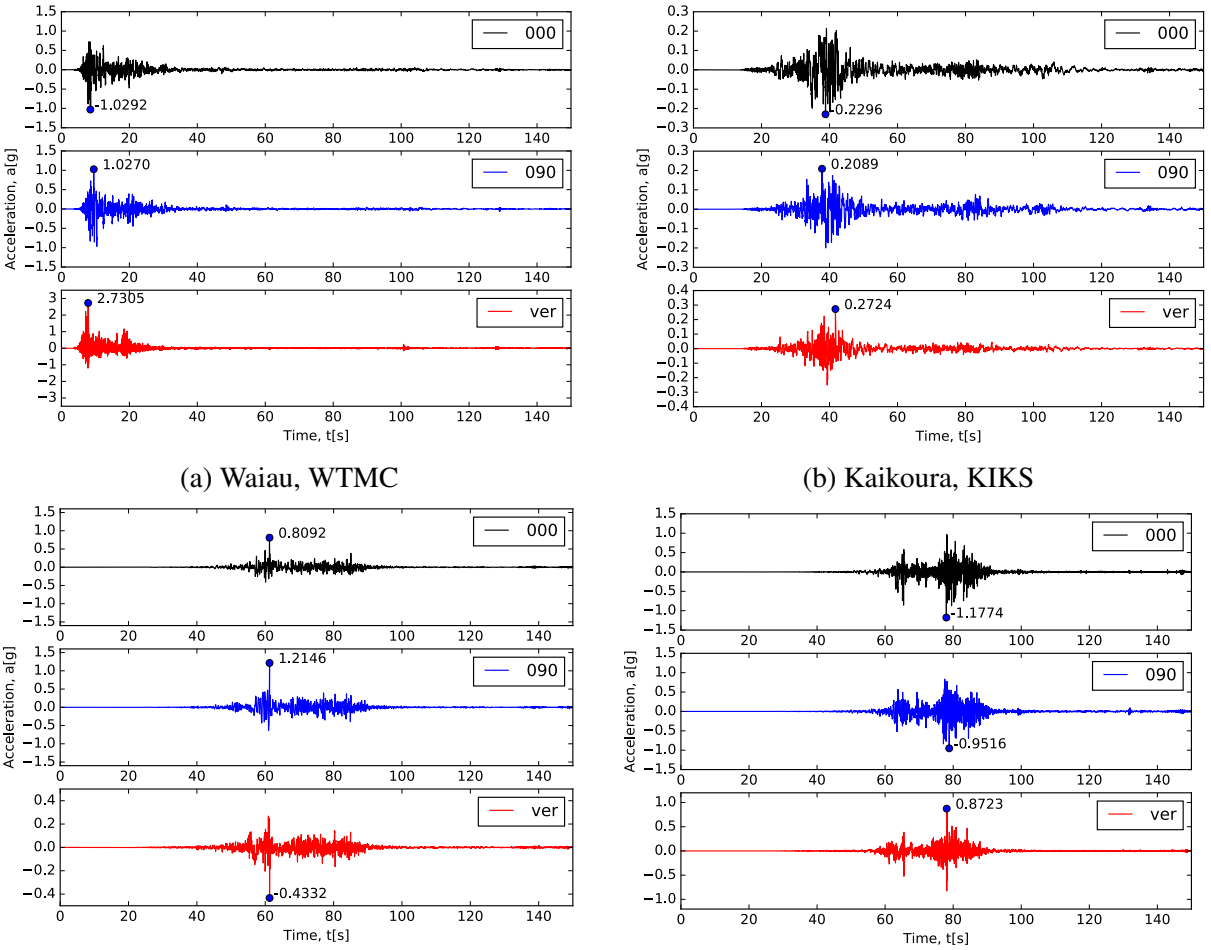

(a) Waiau, WTMC

(b) Kaikoura, KIKS

(c) Kekerengu, KEKS

(d) Ward, WDFS

Figure 3.4: Recorded ground motion accelerations in the immediate vicinity of the rupturing faults (locations noted in Figure 3.2). 000, 090, and ver represent north-south, east-west and vertical components, respectively. Maximum accelerations in each component are explicitly noted. Different vertical axis scales are used for each station, and between horizontal and vertical components for clarity (after Bradley et al. (2017b)).

$t = 80s$. Because of the fact that the KEKS station is within 2.5km of the mapped surface rupture of the Kekerengu fault (Litchfield et al., 2016) (with surface rupture displacements of 5-10m horizontal, and 1-2m vertical in the vicinity) it is reasonable to assume that the peak accelerations in the KEKS record correspond to the through-going rupture past this location. In contrast to KEKS, at the WDFS station the peak accelerations occur near $t = 80s$, which based on the source model in Figure 3.1 is inferred as the result of rupture of the Needles fault. Hamling (2016) inferred some (small) slip on the Grassmere fault located onshore from the Needles fault (and thus closer to the WDFS station). Further inferences of the source rupture from these observed ground motions are discussed in Bradley et al. (2017b).

3.2.3 Observed response spectra

Figure 3.5 illustrates the observed 5% damped (pseudo-acceleration) response spectra of stations in the near-fault region (i.e. Figure 3.4) as well as those in selected regions of North Canterbury, Marlborough, and Wellington. For reference, the site class C and D response spectra from NZS1170.5:2004 (NZS1170.5, 2004) for Z=0.4 are also shown (it is acknowledged that the value of Z varies over the sites/regions illustrated, but a common value is depicted for consistent reference). At short vibration periods ($T < 1s$) it can be seen that the largest response spectral amplitudes are observed in the near-fault region (Figure 3.5a) at the WTMC, KEKS, and WDFS stations, but also that large amplitudes are seen at the WIGC (Waiau Gorge) station in North Canterbury (Figure 3.5b) and SEDS (Seddon) station in Marlborough (Figure 3.5c). The short period ground motion amplitudes in Kaikoura and Wellington, other locations in North Cantebrury and Marlborough, have appreciably smaller values as a result of the attenuation associated with larger source-to-site distances.

The shape of the response spectra in Wellington (Figure 3.5d) are appreciably different than those in the other regions, principally in relation to their predominance of long-period ground motion - the result of both the source-to-site distance (leading to small short period amplitudes, as noted above), but also basin and site response effects (as discussed in depth by Bradley et al. (2017a,b)).

3.3 Comparison of observations with ground motion modelling

Bradley et al. (2017b) provide further insights into the observed ground motions discussed in the previous section via comparison with empirical and physics-based ground motion modelling. Figure 3.6 illustrates snapshots of the simulated ground motion wavefield (in the form of ground motion velocity at the surface) for nine time instants during the simulation (A video is available at: https://youtu.be/ZbI7rgnZ2U8)[2] During the first 30 seconds of the simulation it can be seen that the 'southern' fault segments (The Humps, Hundalee, Hope) rupture in a northerly direction. Approximately at $t = 40s$ the delayed rupture initiation at the southern end of the Jordan Thrust starts, and these 'northern' faults (Jordan, Kekerengu, Papatea, Needles) rupture over the following 40 seconds. Finally, after the rupture itself ceases at approximately $t = 80s$, the wavefield, with pronounced directivity migrating to the northeast, approaches the lower North Island.

Figure 3.7 provides a summary of the ground motion intensities over the simulation domain in the form of the peak ground acceleration, PGV (three-component maximum), and the Modified Mercalli Intensity (MMI) values, based on the MMI-to-PGV correlation of Worden et al. (2012). As implied by the wavefield snapshots in Figure 3.6, it can be seen that significant directivity occurs to the north east as a result of the fault geometries and rupture sequence (fortunately a

[2] The waveform anomaly near Lon:174.5° Lat:-43.2° is the result of a discontinity between the domain-wide model of Eberhart-Phillips et al. (2010), with the offshore portion of the Canterbury Velocity model of Lee et al. (2016). It is present only in the offshore region and the resulting localized spurious wavefield does not have a material effect on the simulated motion onshore.

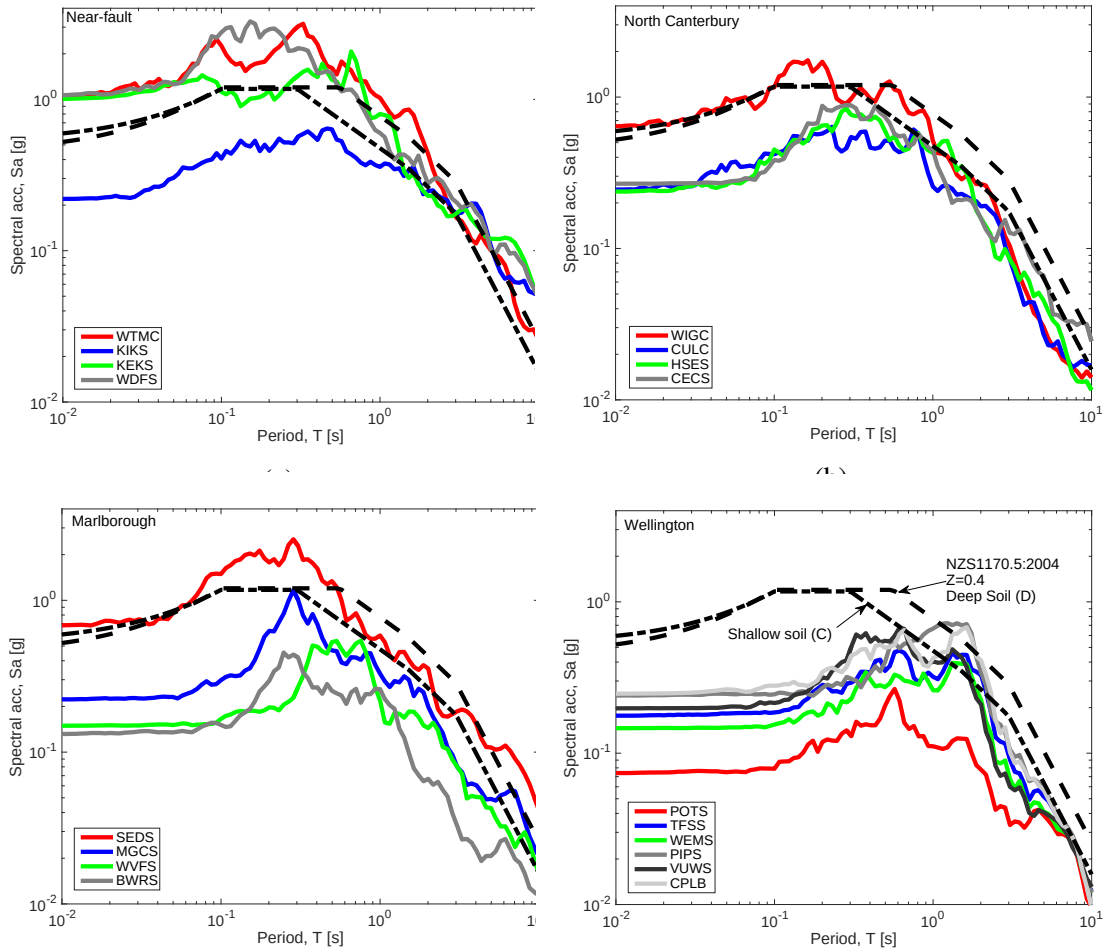

(c) (d)

Figure 3.5: A regional depiction of the geometric mean horizontal 5% damped pseudo-acceleration response spectra observed in: (a) the near-fault; (b) North Canterbury; (c) Marlborough; and (d) Wellington. Four letter station codes in the figure legends can be located spatially in Figure 3.2

significant potion of the $MMI > 8$ region occurs offshore, or in low-population density areas). As a result, the ground motion amplitudes to the south and west of the causative faults were modest in comparison. It can be seen that the Marlborough and Lower North Island was subject to approximately $MMI = 7$ ground motion amplitudes with $PGV = 20 - 40cm/s$.

3.3.1 Comparison of response spectra modelling and observations

Figure 3.8 illustrates the observed and modelled ground motion spectral amplitudes for four vibration periods ($T = 0.0, 0.2, 3.0,$ and $10.0s$) as a function of source-to-site distance. The observed and simulated ground motion amplitudes for the 162 stations within the simulation domain are shown. The stations are also separately annotated based on their location in either the North or South Island. For reference, the NZ-specific empirical ground motion model of Bradley (2013) is also shown. It can be seen that the simulation provides a generally good comparison with the observed amplitudes. In particular, the distance attenuation in the observations

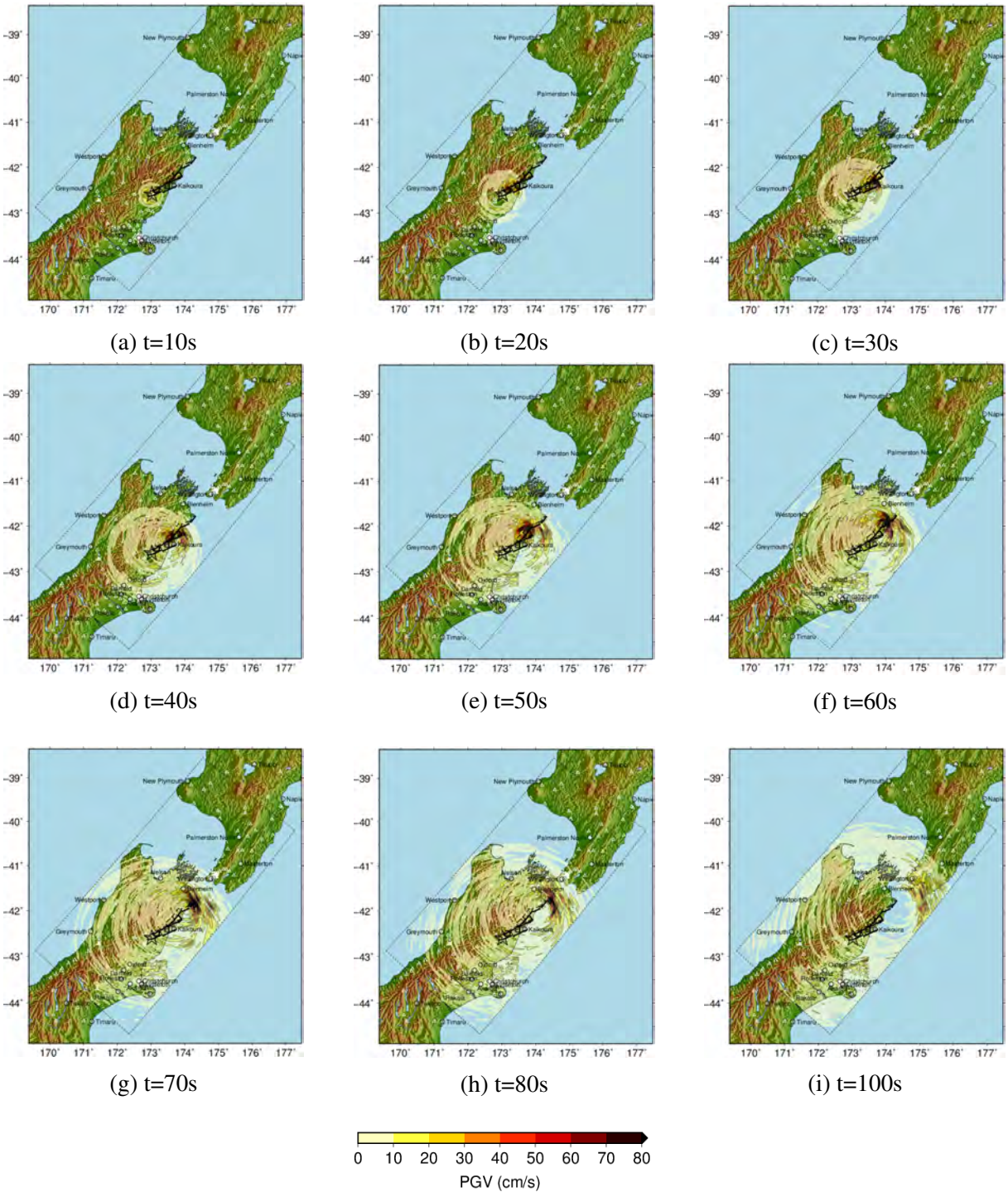

Figure 3.6: Time snapshots of simulated peak ground velocity (three component maximum). The causative fault segments and simulation domain are also indicated. A video of the simulation is available in the electronic supplement to this article and at: https://youtu.be/ZbI7rgnZ2U8 (after Bradley et al. (2017b)).

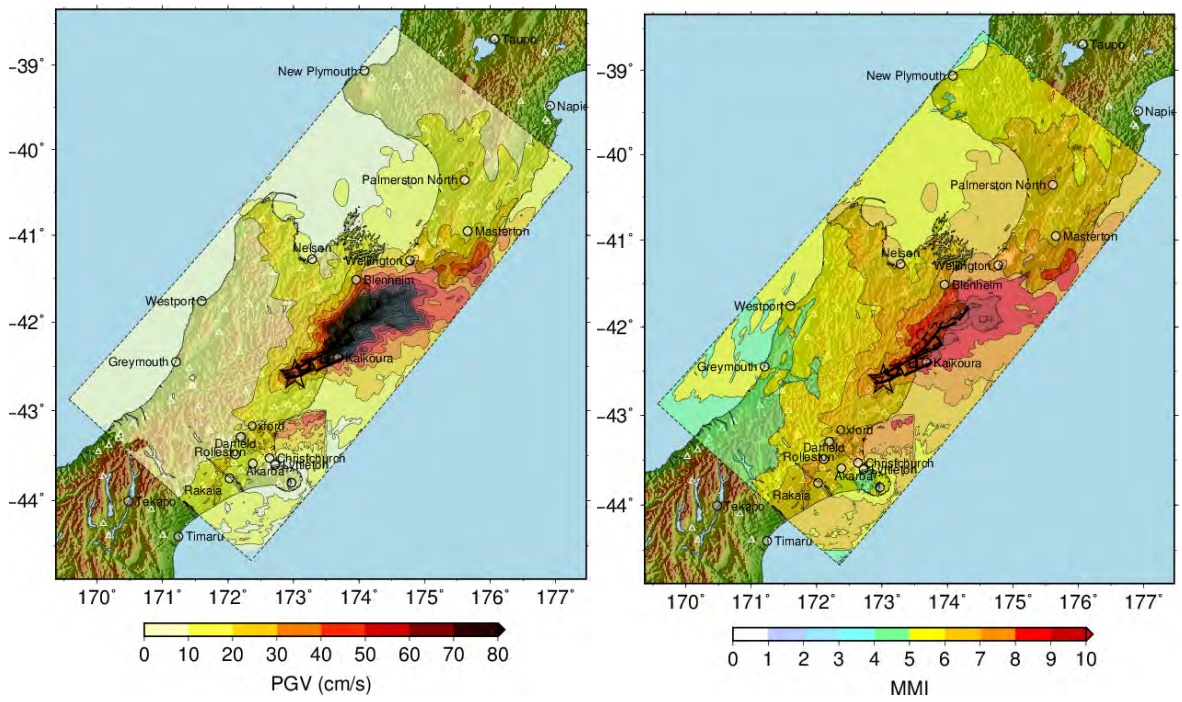

Figure 3.7: Spatial variation of: (a) peak ground velocity (PGV); and (b) Modified Mercalli Intensity (MMI) from the ground motion simulation (vector maximum of the two horizontal components).

at short periods (i.e. $T = 0.0$ and $0.2s$) is consistently predicted by the simulations, while the empirical model predicts a slower attenuation; conversely at long periods, the empirical model predicts a faster attenuation than exhibited by both the observed and simulated amplitudes. Although, not easily evident due to the large number of data points present, the simulations and observations are also broadly consistent in the higher-than-average amplitudes of North Island ground motions relative to those in the South Island for the same source-to-site distance, because of the aforementioned effect of rupture directivity. Bradley et al. (2017b) present further details on the predictive capabilities of the empirical and simulation-based methods.

3.4 Discussion

This chapter has provided a summary of observed ground motions from the 14 November 2016 $M_w 7.8$ Kaikoura earthquake. Ground motions were observed at over 200 strong motion stations, with 47 ground motions exceeding 0.1 g PGA. The strong motion dataset provide a significant complement to prior NZ strong motion data. The near-source ground motions clearly highlight the complexity of the earthquake rupture, with multiple wave packets in time clearly evident, and several very large horizontal and vertical amplitudes recorded. The response spectra of observed ground motions illustrated regions with large short and long period ground motion amplitudes. The long period amplitudes in Wellington are of particular note as discussed further in Bradley et al. (2017a).

Despite the rupture complexity of this event, the observed ground motions are broadly consistent with ground motion modelling. Short period ground motion amplitudes are well approximated

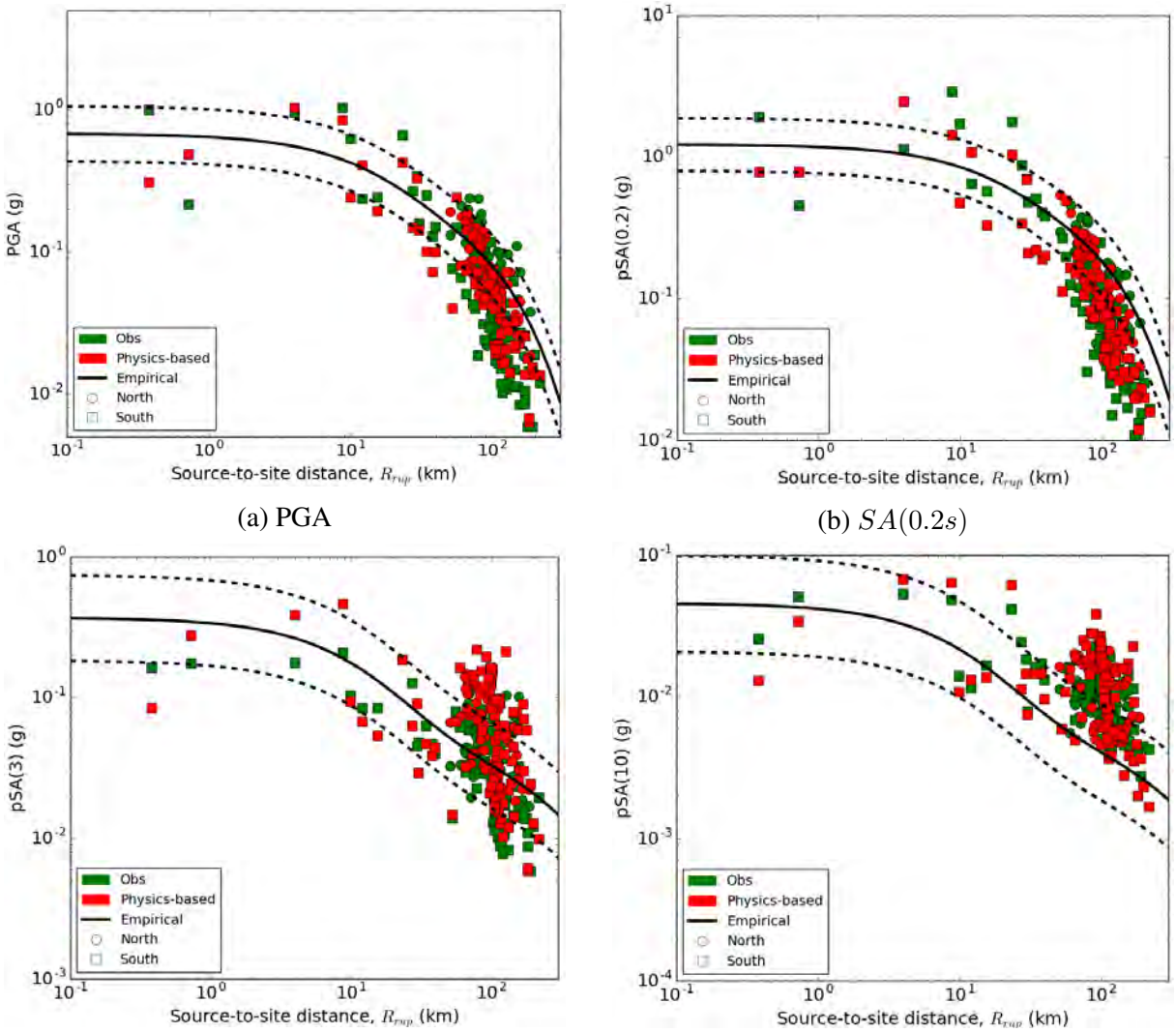

(a) PGA

(b) $SA(0.2s)$

(c) $SA(3.0s)$

(d) $SA(10.0s)$

Figure 3.8: Observed, simulated, and empirically-predicted geometric mean 5% damped response spectra as a function of source-to-site distance, R_{rup}. Symbol shape indicates location of the station in the North or South Island. The median, and 16^{th}/84^{th} percentiles of the empirical prediction Bradley (2013) are represented by solid and dashed lines, respectively (after Bradley et al. (2017b)).

by empirical and simulation models, although the observations (and simulation modelling) indicate greater attenuation at larger distances ($R_{rup} > 60km$) than in empirical modelling. Long period ground motion amplitudes are, on average, well approximated by the simulation-based modelling, and exceed empirical models at long vibration periods. A strong directivity is seen in the long period spectral amplitudes, with larger values at sites located in the general northward direction from the causative faults. Such directivity is captured to some extent in the simulations, but not accounted for in the particular empirical model used (although there are directivity modification models for empirical prediction developed by others).

References

Aoi, S., Kunugi, T., and Fujiwara, H. (2008). "Trampoline effect in extreme ground motion." *Science*, 322(5902), 727–730.

Bradley, B. A. (2013). "A new zealand-specific pseudospectral acceleration ground-motion prediction equation for active shallow crustal earthquakes based on foreign models." *Bulletin of the Seismological Society of America*, 103(3), 1801–1822.

Bradley, B. A. and Cubrinovski, M. (2011). "Near-source strong ground motions observed in the 22 February 2011 Christchurch earthquake." *Seismological Research Letters*, 82(6), 853–865.

Bradley, B. A., Wotherspoon, L. M., and Kaiser, A. E. (2017a). "Ground motion and site effect observations in the Wellington region from the 2016 Mw7.8 Kaikōura, New Zealand earthquake." *Bulletin of the New Zealand Society for Earthquake Engineering*, 50(2), 94–105.

Bradley, B. A., Razafindrakoto, H. N. T., and Polak, V. (2017b). "Ground motion observations from the 14 November 2016 Mw7.8 Kaikōura, New Zealand earthquake and insights from broadband simulations." *Seismological Research Letters*, (DOI: 10.1785/0220160225).

Eberhart-Phillips, D., Reyners, M., Bannister, S., Chadwick, M., and Ellis, S. (2010). "Establishing a Versatile 3-D Seismic Velocity Model for New Zealand." *Seismological Research Letters*, 81(6), 992–1000.

Fry, B., Benites, R., and Kaiser, A. (2011). "The character of accelerations in the Mw6.2 Christchurch earthquake." *Seismological Research Letters*, 82(6), 846–852.

Hamling, I. (2016). "Preliminary source inversion of the 14 November 2016 Mw7.8 Kaikoura earthquake (personal communication).

Jeong, S. and Bradley, B. A. (2016). "Simulation of strong asymmetrical vertical acceleration at Heathcote Valley in the 2010-2011 Canterbury earthquakes." *New Zealand Society for Earthquake Engineering Annual Conference*.

Lee, R., Bradley, B., Ghisetti, F., and Thomson, E. (2016). "Development of a 3D high-resolution velocity model for the Canterbury, New Zealand region." *Bulletin of the Seismological Society of America (submitted)*.

Litchfield, N. J., Benson, A., Bischoff, A., Hatem, A., Barrier, A., Nicol, A., Wandres, A., Lukovic, B., Hall, B., Gasston, C., Asher, C., Grimshaw, C., Madugo, C., Fenton, C., Hale, D., Barrell, D., Heron, D., Strong, D., Townsend, D., Nobe, D., Howarth, J., Pettinga, J., Kearse, J., Williams, J., Manousakis, J., Mountjoy, J., Rowland, J., Clark, K., Pedley, K., Sauer, K., Berryman, K., Hemphill-Haley, M., Stirling, M., Villeneuve, M., Cockroft, M., Khajavi, N., Barnes, P., Villamor, P., Carne, R., Langridge, R., Zinke, R., Van Dissen, R.,

McColl, S., Cox, S., Lawson, S., Little, T., Stahl, T., Cochran, U., Toy, V., Ries, W., and Juniper, Z. (2016). "14th November 2016 M7.8 Kaikoura Earthquake. Preliminary surface fault displacement measurements. Version 2. GNS Science. http://dx.doi.org/10.21420/G2J01F .

NIWA (2016). ""Scientists detect huge fault rupture offshore from Kaikoura" https://www.niwa.co.nz/news/scientists-detect-huge-fault-rupture-offshore-from-kaikoura 22 November 2016 (last accessed 20 Dec 2016).

NZS1170.5 (2004). *Structural design actions, Part 5: Earthquake actions - New Zealand*. Standards New Zealand.

Stirling, M., McVerry, G., Gerstenberger, M., Litchfield, N., Van Dissen, R., Berryman, K., Barnes, P., Wallace, L., Villamor, P., Langridge, R., Lamarche, G., Nodder, S., Reyners, M., Bradley, B., Rhoades, D., Smith, W., Nicol, A., Pettinga, J., Clark, K., and Jacobs, K. (2012). "National seismic hazard model for New Zealand: 2010 update." *Bulletin of the Seismological Society of America*, 102(4), 1514–1542.

Stirling, M. W., Litchfield, N. J., Villamor, P., Van Dissen, R. J., Nicol, A., Pettinga, J., Barnes, P., Langridge, R. M., Little, T., Barrell, D. J. A., Mountjoy, J., Ries, W. F., Rowland, J., Fenton, C., Hamling, I., Asher, C., Barrier, A., Benson, A., Bischoff, A., Borella, J., Carne, R., Cochran, U., M., C., Cox, S. C., Duke, G., Fenton, F., Gasston, C., Grimshaw, C., Hale, D., Hall, B., Hao, K., Hatem, A., Hemphill-Haley, M., Heron, D., Howarth, J., Juniper, Z., Kane, T., Kearse, J., Khajavi, N., Lamarche, G., Lawson, S., Lukovic, B., Madugo, C., Manousakis, I., McColl, S., Noble, D., Pedley, K., Sauer, K., Stahl, T., Strong, D., Townsend, D. B., Toy, V., Villeneuve, M., Wandres, A., Williams, J., Woelz, S., and Zinke, R. (2017). "The Mw7.8 2016 Kaikōura earthquake: Surface fault rupture and seismic hazard context." *Bulletin of the New Zealand Society for Earthquake Engineering*, 50(2), 73–84.

Tobita, T., Iai, S., and Iwata, T. (2010). "Numerical analysis of near-field asymmetric vertical motion." *Bulletin of the Seismological Society of America*, 100(4), 1456–1469.

Van Houtte, C., Bannister, S., Holden, C., Bourguignon, S., and McVerry, G. (2017). "The New Zealand strong motion database." *Bulletin of the New Zealand Society for Earthquake Engineering*, 50(1), 1–20.

Worden, C. B., Gerstenberger, M. C., Rhoades, D. A., and Wald, D. J. (2012). "Probabilistic relationships between ground-motion parameters and Modified Mercalli Intensity in California." *Bulletin of the Seismological Society of America*, 102(1), 204–221.

Yamada, M., Mori, J., and Heaton, T. (2009). "The slapdown phase in high-acceleration records of large earthquakes." *Seismological Research Letters*, 80(4), 559–564.

4 GEOTECHNICAL ASPECTS ON THE SOUTH ISLAND OF NEW ZEALAND

This chapter identifies locations of liquefaction manifestations and discusses the effects of liquefaction and related phenomena on the South Island of New Zealand resulting from the 2016, M_w7.8 Kaikoura earthquake. Detailed observations are recorded to document the occurrence and non-occurrence of liquefaction in areas shaken at different levels of intensity. Strong motion recordings indicate high peak ground accelerations (PGA) occurred in the Waiau valley of North Canterbury (marked "Area C" in Figure 4.1). Horizontal accelerations at the Waiau strong motion station (WTMC) were in excess of 1 g and vertical accelerations in excess of 2.7 g. The ground motions were significantly attenuated in the main urban areas of the South Island; the recorded peak ground accelerations were in the range of 0.14 g to 0.27 g in the areas around Blenheim (Area A) and Kaikoura (Area B). A more detailed summary of the ground motion characteristics across the South Island is provided in Chapter 3 of this report.

In the days and weeks following the earthquake, a collaborative approach was taken to the reconnaissance across the South Island, and involved New Zealand researchers and engineers, as well as visiting academics and members of the Geotechnical Extreme Events Reconnaissance (GEER).Association. Reconnaissance was undertaken in 3 phases. In the days following the earthquake, exploratory missions were undertaken to define broad areas where earthquake-related damage had occurred. Additional field surveys were undertaken in the areas marked A to C in Figure 4.1 between 17th November and 11th December 2016 first to record perishable data (such as evidence of liquefaction, lateral spreading, and damage to structures) and later to characterise specific sites.

Given the geographic distribution of the varying geologic settings, liquefaction hazard, and ground motions, each of the four areas shown in Figure 4.1 are presented separately in subsequent sections of this chapter in order of north to south. In the area of Blenheim, severe liquefaction and lateral spreading occurred on the flood plains of the Wairau River, particularly on inner meander bends and locations of paleo features. In Kaikoura, a series of localised failures in soft soil deposits caused large lateral displacements along Lyell Creek and caused damage to a number of houses built within 30 m of the creek. Despite the extreme ground motions recorded close to the town of Waiau, relatively little evidence of liquefaction was observed, and the main impacts in this area were to the bridges, many of which showed severe structural distress. Detailed reconnaissance in Christchurch (Area D) was not carried out, though observations from four sites in the city and towns to the north are briefly discussed.

It is important to state that while a number of examples of damage are presented in this paper, the most significant impacts of the 2016 Kaikoura Earthquake arose from the numerous landslides across the South Island (which cut off the town of Kaikoura, as well as blocking and severely damaging the N-S highway and railway). These aspects are outside the scope of this report.

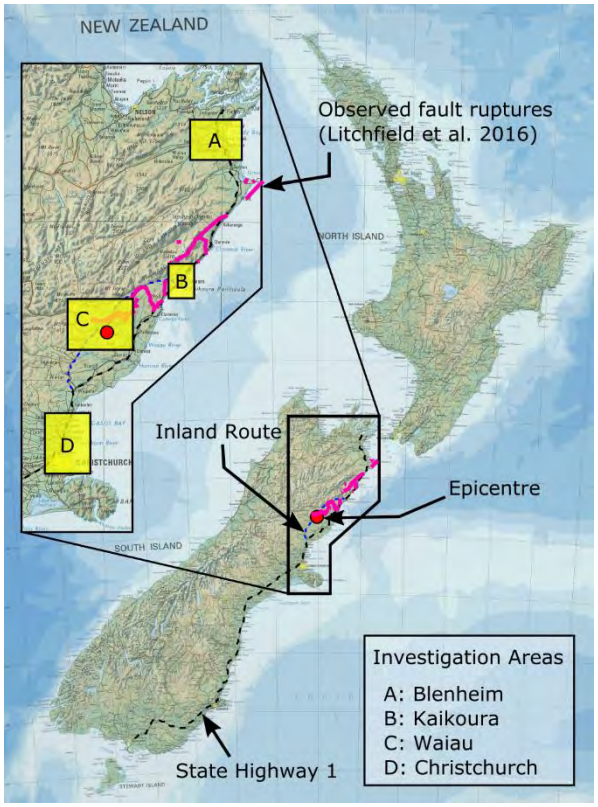

Figure 4.1: Location of main reconnaissance areas. Dashed lines indicate road routes outside of these main areas that were also surveyed by reconnaissance teams.

4.1 Summary of Reconnaissance - Marlborough

The region of Marlborough is located at the north-eastern corner of the South Island, New Zealand. The landscape is dominated by a series of north-east trending mountain ranges and intervening valleys associated with uplift along the major faults within the Marlborough Fault Zone The region has a high level of seismic hazard due to the many active faults within the region, including the Wairau, Clarence, Awatere, Kekerengu and Vernon faults (Begg & Johnston, 2000). The township of Blenheim is situated approximately 5 km from the east coast, within the relatively flat expanse of the Wairau Plain within the Wairau Valley. It has a population of ~30,700 and a total urban area of approximately104 km^2, resulting in a relatively low urban density of ~300 people/km^2.

The Wairau Valley is transected by the braided Wairau River which flows eastwards approximately along the trace of the Wairau Fault. The township is predominantly situated upon Holocene swamp deposits composed of poorly consolidated silt, mud, peat, and sand. To the west, alluvial outwash gravels deposited by the Wairau River predominate while Holocene coastal and marine sands to silts predominate to the east and are locally cross-cut by young fluvial sands to silts. The coastal sediments reflect marine regression and coastal progradation following the mid-Holocene highstand with the coastline approximately extending inland to the eastern extent of the township at approximately 6,500 years before present. The interaction of the alluvial and marine processes proximal to the coast likely resulted in the swamp formed within the township.

Figure 4.2: Overview of the Marlborough region and location of significant historic earthquakes.

Sediments within the township have been re-worked and re-deposited by the Wairau River and meandering Opaoa and Taylor Rivers within the township. The rivers within the region have been extensively modified to improve drainage and reduce flooding within the township. The Opaoa River is fed from the Omaka River and was re-named from the Opawa River in 2015, as a result, the previous spelling is present in historical maps of the region. The loosely consolidated fine sands to silts deposited by these rivers, combined with high water table levels (1-2 m) to the east of the township pose a localized high liquefaction hazard.

The Marlborough region has experienced liquefaction in previous historic earthquakes, namely the 1848 Marlborough earthquake, the 1855 Wairarapa earthquake, and minor episodes during the 2013 Cook Strait earthquake sequence (epicentres of these earthquakes are summarised in Figure 4.2). Written accounts from the M_W7.5 1848 Marlborough earthquake (Mason & Little 2006) suggest the occurrence of lateral spreading, sand ejecta and subsidence in the Wairau Plain (Arnold 1847):

"the effects of the earthquake were very apparent on the river bank: there were a great many large cracks in the ground, some as much as two feet wide: and I also saw numerous deep holes, by which a lower stratum of sand and water had burst its way thro' the overlying ground, and covered everything with sand for some distance."

The M_W8.2 Wairarapa earthquake again resulted in liquefaction surface manifestations across the Wairau Plain, and in the Awatere and Clarence Valleys along the rivers. A basic summary of the

areas affected is presented in Figure 4.3; Thompson (1859) provides an example of a written account from the time:

"in the Wairau Valley … near the river bed, numerous systems of earthquake fissures can be observed, which always trend parallel to the course of the river and are intersected at various angles by abrupt bends in the river" and that "several fissures in the earth, four feet deep, and sufficient to admit a man, yawned…."

Another significant event in this region was the M_W5.8 1966 Seddon earthquake. Structural and infrastructure damage occurred during this event. No evidence of liquefaction was reported, but it is possible minor liquefaction occurred in rural areas and went unreported.

During the 2013 Cook Strait earthquake sequence there was evidence of minor liquefaction manifestation following the 16 August 2013 M_W6.6 Lake Grassmere earthquake. This damage was confined to the highly susceptible sediments to the east of Blenheim (mainly along the Opaoa River) and in the Awatere Valley region, including damage on the southern edge of Lake Grassmere close to the epicentre of the earthquake, at the approaches of the Awatere Bridge and a number of other smaller bridges in the region.

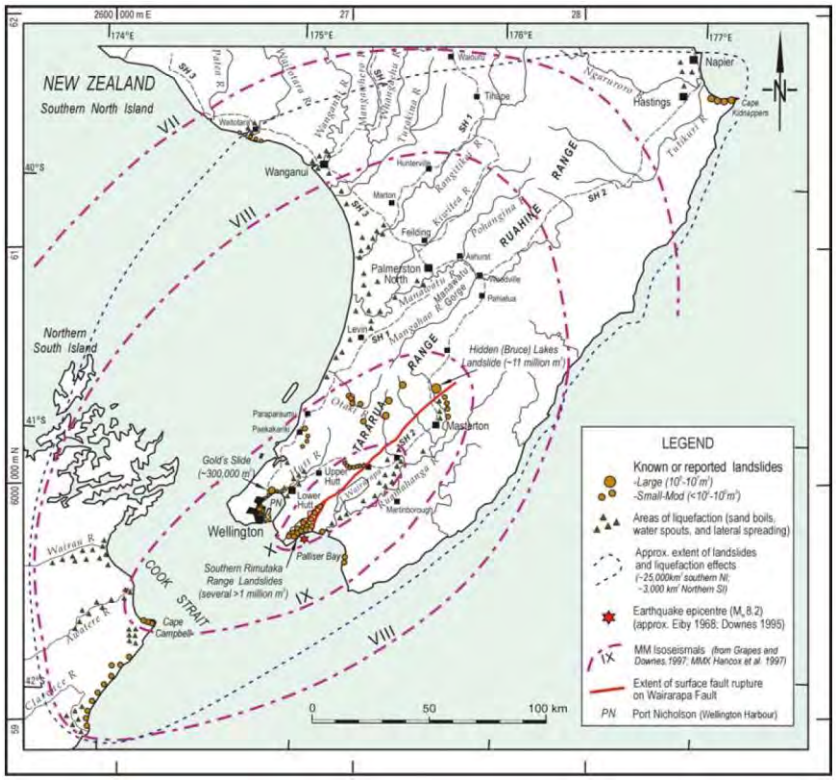

Figure 4.3: Map showing location of known landsliding and manifestation of liquefaction due to the 1855 Wairarapa earthquake (after Hancox 1997). The Marlborough region is in the lower left corner of this figure.

The reconnaissance in the Marlborough region focussed on the outlined area in Figure 4.4. There were two sets of reconnaissance surveys undertaken in this region, the initial survey was conducted between 17 and 18 November 2016 and a follow up survey was conducted between 5 and 7 December 2016. The information collated during these surveys was complemented by information gathered from local consulting engineers and the Marlborough District Council.

Within the Wairau valley, liquefaction and lateral spreading was the major feature of ground damage, and was largely observed along the Lower Wairau and Opaoa Rivers. Severe manifestations of liquefaction were recorded in the area of the Equestrian Park and the Blenheim Rowing Club. However, very few buildings are present in these areas, and the engineering impact was generally low. It is also important to note that despite the very loose nature of these deposits, the extent and quantity of ejecta is significantly less than what was observed in either of the 2010 Darfield or 2011 Christchurch Earthquakes (Cubrinovski et al. 2010, Cubrinovski et al. 2011). Some moderate liquefaction was observed in a few locations within the township of Blenheim, but these locations were either along the river or in the area of the sports fields at the north of the town and had limited impact on infrastructure.

The first part of this chapter focusses on the damage within the urban extents of Blenheim and particular sites of interest in the area. The second part of this chapter focusses on damage along the rivers outside of Blenheim within the Wairau Plains.

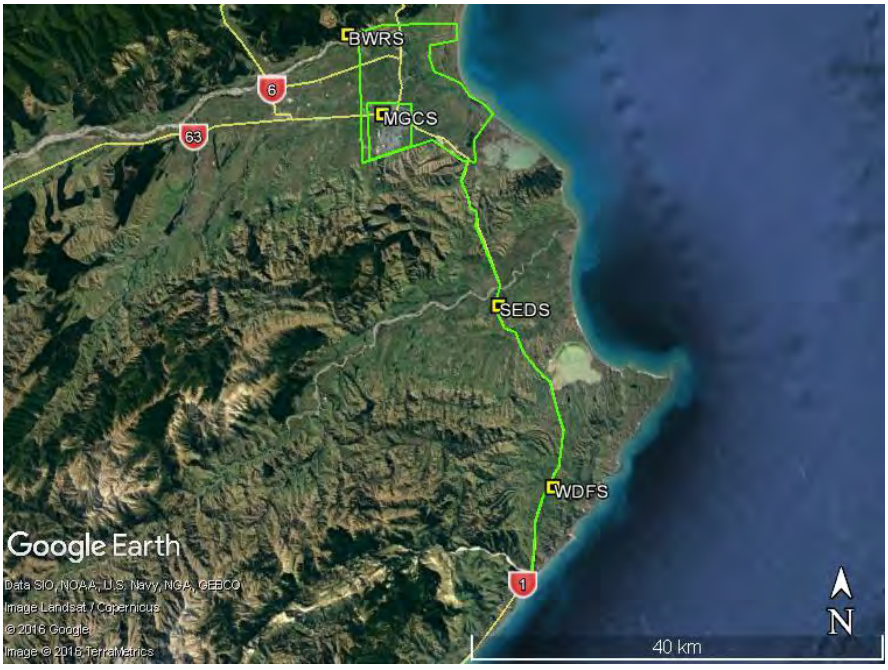

Figure 4.4: Overview map of reconnaissance areas in Marlborough outlined in green and path along State Highway 1. Location of strong motion stations highlighted in this figure, with MGCS in the Blenheim Urban Area.

The ground motion intensity varied significantly over the Marlborough region, with the location of the strong motion stations shown in Figure 4.4. In Ward, the station WDFS recorded a geometric mean horizontal PGA of approximately 1.1 g. Further to the north in Seddon a geometric mean PGA = 0.66 g was obtained (station SEDS), and the shaking was PGA = 0.22 g (station MGCS) in the Blenheim (i.e. Lower Wairau River area).

4.1.1 Blenheim Urban Area

Both reconnaissance surveys and discussions with local engineers and Marlborough District Council were able to provide a detailed summary of the liquefaction related impacts and manifestations in the Blenheim urban area. Figure 4.5 summarises these locations, with all other areas not affected by liquefaction surface manifestations. Localized evidence of lateral spreading and liquefaction ejecta were observed within the inner meander bends of the Taylor River and Opaoa Rivers within this area. No evidence of lateral spreading was observed within the outer meander bends, nor beneath any of the road bridges surveyed.

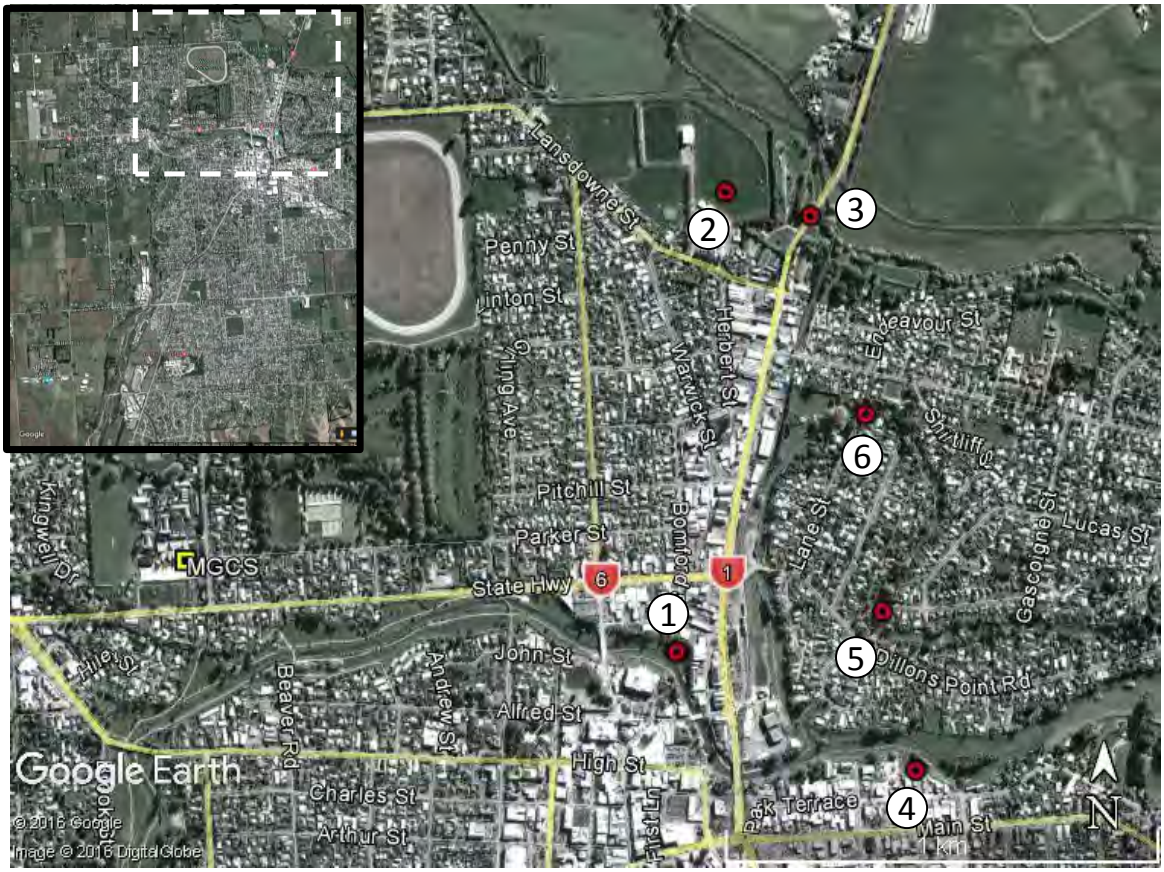

Figure 4.5: Map summarising impacts in urban Blenheim, and location of the MGCS SMS. Inset indicates area where all liquefaction impacts have been summarised and the zoomed in area highlighted in the wider figure (approx. centre of image: S41.5046, E173.9545).

4.1.1.1 Taylor River

Localized cracking and elliptical liquefaction ejecta features were observed along the northern bank of the Taylor River, in the area behind 3-7 Auckland Street (Location 1 in Figure 4.5). This area was less than a metre above the river level and was relatively flat as shown in Figure 4.6. The ejecta were observed in a depression that was filled with standing water and located approximately 10 m away from river bank. The ejecta feature ranges in length from 5 to 7 m, and 1 to 1.2 m in diameter (Figure 4.6). Cracks approximately 2 to 5 cm wide were observed in a garden, also located within the depression, and were surrounded by localized liquefaction ejecta. The ejecta were uniformly composed of grey fine-medium sand and the particle size distributions of these ejecta are shown in Figure 4.7 (marked in the legend as TR-1 and TR-2). No ejecta or cracking was observed within 10 m of the river bank. The area was formerly within the meandering channel of the Taylor River before modification and straightening of the river took place in 1969, subsequently reducing flow levels (Marlborough District Council 2017). No other evidence of liquefaction manifestation was observed upstream of this point along the Taylor River.

Figure 4.6: Localized elliptical liquefaction ejecta features along the northern bank of the Taylor River (Location 1 in Figure 4.5), approximately 10 to 15 m from the river (S41.5096, E173.9577, facing SE).

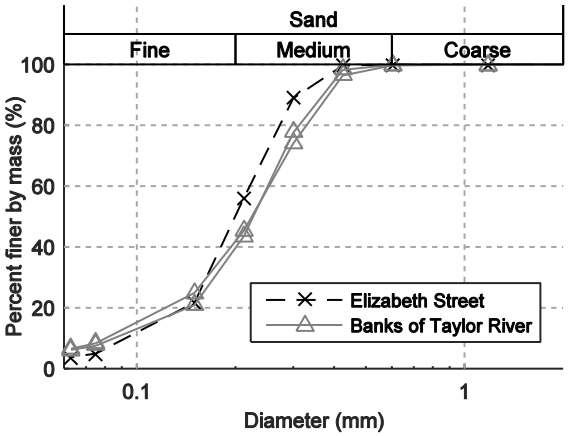

Figure 4.7: Particle size distribution of ejecta samples in the Blenheim CBD area (Taylor River: TR-1 & TR-2 (S41.5095, E173.9575) and Elizabeth Street: EC-1 (S41.5089, E173.9636)).

4.1.1.2 Lansdowne Park

Surficial evidence of liquefaction was observed in the area of Lansdowne Park on the northern edge of Blenheim (Location 2 in Figure 4.5). The main sports facility was built in the area south of the current channel of the Opaoa River. The locations of ejecta in the southern area of the park were surveyed by local engineers and are shown superimposed on aerial photography in Figure 4.8. Additionally, the location where ejecta samples were collected are designated with blue stars. It should be noted that additional liquefaction features formed to the north of the rugby pitch which are not shown.

Cone penetration tests (CPT) at Lansdowne Park suggest that the soil profile at this site includes a silt cap typically between 2.0 to 2.5 m thick, underlain by silty sand, and with the water table between 1.4 to 2.0 m below the ground surface. Wet sieve analyses (carried out in general accordance with ASTM D422-63(2007)e2 were performed on the ejecta specimens recovered from the locations shown in Figure 4.8. In general, the particle size distributions can be separated into two groupings. LDP-3, 4, 5, 8, 9 and 10 are relatively similar fine sands; whereas the samples LDP-1, 2, 4, 6 and 7 are medium sands. The particle size distributions of these two groups are summarised in Figure 4.9.

Historical maps from 1895 indicate that the north-east corner of the site lies in the river channel of that time, which has since been abandoned (Cook, 1895). In particular, the line of ejecta features starting from LDP-6 and moving south east towards LDP-2 in Figure 4.8 correlate closely with the southern edge of the river channel circa 1895. Historic photos show that this area was already filled by 1938 (Marlborough District Council 2017), but the position of the former river channel is indicted by a topographic depression and markings in the vegetation. Additional liquefaction ejecta features were discovered within paleo-channels in the former flood plain to the west of the park (Figure 4.10).

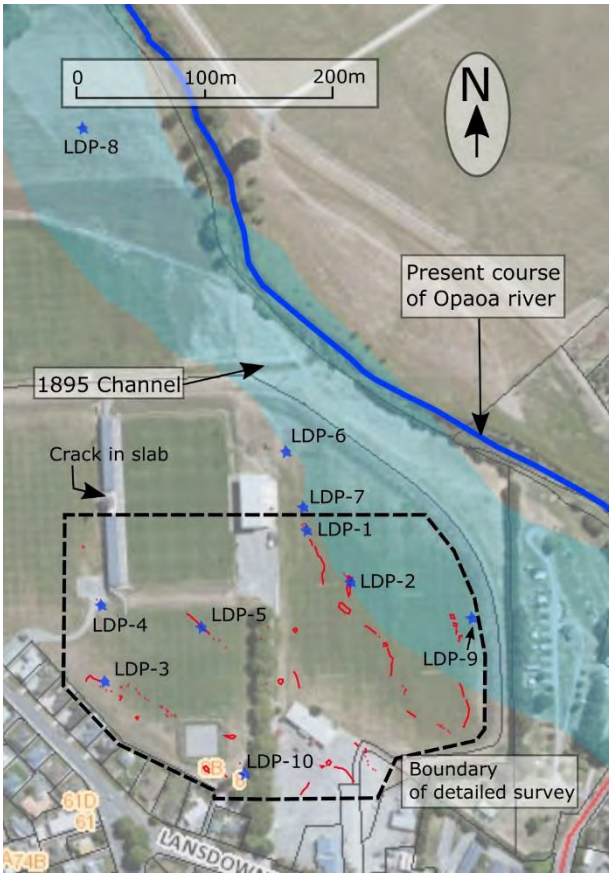

Figure 4.8: Location of ejecta at Lansdowne Park designated by red regions, with sample locations designated by blue stars. The present course and the abandon channel of the Opaoa River are designated by a blue line and blue shading, respectively (approx. centre of image: S41.4980, E173.9587).

The sand boils discovered at Lansdowne Park were typically of the order of 1-2 m in diameter, and in many cases formed linear features, as shown in Figure 4.8, with a typical example shown in Figure 4.11. In a few limited locations, larger ejecta features of around 25 m^2 (plan area) were observed (Figure 4.12). Liquefaction ejecta were not observed around the edges of the foundations of the main stadium buildings. Small features were observed on the earthen bank on the south edge of the stadium (i.e. at the locations of LDP-4 and LDP-5 shown in Figure 4.8). Additionally, a small amount of ejecta was located at the base of a floodlight tower, as shown in Figure 4.13.

The only readily observable damage to the permanent structures at Lansdowne Park was a crack in the concrete foundation slab running east-west at the location of the stadium entrance, mid-way along the western stand (Figure 4.14).

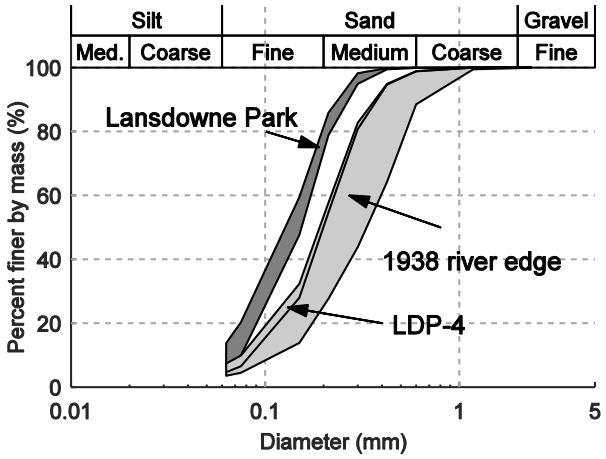

Figure 4.9: Particle size distributions of ejecta samples at Lansdowne Park.

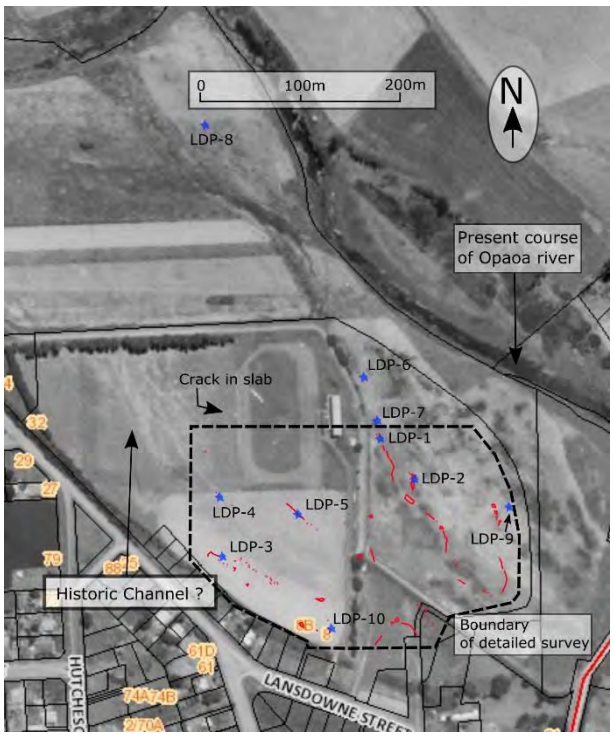

Figure 4.10: Locations of ejecta at Lansdowne Park overlaid on 1938 Photograph (approx. centre of image: S41.4980, E173.9587) (Marlborough District Council, 2017).

Figure 4.11: Linear liquefaction feature at Lansdowne Park (close to location of sample LDP-1, S41.4990, E173.9586, looking SE, 17 Nov 2016).

Figure 4.12: Largest liquefaction feature at Lansdowne Park (17 Nov 2016, S41.4996, E173.959, facing W).

Figure 4.13: Liquefaction ejecta at flood light tower (17 Nov 2016, S41.5003, E173.9572, facing N).

Figure 4.14: Crack in foundation slab on west stand (17 Nov 2016, S41.4993, E173.9569, facing E).

Figure 4.15: Cracking adjacent to the southern pier of the Opawa River Bridge (14 Nov 2016, S41.5006, E173.9616, facing N).

To the east of Lansdowne Park there was evidence of lateral spreading and grey sand ejecta running through the Top 10 Holiday Park and beneath the southern end of the Opaoa River Bridge (Location 2 in Figure 4.5). These features also seem to align with the position of the 1895 river channel described previously. Ground cracking was evident adjacent to the piers of the Opawa River Bridge as shown in Figure 4.15, with a few centimetres of settlement and horizontal displacement recorded.

4.1.1.3 Park Terrace

Moderate volumes of liquefaction ejecta and lateral spreading were observed at an inner-meander bend of the Opaoa River north of Park Terrace, just downstream from the confluence of the Opaoa and Taylor Rivers (Location 4 in Figure 4.5). A summary of the damage at the site is presented in Figure 4.16, with both the riverbanks and the adjacent properties being affected. At this location, the ground between the southern bank of the Opaoa River and the northern edge of the industrial properties was relatively level (Figure 4.17). The ground then steeply slopes upward to form the stopbanks, and behind this the ground is again relatively flat heading back towards the road to the south (Figure 4.19). Damage to the opposing northern bank was inferred from drive-by surveys but was not confirmed by ground reconnaissance due to time constraints.

A hand auger adjacent to the river shown in Figure 4.16 indicated that the soil profile at this site is composed of a silt cap typically 2.2 m thick, underlain by fine-medium sand with trace silt, and the water table is approximately 1.5 m below the ground surface.

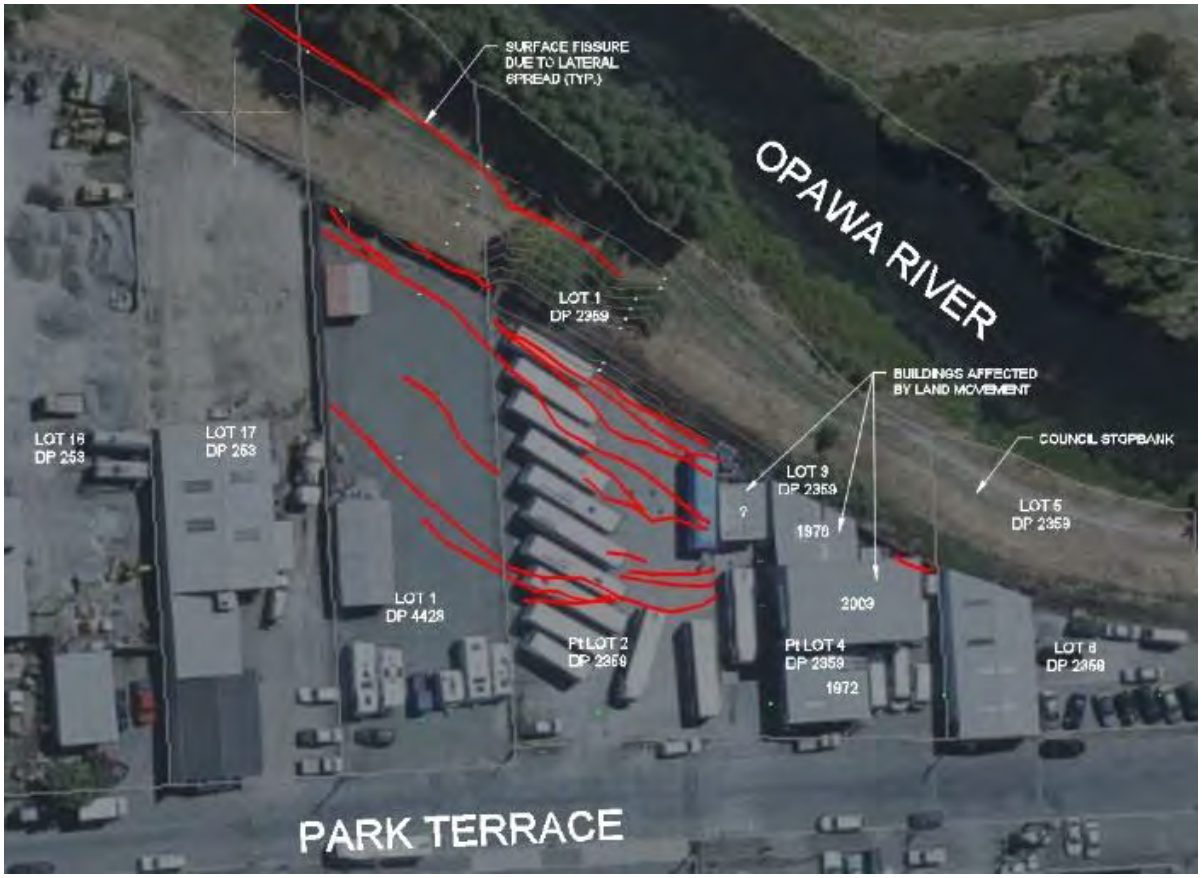

Figure 4.16: Summary of damage at the Park Terrace site. Dashed line indicates location of the historic stopbank (approx. centre of image: S41.5122, E173.9649).

Lateral spread cracks were evident along the river bank, and trees in the area were inclined towards the river suggesting movement towards the open face. The cracks were orientated sub-parallel to the river bank and covered the area extending from the river bank to the base of the stopbank. Cracks ranged in width from a few centimetres to as large as 30 cm (Figure 4.17) and were associated with approximately 1 to 5 cm of vertical settlement. Crack widths decreased with increasing distance from the apex of the inner meander bend and became discontinuous along the river bank further upstream. A block drop of 15-20 cm was also identified in the area. Fine-medium grey sand ejecta up to 10 cm thick was evident in this area and filled many of the lateral spreading cracks (Figure 4.18).

Lateral spreading/deep seated slumping and vertical displacement were observed within the properties on Park Terrace bordering the stopbank, with the location of the cracking summarised in Figure 4.16. Historic photos indicate that the lateral spreading/deep seated slumping in these properties was confined to the areas between the southern river bank and the location of the original stopbanks in this area. The properties affected were constructed on fill that raised the elevation of the zone between the historic stopbanks and the existing stopbanks to the south.

Figure 4.17: Crack parallel to Opaoa River surrounded by grey ejecta to the north of the Park Terrace properties (7 Dec 2016, S41.5121, E173.9651, facing E).

Figure 4.18: Ejecta at the base of the Park Terrace stopbanks (5 Dec 2016, S41.5121, E173.9651, facing E).

Figure 4.19: Ground damage to industrial properties along Park Terrace (5 Dec 2016, S41.5122, E173.9649, facing SE).

Cracks propagated across a number of properties, resulting in permanent ground deformation, differential settlement of structures, separation between foundation slabs and the surrounding ground, and damage to the stopbanks. Details of the cracking are shown in Figure 4.16, Figure 4.19 to Figure 4.21 and Table 4.1.

(a) (b)

Figure 4.20: Examples of cracks along Park Terrace properties (5 Dec 2016): S41.5122 E173.9649, facing E; (b) S41.5121, E173.9647, facing W.

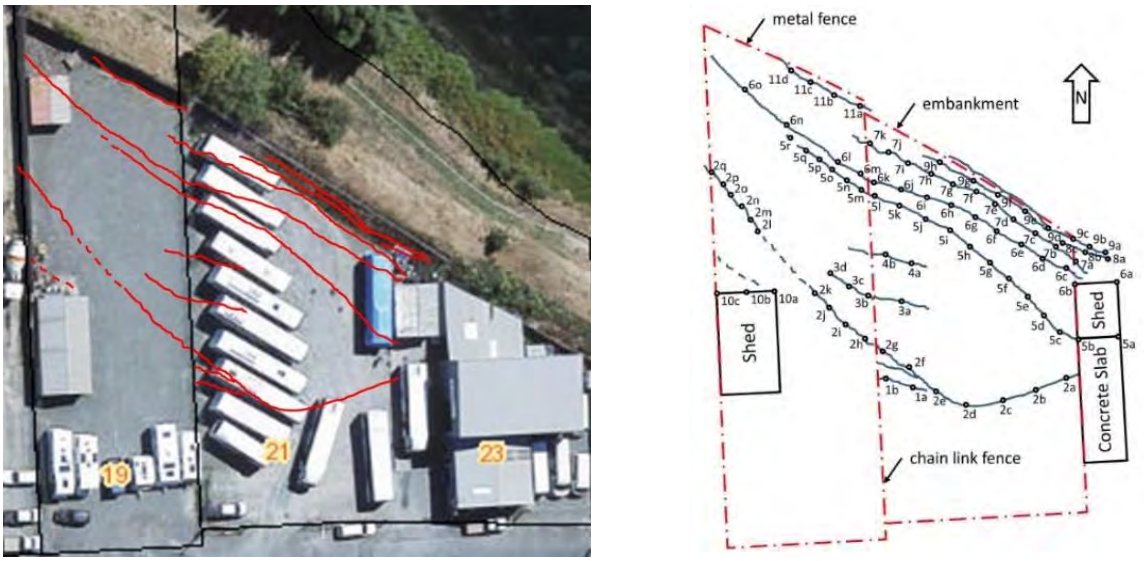

Figure 4.21: Mapping of surficial cracking at two properties on Park Tce. (approx. centre of image: S41.512306, E173.964887): (a) Aerial photograph with locations of observed cracks superimposed; (b) schematic of property boundaries, observed cracks, and approximate locations where horizontal and vertical displacements on cracks were measured (see Table 1).

Table 4.1: Horizontal and Vertical (H:V) displacements measured at locations of Figure 4.21.

location	H:V(mm)	location	H:V(mm)	location	H:V(mm)	location	H:V(mm)	location	H:V(mm)	location	H:V(mm)	location	H:V(mm)	location	H:V(mm)	location	H:V(mm)	location	H:V(mm)	location	H:V(mm)
1a	100:10	2a	10:0	3a	40:0	4a	50:0	5a	130:0	6a	100:20	7a	0:0	8a	0:0	9a	220:0	10a	80:50	11a	400:130
1b	50:50	2b	140:4	3b	60:70	4b	60:0	5b	180:0	6b	130:0	7b	160:0	8b	250:0	9b	120:0	10b	30:60	11b	350:160
-	-	2c	140:0	3c	40:60	-	-	5c	0:0	6c	110:40	7c	170:40	8c	0:0	9c	40:0	10c	0:30	11c	450:190
-	-	2d	190:50	3d	0:0	-	-	5d	40:0	6d	100:10	7d	140:40	-	-	9d	30:0	-	-	11d	190:215
-	-	2e	290:80	-	-	-	-	5e	80:20	6e	60:0	7e	160:80	-	-	9e	50:0	-	-	11e	
-	-	2f	120:100	-	-	-	-	5f	60:40	6f	60:0	7f	130:60	-	-	9f	20:0	-	-	-	-
-	-	2g	40:100	-	-	-	-	5g	50:0	6g	50:0	7g	150:20	-	-	9g	80:0	-	-	-	-
-	-	2h	50:0	-	-	-	-	5h	50:0	6h	50:40	7h	160:-50	-	-	9h	30:-30	-	-	-	-
-	-	2i	150:30	-	-	-	-	5i	30:30	6i	60:10	7i	180:-90	-	-	-	-	-	-	-	-
-	-	2j	400:60	-	-	-	-	5j	0:0	6j	60:0	7j	120:-110	-	-	-	-	-	-	-	-
-	-	2k	210:60	-	-	-	-	5k	150:60	6k	70:-20	7k	180:-90	-	-	-	-	-	-	-	-
-	-	2l	0:0	-	-	-	-	5l	100:90	6l	150:0	-	-	-	-	-	-	-	-	-	-
-	-	2m	60:0	-	-	-	-	5m	110:0	6m	50:0	-	-	-	-	-	-	-	-	-	-
-	-	2n	110:0	-	-	-	-	5n	170:0	6n	130:140	-	-	-	-	-	-	-	-	-	-
-	-	2o	170:0	-	-	-	-	5o	80:0	6o	200:300	-	-	-	-	-	-	-	-	-	-
-	-	2p	320:0	-	-	-	-	5p	120:0	-	-	-	-	-	-	-	-	-	-	-	-
-	-	2q	380:0	-	-	-	-	5q	180:10	-	-	-	-	-	-	-	-	-	-	-	-
-	-	-	-	-	-	-	-	5r	0:0	-	-	-	-	-	-	-	-	-	-	-	-

4.1.1.4 Elizabeth Street

Moderate lateral spreading was observed at a site on an inner meander bend of the Opaoa River at the end of Elizabeth Street, affecting a footbridge and a residential property (Location 5 in Figure 4.5). The meander at this location had the tightest radius of all locations along the rivers in the Blenheim urban area. At this location, the ground slopes up away from the river with an elevation difference of 3.5 m between the riverbanks and a house. A summary of the damage at the site is presented in Figure 4.22.

A hand auger (HA1) adjacent to the river shown in Figure 4.22 indicated that the soil profile had a light brown silt with some sand to a depth of 1.2 m, underlain by fine blueish grey sand to 1.4 m. Below this was blueish grey fine-medium sand, with particle size distribution characteristics shown in Figure 4.7. The water table was at a depth of 1.0 m at this location. Further up the slope from the river banks near the house (HA2) the water table was at a depth of 2.0 m, with the bluish grey fine-medium sand at 2.4 m depth. The ejecta were uniformly composed of grey fine-medium sand and the particle size distributions of these ejecta are shown in Figure 4.7 (EC-1).

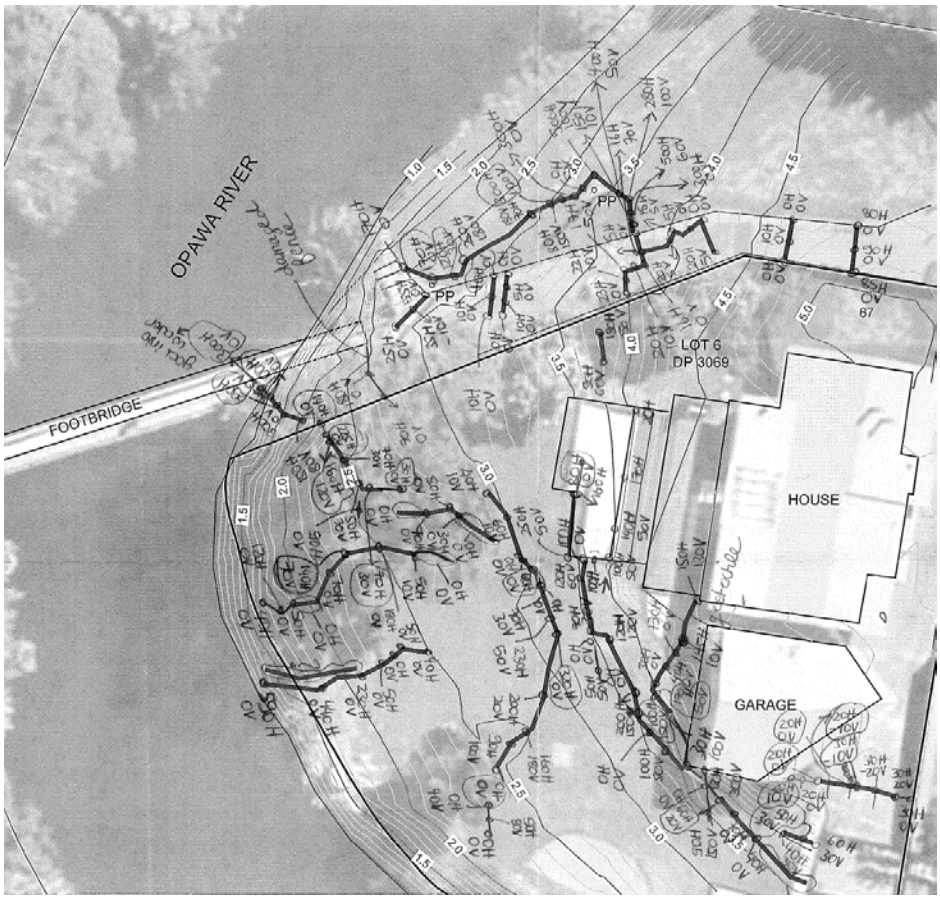

Figure 4.22: Summary of cracking and liquefaction manifestations at the Elizabeth St site (approx. centre of image: S41.5046, E173.9634).

The lateral spreading/slumping cracks in the area was oriented approximately parallel to the riverbanks on either side of the apex of the inner bank of the meander bend. Cracking orientated perpendicular to the river bank occurred at the apex of the meander bend. A summary of the lateral and horizontal displacement across the cracks is presented in Figure 4.22, with up to 50 cm of horizontal displacement and 10 cm of vertical displacement recorded. Cracks were up to 1 m in depth. Near the edge of the river the lateral spreading cracks extended to the water table and were filled with blueish grey fine-medium ejecta. A significant number of roots crossed through the cracks that were oriented perpendicular to the river and may have acted to reduce the severity of the cracking in this area (Figure 4.23).

Lateral spreading/deep seated slumping resulted in damage to the eastern end of the footbridge shown in Figure 4.24. The footbridge had two piers and steel I-beam girders with a wooden deck. The bridge deck warped as a result of the abutment having separated from the footpath by approximately 50 cm due to the lateral movement of the banks (Figure 4.24). A steel water main and an asbestos cement (AC) pipe crossed the river. The steel water main experienced movement but was not damaged, while the AC pipe had cracked and separated adjacent to the abutment.

To the south of the footbridge, cracks in the ground extended from the river up to the house on the property resulting differential movement and settlement of the house and cracks in the brick facade. The western side of the house and the garage moved relative to rest of the structure, resulting in warping of the frame and façade damage. This house was subsequently deemed unsafe for permanent occupancy; it was the only house in Blenheim red-tagged due to liquefaction related damage (Figure 4.25).

Figure 4.23: Crack at Elizabeth Street perpendicular to river filled with bluish-grey ejecta and intersected with roots (7 Dec 2016, S41.5088, E173.9635, facing E).

Figure 4.24: Damage to footbridge abutment at the end of Elizabeth Street (17 Nov 2016, S41.5087, E173.9636, facing W).

Figure 4.25: System of lateral spreading/slumping cracks at Elizabeth Street (7 Dec 2016, S41.5089, E173.9636, facing E).

Between the Lansdowne Park area and Park Terrace, Location 6 in Figure 4.5 was the only other site along the Opaoa River with evidence of liquefaction-related damage. This site was on the inner bank of a meander bend in the river and only experienced minor lateral spreading that had no impact on nearby structures (Figure 4.26).

Figure 4.26: Minor lateral spreading adjacent to the Opaoa River (6 Dec 2016, S41.5046, E173.9633, facing E).

4.1.2 Wairau Plains

Reconnaissance surveys and discussions with local engineers and Marlborough District Council provided a comprehensive summary of the liquefaction related impacts in the Wairau Plains near the coast. Figure 4.27 shows the locations of these impacts based on ground surveys and a robust set of aerial photos taken from a helicopter. The region bounded by the dashed lines indicates the area covered by the surveys, such that all locations within this area where no impacts are shown are unlikely to have any significant liquefaction manifestations.

In the greater Wairau Plains, outside the Blenheim urban area, the liquefaction mainly occurred in zones along the Wairau and Opaoa Rivers. The majority of the impacts of liquefaction were confined by the current stopbank network, with little evidence of liquefaction manifestation observed on the landwards side of the stopbanks. An overview of the damage to the stopbank network is provided in Figure 4.28, with some of these sites discussed in more detail in subsequent sections. Comparison of the observed damage with historical aerial photos of the area suggests that the stopbank damage can be related to the position of paleo-channels and associated swamps. The damaged sections were built on geologically younger deposits, with the adjacent undamaged sections being constructed on older deposits.

Figure 4.27: Overview of the Wairau Plain region and areas of focus outlined in subsequent sections (approx. centre of image: S41.4913, E173.9670).

Of the 180 km length of stopbanks, only 2.5 km were damaged to varying levels of severity across 18 sites. The damaged stopbanks tended to move towards the free-face of the river bank. Horizontal and vertical displacements varied significantly within the failure zone, ranging from a few centimetres to over 1 m. Displacements were accommodated through the development of systems of cracks, usually located on top of the stopbanks and running parallel to the free face of the river bank, with the ground between the cracks and the free face moving as a rigid block.

Accompanying phenomena, which were not observed in all cases, included the development of secondary systems of ground cracks or sand ejecta at the base of the stopbanks. These secondary features, when present, were parallel to the primary system of cracks.

Thirty pump stations for water control are situated in the Wairau Plains, and only three of which suffered relatively minor damage due to liquefaction.

Figure 4.28: Overview of the stopbank network on the Wairau Plains and locations of damage identified by red markers. Orange are the main stopbanks and yellow are the secondary stopbanks (approx. centre of image: S41.4913, E173.9670).

4.1.2.1 Northern Wairau River and the Wairau Diversion

Figure 4.29 provides a summary of the liquefaction related damage in the Northern Wairau River and Wairau Diversion area. The damage mapping was developed from ground reconnaissance and helicopter photos.

Lateral spreading affected the Wairau River Bridge on State Highway 1 (Location 4 in Figure 4.29), resulting in ground cracking at the abutments and piers and horizontal cracking across the base of the abutment and pier walls. There was also approach slumping at the bridge at location 5 in Figure 4.29. Stopbank damage was identified at Spring Creek (Location 6 in Figure 4.29) and to the west of Hillocks Rd (Location 7 in Figure 4.29). The most severe stopbank damage in this area is summarised in the following sections.

4.1.2.2 Wairau Diversion Stopbanks

The Wairau Diversion was constructed in the 1960's to mitigate the effects of flooding on the Wairau River by diverting a portion of the flow of the river away from the Blenheim Township to a direct path towards the coast. Along the Wairau Diversion, lateral spreading-induced or slumping-induced cracking was observed on both the north and the south banks aligned with a paleo-stream channel and swamp, recognizable due to a depression in the landscape and a change in vegetation on both sides of the diversion channel (Location 1 in Figure 4.29 and Figure 4.30). The swamp was present at the time the diversion was built, as indicated by historical conceptual drawings dating back to the first plans for the diversion (Figure 4.31). No other liquefaction or lateral spreading/slumping damage was observed adjacent to the northern or southern banks of the Wairau Diversion between this location and the Equestrian Park outlined in the following section.

Figure 4.29: Map of liquefaction related damage in the northern Wairau River and Wairau Diversion area. Orange are the main stopbanks, and yellow are the secondary stopbanks. (approx. centre of image: S41.4484, E173.9831)

Lateral spreading and slumping of the northern stopbank was characterised by cracking along the top of the stopbank (Figure 4.32). The cracks ranged in width from approximately 30 to 50 cm and were associated with 10 to 50 cm of vertical settlement (Figure 4.33). The cracks all ran sub-parallel to the closest bank of the river. Localized cracking, approximately 2 to 10 cm wide, was observed at the base of stopbank proximal to the river (Figure 4.34a). No liquefaction ejecta were observed at the site, and no liquefaction induced damage was observed proximal to a culvert exiting the stopbank at the easternmost extent of the affected area (Figure 4.34b).

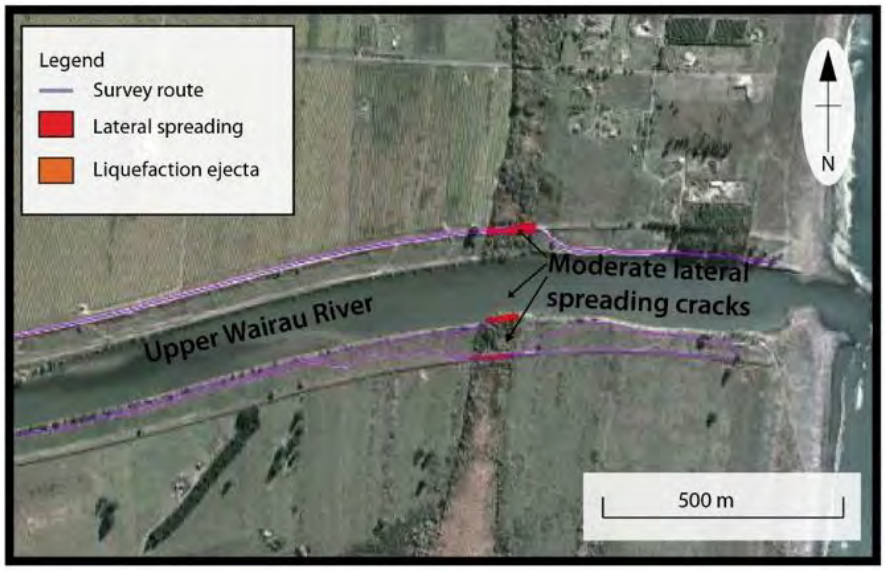

Figure 4.30: Summary of damage observations along the Wairau Diversion (approx. centre of image: S41.4401, E174.0206).

Figure 4.31: Historical drawing of Wairau Diversion. The dotted regions indicate locations of swamps, with the location of failed stopbank highlighted in red (approx. centre of image: S41.4401, E174.0206, Marlborough Catchment Board, 1959)

This site was scanned using a terrestrial LiDAR scanner (Optech, Inc. ILRIS-3D laser scanner) on 6 December 2016. Four scans were performed from the approximate locations shown in Figure 4.35. The data from the scans are still being processed, but will result in a three-dimensional point cloud that will allow cm-scale determination of horizontal and vertical displacements of the stopbank due to lateral spreading or slumping.

Figure 4.32: Lateral spreading induced cracking along top of northern stopbank (17 Nov 2016, S41.4387, E174.0214, facing E).

Figure 4.33: Maximum vertical settlements of 50 cm were observed along the cracks in the northern stopbank (17 Nov 2016, S41.4386, E174.0216, facing N)

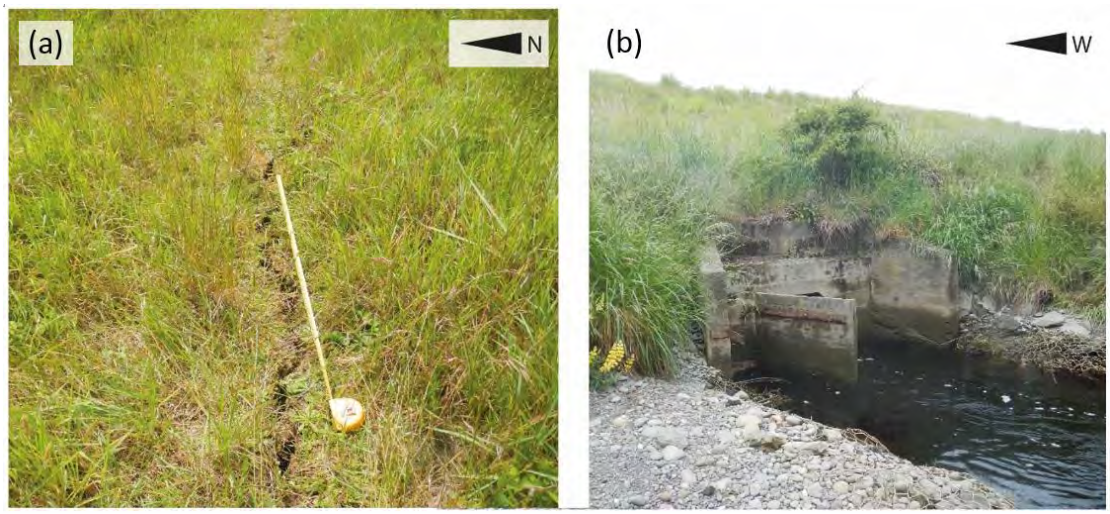

Figure 4.34: a) Cracking observed along the base of the northern stopbank proximal to the river (17 Nov 2016, S41.4390 ,E174.0220, facing E); b) No liquefaction induced damage was observed within the culvert exiting the northern stopbank (17 Nov 2016, S41.4387, E174.0223, facing NE).

Figure 4.35: Approximate locations of four LiDAR scans performed on 6 Dec 2016 (approx. centre of image: S41.4387, E174.0218).

Lateral spreading along southern bank also resulted in cracking along the top of the stopbank (Figure 4.36), although not as severe as the damage on the northern stopbank. The affected area extended for approximately 60 m along the stopbank and consisted of a series of sub-parallel cracks that varied in width from approximately 10 to 40 cm. The cracks exhibited approximately

10 to 40 cm of vertical settlement. No cracking was observed along the base of the stopbank, and no liquefaction ejecta were observed at the site.

Lateral spreading or ground slumping also resulted in cracking of the southern bank of the river (Figure 4.37a). The affected area extends approximately 30 m along the river bank and approximately 3 m inland, with no further cracking observed within the vegetation distal to the river. The cracks range in width from approximately 50 to 60 cm and are associated with 1 to 10 cm of vertical settlement (Figure 4.37b). No liquefaction ejecta were observed at the site.

Figure 4.36: Cracking along the top of the southern stopbank of the Wairau Diversion (Tape set at 1 m) (17 Nov 2016, S41.4414, E174.0219, facing W)

Figure 4.37: Cracking of the southern bank of the Wairau Diversion: (a) 17 Nov 2016, S41.4406, E174.0215; (b) 17 Nov 2016, S41.4406, E174.0215.

4.1.2.3 Marlborough Equestrian Park

The Marlborough Equestrian Park was opened in 2014 and is the home of equestrian sports in Marlborough. It is located NE of Blenheim and is bounded in the west by the Wairau River, in the north by the Wairau Diversion, and in the east and south by a stream that is a remnant of a historic channel of the Wairau River (Location 2 in Figure 4.29). An overview of the site is provided in Figure 4.38. Stopbanks surround the park, with the stopbanks to the east of the park forming part of the main flood defence network of the region and the rest of the stopbanks being part of the secondary protection network. The park itself is relatively flat, with a gradual reduction in elevation of the ground surface moving from north to south.

Hand augers (HA1 and HA2) performed adjacent to the remnant river channel (where the path intersects with Group B cracks in Figure 4.38) shown in indicated that the soil profile had a light brown silt stratum with some sand to a depth of 2.8 m. Below this was blueish grey fine-medium sand, having the particle size distribution shown in Figure 4.66; particle size distribution curves for samples from other locations along the Wairau River are also shown in Figure 4.66. The water table was at a depth of 1.5 – 2.0 m at the two hand auger locations.

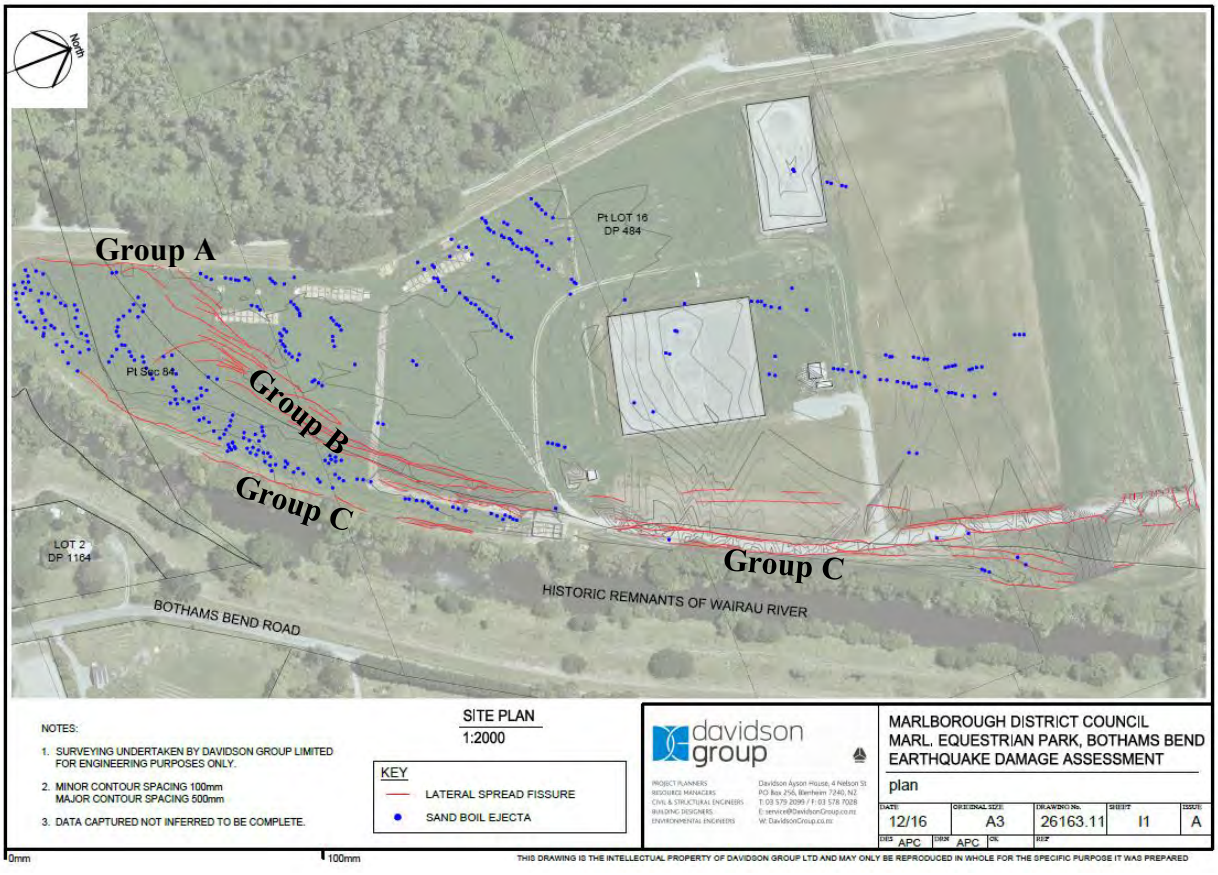

Figure 4.38: Overview of liquefaction induced damage at the Marlborough Equestrian Park (approx. centre of image: S41.4455, E173.9761) (courtesy of Davidson Group)

Figure 4.38 provides a detailed summary of the lateral spreading and liquefaction features across the park, and Figure 4.39 provides an aerial overview of the damage, with extensive lateral spreading, differential settlement, deformation of pavement, and extensive sand boils observed at the site. The red lines represent lateral spreading cracks and the blue dots represent sand boils. This detailed map was developed by Davidson Group and the GEER team after the earthquake. The southern part of the park was more affected by the earthquake than the northern part of the park. It is possible, however, that the mapping of some cracks and sand boils in the northern part of the park was obscured by vegetation

Extensive mapping and surveying of lateral spreading and ejecta were carried out by the reconnaissance team and local engineers. Cracking and ejecta is aligned with the location of the historic Wairau River channel prior to the construction of the Wairau Diversion in the 1960's.

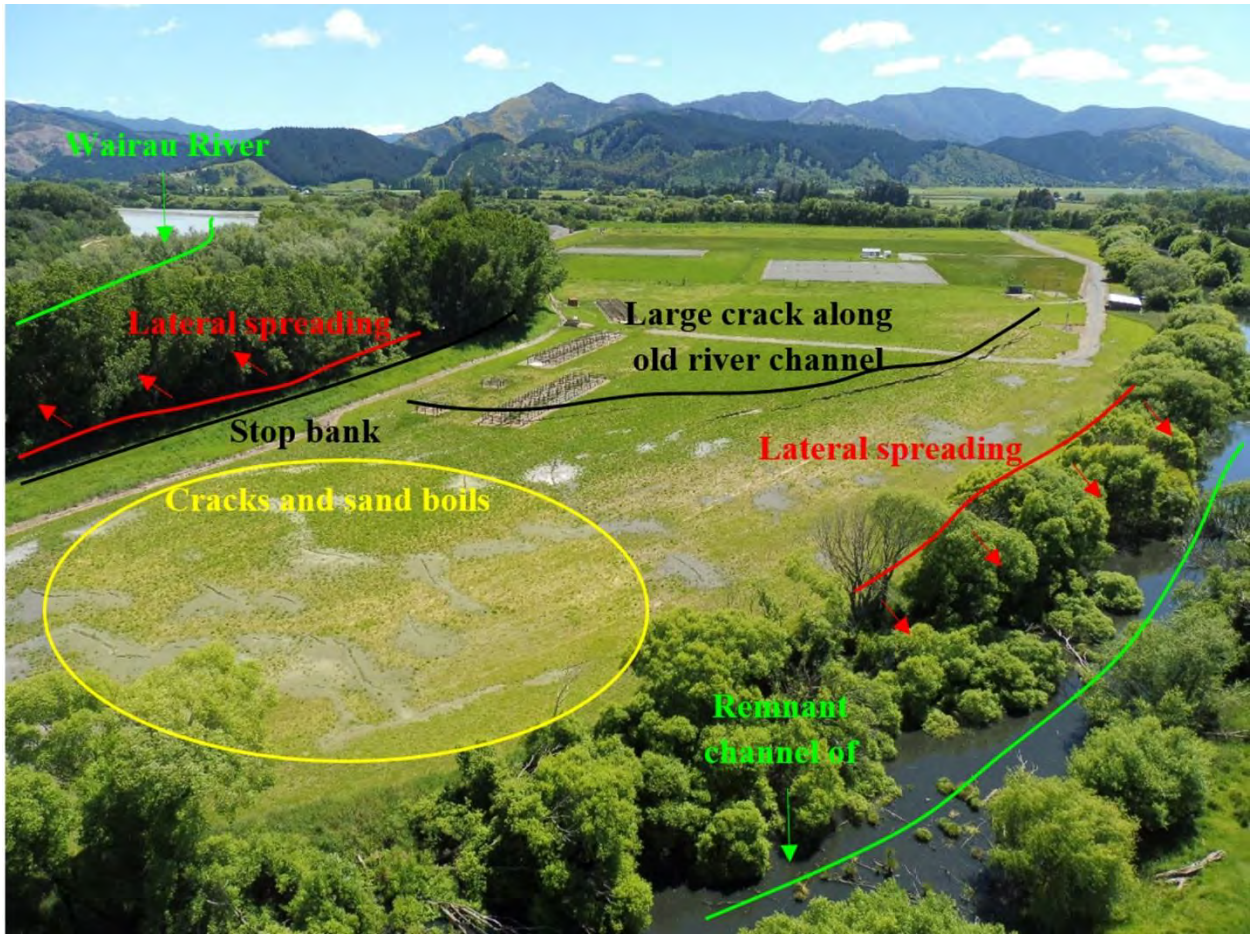

Figure 4.39: Aerial view of Marlborough Equestrian Park (14 Nov 2016, S41.4474, E173.9768, facing NE, Marlborough District Council 2016).

In Figure 4.38, lateral spreading cracks are organised into three groups: Group A cracks ran parallel to the secondary stopbanks on the western edge of the park, Group B cracks were oriented in the SW-NE direction and ran along the edge of the infilled historic river channel; and Group C cracks which run parallel to the stream that is remnant of the historical river channel. The elevation of the ground surface gradually reduced moving south, which correlates with the increase in severity of the lateral spreading.

Group A cracks had a NNE-SSW orientation and were characterized by small to medium horizontal openings (~10-30 cm) with little to no vertical displacement (< ~10 cm). The cracking followed along the base of both sides of the secondary stopbank (Figure 4.40) in areas that used to be part of the Wairau River bed and have since been infilled. The cracks cut through the stopbank where the infilled historic river channel that ran along the east and south of the park merged Wairau River channel that runs north-south. Grey ejecta were present both in the cracks and adjacent to the cracks.

Group B cracks, the most significant crack system in the park, were oriented in the NE-SW direction and were characterized by small to large openings (~10-70 cm) and up to ~70 cm vertical displacement (Figure 4.41a). In this area there was settlement of the ground surface within the infilled historic channel, with the largest cracks aligning with the northern bank of the historic channel (Figure 4.38). Cracking propagated out from this main crack in both directions, with the cracking related to the slumping more than to significant global lateral movement (Figure 4.41b). The cracks in this area were filled with grey ejecta. Further evidence that this cracking followed the infilled historic channel is the coincidence of this cracking with the strip of lush vegetation shown in Figure 4.42.

Figure 4.40: Group A cracking along the base of the secondary stopbanks (4 Dec 2016, S41.4487, E173.9738, facing NE).

The portion of the Group B lateral spread cracks that crossed the dirt access road to the Equestrian Park was scanned using a terrestrial LiDAR scanner (Optech, Inc. ILRIS-3D laser scanner) on 5 Dec 2016. Six scans were performed from the approximate locations shown in Figure 4.43. The data from the scans are still being processed. They will produce a three-dimensional point cloud that will allow cm-scale determination of horizontal and vertical displacements of the lateral spreading features.

(a)

(b)

Figure 4.41: Most severe lateral spreading at the Equestrian Park with 70 cm of vertical offset, with ejecta in the crack: (a) facing NE (b) facing NW (5 Dec 2016, S41.4474, E173.9760).

Group C cracks were oriented in the NE-SW direction and were characterized by small to medium horizontal openings (~10-20 cm) and little to no vertical displacement (< ~10 cm). These cracks aligned with the remnant stream channel and movement was to the east towards this channel. Thick foliage along the riverbanks likely obscured other cracking in this area. However, the submerged trees at the bottom right corner of Figure 4.39 provide evidence of more lateral spreading of these banks.

At the north of the park the access road running along the secondary stopbank was fissured and cracked, and this cracking extended through to the Wairau Diversion channel to the north. Cracking was perpendicular to the road (i.e., cracking ran in the north-south direction; Figure 4.44) adjacent to and parallel with the historic river channel that existed prior to the construction of the Wairau Diversion in the 1960's. However, the cracking ran parallel to the road (i.e., in the east-west direction; Figure 4.45) where it crossed the historic channel as a result of the embankment slumping and spreading horizontally. At this location the crack were up to 10 cm wide.

Lateral spreading was accompanied with widespread sediment ejecta. The volume of ejecta was the most severe in the southern part of the park where the ground elevation was the lowest. The locations of the centres of the mapped sand boils are shown in Figure 4.38 and the volume of ejecta in this region can be seen in the aerial photograph in Figure 4.39, with ejecta up to 20 cm thick in places. In addition to sand boils, ejecta filled up many cracks (Figure 4.41 b). Examples of ejecta deposits are provided in Figure 4.46. Outside of the Equestrian Park, ejecta were also present in the lower lying areas to the north of the Equestrian Park between the stopbank and the Wairau Diversion.

(a) (b)

Figure 4.42: Group B cracks following the historic river channel: (a) facing SW, and (b) facing E (4 Dec 2016, S41.4474, E173.9759). Note the lush vegetation strip identifies the location of the historic river channel.

Figure 4.43: Approximate locations of six LiDAR scans performed on 5 Dec 2016 (The black line is the approximate location of the larges lateral spread crack; approx. centre of image: S41.4477, E173.9760).

Figure 4.44: Crack at the entrance to the Equestrian park at edge of historic river channel (15 Nov 2016, S41.4436, E173.9790, facing W, Marlborough District Council 2016).

Figure 4.45: Cracks in the access road that crosses a historic river channel at the Equestrian Park (15 Nov 2016, S41.4436, E173.9790, facing E, Marlborough District Council 2016).

(a) (b)

Figure 4.46: Examples of ejecta at the Equestrian Park (4 Dec 2016): (a) S41.4471, E173.9748, facing SW; (b) S41.4468, E173.9769, facing N.

4.1.2.4 Blind Creek Stopbanks

At Blind Creek a primary and secondary set of stopbanks are present (Location 3 in Figure 4.29); the secondary set runs parallel to the current channel of the Wairau River while the primary stopbank is set back from the river outside of a cut-off meander bend of the river (Figure 4.47). A 200-m-long section of the secondary stopbank at Blind Creek was heavily damaged (Figure 4.47). The location of this stopbank falls within the historical bed of the Wairau River, with Blind Creek comprising a cut-off meander bend of the Wairau River associated with river avulsion and the construction of the Wairau Diversion in the 1960's.

An aerial view of the stopbank damage is presented in Figure 4.48. Cracks up to 1 m wide and 1 m deep developed along the stopbank (Figure 4.49), suggesting the development of slumping and horizontal displacements away from the major axis of the stopbanks in the north and south directions (Figure 4.47). Sand boils were observed on the foundation soils surrounding the stopbank closer to the river's edge and on the northern side of the stopbank within the paleo-channel (Figure 4.50). Slumping of the stopbank was also observed where Blind Creek flows underneath the stopbank through a culvert.

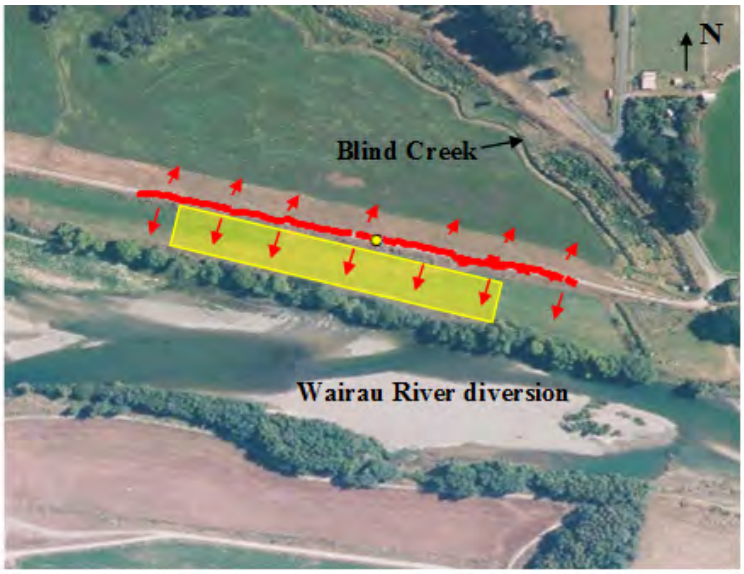

Figure 4.47: Overview of damage at Blind Creek Stopbank (approx. centre of image: S41.4405, E173.9762).

Figure 4.48: Aerial view of the Blind Creek stopbank damage (18 Nov 2016, approx. centre of image: S41.4405, E173.9762, Marlborough District Council 2016).

Figure 4.49: Damage to the secondary stopbank at Blind Creek (5 Dec 2016, S41.4407, E173.9791, facing W).

Figure 4.50: Cracks and ejecta on the foundation soil between the secondary stopbank and the river (5 Dec 2016, S41.440967, E173.980122, facing NE).

4.1.3 Lower Wairau River

Figure 4.51 provides an overview of the liquefaction related damage along the Lower Wairau River between the southern edge of the Equestrian Park and the coast and locations that are discussed in more detail. Particle size distributions of ejecta samples from along the Wairau River are presented in Figure 4.52. The damage mapping was developed from ground reconnaissance and aerial photographs taken from a helicopter.

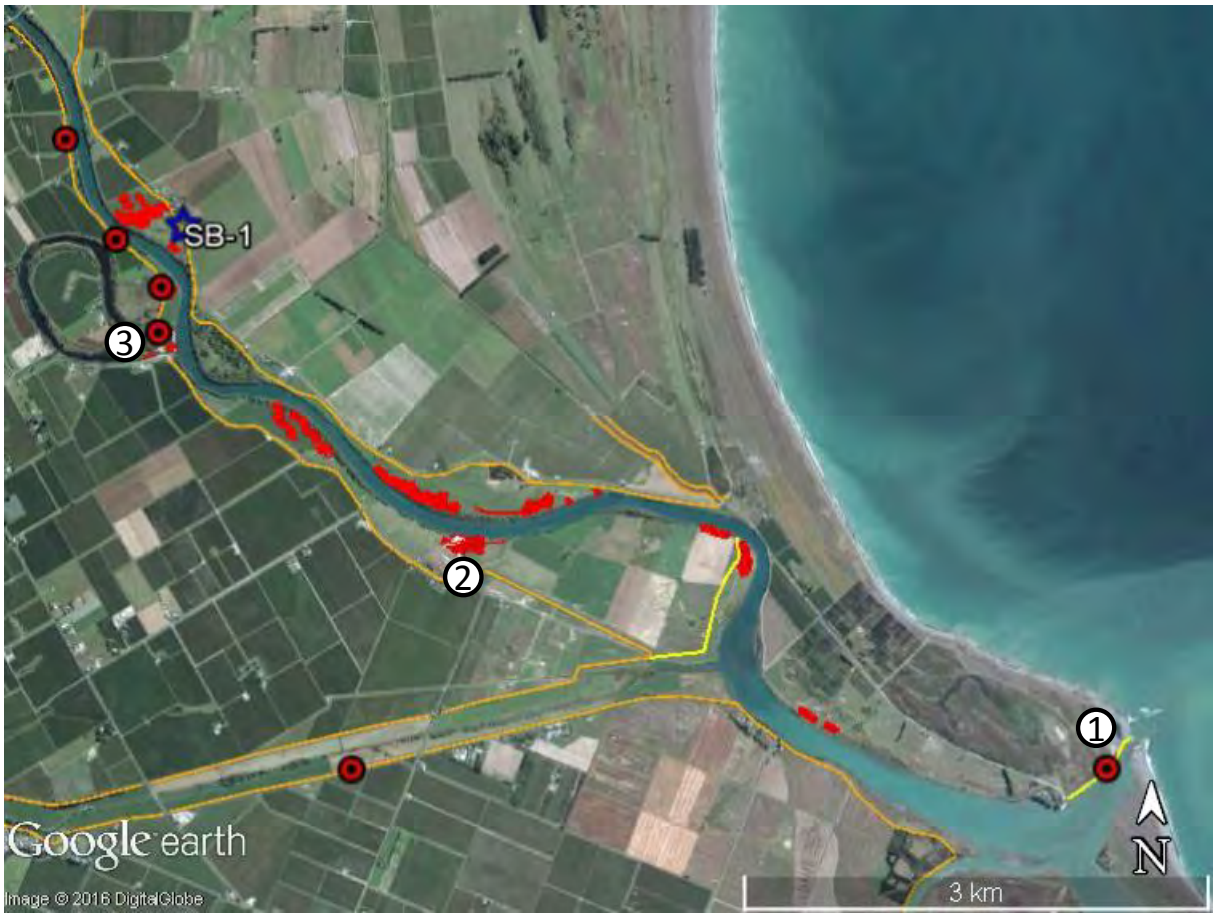

Figure 4.51: Aerial overview of the reconnaissance along the Lower Wairau River. Locations with detailed investigations are identified numerically, and locations where samples have been collected from are shown by blue stars. (Approx. centre of image: S41.4871, E174.0127).

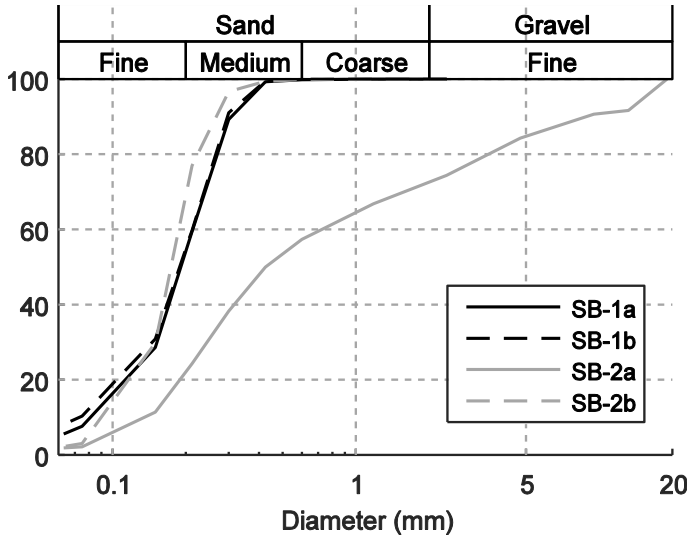

Figure 4.52: Particle size distributions of ejecta samples from the stopbanks along the Wairau River. Locations of these samples summarised in Figure 4.51.

4.1.3.1 Banks of Lower Wairau River

Along the eastern bank of the lower Wairau River are a number of farms, vineyards, and a marae (Maori meeting grounds), with the main stopbank running the length of the river to the Wairau Bar. Severe lateral spreading and large volumes of liquefaction ejecta were observed proximal to the inner banks of the meander bends, and paleo-channels associated with cut-off meander bends. The liquefaction induced damage occurred between the stopbanks and the river bank, with no liquefaction or lateral spreading induced damage observed to the stopbanks or along the road outside of the stopbanks. It is possible that minor lateral spreading and associated liquefaction ejecta occurred along the river banks in this area, but liquefaction features may have been obscured during helicopter reconnaissance or not visited during ground reconnaissance mapping.

A summary of the damage along the lower Wairau River is presented in Figure 4.53. The liquefaction manifestations along the river both followed the old meanders of the river and were parallel to the existing river banks. Aerial views of this damage are presented in Figure 4.54 and Figure 4.55.

Figure 4.53: Summary of liquefaction induced damage along the banks of the Lower Wairau River, with red areas indicating cracking and ejecta locations. Stopbank damage is shown by the red symbols in this figure. (Approx. centre of image: S41.4799, E174.0006).

Figure 4.54: Lateral spreading and liquefaction ejecta on the eastern banks of the Lower Wairau River (18 Nov 2016, S41.4687, E173.9807, taken facing SE).

Figure 4.55: Lateral spreading and liquefaction ejecta on the eastern banks of the Lower Wairau River (18 Nov 2016, S41.4854, E174.0160, taken facing W).

Minor lateral spreading induced cracking was observed proximal to the river bank at 132 Wairau Bar Road (Figure 4.56a and b, location 1 in Figure 4.53). Although at the time of the reconnaissance the property had already been cleared by the owner, manifestations of liquefaction and lateral spreading-induced cracking were still recognizable. Cracking occurred in the area extending approximately 10 m inland from the river bank, and transitioned into a zone of localized elliptical liquefaction ejecta extending to the base of the stopbank. The lateral spreading cracks ranged in width from 10 to 50 cm and extended along the length of the river bank (Figure 4.56a). The cracks did not exhibit any ejecta but were associated with undulations

in the ground that were not present prior to the earthquake. The localized elliptical liquefaction ejecta features ranged from 10 to 20 m in length and 1 to 2 m in width. The features were uniformly composed of grey fine sand and were associated with 10 to 30 cm wide cracks that were orientated sub-parallel to the river bank.

A localized elliptical liquefaction ejecta feature, measuring approximately 8 m in length and 2 m in diameter, was observed in a ditch along the southern margin of the stopbank at 188 Wairau Bar Road (Figure 4.57a, location 2 in Figure 4.53). The feature was composed of grey fine sand which was still wet during the reconnaissance visit on 17 Nov 2016, and was associated with standing water in the ditch. Elliptical liquefaction ejecta features of similar dimensions were observed scattered throughout the adjacent farmland and were orientated sub-parallel with the river in this location (Figure 4.57b). The river bank was not surveyed at this location, but a neighbouring land owner indicated that lateral spreading induced cracking occurred within 10 m of the river bank, while localized ejecta were present at distances >10 m.

Localized cracking was also observed along the southern margin of the stopbank in the farmland opposite 515 Wairau Bar Road (Location 3 in Figure 4.53). The cracks were confined to the stopbank and range from 10 to 20 m in length and approximately 20 to 50 cm in width (Figure 4.58a). No liquefaction ejecta were observed associated with these cracks.

A series of localized elliptical liquefaction ejecta features were observed within the farmland extending from the base of the stopbank to the river bank (Figure 4.58b). The features range in length from 5 to 7 m and 1 to 2 m in diameter, and are uniformly composed of grey, fine sand. The river bank was not surveyed at this location; however, it is assumed that localized lateral spreading occurred within 10 m of the river bank.

(a) (b)

Figure 4.56: a) Lateral spreading induced cracking was observed within 10 m of river bank at 132 Wairau Bar Road. b) Localized liquefaction ejecta associated with cracks were observed at distances >10 m from the stopbank (17 Nov 2016): (a) S41.4671, E173.9802, facing N; (b) S41.4675, E173.9808, facing N.

(a) (b)

Figure 4.57: a) Liquefaction feature in ditch next to the stopbank at 188 Wairau Bar Road. b) Evidence of similar liquefaction features in adjacent farmland, between the stopbank and the river bank (both S41.468902, E173.986465, facing W).

(a) (b)

Figure 4.58: a) Cracks within the southern side of the stop bank opposite 515 Wairau Bar Road. Features ranged in width from 20 to 50 cm (tape set at 1 m for scale). b) Liquefaction ejecta features within the farmland between the stop bank and river mouth (tape set at 1 m for scale). (17 Nov 2017): (a) S41.4843, E174.0147, facing N; (b) S41.4847, E174.01523, facing N.

4.1.3.2 Wairau Bar

Lateral spreading was observed along Wairau Bar stopbank on the northern bank of the mouth of the Wairau River (Location 1 in Figure 4.51). An overview of the site is presented in Figure 4.59, where cracking was observed along an approximately 100 m long section of the stopbank. Historical aerial photos of the river mouth showed that the damaged section of the stopbank was built on an old river channel that ran parallel to the coast prior to the stopbank construction (Figure 4.60).

An aerial view of the damage is presented in Figure 4.61. The eastern and western termini of the affected area exhibited cracks that varied in width from approximately 2 to 5 cm and were associated with vertical displacements of 1 to 5 cm. The central affected area exhibited a series of sub-parallel cracks that varied in width from 30 to 50 cm and were associated with vertical settlements of 20 to 120 cm (Figure 4.62 and Figure 4.63). No liquefaction ejecta were observed in the cracks along the stopbank nor in the mudflats exposed within the river channel.

Figure 4.59: Top view of stopbank along Wairau River (centre of image S41.502404, E174.058915).

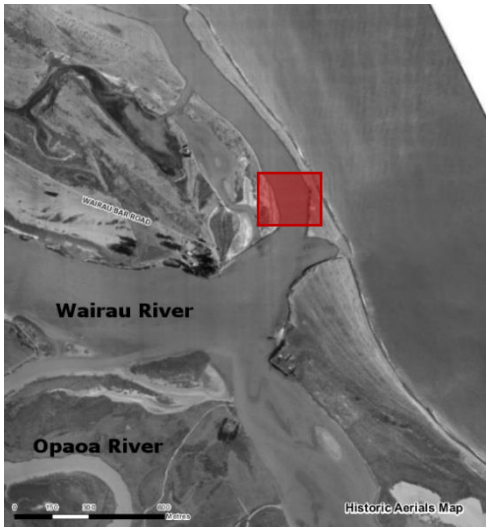

Figure 4.60: Aerial photo of the Wairau river mouth in 1948. In red: location of failed stopbank (centre of image S41.5027, 174.05777, Marlborough District Council 2017).

Figure 4.61: Aerial view of left stopbank at Wairau River mouth (18 Nov 2016, S41.5003, E174.0600, facing S, Marlborough District Council 2016).

Figure 4.62: Severe cracking of levee (17 Nov 2016, S41.50122, E174.060071, facing E).

Figure 4.63: Measurement of vertical relative displacement along crack, tape set at 150 cm (17 Nov 2016, S41.5012, E174.0603, facing N).

(a)

(b)

Figure 4.64: a) Cracks, running sub-parallel to the stopbank, with associated liquefaction ejecta along the northern (inland) margin of the stopbank. b) Fissure with associated liquefaction ejecta in a side road; the feature is orientated parallel to an adjacent small stream and perpendicular to the stopbank (17 Now 2016): (a) S41.5005, E174.0607, facing E; (b) S41.5016, E174.0589, facing N..

A series of lateral spreading cracks were also observed along the inland (northern) margin of the stopbank and extended 15 to 20 m inland (Figure 4.64a). The cracks varied in width from 20 to 40 cm and were surrounded by liquefaction ejecta composed of grey fine sand. The features were observed on the road running along the base of the inland margin of the stopbank and were all orientated parallel with the stopbank.

A lateral spreading crack surrounded by liquefaction ejecta composed of grey fine sand was observed in a side road that runs perpendicular to the stopbank (Figure 4.64b). The feature was located adjacent and sub-parallel to a small stream that feeds into the Lower Wairau, and perpendicular to the cracking observed within the stopbank.

4.1.3.3 Blenheim Rowing Club

The Blenheim Rowing Club (BRC) is located on the western bank of the Wairau River, and severe liquefaction manifestations and lateral spreading occurred in the area (Location 2 in Figure 4.51). This was the only location in the region where significant liquefaction related damage was present on the outer bend of a river. However, historic maps (Cook, 1895) and property boundaries show that there was an S-bend in the river in this area that was straightened (Figure 4.65). Much of the damage that occurred was confined to the boundaries of the paleo-channel. Figure 4.65 provides a summary of the damage in and around the rowing club, with large areas affected by lateral spreading and significant volumes of ejecta. A sample of ejecta was taken north of the main clubhouse building, and the particle size distribution is presented in Figure 4.66.

Aerial views of damage in the area presented in Figure 4.67 and Figure 4.68 provide a clear indication of the severity of damage in this area. Severe liquefaction ejecta were observed at the physical site of the rowing club and surrounding fields to the east and west of the rowing club. Sand boils were typically several metres in diameter and many linear arrays of sand boils were located across the site. Approaching the river, these lines of sand boils tended to become orientated parallel to the river, and in many cases, were associated with lateral spreading cracks.

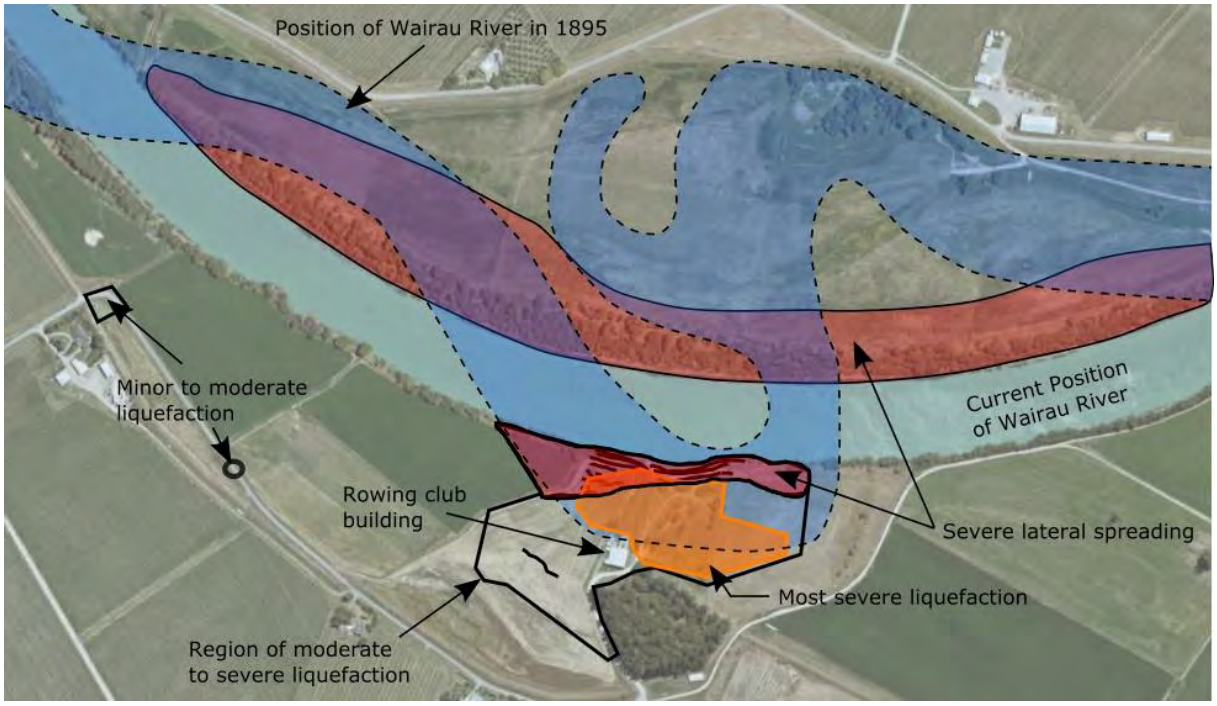

Figure 4.65: Summary of observations at Blenheim Rowing Club (approx. centre of image: S41.4860, E174.0105, Basemap: Marlborough District Council, 2017)

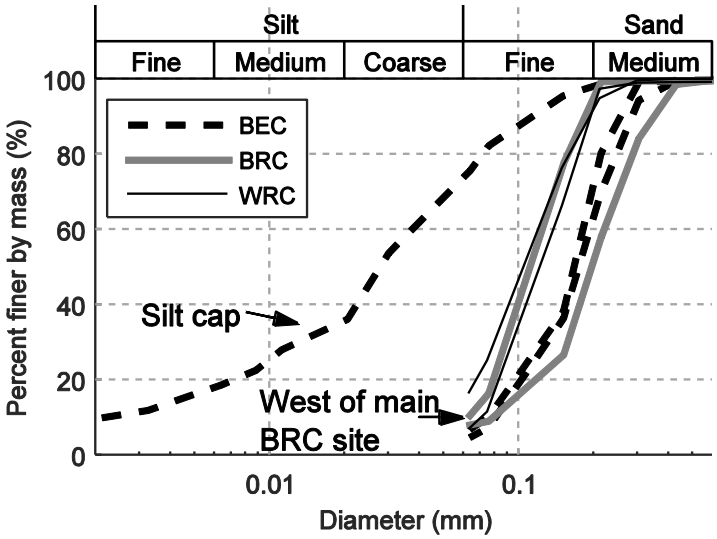

Figure 4.66: Particle size distributions of ejecta samples from along the Wairau River. (BEC=Equestrian Club (S41.4476, E173.9761), BRC=Blenheim Rowing Club (S41.4882, E174.0088), and WRC=Wairau Rowing Club (S41.5003, E174.0600)).

Figure 4.67: Aerial view of liquefaction manifestation at the Blenheim Rowing Club looking south (18 Nov 2016, approx. centre of image: S41.4890, E174.0094, Marlborough Regional Council, 2016).

Numerous lateral spreading cracks were observed at this site and varied in width from approximately 10 cm (at distances of approximately 60 m from the river) to over 1 m at locations close to the river channel (Figure 4.69 and Figure 4.70). Transects of the cumulative crack widths at this site summarized in Figure 4.71 and Table 4.2 show that lateral spreading displacements of the order 2-5 m accumulated over a horizontal distance of approximately 60 m from the river.

Figure 4.68: Aerial view of liquefaction manifestation at the Blenheim Rowing Club looking east (18 Nov 2016, approx. centre of image: S41.4883, E174.0096, Marlborough Regional Council, 2016).

Figure 4.69: Lateral spreading at the east end of the rowing club site. Note: measuring tape set to 1m. (17 Nov 2016, S41.4882, E174.0105, facing E).

Figure 4.70: Lateral spreading at the west end of the rowing club site. (17 Nov 2016, S41.4881, E174.0101, facing E).

Figure 4.71: Transects where cumulative crack widths were measured to estimate lateral spreading displacements. (Approx. centre of image: S41.4886, E174.0102, Imagery from GoogleEarth).

Table 4.2: Summary of transects at Blenheim Rowing Club summarised in Figure 4.71.

Transect Number	Cumulative crack widths (m)	Distance of first crack from river (m)
1	5.2	64
2	3.6	46
3	2.3	72

Figure 4.72: View close to river looking back towards clubhouse. Lines of ejecta are associated with lateral spreading cracks. (17 Nov 2016, S41.4881, E174.0099, facing W).

Figure 4.73: Liquefaction ejecta located 90 m east of clubhouse. (17 Nov 2016, S41.4890, E174.0105, facing E).

Figure 4.74: View of Blenheim rowing clubhouse from the north (17 Nov 2016, S41.4886, E174.0096, facing S).

The clubhouse structure at the site was a light-weight timber framed structure, with a number of timber and concrete piles visible at the rear of the structure (Figure 4.74). While ejecta were observed across large areas around the clubhouse, only minor evidence of liquefaction was observed around the perimeter of the building itself. On the western side of the building, some minor gapping (approximately 2.5 cm) was observed on the North side of a limited number of piles (Figure 4.75).

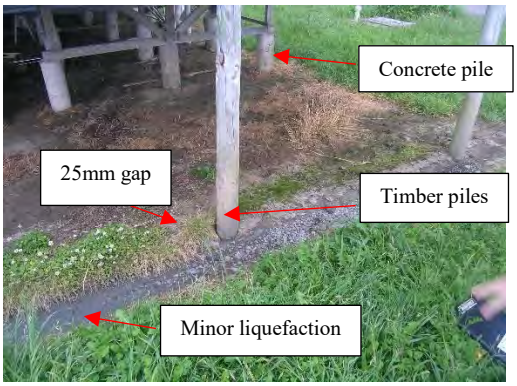

Figure 4.75: Gapping on North side of timber pile (17 Nov 2016, S41.4890, E174.0092).

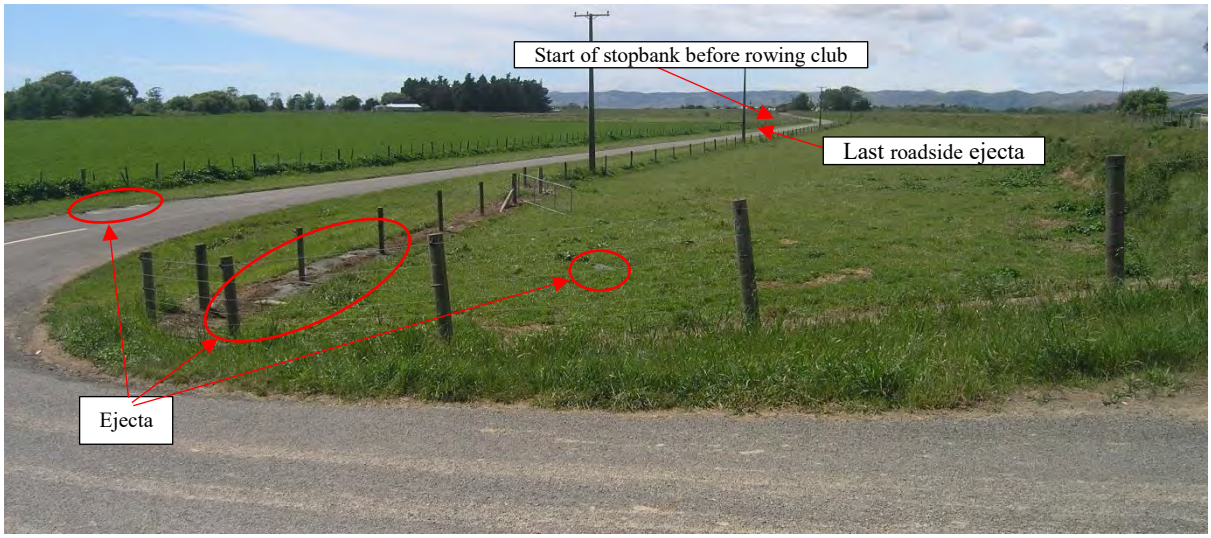

Figure 4.76: Evidence of liquefaction on approach to the Blenheim Rowing Club (17 Nov 2016, S41.4862, E174.0022, facing S).

Further back from the river, the drive-through survey first encountered sand boils 1 km to the north-west of the rowing club at the point where Jones Road crosses over the stopbank and drops onto the Wairau River terrace (highlighted in Figure 4.65 and Figure 4.76). A stopbank was present on the river side of Jones Road, starting at a distance of 500 m from the rowing club. No liquefaction manifestations were observed to the south of the embankment, nor along the roads to the east of the rowing club. The particle size distribution of a sample of ejecta taken from the location shown in Figure 4.76 is presented in Figure 4.66 and is classed as a fine sand. The gradation of this ejecta is noticeably finer than the material observed at the main Blenheim Rowing Club site.

4.1.3.4 Wairau Rowing Club

The Wairau Rowing Club is located adjacent to the southern bank of the Wairau River and encompassed by the Grovetown Lagoon (Location 3 in Figure 4.51), an ox-bow lake associated with a meander bend cut off from the main channel during a flood in 1861. Satellite imagery indicates that the main channel of the Grovetown Lagoon was originally much wider than the two manmade drainage channels joining the lake with the Wairau River. The club house and launching area are located adjacent to the paleo-channel of the Wairau River. The most significant damage in this area is summarized in Figure 4.77 and is constrained between the two manmade drainage channels linking the oxbow lake to the Wairau River.

The largest lateral spreading cracks were observed in an area up to 20 m from the riverbanks, with the largest crack width being approximately 2 m. At the northern end of the grassed area to the east of the clubhouse the lateral spreading was associated with a 50 cm vertical settlement. This lateral spreading extended between the two drains linking the Wairau River and the Oxbow lake. Examples of this lateral spreading in the grassed area is shown in Figure 4.78 and near the northern drain in Figure 4.79.

A line of sand boils was located approximately parallel to the river, half way between the embankment and the river bank, and extended into the bushes immediately north of the grassed area (Figure 4.80). A 10 cm wide lateral spreading crack was observed at the northern end of this line of sand boils. A significant volume of ejecta was identified in the drainage channel between the oxbow lake and the Wairau River on the day of the earthquake (Figure 4.81a). The ejecta were quickly removed and stockpiled adjacent to the drain as shown in Figure 4.81b.

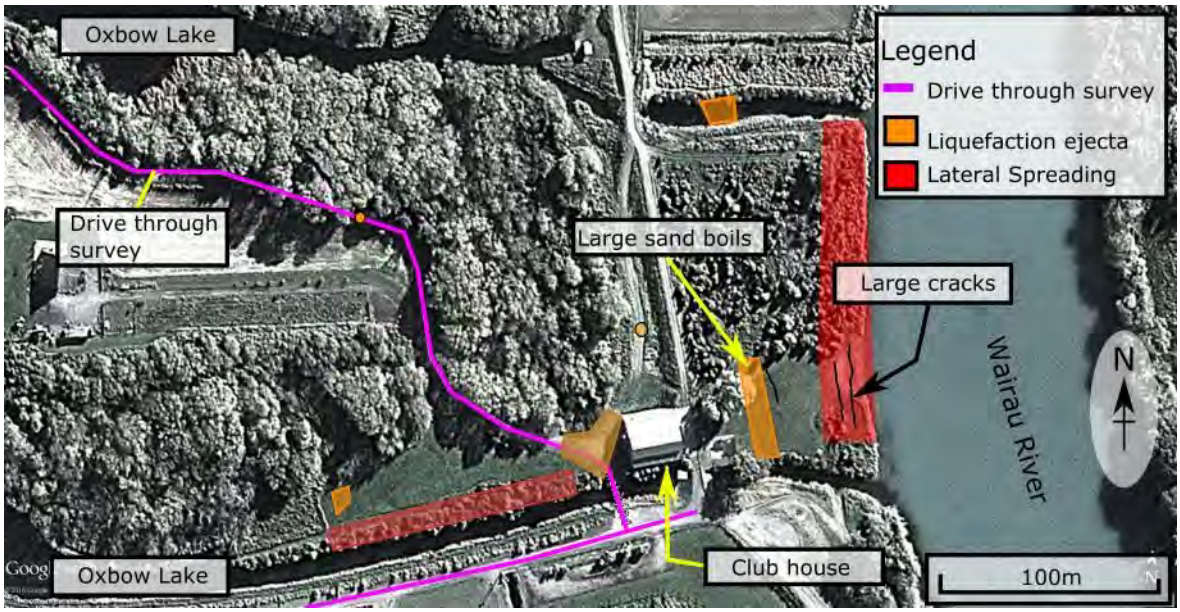

Figure 4.77: Summary of observations at Wairau Rowing Club (approx. centre of image: S41.4762, E173.9843, Imagery from GoogleEarth).).

Figure 4.78: Lateral spreading cracks close to the Wairau River in the grassed area to the east of the clubhouse (17 Nov 2016, S41.4765, E173.9862, facing S).

Figure 4.79: Lateral spread crack approximately 2 m wide filled with fine grey ejecta (6 Dec 2016, S41.4761, E173.9860, facing NE).

Figure 4.80: Sand boils on lawn in front of club house shown as large sand boils in Figure 4.77 (17 Nov 2016, S41.4766, E173.9858, facing N).

(a) (b)

Figure 4.81: a) Ejected sand evident in the drain channel (14 Nov 2016). b) Pile of excavated ejecta from the drain channel (6 Dec 2016, S41.4754, E173.9854, facing E).

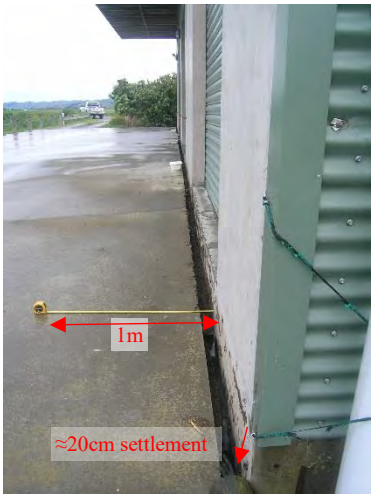

Figure 4.82: Gapping and settlement on eastern side of club house (17 Nov 2016, S41.4766, E173.9855, facing S).

The clubhouse building consists of three vertical levels and four lateral bays. The bottom level is accessible on the western side of building, while an embankment runs along the eastern side of the building with the 2nd level of the building opening out onto the top of the embankment. A 10 cm gap between the structure and the surrounding soil was apparent along the northern and eastern sides of the building. On the Eastern side in Figure 4.82, the exterior concrete slab had pulled free of the main clubhouse (attached by straight rebar), while at the north-east corner, the slab had settled 20 cm relative to the building (Figure 4.83).

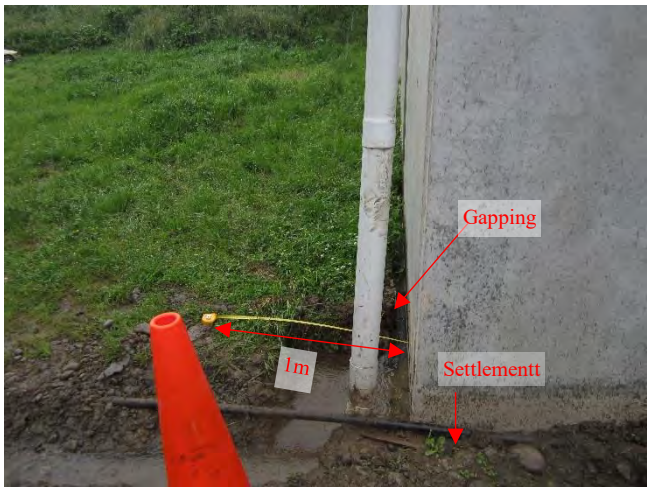

Figure 4.83: Gapping and settlement on northern side of club house (17 Dec 2016, S41.4767, E173.9851, facing E).

Figure 4.84: Cracks and ejecta to the west of the Wairau Rowing Club (17 Nov 2016, S41.4768, E173.9849, facing E).

Numerous sand boils were located around the rowing club building, as well as a small number of isolated sand boils up to 200 m to the north-west on Cemetery Road. In the level area immediately to the west of the clubhouse, cracks of approximately 5 cm in width were identified, along with a number of areas of grey fine sand ejecta (Figure 4.84 and Figure 4.85) that extended parallel to the paleo-channel comprising the oxbow lake as shown in Figure 4.77.

Figure 4.85: Fine grey sand ejecta west of the Wairau Rowing Club (7 Dec 2016, S41.4771, E173.9836, facing E).

4.1.4 Lower Opaoa River

Downstream of the Blenheim urban area there was significant lateral spreading and large volumes of ejecta were observed along the inner banks of the meander bends of the Lower Opaoa River. Figure 4.86 provides a summary of the damage observed from ground and aerial reconnaissance.

There was damage to the stopbank network in four locations along this stretch of the river as shown in Figure 4.86. The main impact was to wineries situated along the river, with large areas of vines affected as indicated in Figure 4.87 and Figure 4.88. Many of these areas were rapidly cleared following the earthquake, and new end-posts were installed to allow the rest of the vines to continue to grow.

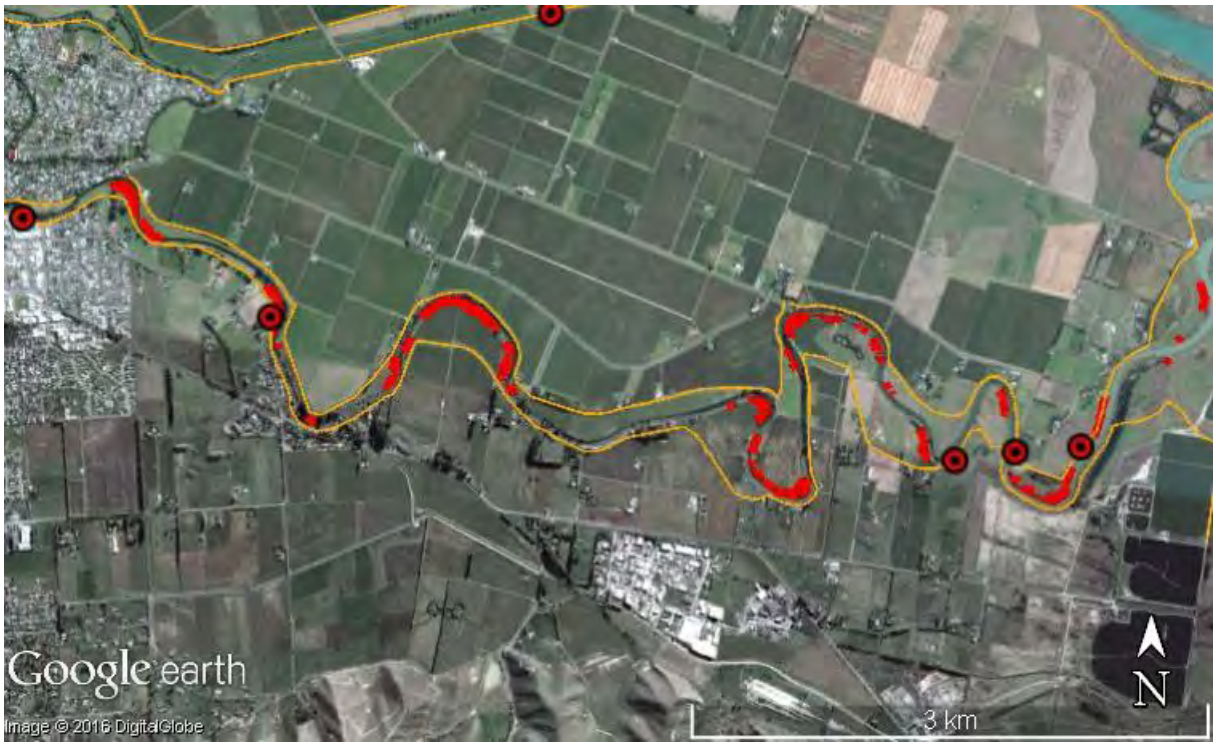

Figure 4.86: Summary of damage along the Lower Opaoa River. Red areas indicate locations of cracking and ejecta, with stopbank damage shown by the red symbols in this figure. Orange lines indicate locations of stopbanks. (Approx. centre of image: S41.5219, E174.0076, Imagery from GoogleEarth).

Figure 4.87: Lateral spreading and sand ejecta damage to vineyards along the Lower Opaoa River. Photo taken 4 days after the earthquake showing vine repair yet to commence (18 Nov 2016, S41.5217, E174.0160, facing W, Marlborough District Council 2016).

Figure 4.88: Lateral spreading and sand ejecta damage to vineyards along the Lower Opaoa River. Photo taken 4 days after the earthquake showing completed vine repair and remnants of damaged vines. (18 Nov 2016, S41.5270, E174.0179, facing N, Marlborough District Council 2016).

4.1.5 Opaoa and Omaka River (upstream of Blenheim)

Upstream from the Blenheim urban area (starting at Lansdowne Park) there was evidence of minor liquefaction, but it did not have any significant effect on the built environment. Ejecta were observed at the side of O'Dwyers Road as indicated in Figure 4.89, between 85 and 65 m from the crossing over the Opaoa River. Ejecta closest to the river were brown in colour, while it became grey in color moving away from the river. At this location, a small tributary stream runs parallel to the road, 15 m to the East.

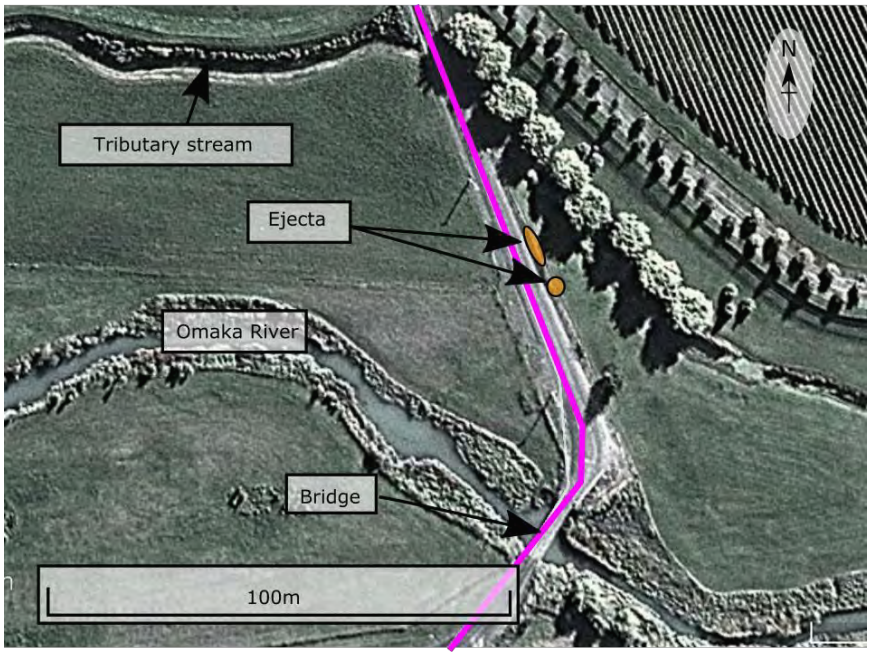

Figure 4.89: Summary of observations at O'Dwyers Road/Thomsons Ford Road bridge (approx. centre of image: S41.4825, E173.9336, Imagery from GoogleEarth).

(a) (b)

Figure 4.90: Sand boils at O'Dwyers Road. (a) facing SE (b) facing NW (17 Nov 2016, S41.4822, E173.9340).

4.1.6 Greater Marlborough Area

Outside of the Wairau Plain and Blenheim, reconnaissance moved south along State Highway 1 towards the town of Ward. The main liquefaction related impacts were associated with bridge damage. A more complete summary of the liquefaction related impacts to bridges is provided in Chapter 6.

4.2 Overview of Kaikoura Reconnaissance

The town of Kaikoura is located on the east coast of the South Island of New Zealand, approximately 160 km NNE of Christchurch and 100km SSE of Blenheim. The urban area of Kaikoura covers an area of approximately 7 km^2 and has population of around 2000, with an additional 2000 people living in the nearby rural areas at the time of the 2013 census (Statistics NZ, 2013). The township is mainly concentrated in a thin band extending 500 m inland from the coast. Before the earthquake, the economy of Kaikoura was focused on tourist activities, as well as agriculture on the coastal plains. Following the earthquake, all roads to Kaikoura were impassable as a result of the many landslides in the area. Initial evacuations took place by sea and air (helicopters) until partial road access was restored on the 18th November 2016.

Members of the GEER reconnaissance team were able to briefly visit Kaikoura with assistance from the local consulting firm Tonkin + Taylor Ltd. (T+T) between 8th and 10th December 2016. T+T engineers had been conducting damage surveys on behalf of the New Zealand Earthquake Commission (EQC); photographs collected during their efforts in Kaikoura have been included within this section of the report.

There is one strong motion station in the Kaikoura area, located on the rocky Kaikoura Peninsula to the south of town (Site Class B according to NZS1170.5, SNZ 2004). During the main earthquake event, PGAs of 0.22 g (horizontal geometric mean) and 0.27g (vertical) were recorded. Several aftershocks occurred within 24 hours, including 3 events with M_w greater than 6 with nominal epicenters within 35 km of Kaikoura. However, accelerations during the main shock were significantly larger than the aftershocks which had horizontal PGAs less than 0.1 g. It is assumed that the damage sustained in Kaikoura arose as a result of the main earthquake, though significant excess pore pressures may have remained at the time of the aftershocks.

The area covered by the overall reconnaissance efforts is shown in Figure 4. along with key locations where damage was observed. Due to the rural nature of this area, the damage to infrastructure was quite low. Damage was concentrated along Lyell Creek, where large lateral displacements were observed within 30 m of the creek resulting in heavy damage to many houses built close to the river, and to one short-span bridge (see Chapter 6 of this report). While these displacements resulted in cumulative crack widths of up to 3 m, it was apparent that the driving mechanism was not due to classic liquefaction-induced lateral spreading, as discussed subsequently. Other damage in the region included cracking and deformation of the roads, as well as some damage to the liner systems in embankments at the oxidation ponds to the north of the town. Liquefaction ejecta was noted in some areas outside of the main township, though the overall impact of liquefaction was quite small.

Figure 4.91: Reconnaissance in Kaikoura (approx. centre of image: S42.389, E173.682).

4.2.1 Geology of the Kaikoura Area

The township of Kaikoura is situated within a highly tectonically and geomorphically active region along the eastern coast of New Zealand's South Island. The region is located at the eastern-most extent of the north-east trending strike-slip transpressive Hope Fault. Uplift along the Hope Fault results in the northeast-trending Seaward Kaikoura range located to the west of the township. The Hope Fault is currently the most active structure of the Marlborough Fault System with a right-lateral slip rate of 20–40 mm/year (see Chapter 2; Cowan 1991; Van Dissen & Yeats 1991).

The town centre is situated proximal to the coast and upon uplifted beach deposits and alluvial out-wash fans of the braided Kowhai and Hapuku Rivers which flow eastward from the Seaward Kaikoura Range. The region is predominantly underlain by alluvial gravels with interspersed sands deposited by the braided rivers which avulsed across the region. These alluvial sands are cross-cut by channels and associated flood deposits of smaller streams. Late Quaternary displacements on the Hope Fault have offset the watershed of the Kowhai River, which combined with likely co-seismic aggradation, have resulted in channel avulsion across the region. The alluvial sediments within ~500 m of the coast are inter-fingered with coastal gravels and sands associated with historical coastlines. The maximum inland extent of the coastal sediments is likely reflected by Lyell Creek running along the western most extent of the township, and tectonic uplift of the region combined with marine regression following the mid-Holocene high-stand. The loosely consolidated nature of the flood deposits from the small streams within the township, combined with shallow water-tables (1 to 2-m depth)

poses a localized high liquefaction hazard for the region. Localized pockets of beach sand within the gravels are also potentially liquefiable.

The southeast section of the township is located upon the Kaikoura Peninsula and associated bays. The peninsula is comprised of a flight of uplifted and folded marine terraces underlain by a Late Cretaceous-Paleogene Siltstone and Limestone succession that unconformably overlie Torlesse greywacke. The rocks comprising the peninsula are folded on kilometre scale wave lengths reflecting crustal shortening on multiple, southeast-facing thrust faults present both on land and continuing offshore. Paleo-sea-cliffs and uplifted beach deposits surround the base of the Peninsula and provide a high rockfall and landslide hazard for the settlement.

4.2.2 Liquefaction in and around Kaikoura

Liquefaction was observed in a limited number of locations in the Kaikoura area, with most located along Mt Fyffe Road and along Lyell Creek which runs parallel to and just west of Beach Rd (shown in Figure 4.). The locations where liquefaction ejecta was observed are shown in Figure 4.92. In each case, the amount of ejecta was considered minor to moderate; examples of the ejecta features observed are shown in Figure 4.93 to Figure 4.98. Surface colouring visible in aerial photography of the area (courtesy LINZ) suggests that these ejecta could be associated with paleo channels of the Kowhai River, which currently reaches the sea to the south of Kaikoura. Samples of ejecta material were recovered from two locations, marked as "SR-1" and "BR-1" in Figure 4.92; the first from a sand boil at the roadside on Schoolhouse Road (Figure 4.93), and the second from an area of intense cracking along Lyell Creek, behind Beach Road (Figure 4.94). Figure 4.93 (b) shows the particle size distributions of these samples, which were obtained by wet sieving. Laboratory testing confirmed that both samples were non-plastic.

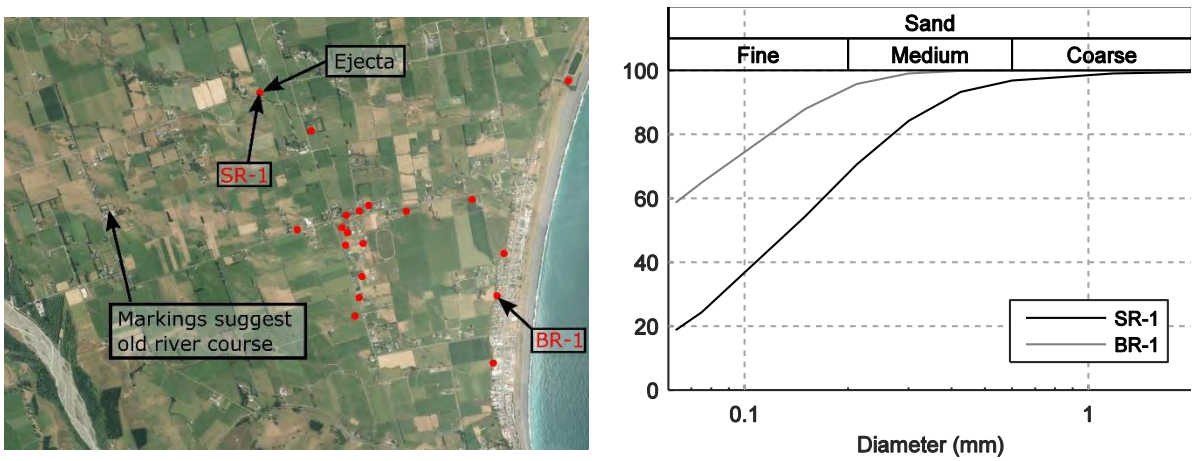

(a) (b)

Figure 4.92: (a) Locations of observed liquefaction ejecta; SR-1 and BR-1 refer to locations where ejecta samples were obtained (approx. centre of image: S42.375, E173.647). (b) Particle size distribution of the samples SR-1 and BR-1.

Figure 4.93: Liquefaction ejecta on Schoolhouse Road where sample SR-1 was taken (–9 Dec 2016, S42.3681, E173.6496, facing SE).

Figure 4.94: Liquefaction ejecta in the bank of Lyell Creek inland of Beach Road where ejecta sample BR-1 was obtained. Note the light colour of the material (–9 Dec 2016, S42.3916, E173.6777, facing E).

Figure 4.95: Liquefaction in a vegetable patch on Mt Fyffe Road. Note the ejecta issued from ground cracks (–date to be added in V2.0 of report, S42.3813, E173.6622, facing S).

Figure 4.96: Liquefaction in driveway on Mt Fyffe Road (– date to be added in V2.0 of report, S42.3800, E173.6600).

Figure 4.97: Ejecta in the field 50 m west of Mt Fyffe Road (– date to be added in V2.0 of report, S42.3877, E173.6610).

Figure 4.98: Liquefaction ejecta in the field south of Mill Road. Note: the ejecta is concentrated in lines which continue in the background over a total length of 100 m (– date to be added in V2.0 of report, S42.3772, E173.6753, facing SE).

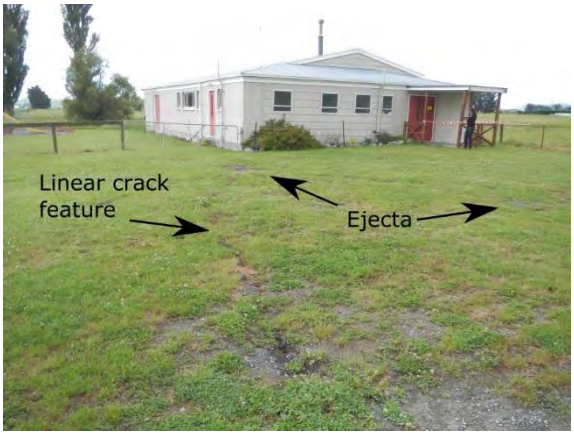

Figure 4.99: Front area of house on Schoolhouse Road (–9 Dec 2016, S42.3680, E173.6500, facing SW).

On Schoolhouse Road north of Mt Fyffe Road (Figure 4.93 and Figure 4.99), a structure had visibly settled, with markings on a wastewater vent pipe suggesting the settlement on the eastern side of the house was approximately 6 cm (Figure 4.100). Misalignment of a drainpipe with its associated drain shown in Figure 4.101 indicates that the house had also moved 10 cm parallel to its major plan axis (SSE) relative to the ground. Additionally, a vertical gap up to 20 cm wide was present on the eastern side of the house. The combined settlement and lateral movement of the house resulted in cracking of the unreinforced block (Figure 4.102). On the front lawn of the structure, a 5 cm ground crack appeared to follow the line of buried services to the road (Figure 4.100).

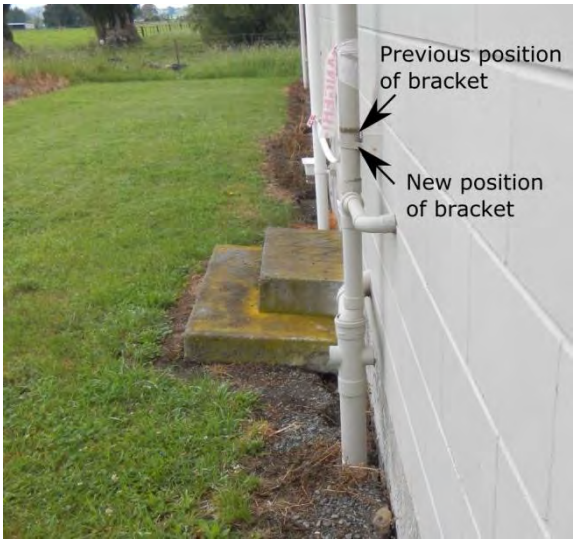

Figure 4.100: View of east wall of house on Schoolhouse Road (–9 Dec 2016, S42.3682, E173.6501, facing S).

Figure 4.101: Misalignment of drain pipe and drain on east side of house on Schoolhouse Road (–9 Dec 2016, S42.3683, E173.6501).

Figure 4.102: Cracking through brick work on SW corner of house on Schoolhouse Road (–9 Dec 2016, S42.3684, E173.6501, facing W).

Figure 4.103: Damage caused to house on Mill Road by lateral ground movements (– date to be added in V2.0 of report, S42.3784, E173.6675, facing NE)

A number of sand boils were observed around the intersection of Mt Fyffe and Mill Road, minor to moderate in size. At a house on Mill Road, damage to the structure shown in Figure 4.103 was caused by an outdoor concrete slab displacing laterally to the north relative to the house (Figure 4.104). Also, a newly built house located on Mt Fyffe Road experienced some settlement, and vertical gaps up to 10 cm wide had formed at some places around the perimeter (Figure 4.105). In front of the house, a buried septic tank had floated approximately 30 cm relative to the ground (Figure 4.106). While no obvious ejecta were observed at the house, small sand boils were discovered in the fields approximately 50 m west of the house (Figure 4.97).

Figure 4.104: Separation of outdoor slab from main foundation slab (date to be added in V2.0 of report, S42.3784, E173.6675, facing E)

Figure 4.105: Southern side of new house on Mt Fyffe Road (8 Dec 2016, S42.3877, E173.6620, facing W).

Figure 4.106: Floatation of septic tank at SE corner of house on Mt Fyffe Road (8 Dec 2016, S42.3876, E173.6621, facing N).

4.2.3 Lateral Displacements and Ground Failure

Many instances of lateral ground movement were observed on the banks of the creeks and drainage ditches in the Kaikoura area. The most significant impacts to infrastructure, as well as some of the most severe lateral displacements and/or ground failures, occurred along an ~2 km stretch of Lyell creek which forms the western boundary of the heavily developed region of Kaikoura, as shown in Figure 4.107.

Ground cracks were observed on both sides of Lyell creek, with the lateral displacements varying significantly in magnitude. Some of the largest displacements were located between and 140 and 190 Beach Road (including Gillings Lane) where displacements in excess of 2.5 m occurred within 30 m of the creek in a few locations, while cumulative displacments in the range of 0.5 – 2 m were common elsewhere. A selection of photographs showing some of the lateral displacements and their effects on the residential buildings in this area are shown in Figure 4.109 to Figure 4.122. It was also noticeable that at a number of locations, the cracks were also associated with large vertical offsets, with the soil blocks rotating with their bases moving inwards towards the river relative to their tops; Figure 4.111 and Figure 4.120 show two examples of this. This deformation mechanism may imply the occurrence of cyclic softening and deeper seated slumps, rather than solely lateral spreading

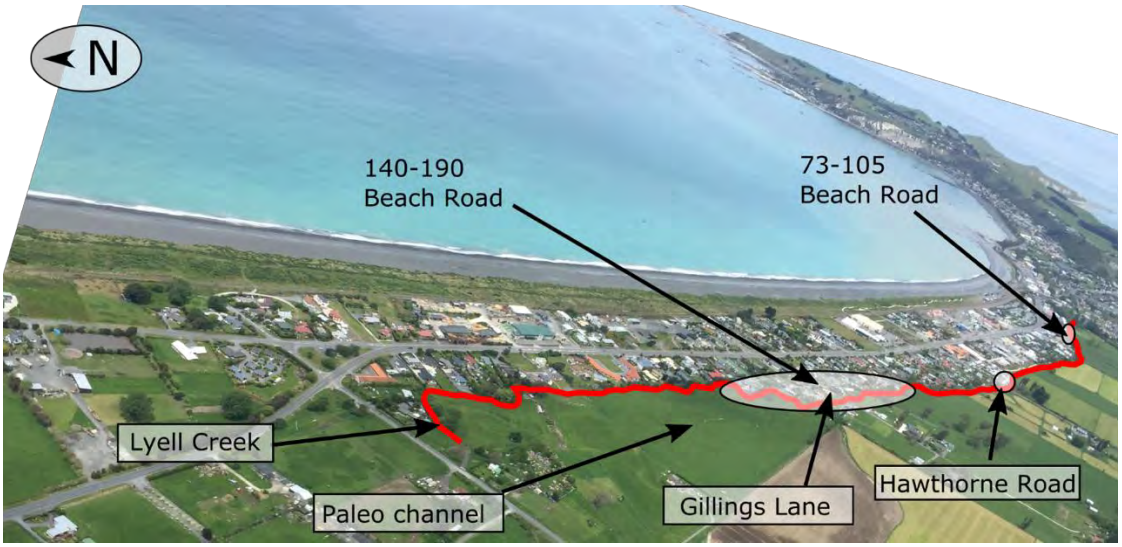

Figure 4.107: Lyell Creek and locations of photographs of interest (for reference the coordinates of 4 Gillings Ln are S42.3841, E173.6786).

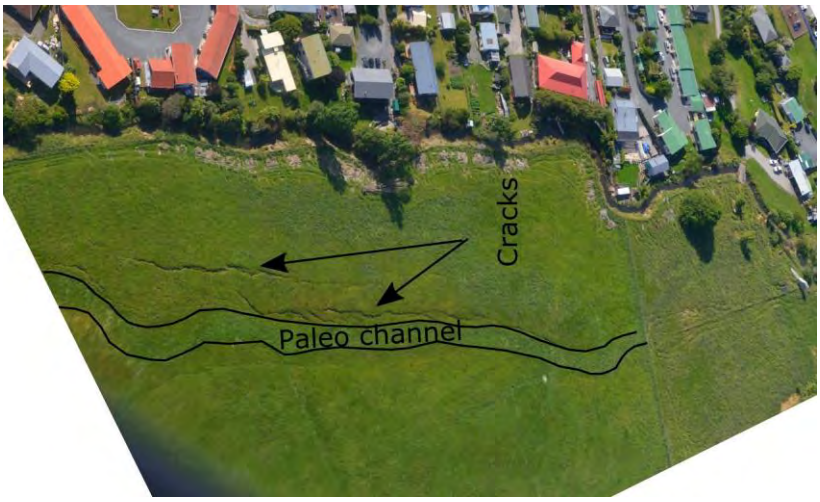

Figure 4.108: Lateral displacement associated with a paleo channel (approx. centre of image: S42.3808, E173.6787).

(a) (b)

Figure 4.109: Separation of concrete slabs and garage (70 cm wide) due to lateral ground movements towards Lyell Creek (date to be added in V2.0 of report,): (a) S42.3822, E173.6801; (b) S42.3821, E173.6802. Note the garage has moved laterally in the picture (i.e. Lyell Creek is behind the garage, to the left of the picture).

Figure 4.110: Lateral displacements (approx. 1.5 m in total) caused a loss of support at the NW corner of a house on Beach Road, causing cracking in the brick wall (date to be added in V2.0 of report, S42.3823, E173.6800).

Figure 4.111: Large vertical offset (50 cm) associated with the ground movement north of Gillings Lane (– date to be added in V2.0 of report, S42.3841, E173.6784).

Figure 4.112: Lateral displacements with large vertical offsets at Gillings Lane (– date to be added in V2.0 of report, S42.3841, E173.6784).

Figure 4.113: Floatation of manhole on Beach Road near to Lyell Creek (– date to be added in V2.0 of report, S42.3848, E173.6783).

(a)

(b)

(c)

Figure 4.114: Complete loss of support to foundations at west end of house on Beach Road (– date to be added in V2.0 of report, S42.3851, E173.6783).

(a)

(b)

Figure 4.115: Lateral ground movement caused separation of two semi-detached houses on Beach Road (– date to be added in V2.0 of report, S42.3857, E173.6783).

Figure 4.116: Cracks running through the house closer to Lyell Creek (– date to be added in V2.0 of report, S42.3857, E173.6783).

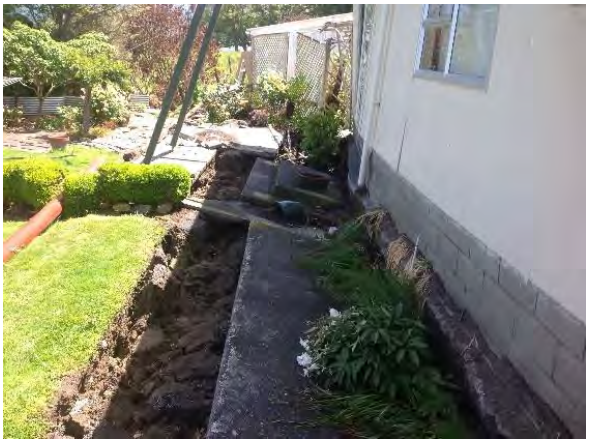

Figure 4.117: Gapping at the west side of the house closer to Lyell Creek (date to be added in V2.0 of report, S42.3857, E173.6783).

(a)

(b)

Figure 28: A garage/shed at a house on Beach Road displaced approx. 1 m towards the Lyell Creek, and moved downwards approx. 1 m (– date to be added in V2.0 of report, S42.3860, E173.3860).

Figure 4.118: Lateral displacement with vertical offsets close to Hawthorne Road Bridge (– date to be added in V2.0 of report, S42.3885, E173.6776).

(a) (b)

Figure 4.119: Lateral movement south of Hawthorne Road Bridge (– date to be added in V2.0 of report, S42.3894, E173.6775).

Figure 4.120: Lateral displacements at 105 Beach Road. Note: Cracks are associated with vertical offsets and blocks have rotated away from the river (i.e., slumped) (9 Dec 2016, S42.3902, E173.6777).

(a) (b)

Figure 4.121: Cracks in footpath between 105 and 73 Beach Road, running east of and parallel to Lyell Creek. Largest crack in footpath (right hand photo) was 1 m wide and 70 cm deep (9 Dec 2016): –(a) S42.3916, E173.6778; (b) S42.3926, S173.6777.

Figure 4.122: Lateral displacement at 87 Beach Road 13 m east of Lyell Creek (date to be added in V2.0 of report, S42.3917, E173.6778).

Figure 4.123: Recent earthworks on west side of Lyell Creek, opposite 87 Beach Road. (9 December 2016, S42.3922, E173.6777).

No foot surveys were carried out on the western side of the creek; however, some cracks were visible from the eastern bank and in aerial photographs. Figure 4.108 shows a pair of large lateral spreading cracks which were spotted during a helicopter flight. These cracks are approximately 50 m west of Lyell Creek, significantly further than the majority of other cracks. Inspection of aerial photographs indicates that these cracks are likely to be associated with the paleo channel marked in Figure 4.107.

It is expected that there were many cracks that were not observed as a result of the heavy vegetation obscuring individual cracks. Additionally, at the time of the visit on the 9th December 2016, recent earthworks were visible on the western bank of the creek (shown in Figure 4.123) , which are assumed to indicate that some bank stabilization or dredging of the creek was carried out soon after the earthquake.

Detailed transects were carried out at three locations along Beach Road following the approach used by Robinson et al. (2011), as shown in Figure 4.124. At each location, individual crack widths, distance from the river channel, and the change in vertical elevation were measured using a tape measure and a range finder. Additionally, the height of the free-face, determined using a tape measure, was used to estimate the difference in height between the bank and the base of the river channel directly next to the start of the transect. The red

lines in the figure indicate the zone of significant cracking. The data from these transects (summarised in Table 4.3) indicate that the lateral displacements in these locations were in the range of 0.6 to 1.1 m, while cracking was typically concentrated within 15 m of the river channel.

Despite the large lateral movements, ejecta were not widespread on the east side of Lyell Creek, with only relatively small sand boils (~50 cm diameter) being observed at a few locations along Beach Road (visible in Figure 4.94).

Figure 4.124: Location of transects (approx. centre of image: . S42.3922, E173.6791).

Table 4.3: Summary of transects along Lyell Creek

Transect Number	Cumulative crack width (m)	Max distance of crack from creek (m)	Creek depth (m)
1	1.12	7.3	0.3
2	0.62	15.0	0.7
3	0.96	13.3	1.0

4.2.4 Impacts on Infrastructure & Structures

4.2.4.1 Oxidation Ponds

Kaikoura's waste water is treated at a facility located north of the main town adjacent to the railway line, and immediately south of School House Road. Between March 2015 and March 2016, the total discharge from the ponds was approximately 320,000 m^3, an average of 880 m^3 per day (KDC 2016). At its southern end, the facility is bordered by Middle Creek, while beach exists to the east. On both the southern and eastern sides, the land slopes steeply to the level of the current river and the beach respectively. An overview of the site is shown in Figure 4.125, and for the purposes of this section, the northern and southern ponds are referred to as KK-OPN and KK-OPS.

This facility was inspected by Tonkin +Taylor engineers following the earthquake on the 22nd November 2016. At the time of inspection, KK-OPS had been fully drained. Lateral spreading cracks were present on the river side of the bank at the south end of the pond (Figure 4.126) while liquefaction ejecta were also present on the river terrace close to one of the piers of the railway bridge (discussed in Chapter 6). Deformations were visible along the crest of the pond, particularly at the most westerly corners, where significant settlement was visible (Figure 4.127 to Figure 4.129). The deformation at these corners was sufficient to cause tearing in the pond's geo-liner, shown in Figure 4.127. Significant settlement was also evident on the eastern side, and a second major tear in the geo-liner was present close to a number of transverse cracks in the bank (Figure 4.128). A concrete slab supporting a vent pipe was completely exposed by the settlement of the ground (Figure 4.131). Aeration lines were strung between posts on the north and south edges of the pond. These posts rotated significantly, particularly on the south edge of the pond (Figure 4.132).

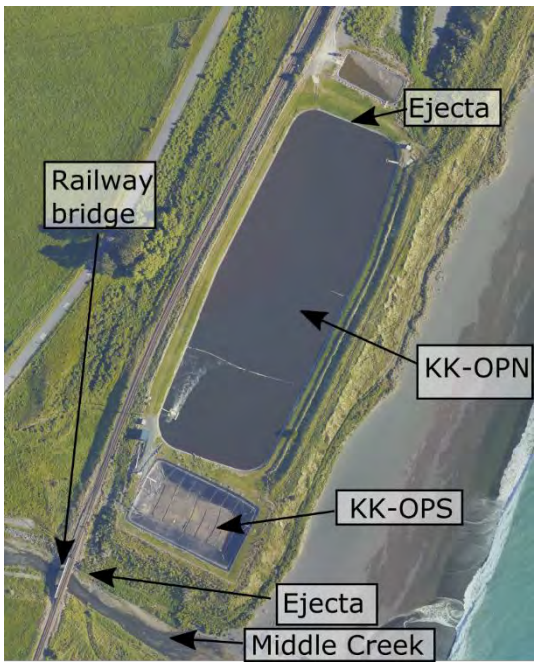

Figure 4.125: Overview of Oxidation Ponds north of Kaikoura (approx. centre of image: S42.366, E173.687). (modified from LINZ, 2016)

Figure 4.126: Lateral spreading in the bank on south edge of oxidation ponds (– date to be added in V2.0 of report,, S42.3672, E173.6866, facing W.)

Figure 4.127: KK-OPS looking from the SW corner. Note: geo-liner in the foreground has ripped (– date to be added in V2.0 of report,, S42.3668, E173.6865, facing E).

Figure 4.128: KK-OPS from eastern edge. Note geo-liner is ripped in foreground and uneven settlement on the west side is visible in the background (– date to be added in V2.0 of report, S42.3669, E173.6874, facing W).

Figure 4.129: West edge of KK-OPS. Large differential settlements of the crest are visible (– date to be added in V2.0 of report, S42.3668, E173.6865, facing N).

Figure 4.130: East side of KK-OPS. Note ripped geo-liner in line with crack by third post from left (– date to be added in V2.0 of report, S42.3667, E173.6875, facing SE).

Figure 4.131: Protruding vent pipe on east edge of KK-OPS due to ground settlement (– date to be added in V2.0 of report, S42.3668, E173.6875, facing S).

The larger oxidation pond (KK-OPN) was still full at the time of the inspection, however, transverse cracks in the concrete lining were visible (Figure 4.133). Figure 4.134 shows a section of concrete lining which had moved laterally towards the centre of the pond near the SW corner of KK-OPN. In addition to this movement, general lateral movement of the ground towards the pond was highlighted by gapping around a metal anchor rod at the edge of the pond.

Figure 4.132: Rotation of the aeration-line control posts on the south side of KK-OPS (– date to be added in V2.0 of report, S42.3669, E173.6867, facing E).

Figure 4.133: North edge of KK-OPN. Note cracking and overlayering of concrete. Ejecta visible on concrete. (– date to be added in V2.0 of report, S42.3647, E173.6884, facing W).

Figure 4.134: West edge of KK-OPN. Note concrete panel has displaced into pond (– date to be added in V2.0 of report, S42.3660, E173.6868, facing N).

4.2.4.2 Retaining Walls

Several properties to the east of Lyell Creek had constructed wooden retaining walls. At 87 Beach Road, a 2 m tall wooden retaining wall had been built at approximately 70 m west of Lyell Creek and appeared to have performed well with no signs of lateral displacement (Figure 4.135). However, at 29, 33, and 35 Beach Road, the retaining walls showed signs of failure.

On Beach Road, a retaining wall had been built at the rear of a long motel building. The timber retaining wall was constructed approximately 12 m from Lyell creek, on a section of raised ground, which is visible in Figure 4.136. The crest of the retaining wall had moved 30-40 cm towards the river, based on gaps which had opened up between the concrete slab and the fence on the retained side of the wall.

A second retaining wall on Beach Road is located roughly 30 m east of Lyell Creek. Figure 4.138 shows this retaining wall, where the top of the retaining wall had bulged 20-30 cm towards the creek. Cracks of up to 5 cm wide were present in the concrete slab approximately 5 m back from the top of the wall and are visible in Figure 4.139.

(a) (b)

Figure 4.135: Good performance of retaining wall at 87 Beach Road (–9 Dec 2016, S42.3917, E173.6785: (a) facing E; (b) facing SE.

Figure 4.136: Failure of retaining wall (– date to be added in V2.0 of report, S42.3973, E173.6798, facing N).

Figure 4.137: Cracks behind retaining wall (– date to be added in V2.0 of report, S42.3971, E173.6798, facing N).

Figure 4.138: Failure of retaining wall (– date to be added in V2.0 of report, S42.3964, E173.6793, facing N). Note: Cracks visible in the car park on the retained side of the wall.

Figure 4.139: Cracks visible behind retaining wall (– date to be added in V2.0 of report, S42.3968, E173.6796, facing S).

4.3 Summary of Reconnaissance Amuri and Emu Plains

The Amuri and Emu Plains (lying south and north of the Waiau River, respectively) comprise the relatively flat bottomed Waiau valley in North Canterbury bounded to the north by the Amuri Mountain range and the Lowry Mountain range to the south and east. The area is rural, with two minor towns (Rotherham and Waiau) located towards the north-east of the valley. Waiau is the larger of the towns and has a population of ~260 (Statistics NZ, 2013) and is located at the confluence of the braided Waiau and Mason Rivers. Additional townships are located within this valley, but they are similarly small in population.

The township of Waiau is built upon alluvial fill sequences, predominantly comprised of gravels, associated with Pleistocene glaciation and the subsequent outwash surface, and the later development of the Waiau River (Rother, 1996). Much of the overbank flood-plain surrounding the Waiau River is used as farmland and is underlain by alluvial gravels with localised sand lenses and capped by over-bank silts. Smaller active and paleo-stream channels are present within the flood plain, along with paleo-channels of the Waiau River which are recognizable as topographic depressions within the farmland. The active and paleo-channels are likely comprised of alluvial gravels and sands.

The sequence of fault ruptures associated with the Kaikoura earthquake began relatively close to the township of Waiau and propagated in a north-easterly direction. The WTMC strong motion station, located approximately 4 km north of Waiau town (position marked in Figure 4.), indicated that this region experienced extremely strong shaking, with horizontal accelerations in excess of 1 g, and vertical accelerations of 2.7 g. Evidence of the strong ground motions in this regions included broken wooden power pylons (observed in Waiau and along River Road), clear displacement of large stone blocks in Waiau, and the toppling of gravestones in the town of Rotherham.

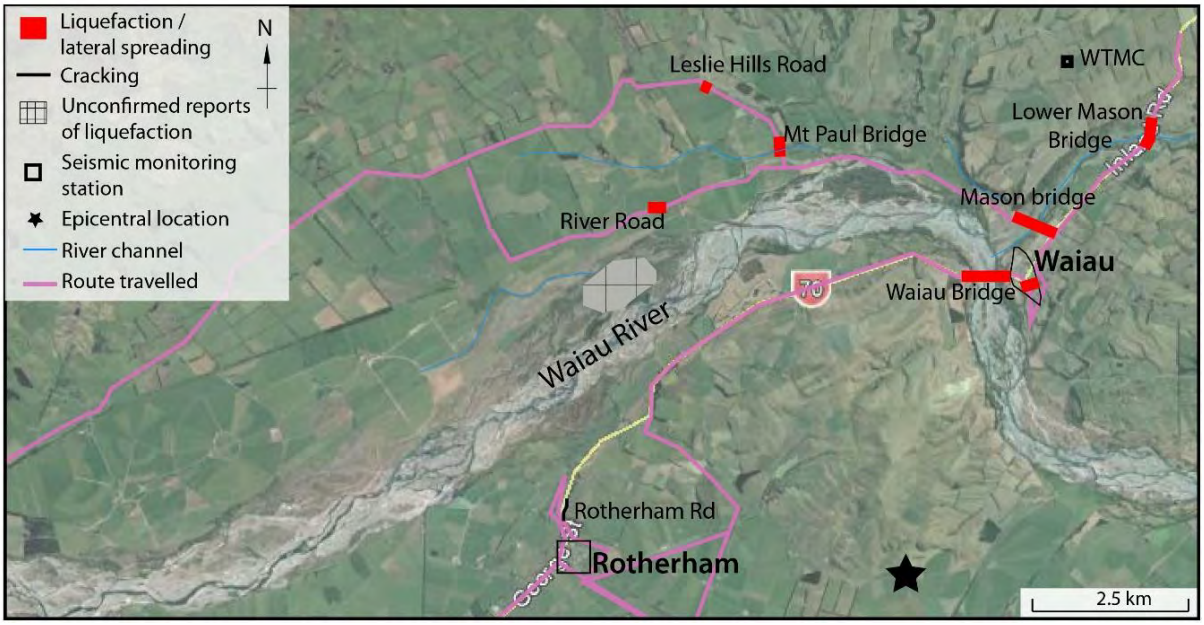

Figure 4.140: Map of the Waiau area indicating areas with liquefaction manifestation. (approx. centre of image: S42.658, E173.005).

Reconnaissance in this area was undertaken relatively soon after the earthquake, with the first exploratory visit to the region taking place on the 15 Nov 2016. Additional visits occurred on the 17 and 18 Nov 2016. The extent of damage in this area was not well-known immediately, and the reconnaissance on the 15 Nov 2016 aimed only to see as much as possible to assess the levels of earthquake related damage. The additional trips on the 17 and 18 Nov aimed to visit the town of Waiau and the surrounding bridges. Most of the reconnaissance in these regions involved drive-through surveys, because it was not logistically possible to carry out reconnaissance in most areas away from the main roads. The routes covered during the reconnaissance are shown in Figure 4..

Damage to buildings and infrastructure in this region was largely caused by the high inertial loads. Due to the sparse population in the area, the building stock is largely single storey, light residential buildings, and there were damaged brick facades, fallen chimneys and damage to unreinforced masonry walls throughout the town of Waiau. The main impacts to infrastructure in the region were to the multi-span bridges crossing the Waiau, Mason, and Wandle Rivers, where the inertial loading caused severe structural damage. These bridges are discussed in Chapter 6 of this report and by Palermo et al. (2017). Common geotechnical issues included settlement and outward cracking of the approaches, while abutment rotation and cracking was observed at a small number of bridges. Liquefaction was observed in some locations but was generally not widespread in the surveyed areas. Major liquefaction-induced lateral spreading was not observed by the reconnaissance teams in this region, though it may have contributed to some of the bridge abutment damage and road cracking.

It is important to state that surface expressions of fault rupture were present in the region, and in particular, part of the rural Leslie Hills Road was completely destroyed by a rupture transverse to the road. In this same area, there were both tension cracks and compressional features, the latter of which was made obvious by sagging fence lines and by ridges in the road surface. Further information on the observations made at this site are provided in Chapter 6.

4.3.1 Rotherham

Despite the strong shaking in Rotherham, no evidence of liquefaction was observed in the town. North of Rotherham, cracking both in the road and on the road sides were observed as shown in Figure 4.141 and Figure 4.142, and are representative of damage in the area (noting that the area was more severely affected by landslides).

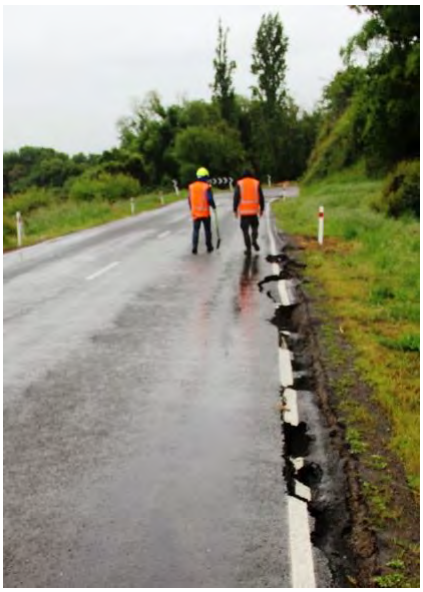

Figure 4.141: Cracks alongside Rotherham road (S42.6908, E172.9470, 17 Nov 2016).

Figure 4.142: Large crack in middle of roadway on Rotherham Road. Crack width 20-30 cm. Vertical offset is approximately 4 cm (S42.6900, E173.9462, 17 Nov 2016).

4.3.2 Waiau

In the town of Waiau, the strong shaking caused damage to a large number of building facades and chimneys (examples are shown in Figure 4.143), however there was only evidence of liquefaction at two locations at the south end of the town. In this part of town, there were a number of cracks in the road, and the two locations of ejecta were either associated with the cracks (Figure 4.144), or with fence posts which surrounded a paddock SW of the end of Parnassus Street. The particle size distribution of a sample of this ejecta is shown in Figure 4.145. It was reported by utility workmen that there was a significant amount of ejecta inside the paddock, but the owner could not be located to obtain access to this area.

(a) (b)

Figure 4.143: Damage to houses in Waiau. (a) fallen chimney (b) damage to façade. (S42.66, E173.04, 17 Nov 2016)

Figure 4.144: Liquefaction at the south of Waiau town (date to be added in V2.0 of report, S42.6592, E173.0440, 17 Nov 2016).

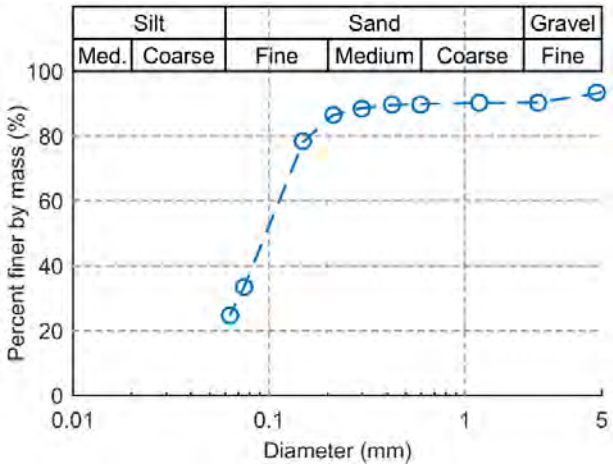

Figure 4.145: Particle size distribution of liquefaction ejecta in Waiau town

Figure 4.146: Standing water and ejecta west of Waiau town (date to be added in V2.0 of report, S42.638, E172.993).

Figure 4.147: Liquefaction ejecta on River Road (S42.6427, E172.9743, 17 Nov 2016).

Liquefaction was observed in the agricultural areas close to the Waiau River, west of Waiau town. Aerial photography of this area (Figure 4.146) shows standing water and ejecta in the fields as well as on the roads. The presence of sand boils in this area was confirmed by ground teams, who noted the presence of a number of ground cracks in the same area.

4.4 Greater Christchurch Urban Area

The greater Christchurch area is located south of the fault ruptures associated with the Kaikoura earthquake on the eastern coast of the South Island and experienced relatively low peak ground accelerations, with the largest recordings showing around 0.08 g in Kaiapoi and 0.04 g within Christchurch itself. The low peak accelerations recorded at the strong motion stations within Christchurch and were considered unlikely to cause any significant impact. However, given the repeated liquefaction during the larger shocks of the 2010–2011 Canterbury Earthquake Sequence, as well as relatively minor events such as the 2016 Valentine's Day earthquake when there were relatively low levels of shaking, it was decided to investigate whether there were any signs of fresh liquefaction at sites which had displayed particularly low liquefaction resistance in the past.

Four sites were selected for this purpose as shown in Figure 4.148: Swindells Road in Waikuku Beach (S42.2839, E172.7180); Cassia Place in Kaiapoi (S43.3851, E172.6704); Atlantis Street in New Brighton (S43.4956, E172.7038); and Seabreeze Close in Bexley (S42.5184, E172.7203). There was no indication that liquefaction triggered during the 2016 Kaikoura earthquake at any of these sites, and on this basis the decision was taken not to carry out any additional reconnaissance. Isolated cases of minor liquefaction were reported, and others may have gone unnoticed and unreported, but the impacts of these features on infrastructure were negligible

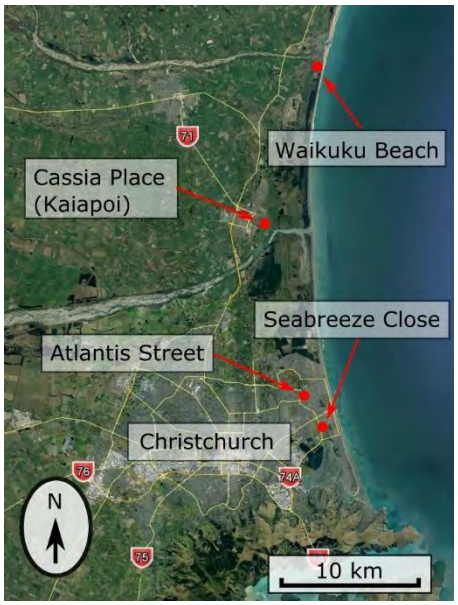

Figure 4.148: Locations of potential liquefaction sites in and around Christchurch (approx. centre of image: S43.417, E172.647).

4.5 Summary

The M_W7.8 Kaikoura earthquake involved the rupture of multiple faults in the Marlborough Fault Zone and caused widespread disruption in the north-east region of the South Island of New Zealand. Despite the large magnitude of the earthquake and high ground accelerations, relatively limited liquefaction and ground damage were observed in the Waiau Valley (where ground motions were strongest) and in the townships of Blenheim and Kaikoura.

Severe manifestations of liquefaction and lateral spreading were observed within the floodplains of the Lower Wairau and Opaoa Rivers in the area the north and east of Blenheim township. Few structures exist in this area, and hence the immediate impact on infrastructure was negligible. The locations worst affected correspond with abandoned channels or inner meander bends of the rivers. Stopbank damage occurred in locations where they crossed younger deposits in paleo channels and exhibited heavy cracking and slumping in the direction parallel to the stopbank itself. Damage within the township of Blenheim was restricted to a small number of locations, and the impact on structures was low.

Significant damage occurred to a limited number of residential structures and two retaining walls in the town of Kaikoura, due to large ground movements which occurred in a concentrated zone within 30 m of Lyell Creek. Ejecta were not a common feature along the creek, and it is likely that soft silty/clayey materials in the upper soil profile are responsible for the movements. The wastewater treatment facility located just north of Kaikoura also suffered damage as a result of ground movements, which included tears in the liners of the oxidation ponds and distortions in the aeration system.

The impacts of liquefaction and general ground distress across the Amuri and Emu Plains of the Waiau Valley were extremely modest given the large peak accelerations observed in the area (i.e., horizontal accelerations of $\approx$ 1 g). The most significant impacts in this area were to the infrastructure where the high inertial loading caused structural damage to some of the bridges. Liquefaction and lateral spreading were observed at some bridge sites, but the impact and damage was generally secondary to those arising from the inertial loads. Characteristic damage to the bridges included settlement of the approach fills, outward cracking of the approach embankments, and some limited back-rotation of the bridge abutments.

No evidence of liquefaction was observed at four sites (located in Christchurch, Kaiapoi, and Waikuku Beach) where visible manifestation of liquefaction had occurred in many of the events of the 2010-2011 Canterbury Earthquake Sequence.

References

Arnold, T. (1847) *Letters from New Zealand and Tasmania*, 1847–50, p.83. ATL.

ASTM (2007). "Standard Test Method for Particle-Size Analysis of Soils". ASTM International, West Conshohocken, PA, 2011

Begg, J. & Johnston, M. (2000). Geology of the Wellington Area. Lower Hutt, New Zealand: Institute of Geological and Nuclear Sciences 1:250 000 Map 10.

Brown, L. (1981). Late Quaternary geology of the Wairau Plain, Marlborough, New Zealand. *New Zealand Journal of Geology and Geophysics*, 477-490.

Cook, J. (1895) Map of Cloudy Bay survey district. Department of Lands and Survey

Cowan, H.A. (1991). The North Canterbury earthquake of September 1, 1888, *Journal of the Royal Society of New Zealand*, **21**(1): 1-12.

Cubrinovski, M., Green, R.A., Allen, J., Ashford, S., Bowman, E., Bradley, B.A., Cox, B., Hutchinson, T., Kavazanjian, E., Orense, R., Pender, M., Quigley, M., and Wotherspoon, L. (2010) Geotechnical reconnaissance of the 2010 Darfield (New Zealand) earthquake. *Bulletin of the New Zealand Society of Earthquake Engineering*. **43**(4): 243-321

Cubrinovski, M., Bradley, B.A., Wotherspoon, L., Green, R.A., Bray, J.D., Wood, C., Pender, M., Allen, J., Bradshaw, A., Rix, G., Taylor, M., Robinson, K., Henderson, D., Giorgini, S., Ma, K., Winkley, A., Zupan, J., O'Rourke, T., DePascale, G., and & Wells, D. (2011) Geotechnical aspects of the 22 February 2011 Christchurch Earthquake. *Bulletin of the New Zealand Society of Earthquake Engineering*. **44**(4): 205-226

Hancox G.T., Perrin, N.D. & Dellow, G.D. (1997). *Earthquake-induced landslides in New Zealand and implications for MM intensity and seismic hazard assessment.* Institute of Geological & Nuclear Sciences Client Report 43601B (prepared for EQC).

Litchfield, N.J., Benson, A., Bischoff, A., Hatem, A., Barrier, A., Nicol, A., Wandres, A., Lukovic, B., Hall, B., Gasston, C., Asher, C., Grimshaw, C., Madugo, C., Fenton, C., Hale, D., Barrell, D.J.A., Heron, D.W., Strong, D.T., Townsend, D.B., Nobe, D., Howarth, J.D., Pettinga, J., Kearse, J., Williams, J., Manousakis, J., Mountjoy, J., Rowland, J., Clark, K.J., Pedley, K., Sauer, K., Berryman, K.R., Hemphill-Haley, M., Stirling, M.W., Villeneuve, M., Cockroft, M., Khajavi, N., Barnes, P., Villamor, P., Carne, R., Langridge, R.M., Zinke, R., Vvan Dissen, R.J., McColl, S., Cox, S.C., Lawson, S., Little, T., Stahl, T., Cochran, U.A., Toy, V., Ries, W.F., and Juniper, Z. (2016). 14th November 2016 M7.8 Kaikoura Earthquake. Preliminary surface fault displacement measurements. Version 2. GNS Science. http://dx.doi.org/10.21420/G2J01F

Marlborough Catchment Board (2017) *Wairau Valley Scheme*. Blenheim, Marlborough Catchment Board.

Marlborough District Council (2016). Post-Kaikoura Earthquake Aerial Reconnaissance. Blenheim, Marlborough District Council.

Marlborough District Council (2017). Smart Maps, https://maps.marlborough.govt.nz/smartmaps, Accessed 1 February 2017.

Mason, D.P.M. & Little, T.A. (2006). Refined slip distribution and moment magnitude of the 1848 Marlborough earthquake, Awatere Fault, New Zealand. *New Zealand Journal of Geology and Geophysics*, 49, 375–382.

Palermo, A., Liu, R., Rais, A., McHaffie, B., Andisheh, K., Pampanin, S., Gentile, R., Nuzzo, I., Granerio, M., Loporcaro, G., McGann, C. & Wotherspoon, L. (2017) Performance of road bridges during the 14th November 2016 Kaikoura Earthquake. *Bulletin of the New Zealand Society for Earthquake Engineering*. **50**(2): 253-270

Robinson, K., Cubrinovski, M., Kailey, P. & Orense, R. (2011) "Field measurements of lateral spreading following the 2010 Darfield earthquake". *Proceedings of the 9th Pacific Conference on Earthquake Engineering*, Auckland, New Zealand.

Statistics NZ (2013) *Number of Electorates and Electoral Populations: 2013 Census*. Statistics NZ. ISBN 978-0-478-40854-6

Thompson, A.S. (1859*). The story of New Zealand: past and present – savage and civilised*. Vol. 2. John Murray, London.

Van Dissen, R.J. & Yeats, R.S. (1991). Hope fault, Jordan thrust, and uplift of the Seaward Kaikoura Range, New Zealand. *Geology,* **19**(4): 393-396.

5. LIQUEFACTION EFFECTS AND ASSOCIATED DAMAGE AT THE PORT OF WELLINGTON

5.1 Introduction

In the M_w7.8 Kaikoura Earthquake, the port of Wellington (CentrePort Limited) experienced liquefaction of the reclamations, lateral spreading, and ground deformations that led to building and wharf damage. The liquefaction caused global settlement of the fill deposits and lateral movement (spreading) of the fills towards the sea. There was evidence of lateral spreading in the fills behind the pile-supported wharves whereas signs of lateral spreading and liquefaction-induced settlement were evident in the soils surrounding buildings on various foundations. The QuakeCoRE-GEER team performed on-site reconnaissance on November 17, 20, 21, 22, 23 and 30, and December 1 and 2, 2016.

This chapter summarizes key observations from the field surveys and focuses on the geotechnical aspects of the performance of reclamations, wharves and buildings at the port. The chapter is organized into the following sections: background information on the CentrePort reclamations, recorded ground motions in the context of CentrePort reclamations, observations of liquefaction manifestation and consequent ground deformation, and geotechnical aspects of the seismic performance of wharf structures, and geotechnical aspects of the seismic performance of building structures.

5.2 CentrePort reclamations

5.2.1 Land reclamation in the Wellington Harbour

From the early stages of European settlement and the relatively rapid expansion of Wellington in the 1840s, there was a need for reclamation in the Wellington Harbour to provide flat land for development, wider public ways, tidal protection, and deeper water along the coastline. The first notable reclamation work was along the water edge in 1847. Early reclamation works were of relatively small scale (Anderson, 1984).

Reclamation works in the Wellington Harbour were carried out in essentially three major stages: (1) early reclamations in the period 1852 – 1879; (2) early 20th century reclamations in the period 1901 – 1932; and (3) final reclamations in the period 1965 – 1975. According to Anderson (1984), until the 1960s the reclamation growth in the inner harbour and along the waterfront was a series of independent projects to serve wharves, railways, buildings, industry, and commerce rather than land formations with an overall concept. The Container Terminal of the CentrePort was established in the final stage of reclamations from 1967 to 1975.

The historical development of land reclamation in the Wellington Harbour in the vicinity of CentrePort is illustrated in Figure 5.1. In this figure, the original coastline in the 1850s is shown with the dashed line, and areas of different stages of reclamations are indicated. A large portion of the current CentrePort area was reclaimed in the final phase of reclamations

between 1965 and 1975 when Thorndon Container Terminal and Thorndon Wharf were constructed. Some of the old structures from previous reclamation stages remained in place during subsequent reclamation works either as part of the current port facilities or as remnants of abandoned structures that were left in place during subsequent reclamations. The most important structures in this context are the Kings Wharf, Pipitea Wharf, and the mass concrete Old Seawall. The Kings Wharf was completed in 1906 and is part of the current port facilities, whereas the Pipitea Wharf, which was completed in 1930, was partially demolished during the Stage 3 reclamation works, but its piles and portions of the deck were left in place to provide foundation for the S37 building and are now buried in the reclaimed land. Similarly, the Old Seawall, which is aligned in the south-west to north-east direction (see Figure 5.1 and 5.2), is still in place and is part of the current reclamation. It separates the Stage 2 and Stage 3 reclamations. These structures are important references with regard to the characteristics of the reclaimed soils, because different soils and reclamation techniques were used in different stages of the reclamation works. These differences influenced the observed land performance during the Kaikoura earthquake with the old structures causing distinctly different movements relative to the surrounding reclaimed soils. Their presence was clearly manifested on the ground surface through differential settlements between the structures and their surrounding reclaimed soils.

5.2.2 *Characteristics of reclaimed land at CentrePort*

Construction of CentrePort Reclamation

There are several important aspects of land reclamations with regard to their performance under earthquake loading and liquefaction resistance. The composition and characteristics of soils used for land reclamation, the method of construction, and the age of the reclamation are particularly important in terms of understanding the seismic performance of the ground and structures at CentrePort.

Two methods of reclamation were primarily used to construct the reclaimed land at CentrePort: end-dumping (tipping) of gravelly soils from truck and barge operations using soils from quarries in the Wellington region, and constructing hydraulic fill using dredged material from the original seabed in the vicinity of the reclamation works. Figure 5.2 shows that hydraulic fills were constructed along the waterfront north of the Old Seawall during the second stage of reclamations whereas the majority of the reclaimed land at CentrePort was constructed by the end-tipping method. Importantly, a relatively small volume (i.e., about 250,000 m^3) of the Thorndon Reclamation might have been constructed using dredged material from the harbour entrance (Hutchison, 1973; Tonkin+Taylor, 2012).

As summarized in Figure 5.2, reclaimed land that is south of the Old Seawall is generally composed of gravelly soils with an age of approximately 40 years, with a possible exception for a relatively small volume of dredged material mentioned previously. The age of similar end-tipped gravelly reclamations north of the Old Seawall is about 100 years. The hydraulic fills, which are located north of the Old Seawall, are about 80 years old, and are

predominantly composed of sand and silt dredged from the original seabed. The ages of each reclamation stage are listed in Table 5.1.

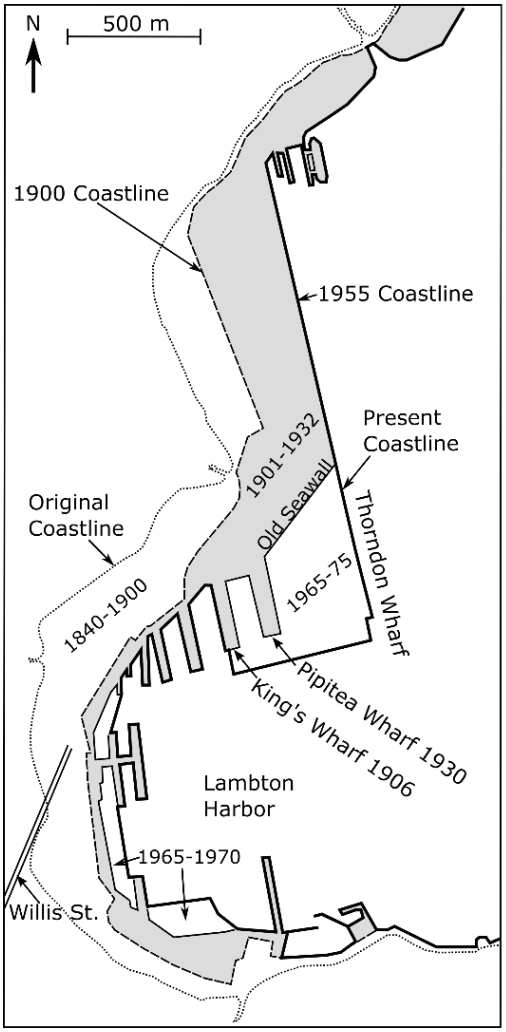

Figure 5.1: Historical development of land reclamation in Wellington Harbour (reproduced based on maps from Anderson, 1984).

Table 5.1 Age of Reclaimed Deposits

Reclamation	Age (Years)
Stage 2 end-tipped gravelly reclamations north of the Old Seawall	100
Stage 2 hydraulic fills of dredged marine deposits	80
Stage 3 end-tipped gravelly reclamations south of the Old Seawall	40

Details of reclamation works performed during various development stages are relatively sparse. The characteristics of the materials used for the Thorndon Reclamation are summarized as follows (Tonkin+Taylor, 2012):

- The reclamation was constructed using "common fill." By specification, the "common fill" was gravelly soil with sand, some cobbles, and some fines; the maximum dimension of the cobbles was 150 mm (with particles larger than boulders randomly permitted); soils passing the 0.036 mm sieve should be either non-plastic or have a Plasticity Index (PI) value not greater than 5.
- A rockfill "filter" layer and overlying rockfill armour layer were placed along the edges of the slopes of the "common fill" to provide coastal protection. The rock material used for the filter was specified as a uniform material graded between 25 mm and 125 mm in diameter with up to 5% undersize material and up to 10% oversize material (up to a maximum of 300 mm in diameter). The rockfill armour was constructed of "C-grade rock" (evenly graded rock between 22 kg and 90 kg) and "A-grade rock" (graded between 90 kg and 700 kg, with at least 60% of the supplied rock being over 450 kg). The "A-grade rock" was placed into position by a crane (i.e., it was not dropped).

The construction involved the following key stages and features:

- Prior to deposition of the "common fill" material, the seabed was dredged to remove the soft sediments.
- Approximately 2,900,000 m^3 of "common fill" from the quarries were dumped by end-tipping to construct the Thorndon Reclamation. An additional 250,000 m^3 of dredged material were also used in this reclamation.
- Fill was not compacted below the water level, because of the nature of the material used and to speed construction.
- Once the reclaimed ground reached 0.9 m above the water table, the soils were compacted to support the pavement. Static rollers (without vibration) were used to compact the fills in layers less than 0.23 m thick above the water table (WT). This created a compacted crust about 1.5 m to 2.0 m thick below the pavement.
- The reclamation was then covered by asphalt pavement overlying a base course. The thickness of the pavement varies across the reclamation area and is predominantly 0.2 m to 0.3 m thick, whereas the base course is about 0.5 m thick.
- To place the protective armour rock, small (i.e., about 6 meters wide), rock mounds were built near the toe of the "common fill" reclamation to laterally restrain the rock as it was placed over the sloped face of the reclamation fill.

Characteristic Layers at CentrePort

The characteristic soil profile at the Thorndon Reclamation consists of the following layers:

- Compacted earth fill and pavement layer, which is typically about 2.0 to 3.0 m thick. This layer was above the water table during construction.
- Un-compacted reclamation fill (below the WT during construction), which varies in thickness between 10 m and 18 m.
- Marine deposits of interbedded sand/clay/silty clay, or soft to very stiff clay, which are relatively thin layers with a total thickness of about 1 m to 2.5 m.
- Wellington Alluvium, which is an approximately 200-m thick layer composed of interbedded dense gravel and stiff to very stiff silt.

- Greywacke sandstone/siltstone bedrock, which is estimated to be at a depth of about 200 m to 250 m.

The thickness of the reclaimed deposit is variable depending on the horizontal distance from the original coastline (or depth to the original seabed). It is approximately 10 m to 15 m at the location of the buried mass concrete seawall (see Figures 5.1 and 5.2) and increases to approximately 18 m to 20 m at the south-most end of the Thorndon Reclamation. Underlying the reclamation fill is a relatively thin marine deposit, underlain by Wellington Alluvium.

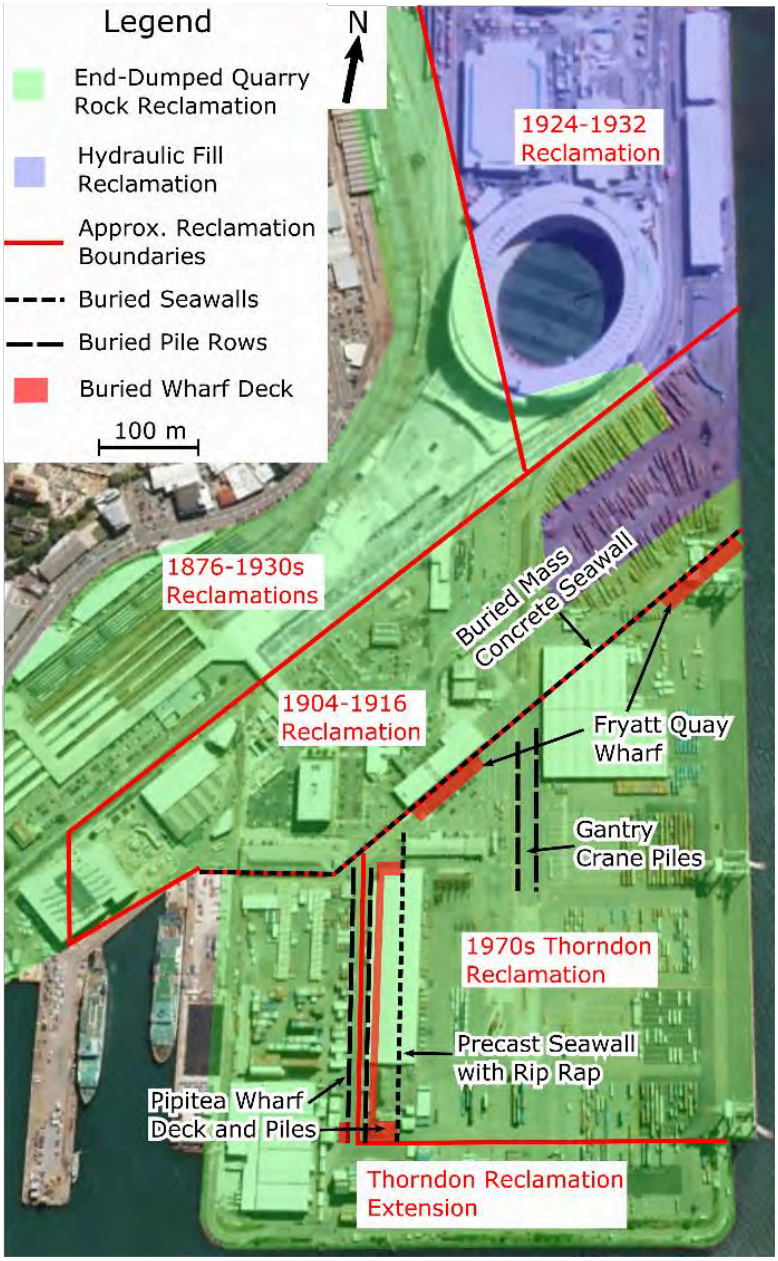

Figure 5.2: Approximate boundaries of various land reclamations at CentrePort Wellington with reference to existing and old structures and different methods of reclamation construction. (Hutchinson, 1973; Tonkin & Taylor, 2012; Semmens et al., 2010; Wellington Harbour Board, 1936. Base image from Google Earth™)

The Wellington Alluvium is generally dense to very dense gravel with sand and silt but also consists of stiff to hard silt with sand and gravel (Tonkin+Taylor, 2012 and 2014). Characteristic cross sections that illustrate the key soil layers and their thicknesses are shown in Figure 5.3. The locations of these cross-sections and borings used to develop them are shown in the site plan in Figure 5.4. Mean high water (MHW) is approximately 3 meters below the existing pavement surface.

Penetration resistances are provided in the soil exploratory borings conducted at CentrePort as Standard Penetration Test (SPT) blow count data (Tonkin+Taylor; 1998, 2000, 2006, and 2012). However, the SPT procedures employed during the previous site investigations are not always described sufficiently to ascertain if the recorded N values are N_{60} values (i.e., 60% free-fall energy, which is the standard). In fact, some of the historically acquired SPT data were obtained by non-standard SPT procedures using a solid cone instead of a split-spoon sampler. SPT N values performed in the un-compacted gravelly fill range from approximately 5 to 15 blows/300 mm. In the compacted fill layer above MHW, N-values are generally in the range between 13 and 50+ blows/300 mm (Tonkin+Taylor, 2012 and 2014). SPT N values of the soil layers from some of the available borings are indicated in the simplified soil profile cross-sections shown in Figure 5.3.

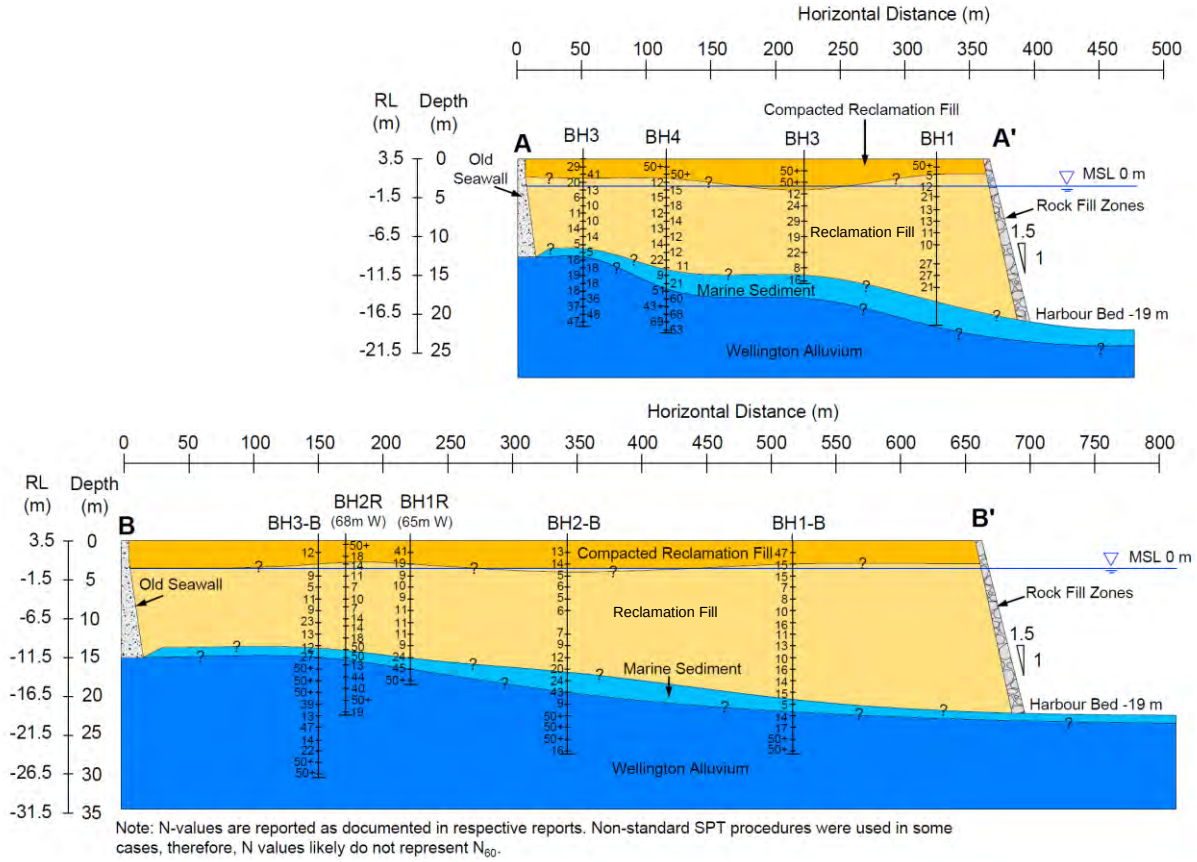

Figure 5.3: Schematic soil cross sections illustrating key layers and their thicknesses at CentrePort; note the different horizontal and vertical scales for the cross sections.

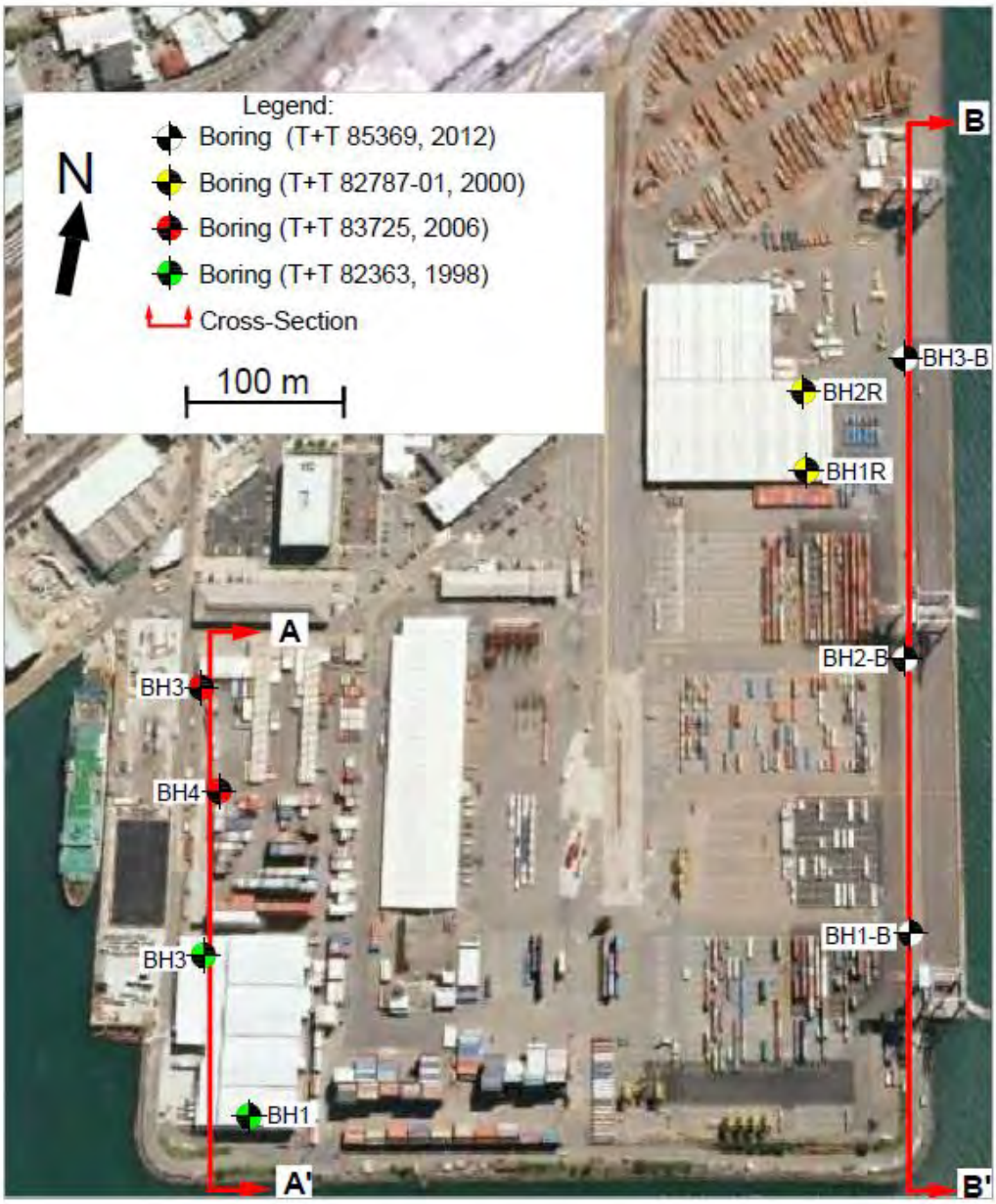

Figure 5.4: Site plan showing location of cross sections and borings used to develop the cross-sections shown in Figure 5.3; (Base image from Google Earth™).

Figure 5.5 shows grain-size distribution curves for samples (collected from subsurface explorations) of the reclaimed fill layer located approximately 5 to 40 m behind Thorndon Wharf. The fill is composed of gravelly soil including 10% to 40% sand and low fines content of less than 15%. Comparative grain-size distribution curves for samples of the marine deposits are also shown in Figure 5.5. The test data indicate the marine deposits are predominant sandy soils with fines content in the range between 15% and 35%.

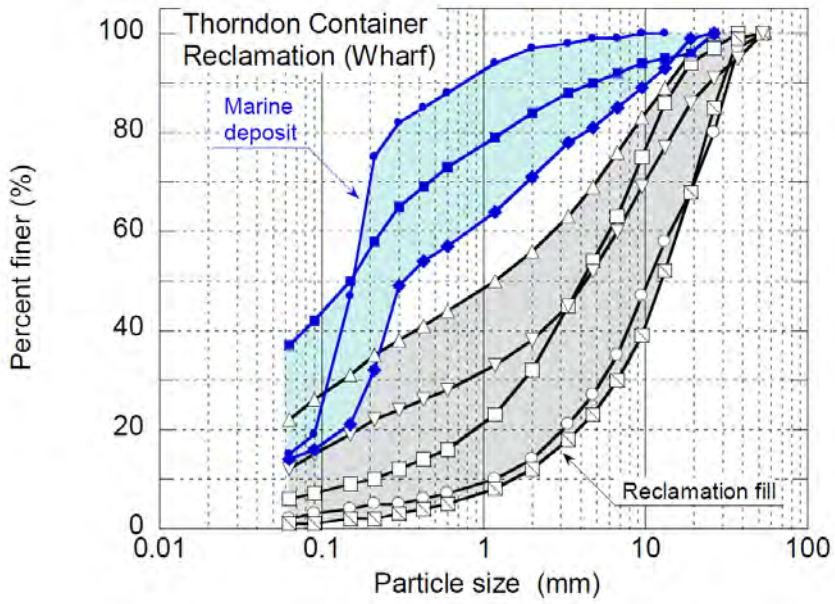

Figure 5.5: Grain-size distribution curves for borehole samples of the reclaimed fill and marine deposit.

5.3 Liquefaction demand generated by the 2016 Kaikoura Earthquake

5.3.1 Recorded ground motions

Ground motions generated by the 2016 Kaikoura earthquake were recorded by a relatively dense array of strong motion stations (SMS) in Wellington. Figure 5.6 shows the locations of eight strong motion stations (SMS) that recorded the event near CentrePort Wellington. No records were obtained directly at the Thorndon Reclamation of CentrePort. A summary of important information for the recorded accelerations and characteristics of the sites is given in Table 5.2 which includes: geometric mean horizontal peak ground acceleration (HPGA) recorded at the SMS during the 2016 Kaikoura earthquake, cyclic stress ratios at the water table (CSR_{wt}), site class per NZS1170.5, and site period estimates based on horizontal-to-vertical spectral ratios from all strong motions in GeoNet database with PGA less than 0.15 g. Note that POTS is a rock site, located about 1.0 km north-west from CentrePort. CPLB and TFSS are closest to the CentrePort; they are located about 200 m to 800 m west and northwest of the final stage reclamations at the port.

Figures 5.7 through 5.14 show ground surface acceleration-time traces and their respective 5%-damped pseudo acceleration response spectra in three orthogonal directions at stations TFSS, WEMS, CPLB, and POTS. The recorded PGAs at soil sites are generally between 0.15 g and 0.25 g (Table 1), and acceleration-time traces show a relatively large number of strong amplitude cycles (i.e., indicative of long significant duration) which is consistent with the Mw = 7.8 of the event. These ground motion characteristics on their own indicate that this

area of the Wellington Harbour and CentrePort itself were subjected to significant seismic demand (earthquake loading).

The QuakeCoRE-GEER team inspected each of the SMS sites mentioned previously. There was no evidence of liquefaction manifestation in the form of sediment ejecta at the ground surface at any of these SMS sites. CPLB is at the B building, the perimeter of which was documented in brief walk-through inspections. A small settlement of the surrounding soil relative to the B building was observed at some locations. At other locations, the settlement of the ground relative to the building was negligible to minor. There was no evidence of significant ground deformation at any of the other SMS sites.

As mentioned earlier, POTS is located on rock and therefore, is valuable as a reference site for investigation of basin effects and local soil response (site effects) on the recorded motions in the Kaikoura event. It could also be beneficial for performing seismic site response analyses of various sites (including SMS sites) at which nonlinearity and liquefaction may have significantly influenced the response. Figure 5.15 shows envelopes of 5%-damped elastic pseudo-acceleration response spectra, for the eight SMS sites considered, grouped in terms of site characteristics as: rock (POTS), natural soil deposit (VUWS, WEMS), and reclaimed soil sites (PIPS, TFSS, CPLB, FKPS, TEPS). The plots for the reclaimed soil sites have been shown with and without FKPS and TEPS spectra, because these two sites are affected by the Te Aro Basin as opposed to the Thorndon Basin effects at CentrePort and nearby SMS sites. The spectra reflect the combined effects of several factors including depth to bedrock, soil response, and basin geometry in conjunction with the excitation characteristics (e.g., source and path effects). The complex potential influence of various factors should be considered when interpreting the recorded ground motions. The comparative plots show strong amplification of amplitudes at both natural and reclaimed sites as compared to the rock accelerations across all periods up to 4 seconds. The amplification is particularly pronounced in the range between T = 1.0 s and 2.0 s, and for this and greater periods is more pronounced at the reclaimed sites located along or closer to the waterfront. In Figure 5.15(a), the enveloped geometric mean spectra are compared to the design spectrum from NZS1170.5 for Site Class D. Observed ground motions exceeded this design spectrum only at periods between approximately 1 and 2 seconds for sites on reclaimed soil, and are significantly less than the design spectrum at periods shorter than 1 seconds and longer than 2 seconds.

Table 5.2: Strong motion stations near CentrePort with geoemetric mean PGA for the 2016 Kaikoura earthquake and site characterisation metrics.

Station ID	Kaikoura EQ Geomean HPGA (g)	CSR_{wt} = 0.65 PGA/g	NZS1170 .5 Site Class	Site Period Estimate (sec)	Site (soil) type
POTS	0.074	-	B	-	Rock
TFSS	0.177	0.11	D	1.3	Natural soil deposit
WEMS	0.146	0.09	D	0.80	Natural soil deposit
CPLB	0.235	0.15	D	1.2	Reclaimed soil
VUWS	0.198	0.13	D	0.75	Reclaimed soil
TEPS	0.126	0.08	D	1.0	Reclaimed soil
FKPS	0.159	0.10	D	1.0	Reclaimed soil
PIPS	0.240	0.16	Unknown	> 2	Reclaimed soil

Figure 5.6: Aerial view of Wellington highlighting CentrePort. The location of strong motion stations near CentrePort Wellington that recorded the Kaikoura earthquake are also shown (Base image from Google EarthTM).

TFSS – Wellington Thorndon Fire Station

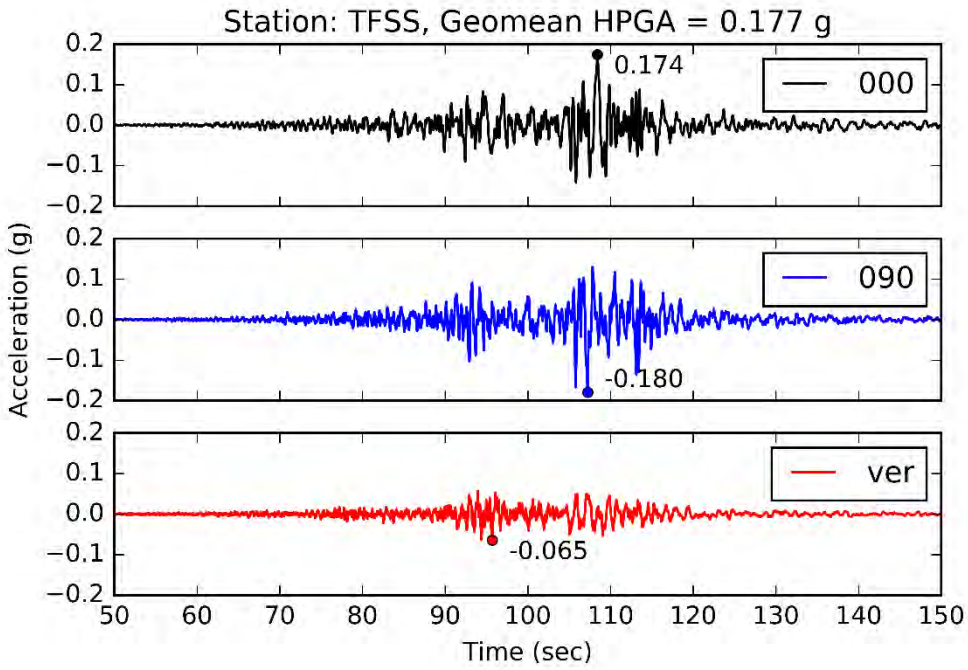

Figure 5.7: Acceleration traces from station TFSS.

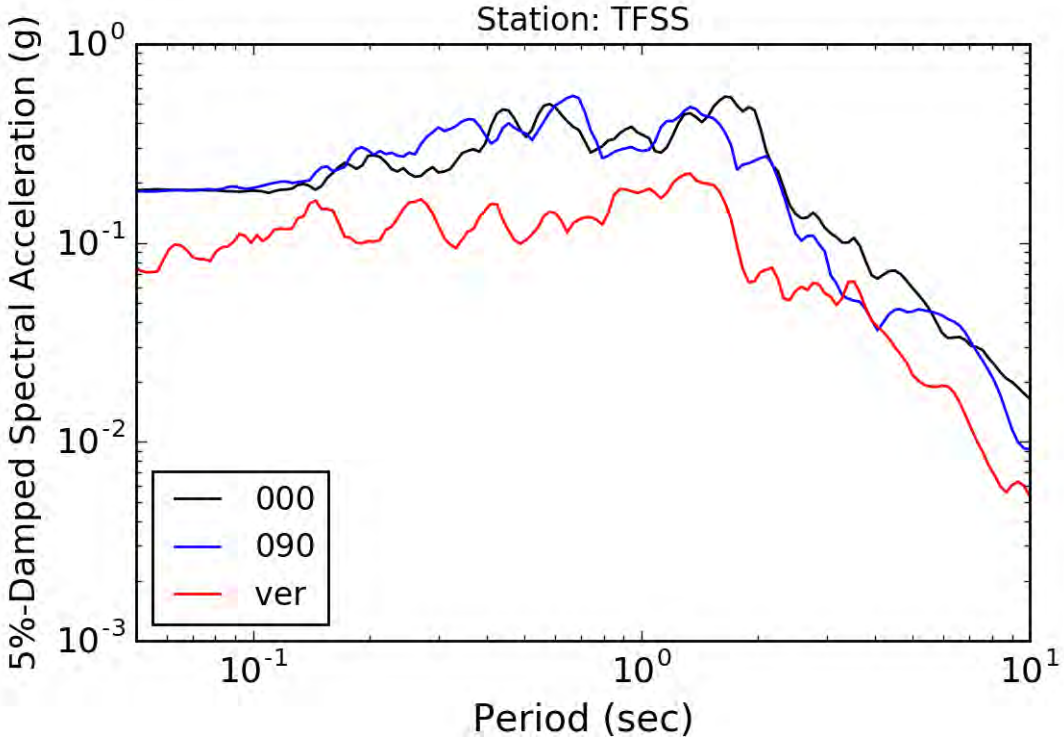

Figure 5.8: Acceleration response spectra (5% damped) from TFSS station recording.

WEMS – Wellington Emergency Management Office

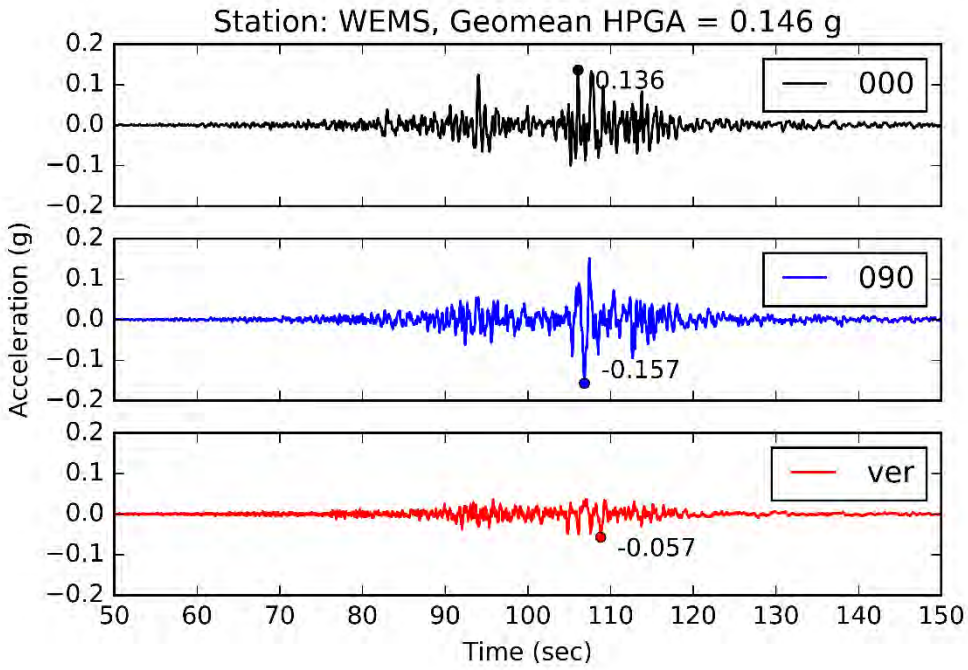

Figure 5.9: Acceleration traces from station WEMS.

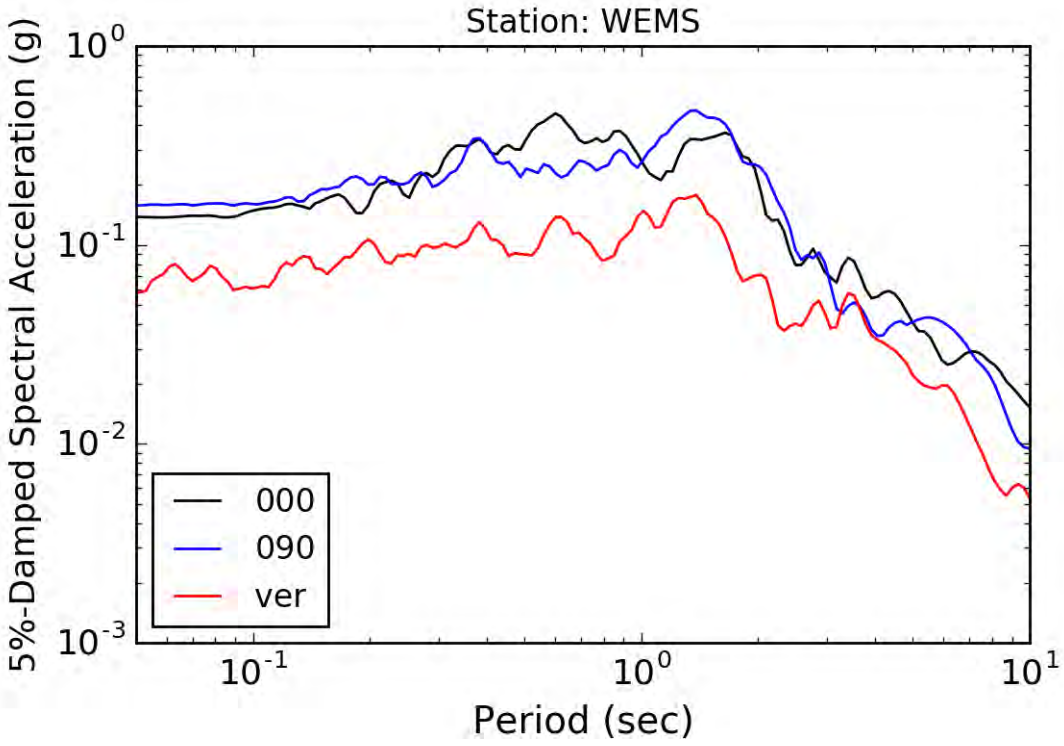

Figure 5.10: Acceleration response spectra (5% damped) from WEMS station recording.

CPLB – Wellington CentrePort BNZ Building

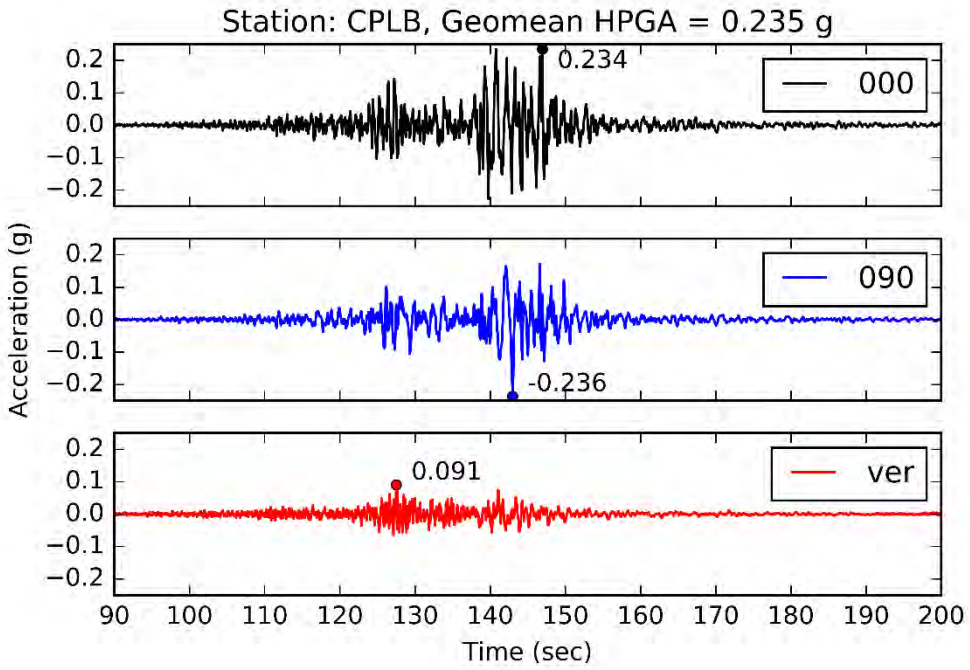

Figure 5.11: Acceleration traces from station CPLB.

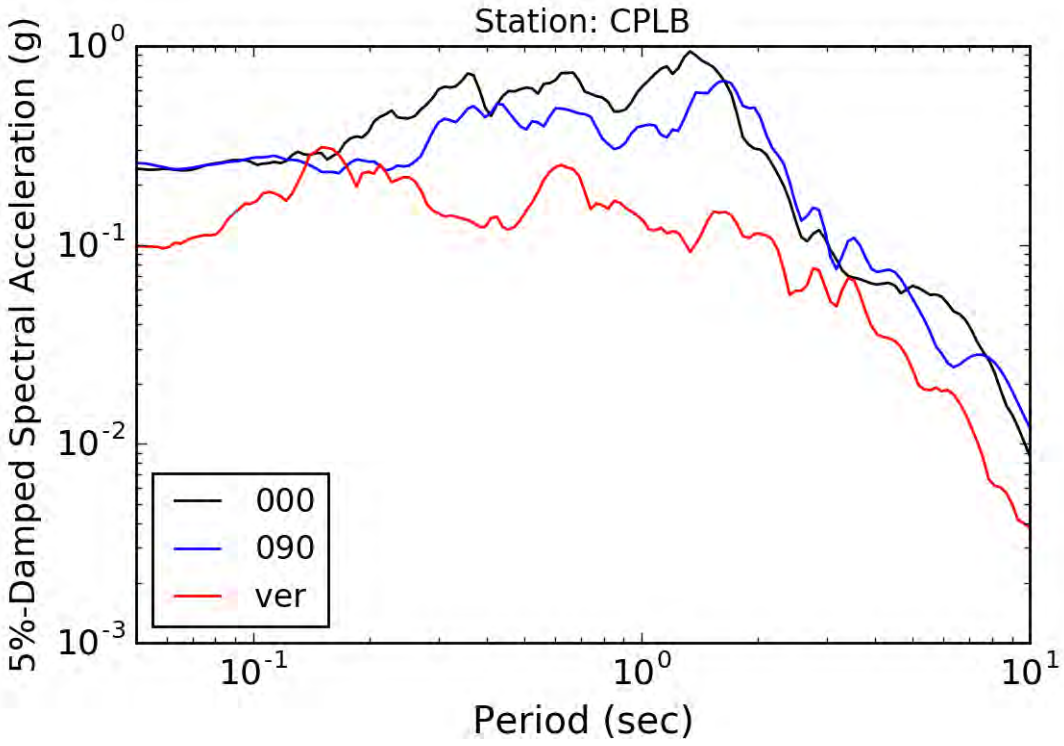

Figure 5.12: Acceleration response spectra (5% damped) from CPLB station recording.

POTS – Wellington Pottery Association

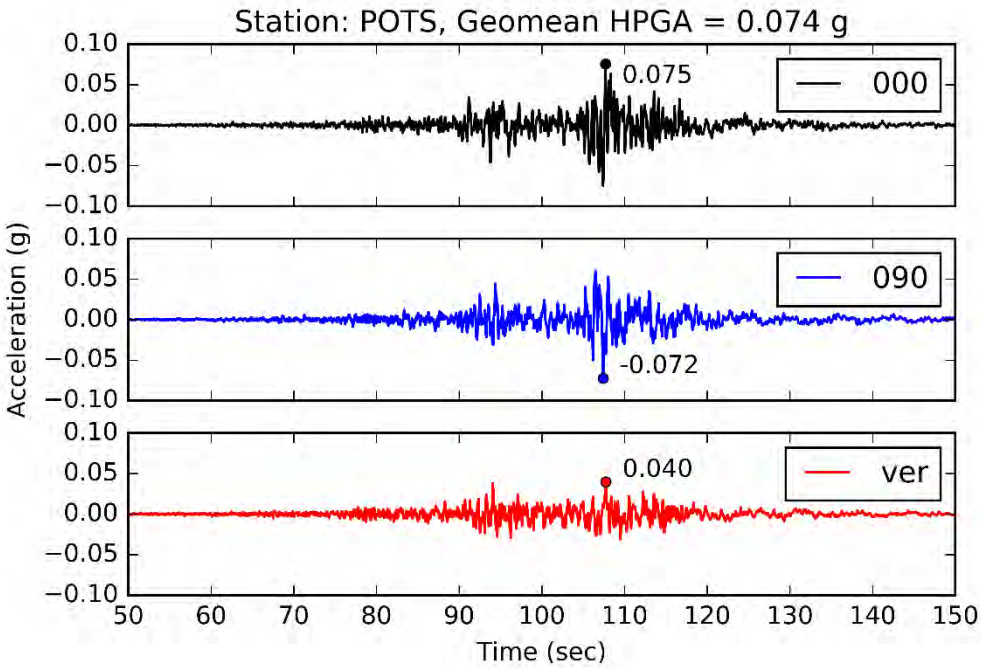

Figure 5.13: Acceleration traces from station POTS.

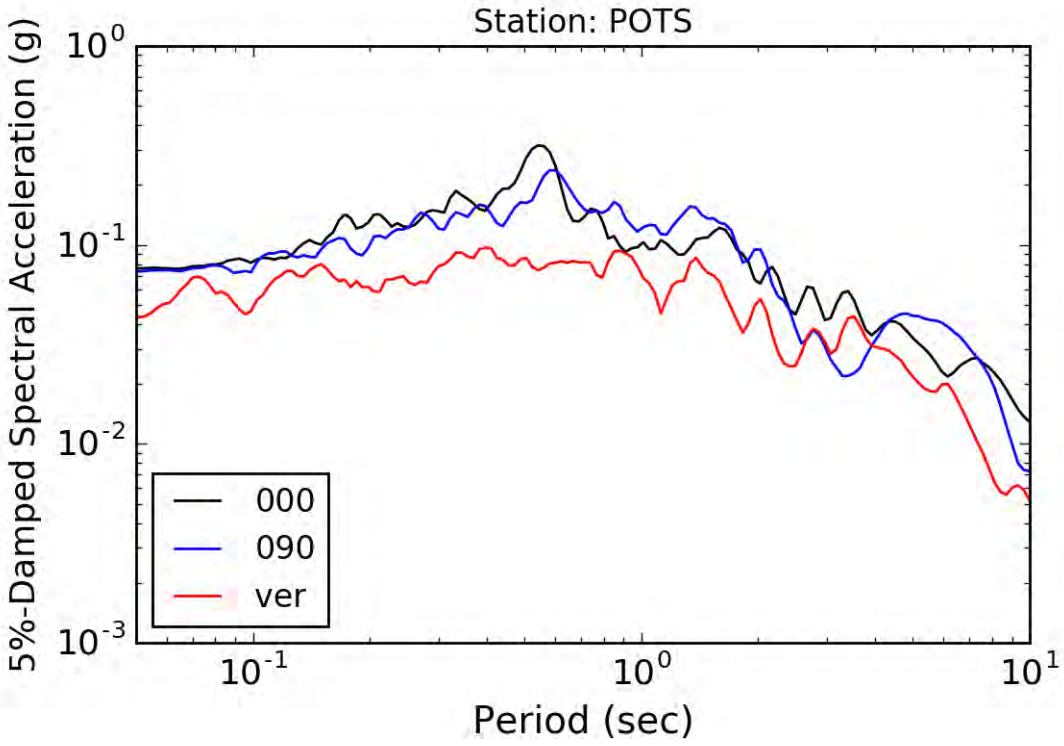

Figure 5.14: Acceleration response spectra (5% damped) from POTS station recording.

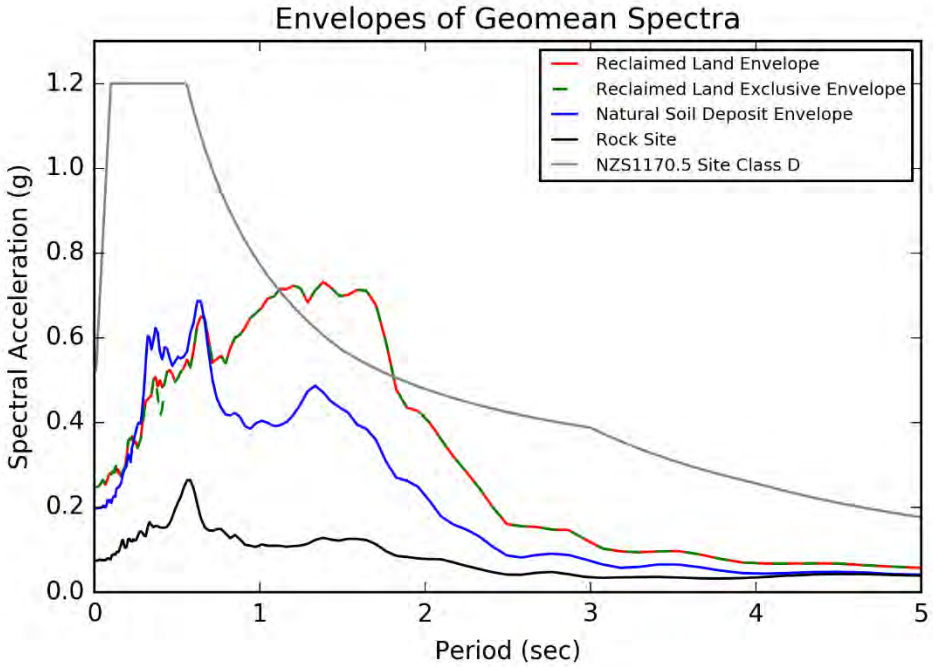

(a)

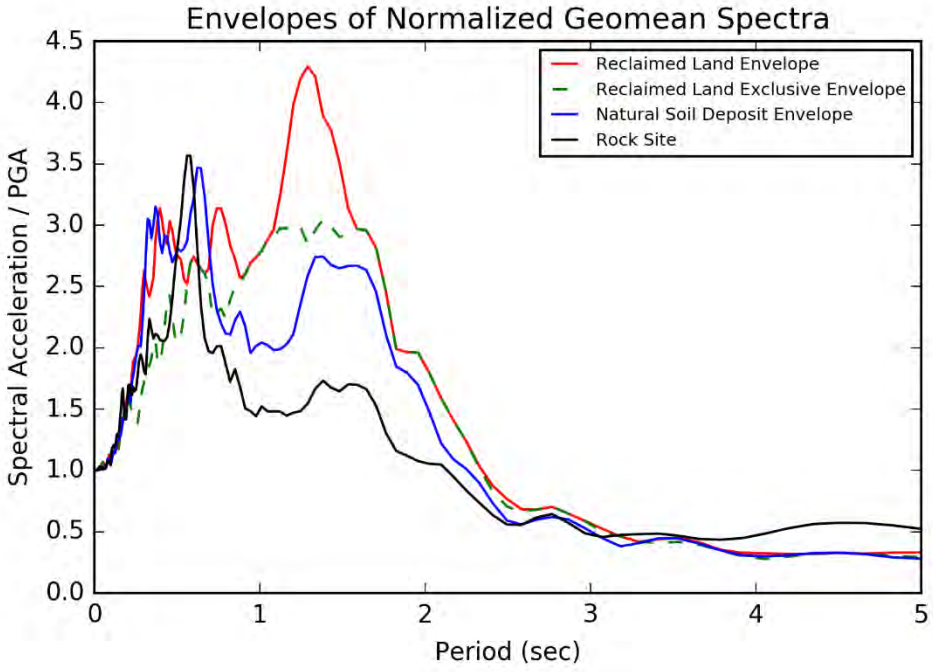

(b)

Figure 5.15: Acceleration response spectra (5% damped) for rock, natural deposits, and reclaimed soils sites: (a) envelopes of geometric mean horizontal acceleration response spectra (NZS1170.5 design spectrum is also shown for reference); (b) envelopes of normalized geometric mean spectra.

5.3.2 Seismic demand for liquefaction assessment

In the widely used simplified liquefaction triggering procedures (e.g., Boulanger and Idriss, 2014), a factor of safety against liquefaction triggering is estimated as

$$FS = \frac{CRR_{7.5,100}}{CSR} MSF \times K_\sigma \qquad (1)$$

in which $CRR_{7.5,101}$ is the Cyclic Resistance Ratio for a M_w7.5 event and an effective overburden stress of 101 kPa (atmospheric pressure) at a level ground site, MSF is the magnitude scaling factor, K_σ is overburden stress correction factor, and CSR is the Cyclic Stress Ratio, which is a proxy for the amplitude of the seismic demand. CSR is a function of the PGA at the ground surface, the ratio of the total and effective vertical stresses, the depth within the deposit, and the depth below the water table, i.e. CSR = $f[PGA, \sigma_{vo} / \sigma'_{vo}, r_d(z), z_{wt}]$. For shallow depths at the water table, the depth dependent factors are equal to unity (i.e., there are no effects of soil flexibility [r_d = 1.0], water table depth on CSR [$f(z_{wt})$ =1.0], and $\sigma_{vo} / \sigma'_{vo}$ = 1.0 at the water table). Hence, the cyclic stress ratio is effectively a function of the PGA alone. With these simplifications in mind, the cyclic stress ratio at a shallow depth of the water table (CSR_{wt}) can be approximated with Equation 2 using the geometric mean peak ground accelerations (a_{max}) recorded in the horizontal directions at the strong motion stations:

$$CSR = 0.65 \frac{a_{max}}{g} \qquad (2)$$

The estimated CSR_{wt} values for the SMS sites are summarized in Table 1. CSR_{wt} = 0.11 – 0.16 for the three SMS sites closest to the port (i.e., CPLB, TFSS, and PIPS). This demand in terms of CSR is illustrated in Figure 5.16 together with the equivalent sand liquefaction resistance ($CRR_{7.5,101}$) as a function of the SPT blow count (shown with the solid line), as defined in the semi-empirical liquefaction evaluation procedure of Boulanger and Idriss (2014). Note that the product of $MSF \times K_\sigma$ in Equation (1) is approximately 1.0 for the combination of M_w7.8 earthquake and an effective overburden stress of about σ'_{vo} = 40 to 60 kPa corresponding to a water table depth of 2 m to 3 m. Thus, the computed CSR_{wt} can be directly compared to the liquefaction resistance expressed in terms of $CRR_{7.5,101}$ shown in Figure 5.16. If one accounts for the conservatism in this deterministic relationship of $CRR_{7.5,101}$, which corresponds to a 15% liquefaction probability (Boulanger and Idriss, 2012), then the plot roughly indicates that the seismic demand was sufficient to trigger liquefaction in deposits having an equivalent clean sand SPT blow count of less than 10 to 14 blow counts. This simplified estimate of seismic demand applies to the soil at the depth of the ground water table and serves only as a rough indicator of the imposed seismic demand for assessing liquefaction triggering. The Boulanger and Idriss (2014) CRR correlation was developed based on case histories on sandy soils, and therefore its applicability to gravelly soils is affected by several factors including the conversion of the penetration resistance of gravelly soils to an equivalent clean sand blow count. Hence, the plot shown in Figure 5.16 is only an indicator of the seismic demand in relative terms (i.e., in relation to an equivalent clean sand liquefaction resistance), and further research is needed to determine directly the cyclic resistance of the reclaimed deposits.

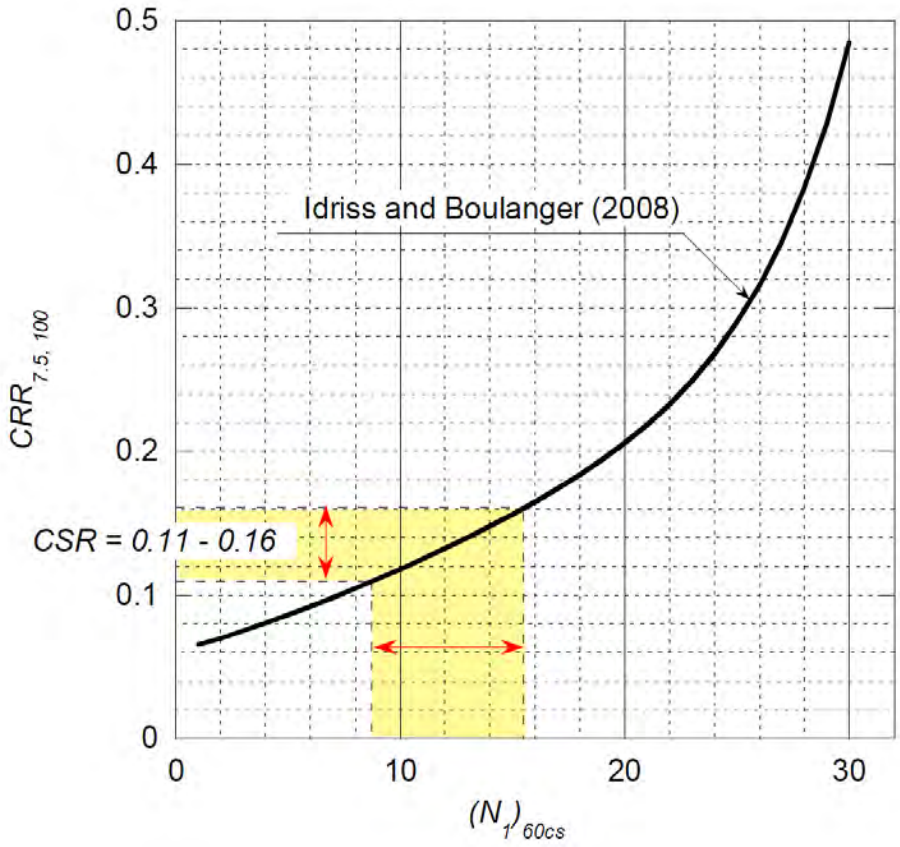

Figure 5.16: Illustration of seismic demand for assessing liquefaction triggering by the 2016 Kaikoura earthquake at depth of the water table for the three sites on reclaimed soils in the vicinity of the port (PIPS, TFSS and CPLB).

5.4 Liquefaction-induced land deformation

The first QuakeCoRE-GEER team survey at CentrePort was conducted on 17 November 2016, three days after the earthquake, while most of the liquefaction evidence remained on the ground surface. These inspections covered most of the port area and focused on documenting key observations on the seismic performance of the reclamations, and wharf and building structures including measurements of vertical offsets and horizontal movements along selected transects, and collecting representative samples of the ejected materials from various locations at the port. Subsequent surveys were performed from 20 November to 1 December, which focused on obtaining additional evidence and measurements of ground movements and relative movements between the wharves or buildings and the surrounding soils. In the later part of this period, ground-based LiDAR scanning was conducted along transects of the reclamations and around and within structures of interest. The observations and measured values (approximate values obtained from measurements during the inspections) presented in this document were obtained from the above field reconnaissance activities, if not stated otherwise. Additional detailed observations have been compiled and shared when permitted by the CentrePort Limited.

Liquefaction Manifestations

Relatively widespread liquefaction was observed in both the end-dumped quarry fill and hydraulically-placed dredged fill. Liquefaction was manifested in various forms either directly as soil ejecta on the pavement surface of the port or indirectly in the form of vertical and horizontal ground movements often accompanied by ground cracks and fissures, or vertical offsets especially along the interface zones with wharves and buildings. From these general observations, one could infer a substantial global (mass) settlement across much of the reclamation, and lateral movement (spreading) of the fills towards the sea. These lateral movements and associated ground distress were generally more pronounced along the edges of the reclamation. The ground movements affected the wharves and buildings at CentrePort in various ways, as discussed in Sections 5.6 and 5.7 of this report, respectively.

The liquefaction was most evidently manifested by ejected soils on the paved surface of the port. The areas covered by ejecta were scattered and somewhat non-uniform both in their spatial distribution and thickness of the ejected soils. The manifestations of liquefaction varied from traces of ejected soil and water to larger volumes of ejecta with thicknesses of up to 150 mm to 200 mm. The latter were typically found near cracks and fissures through which the liquefied soils reached the ground surface. In a few isolated cases, a larger amount of ejecta was observed near partially collapsed pavement and cavities, or along existing drainage conduits beneath the pavement.

The ejected soils in the area south of the Old Seawall (i.e., in the area of the end-tipped ‘common fill’ reclamation) consisted of gravelly soils including some cobble-sized particles. There was one notable exception in this regard, where a smaller area of the Thorndon Container Terminal was covered by uniform sand ejecta. Sand ejecta was also observed in the hydraulically-placed fill of the Log Yard, north of the Old Seawall.

The photos shown in Figures 5.17 to 5.21 illustrate some of the key liquefaction manifestation features observed in several areas of CentrePort.

(a)

(b)

(c)

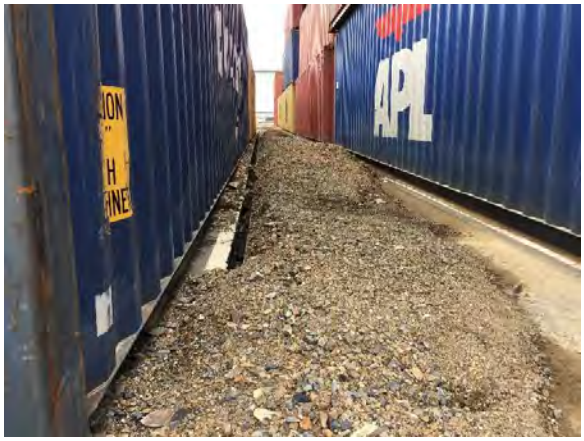

(d)

Figure 5.17: Gravelly ejecta at the Thorndon Container Terminal: (a) pavement cracking and ejected gravelly material (S41.280175°, E174.787308°); (b) characteristic gravel-size fractions of the ejecta with some cobbles observed in this area (S41.280206°, E174.787431°); (c) larger amount of gravelly ejecta around a cavity and collapsed pavement surface (S41.280361°, E174.789336°); (d) large volumes of ejecta observed along drainage lines (S41.278347°, E174.788069°, taken on 17NOV16).

(a) (b) (c)

(d) (e)

Figure 5.18: High gravel content quarry rock ejecta in the container storage area upland of Thorndon Container Wharf. (a) Looking south along eastern wall of Substation B (S41.277699°, E174.788277°), (b) looking south along lateral spread crack and ejecta 45 m upland of bulkhead at approximately STA 230 (S41.278286°, E174.788830°), (c) coarse gravel and cobble ejecta (S41.280225° E174.787828°), (d) containers 20 m south of Substation B (S41.278020°, E174.788213°), and (e) looking south along lateral spread crack and ejecta 12.5 m upland of bulkhead at approximately STA 150 (S41.278887°, E174.789413°, taken on 21NOV16).

Figure 5.19: Sandy liquefaction ejecta with trace gravel among area of 1970's end-dumped quarry rock reclamation (i.e., Thorndon Reclamation) at STA 145 and approximately 60 m upland of the bulkhead. The ejecta deposit was approximately 170 mm thick at this location. Samples S11 and S12 were collected here (S41.279067°, E174.788792°, taken on 17NOV2016 and 21NOV16).

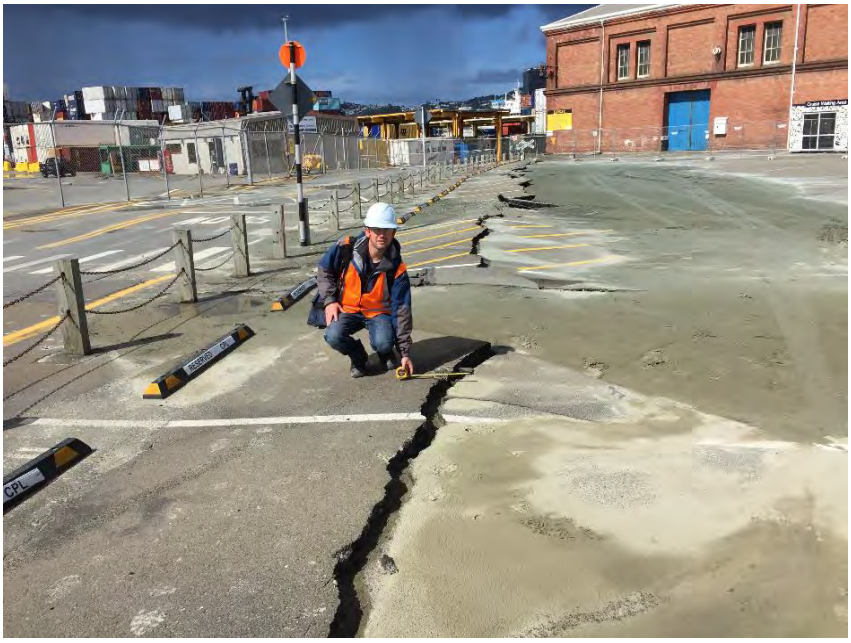

Figure 5.20: Sandy liquefaction ejecta behind buried mass concrete seawall looking southwest along seawall. On the right side of seawall: area of end-dumped quarry rock reclamation from 1904-1916 (Sample S2), left side of seawall: area of end-dumped quarry rock reclamation from 1970's Thorndon Reclamation. (S41.278454°, E174.785154°, taken on 17NOV16)

Figure 5.21: Sandy liquefaction ejecta in the log stacking area in the northeast corner of CentrePort (Sample S13). Area of hydraulic fill reclamation. (S41.274972°, E174.788347°, taken on 17 NOV16)

During the first field survey on 17 November, several ejecta samples were collected for index testing in the laboratory. Thirteen of those samples, indicated as S1 to S13 in this report, were collected from the locations shown in Figure 5.22. Sand liquefaction ejecta were observed at three different areas. These areas are: (1) in the Thorndon container stacking area at samples S11 and S12 (Figure 5.19), (2) immediately upland of the buried mass concrete seawall at sample S2 (Figure 5.20), and (3) in the log stacking area at sample S13 (Figure 5.21). Interestingly, only the log stacking area at S13 coincides with mapped area of sandy hydraulically-placed dredged fill (i.e., purple shaded area in Figure 5.2). Gravelly liquefaction ejecta were present over large portions of the Thorndon Reclamation and the Thorndon Reclamation Extension. This material is the end-dumped quarry rock referred to above as "common fill." The remaining samples were collected from this material. Several photos of this gravelly liquefaction ejecta are shown in Figures 5.17 and 5.18.

Grain size distribution curves obtained in the laboratory for the 13 ejecta samples are shown in Figures 5.23c and 5.23d where gravelly and sandy soils ejecta are shown respectively. The shaded areas in the background of these figures show the range of grain size distributions for

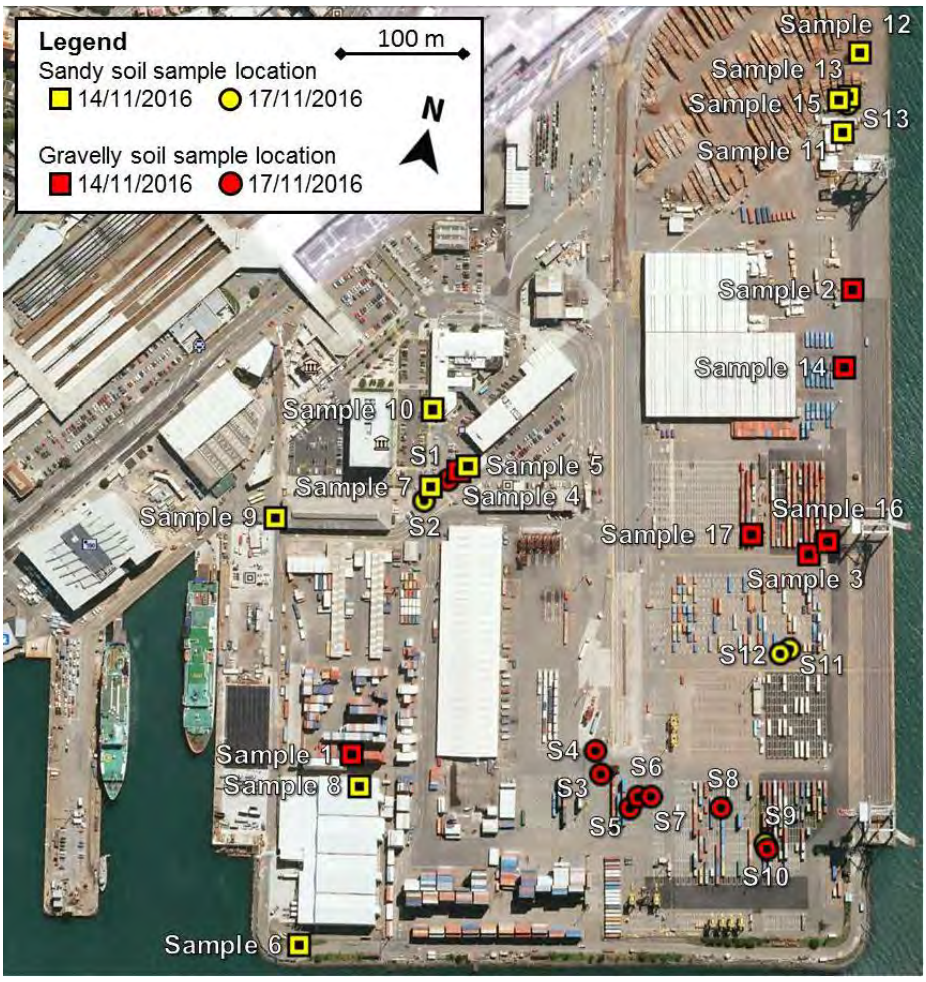

Figure 5.22: Location of liquefaction ejecta samples collected on 14 November (Sample 1 to Sample 17), and 17 November (S1 to S13). (Base image from Google Earth™)

the reclamation fill and marine deposit samples (collected from subsurface explorations) indicated in Figure 5.5. The grain-size curves of the gravel ejecta (solid lines in Figure 5.23c) are in good agreement with the grain-size distribution range of the gravelly soils of the Thorndon reclamation (shaded zone in Figure 5.23c). Similarly, the grain-size distribution curves of the sand ejecta (solid lines in Figure 5.23d) are generally consistent with those of the marine deposits, except that ejecta samples show more uniform composition. Note that the hydraulically placed sandy fill was dredged from the original seabed, and hence has the same composition as marine deposits. The grading of the ejected soils is also consistent with the sand fractions of the fill material. Samples from the ejected soils were also collected from additional 15 locations (shown in Figure 5.22) by Tonkin+Taylor, on 14 November. Importantly, these samples were collected before the severe rainfall on 14-15 November that potentially washed out some of the fines fractions of the ejected soils. Grain size distribution curves of the gravelly samples and sandy samples collected on 14 November are shown in Figures 5.23a and 5.23b in the same fashion as Figures 5.23c and 5.23d. By and large, both gravelly samples (solid lines in Figure 5.23a) and sandy samples (solid lines in Figure 5.23b) are in good agreement with the respective range of grain-size distribution curves obtained from borehole samples (shaded areas). Tables 5.3a and 5.3b summarize the field visual classification (Tonkin+Taylor, private communication), the mean grain size (D_{50}), and fines content (FC) obtained from the laboratory tests on the samples collected on 14 November (Sample 1 to 15) and 17 November (S1 to S13) respectively.

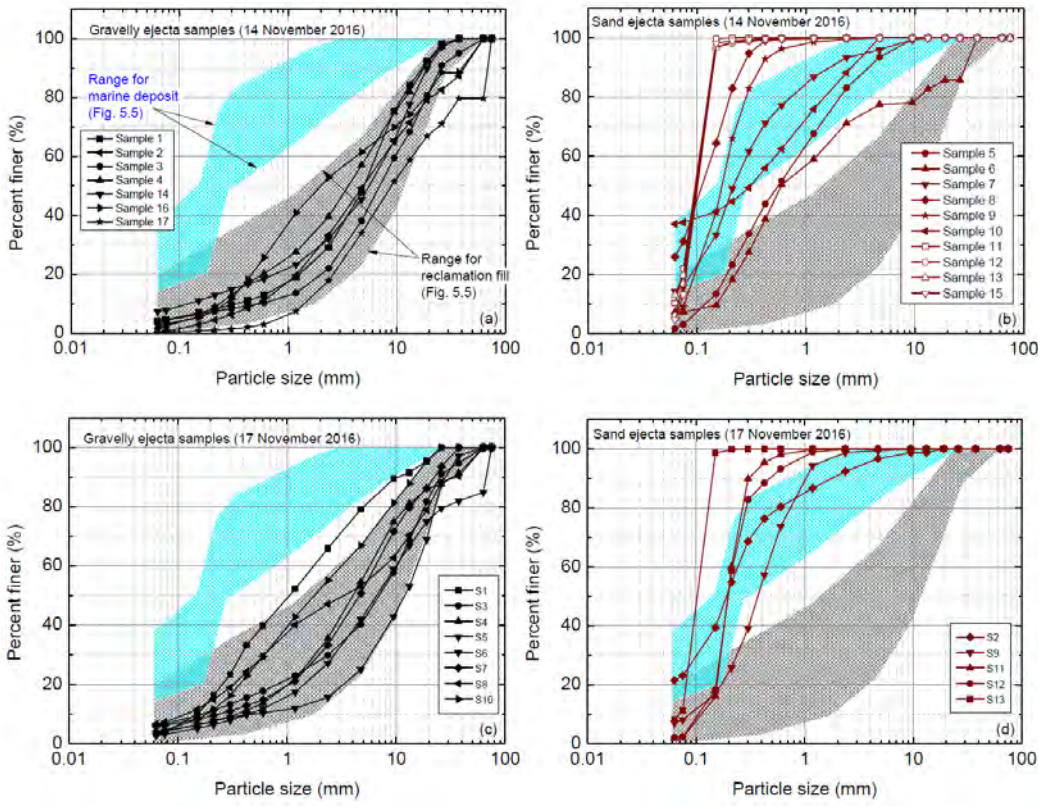

Figure 5.23: Grain size distribution for liquefaction ejecta samples collected on reclaimed land from (a) gravelly quarry rock fill on 14 November, and (b) sandy fill on 14 November, (c) gravelly quarry rock fill on 17 November, and (d) sandy fill on 17 November. Shaded regions show ranges of grain size for marine deposits and reclamation fill collected from subsurface explorations (plotted in Figure 5.5).

Table 5.23a: Field visual classification, fines content, and D_{50} of liquefaction ejecta samples collected on 14 November 2016.

Sample ID	D_{50} (mm)	Fines Content (%)	Field Visual Classification
Sample 1	5.12	4.51	Fine to coarse GRAVEL with trace sand, dark brownish grey. Saturated, poorly graded, angular, slightly weathered sandstone and mudstone, moderately strong. Sand is fine to coarse.
Sample 2	4.98	0.2	Fine to coarse GRAVEL with minor sand and cobbles, brown. Saturated, poorly graded, angular, moderately weathered sandstone and mudstone, moderately strong. Sand is medium to coarse.
Sample 3	6.98	4.09	Fine to coarse GRAVEL with minor sand and trace cobbles, dark brown. Wet, well graded, subrounded to angular, moderately weathered sandstone and mudstone, weak. Sand is coarse.
Sample 4	3.56	2.3	Fine to coarse GRAVEL with some sand, dark brownish grey. Wet, well graded, subrounded to angular, slightly weathered sandstone, moderately strong. Contains shell hash.
Sample 5	0.56	3.1	Fine to coarse SAND with trace gravel, dark brown. Saturated, poorly graded. Gravel is fine, subrounded.
Sample 6	0.41	9.6	Fine to coarse SAND with minor gravel, dark brownish grey. Wet, well graded. Gravel is fine to medium, subangular
Sample 7	0.22	15.9	Fine to medium SAND with minor silt and trace gravel, dark bluish grey. Saturated, poorly graded, dilatant. Gravel is fine to coarse, angular. Contains shell hash and wood fragments.
Sample 8	0.11	31.2	Silty, fine SAND, brown. Saturated, poorly graded, dilatant.
Sample 9	0.17	9.1	Fine to medium SAND, dark grey. Wet, poorly graded, dilatant. Contains shell hash.
Sample 10	0.31	35.6	Fine to medium SAND with minor gravel, bluish grey. Wet, poorly graded. Gravel is coarse, subrounded, slightly weathered sandstone, moderately strong. Contains shell hash.
Sample 11	0.096	21.9	Fine SAND, dark grey. Saturated, dilatant. Contains shell hash.
Sample 12	0.100	16.9	Fine SAND, dark grey. Saturated, dilatant. Contains shell hash.
Sample 13	0.098	19.7	Fine SAND, dark grey. Saturated, dilatant. Contains shell hash.
Sample 14	3.61	7.29	Fine to coarse GRAVEL with minor sand, brown. Wet, well graded, subrounded to angular, slightly weathered sandstone and mudstone, moderately strong to weak.
Sample 15	0.102	13.2	Fine SAND, dark grey. Saturated, dilatant. Contains shell hash.
Sample 16	2.00	2.75	Sandy, fine to coarse GRAVEL, brown. Wet, well graded, angular, moderately weathered sandstone and mudstone, weak. Sand is fine to coarse.
Sample 17	9.00	0.17	Fine to coarse GRAVEL with minor sand and trace cobbles, dark brown. Wet, well graded, subrounded to angular, moderately weathered sandstone and mudstone, weak. Sand is coarse.

Table 5.3b: Field visual classification, fines content, and D_{50} of liquefaction ejecta samples collected on 17 November 2016.

Sample ID	D_{50} (mm)	Fines Content (%)	Field Visual Classification
S1	1.08	3.1	Fine to coarse SAND with some gravel, dark grey. Moist, poorly graded. Gravel is subangular to angular, slightly weathered mudstone, moderately strong.
S2	0.19	21.5	Fine to coarse SAND, bluish grey. Moist, poorly graded. Contains shell hash.
S3	7.38	6.2	Fine to coarse GRAVEL with some sand and minor cobbles, dark brown. Moist, well graded, subangular to angular, moderately weathered sandstone and mudstone, moderately strong to weak. Contains shell hash.
S4	4.17	3.9	Fine to coarse GRAVEL with some sand and trace silt, dark brown. Wet, well graded, subangular to angular, slightly weathered mudstone, weak. Sand is fine to coarse.
S5	12.09	3.7	Fine to coarse GRAVEL with minor sand and cobbles, brown. Moist, well graded, subrounded to angular, moderately weathered sandstone and mudstone, moderately strong. Sand is fine to coarse.
S6	7.02	2.8	Fine to coarse GRAVEL with some sand and minor cobbles, dark brown. Moist, well graded, subangular to angular, moderately weathered sandstone and mudstone, moderately strong to weak. Contains shell hash.
S7	4.64	5.8	Fine to coarse GRAVEL with some sand, dark brown. Moist, well graded, subangular to angular, moderately weathered sandstone and mudstone, moderately strong to weak.
S8	3.51	6.5	Fine to coarse GRAVEL with some sand and minor cobbles, dark brown. Moist, well graded, subangular to angular, moderately weathered sandstone and mudstone, moderately strong to weak.
S9	0.37	7.0	Fine to coarse SAND with trace gravel and silt, brownish grey. Moist, poorly graded. Gravel is fine to medium, angular, moderately weatheredemudstone, moderately strong.
S10	1.87	3.9	Sandy, fine to coarse GRAVEL, brownish grey. Moist, well graded, subangular to angular, moderately weathered sandstone and mudstone, moderately strong to weak. Sand is fine to coarse.
S11	0.20	1.9	Fine to medium SAND, dark grey. Moist, poorly graded. Contains shell hash.
S12	0.20	2.1	Fine to medium SAND, dark grey. Moist, poorly graded. Contains shell hash.
S13	0.11	8.3	Fine SAND, dark grey. Saturated, poorly graded, dilatant.

Settlement

Differential hand-measured vertical settlement measurements are summarized in Figure 5.24. These measurements are of ground settlement relative to pile supported structures. Settlement of fill relative to buildings supported on a shallow foundation are excluded from this figure. The settlement of the fill south of the Old Seawall is generally in the range from 300 mm to 500 mm, whereas settlement of the order of 100 mm to 200 mm was observed in the hydraulic fill north of the seawall. The largest settlement was observed at the Thorndon Container Terminal just behind the wharf where a vertical offset of about 600 mm was observed. Approximately 180 meters inland of the Thorndon Wharf bulkhead, 180 mm of settlement were measured relative to what appeared to be the piles of the historic gantry crane at North Rail (see Figure 5.2).

Lateral spreading

Lateral spreading generally was manifested by typical cracks and fissures on the pavement surface running perpendicular to the direction of spreading. Characteristic spreading-induced movements are illustrated for the Thorndon Container Terminal (TCT) in this section, whereas additional observations on lateral spreading are discussed in the subsequent sections on wharves and buildings.

To quantify the magnitude and spatial distribution of lateral spreading at TCT, lateral spreading measurements were performed by ground surveying along two transects in the east-west direction, denoted as TCW-1 and TCW-2 in Figure 5.25. Along each transect, ground cracks were identified and their location (horizontal distance from a reference point) and width were recorded. By summing up the crack widths one can estimate the size of lateral ground displacements as a function of the distance inland from the wharf, as illustrated in the plot shown at the top of Figure 5.25. Note that along TCW-2 two independent transects were performed approximately 10 m apart (in the N-S direction) to check the accuracy in the estimates of ground displacements. Table 5.4 lists the width and horizontal distance to each crack from the reference point of each transect. The cumulative opening of the cracks measured across TCW-1 and TCW-2 are 960 and 785 mm, respectively, implying that the edge of the fill moved laterally towards the sea (Thorndon Wharf) about 0.8 m to 1.0 m.

The lateral spreading was accompanied by a typical slumping mode of deformation involving lateral expansion and associated vertical settlement. Ground settlement immediately inland of the bulkhead, relative to the wharf deck, was estimated to be 600 mm, as indicated in Figure 5.25. Further details on the vertical offsets and settlement induced by the liquefaction and lateral spreading are described in Section 5.6 where observations on the Thorndon Wharf are provided.

Figure 5.24: Location and magnitude of differential settlement measurements obtained during inspections. All values are in mm, and represent settlement of the ground surface relative to a pile supported structure. (Base image from Google Earth™)

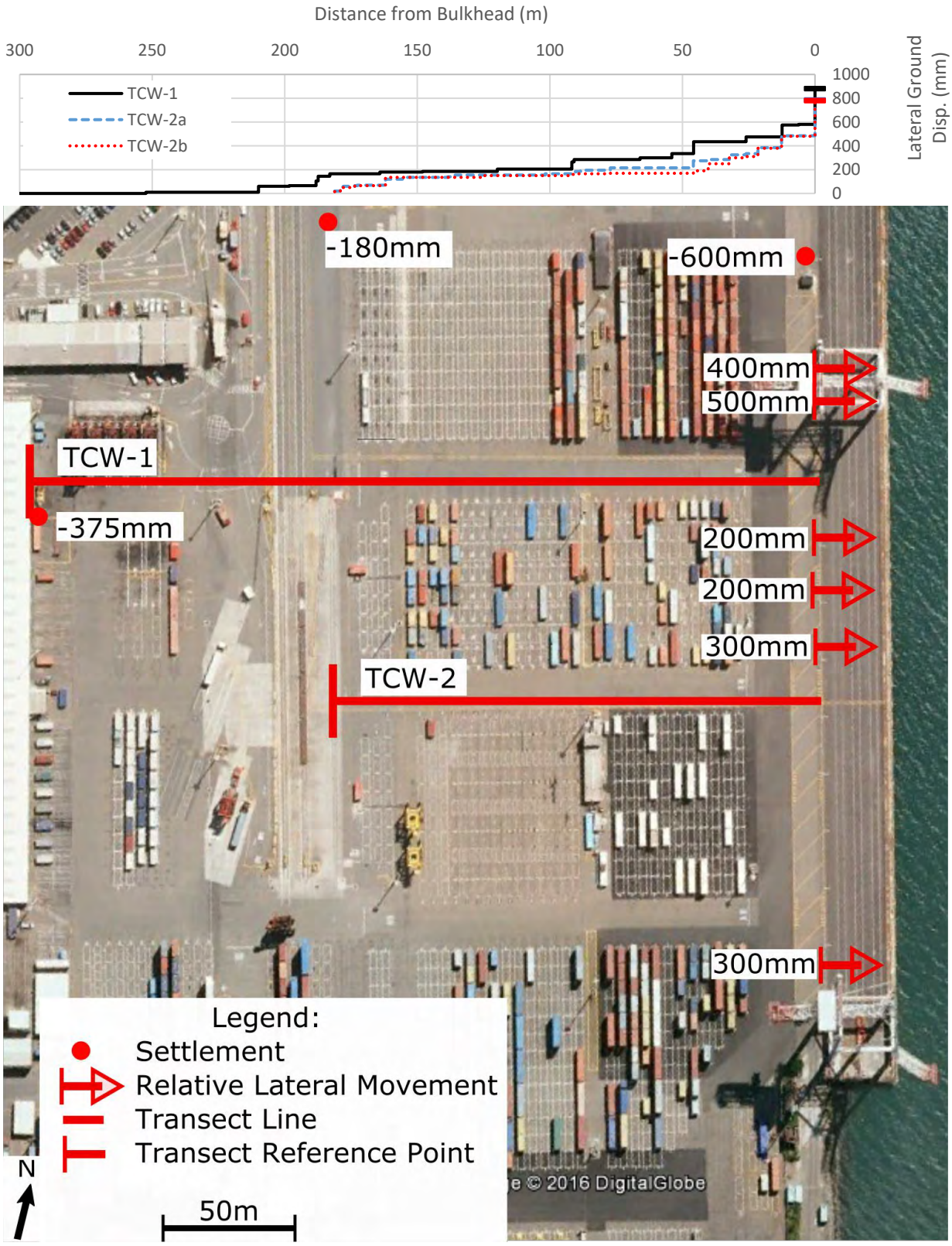

Figure 5.25: Location of west-to-east transects for lateral spreading measurements towards Thorndon Wharf during inspections. Plots at the top show cumulative lateral ground displacement versus horizontal distance from the bulkhead. Transect measurements are in Table 5.4. (Base image from Google Earth™)

Table 5.4: West-to-east lateral ground displacement measurements toward Thorndon Wharf.

TCW-1		TCW-2		
Horizontal Distance from Reference Point (m)	**Crack Width (mm)**	**Horizontal Distance from Reference Point (m)**	**Crack Width[1] (mm)**	
48.80	10	0.00	20	15
91.30	50	2.14	35	35
102.90	5	3.32	5	–
113.00	40	7.62	5	15
113.80	40	8.50	5	–
118.20	20	19.20	50	70
137.10	15	25.60	5	–
153.20	5	26.75	10	–
181.40	20	42.65	5	–
209.50	60	45.45	15	–
210.30	20	55.55	–	15
235.20	15	79.45	10	10
247.20	35	89.95	5	5
255.40	100	90.85	15	5
275.20	40	92.8	10	–
288.8	100	104	20	20
295.1	5	135.3	60	60
301.20	300	140.9	10	–
48.80	10	148.9	40	50
–	–	155.20	10	10
–	–	159.70	50	70
–	–	168.60	100	100
–	–	181.20	300	300
Total:	880	Total:	785	780

1) Two measurements were taken approximately 10 m apart (North to South)

5.5 LiDAR field survey and data processing

5.5.1 Background

Terrestrial laser scan (TLS) surveys (also known as ground-based LiDAR) were completed at CentrePort from 28 November to 1 December 2016 to document the ground and structural performance during the 2016 Kaikoura earthquake. The primary purpose of the surveys was to collect TLS data to supplement and validate structure from motion (sfm) point clouds from recent UAS surveys. As such, TLS data were collected along North/South and East/West transects across the site, and around and on the inside of several key structures. Most scans were conducted outside; however, scans were completed in three buildings (i.e., CPH, S37, and CS buildings).

The surveys were completed using a Leica P40 terrestrial laser scanner with a Leica GS14 GNSS receiver mounted above (Figure 5.26) at a calibrated offset of 0.1580 m. Scans were spaced generally at 30-40 m apart along transects (Figure 5.27); however, the spacing varies substantially to accommodate visibility constraints as well as safety considerations on the operating port facility. Scans were completed for a 360 degree panoramic view. Most scans also have co-acquired, high resolution imagery utilizing the internal calibrated camera in the P40 scanner. The camera captured over 270 (1920x1920) images for the full dome and mosaics and blends them together to map colors to the point cloud. For some of the indoor scans with poor lighting conditions or where scans needed to be completed rapidly, the camera imagery was not acquired. For indoor scans, the GNSS receiver and handle were removed prior to scanning, in most cases, for full overhead scanning. A second GNSS receiver was utilized as a base station over a control point (CARDNO 19) for one of the scan dates. For the other days a local Continually Operating Reference Station (CORS) WGTT was utilized as the base station.

Figure 5.26: Example scan setup with a Leica P40 terrestrial laser scanner and Leica GS14 GNSS receiver mounted directly above the scanner.

Figure 5.27: Locations (green circles) where terrestrial laser scans were obtained at the CentrePort. Additional scans were captured inside the Cruise Ship Terminal to the North that are not shown on the map because they are being processed. Transects from the LiDAR data shown later in the report are identified. Note that the basemap is from ESRI prior to the earthquake.

This document assumes the reader has a basic knowledge of TLS and its use in reconnaissance. Additional background on TLS can be found in Kayen et al. (2010), Olsen and Kayen (2012), and its use in similar type reconnaissance is well documented in multiple GEER reports (http://www.geerassociation.org/).

5.5.2 GNSS processing

A local CORS, WGTT (http://apps.linz.govt.nz/gdb/index.aspx?code=WGTT), was utilized as the reference for all Global Navigation Satellite System (GNSS) processing to provide geo-referenced coordinates to all of the TLS data acquired. However, the current published coordinates for WGTT are pre-earthquake coordinates, which do not account for the earthquake-induced deformations (Figure 5.28). Hence, RINEX files for the four dates of

survey were post-processed in *PositioNZ* using other CORS in the network. The resulting coordinates were subsequently averaged to obtain post-earthquake coordinates (January 6, 2017). *PositioNZ* has updated the positions of CORS to post-earthquake coordinates (and updates those on a daily basis).

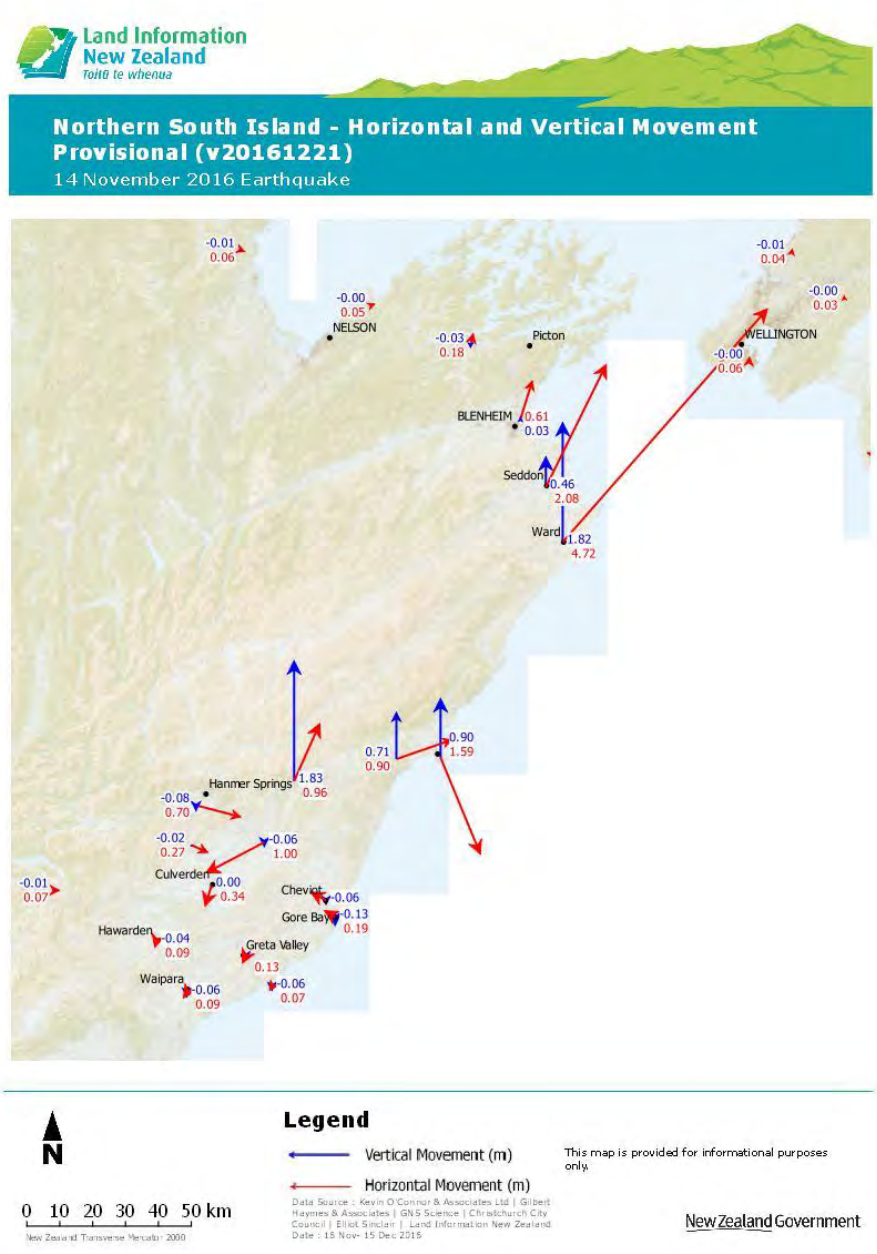

Figure 5.28: Estimated earthquake displacements at CORS (Source: LINZ).

GNSS baselines to scan locations were post processed in Leica GeoOffice v8.4 using WGTT as the reference station. The resulting 3D (Earth Centered Earth Fixed, ECEF) coordinates were then converted to the coordinate system in Table 5.5 using the LINZ online coordinate conversion tool. A summary of the coordinate system and reference datums used for the survey is in Table 5.6.

A temporary base station was set up on point CARDNO 19 on 11/30/2016 for a portion of the lidar survey. This station was used as a check against the data processed with the WGTT CORS. The coordinates were consistent to less than 1 cm. Additional checks against CARDNO control points were completed and were consistent within 1 cm after accounting for general differences in pre/post-earthquake coordinates. Coordinates for these points were extracted directly from the scans.

TLS scans were import into Leica Cyclone 9.1.4. On import, saturated pixels were removed (highly reflective objects at close range that result in incorrect coordinates) in addition to moderate mixed pixel removal (locations where the light is split between objects too close to distinguish) to minimize noise present in the point clouds.

Table 5.5: Post-earthquake coordinates utilized for CORS WGTT compared with the pre-earthquake results.

Coordinate	Easting (m)	Northing (m)	Elevation (m)	ΔE# (m)	ΔN# (m)	ΔElev# (m)
Pre-Earthquake* (Published)	400436.134	801185.183	30.316	-	-	-
Pre-Earthquake (PositioNZ)	400436.139	801185.184	30.319	0.005	0.001	0.003
Post-Earthquake (PositioNZ)	400436.153	801185.264	30.308	0.019	0.081	-0.008

**Pre-earthquake coordinates are Wellington Circuit 2000, NZGD2000, defined at nominal epoch 2000.0 with deformation model version 20160701.*

#Differences in Easting, Northing, and Elevation are relative to the published coordinates.

Table 5.6 Summary of Coordinate System and reference datums utilized for the survey.

Horizontal Datum: New Zealand Grid Datum 2000 (NZGD 2000)
Datum Version: v20160701
Vertical Datum (Heights): Wellington 1953 (NZVD 2016)
Circuit\Projection: Wellington Circuit 2000
Coordinate Epoch: 20161129 (Observation Date(s): 11/28-12/1, 2016)
Coordinate Source: PositioNZ-PP, Processed 1/X/2017

5.5.3 TLS registration

During the survey, pivoting 114-mm diameter black and white pattern targets with a metallic base were utilized to provide tie points between scans. These targets can be rotated to provide ideal incidence with the scanner from each scan position while ensuring that the center remains in the same location. The targets were strategically moved throughout the scanning process. Additional 152-mm diameter black and white pattern targets printed on durable label paper were utilized for some locales to provide additional tie points.

Center points for these targets were extracted using fitting algorithms in Leica Cyclone 9.1.4 software. These points were then used to build a preliminary registration. In some locales where there were insufficient targets, visual registration processes to approximately register two scans were followed by cloud-to-cloud surface matching. Cloud-to-cloud constraints were then added for significantly overlapping scans and added as additional constraints in the registration. These additional constraints help improve results at farther angles. A reference target was placed at the origin of each scan and linked to GNSS coordinates obtained for most scan origins.

A weighted, least-squares adjustment was utilized using all scans and constraints to determine the appropriate transformations (translations and rotations) for each scan. The following weights were utilized for this registration: 1.0 for targets that were clearly visible in each scan, cloud-to-cloud matches between close scans with substantial overlap, and GNSS coordinates for scan origins; 0.5 for targets of lower confidence; 0.3 for cloud-to-cloud matches between scans with some overlap but spaced further; and 0.2 for some GNSS coordinates of lower, but still acceptable, quality due to visibility obstructions. Periodically, distant features (e.g., light poles) visible in many scans across the port were utilized for quality control. Some GNSS coordinates with high residuals were removed in areas with very poor sky visibility due to the narrow pathways between shipping containers. The 3D weighted mean absolute error for all of the constraints was 0.0026 m. RMS differences between scan pairs for cloud-to-cloud registrations were typically less than 0.015 m.

Following the registration, a variety of quality control checks were implemented in addition to statistical analysis. These include coloring each scan a unique color and verifying the dataset was free of significant offsets between scans in cross sections.

5.5.4 DEM creation

Preliminary Digital Elevation Models (DEMs) were created across CentrePort. Refined models are in the process of being created. The following process was utilized:

1. The registered point cloud of the port was segmented into distinct geographic regions with overlap for processing efficiency.
2. Point clouds for each section were manually cleaned to remove building exteriors, walls, shipping containers, noise, and artificially low points resulting from multipath effects of the laser from wet or highly reflective surfaces. Lower level floors of buildings were left in the models to include in the DEMS.
3. The point clouds were then processed further in a custom ground filtering algorithm to remove additional spurious points.
4. The data were then organized into spatial bins of 0.05 to 0.10 m (depending on location).
5. Small holes were filled using a roving thin plate spline (see Olsen et al. 2015).
6. The data were then triangulated using the approach of Olsen et al. (2015) to create a DEM.

7. Derivative products such as slope maps and hillshades were then created for the DEMs to highlight discontinuities.
8. The resulting DEMs were used for settlement analyses as well as for generating cross sections.

Figure 5.29 shows a cross-section obtained on the west edge of the road immediately west of Building S37. The peaks are locations of the buried piles and the lower portions are settlement of the pavement surface around those piles. In absence of detailed survey data prior to the event, the original surface was estimated by fitting a 3rd order polynomial (R^2 = 0.99) to the tops of piles with higher elevations in the local area. Given this assumption, the differential settlement calculations (Figure 5.29(b)) do not account for any settlement of those piles which may have occurred given that some of the piles in that sequence appear to have settled. Regardless, the trends are reasonably consistent with the values shown in Figure 5.24.

Several TLS observations were obtained throughout the area surrounding the CS building at the southwest corner of the port, which experienced widespread liquefaction-induced ground deformations. The lidar DEM was converted to a hillshade to enhance visualization of cracks and other features in this area (Figure 5.30). The hillshade visualization highlights discontinuities in the data and provides detailed information on cracking patterns observed. In addition, differential settlement between the concrete slabs between the road and cold store building are apparent.

Figure 5.31 presents example DEMs with perspective views. From the lidar scans, significant differences in elevation from liquefaction are apparent. Figure 5.32 presents two cross-sections through this locale, one running north to south (Figure 5.32(a)) and one running west to east (Figure 5.32(b)). Although the pre-event surface was not available for comparison, it is likely that settlement increases significantly towards the south as a result of the increased liquefaction-induced ground spreading towards the south and west.

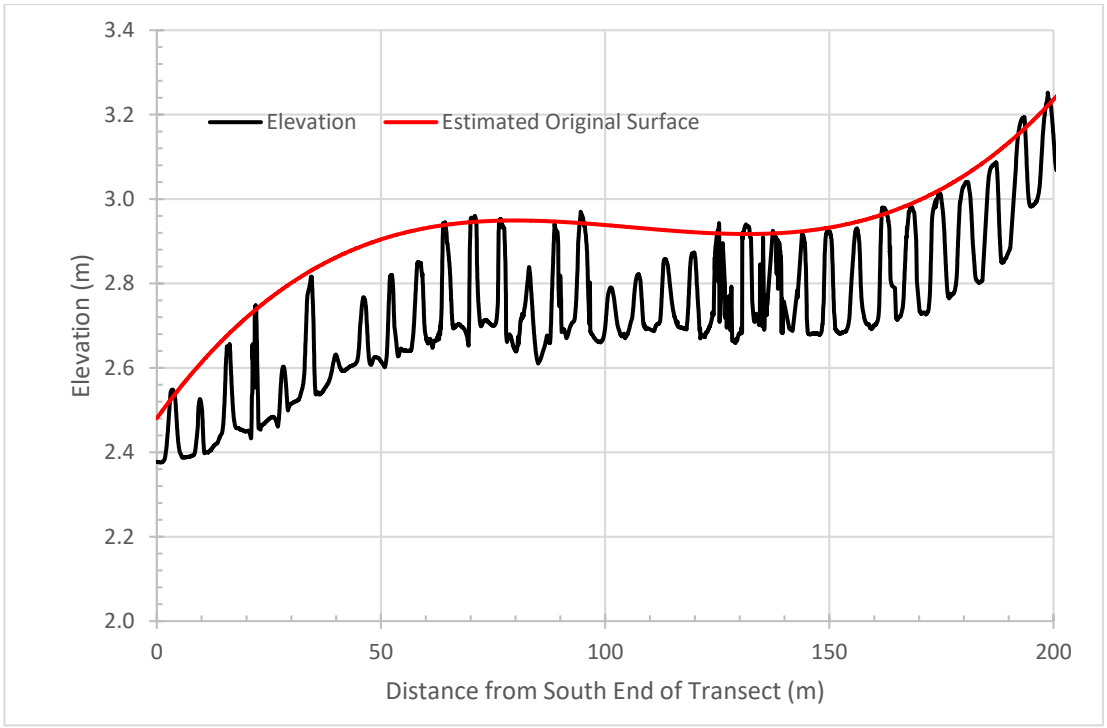

(a)

(b)

Figure 5.29: (a) Post-earthquake elevations for transect (LT1) along west side of roadway west of S37; the red line represents the estimated pre-elevation surface. (b) Estimated settlements. (Distance 0 is approximately 15 m south of the south wall of Building S37 and the 200 m transect runs to about 3 m north of the north wall of Building S37).

Figure 5.30: Example hillshade for the SW corner of the port, south of the CS building. This dataset was coarsely cleaned and still contains several artifacts from railing and metal racks.

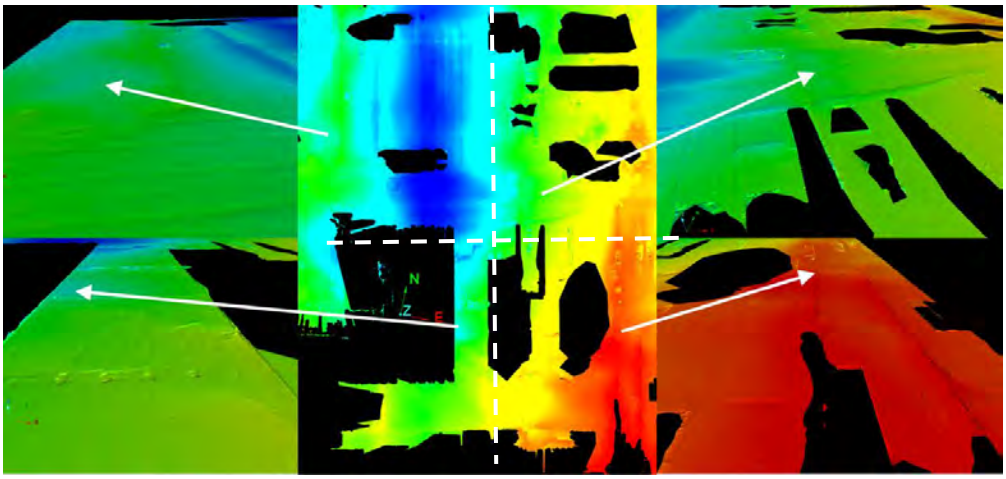

Figure 5.31: Example DEMs of the southeast portion of the port (next to, but not including Thornton Wharf) highlighting various liquefaction settlements and accretion of materials. Elevation ranges from 2.05 m (Red) to 3.80 m (Blue). The center image is a plan view, and the other images are perspective views to show detail.

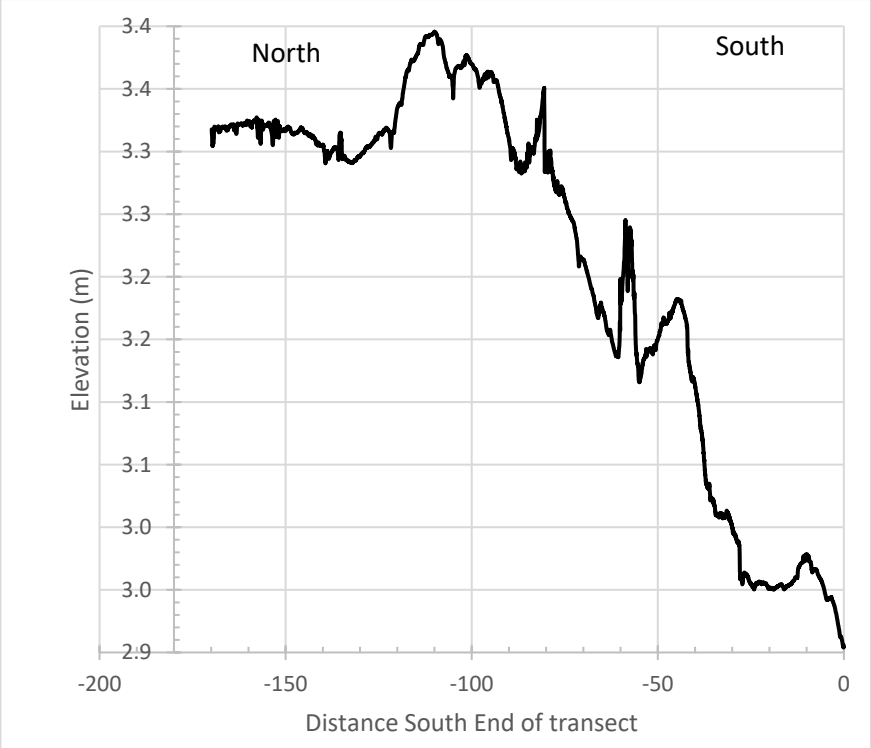

(a)

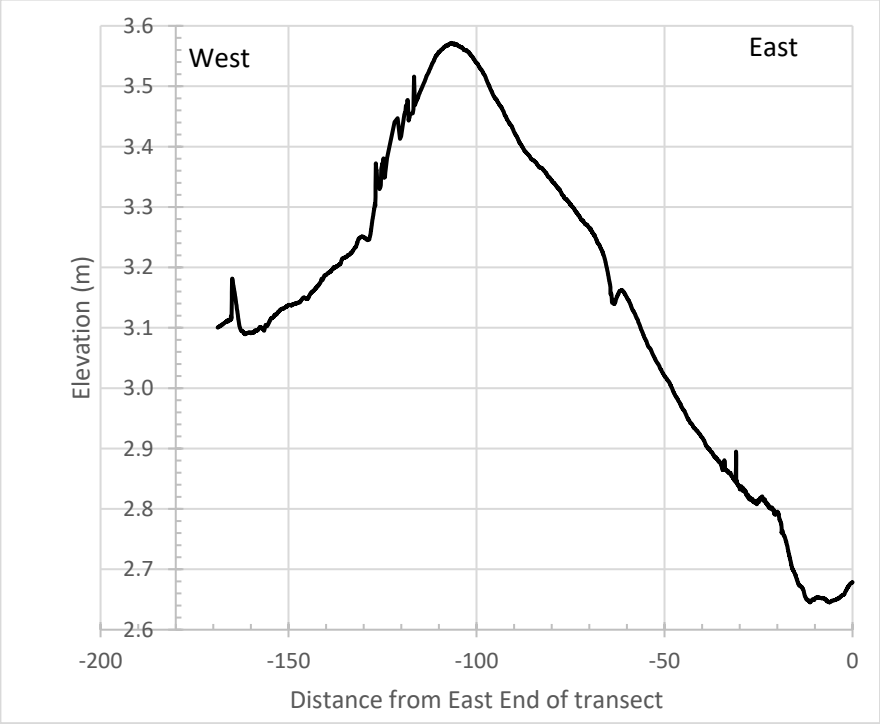

(b)

Figure 5.32: Cross sections across the southeast portion of the Thorndon Reclamation: (a) North South Transect LT2, and (b) East-West Transect LT3. Locations of transects are identified in Figure 5.27.

5.6 Effects on wharves

5.6.1 General

CentrePort Limited has Thorndon Container Wharf and King's Wharf. Figure 5.33 is a plan view of the port showing the location of the two wharf structures. The port's primary container operation takes place on Thorndon Container Wharf, which is on the eastern side of the port. King's Wharf, which is on the western side of the port, supports primarily roll-on/roll-off cargo.

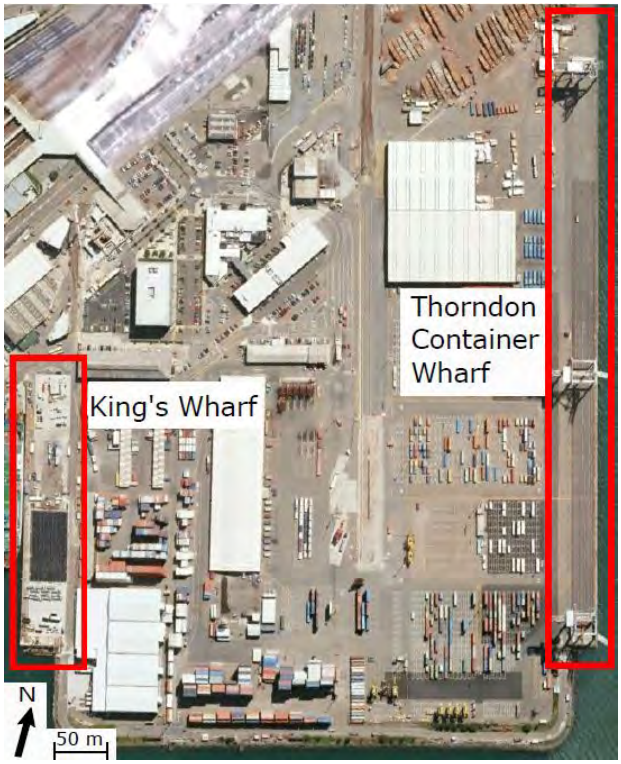

Figure 5.33: CentrePort Wellington map identifying the two wharves documented in this report. (Base image from Google Earth™)

5.6.2 Thorndon Container Wharf

The Thorndon Container Wharf is supported on 7 rows of 508x508-mm square, pre-stressed concrete piles. Pile bents are spaced 3.66 m on center or at approximately $s = 6B$. The piles are generally 18 m long under the eastern crane rail and 20 to 23 m long (increasing in length to the south) under the western crane rail (Tonkin & Taylor Ltd. 2012). Widespread liquefaction of the Thorndon Reclamation (Figures 5.34, 5.17 and 5.18) was accompanied with settlement of the fill and lateral spreading towards Thorndon Wharf. As described in Section 5.4, the lateral spreading displacements at the edge of the fill (bulkhead) reached about 0.8 m to 1.0 m (Figure 5.25 and Table 5.4). The lateral thrust from the displaced fill pushed the inland piles of the wharf causing tilt of the wharf. The crane rail tilted 2.5° down towards the sea at TWC-1 and 1° down towards the sea at TWC-2 (see Figure 5.25 for transect locations). Lateral seaward movement measurements of the bulkhead relative to the

ground immediately inland of it are listed in Table 5.7 and indicated in Figure 5.25. These measured values range from 200 to 500 mm. Ground settlement immediately inland of the bulkhead, relative to the wharf deck, was estimated to be 600 mm. Figures 5.35 and 5.36 show the vertical offset created between the pile supported wharf and reclaimed fill behind the wharf.

The QuakeCoRE-GEER team was informed that concrete piles had been sheared near the pile cap (from a boat survey by others; T+T (2016) private communication). From the south side of the port, the QuakeCoRE-GEER team did observe a vertical bulkhead pile sheared just below the pile cap (Figure 5.37a). During a site visit in May 2017, the team observed that the bulkhead piles (both plumb and battered) near the north end of the Thorndon Reclamation were damaged immediately below the deck (Figure 5.37b). Cardno performed an aerial survey of the port that captured vertical settlement and lateral movement, which is shown in Figure 5.38.The magnitude of lateral spreading displacement and settlement measured by Cardno are generally consistent with those measured by the QuakeCoRE-GEER team, which are provided in this report.

Figure 5.39 shows the LiDAR-derived DEM for the Thorndon Wharf and surrounding terrain. The wharf deck has substantial concavity as observed in the cross section in Figure 5.40. Differential settlements between the wharf deck and adjacent pavement ranged from 435 mm to 780 mm, generally increasing towards the North. Figure 5.41 provides a close up of ejecta and offsets at the northern end of this portion of the wharf.

Figure 5.34: Widespread liquefaction of gravelly end-dumped quarry rock reclamation in container stacking area inland of Thorndon Wharf (S41.276608° E174.786309°, taken on 21NOV16)

Table 5.7: Estimates of seaward movement of bulkhead relative to inland soil.

TWC Station	Seaward Separation at Bulkhead (mm)
40+00	300
160+00	300
180+00	200
200+00	300
250+00	500
260+00	400

Figure 5.35: Looking south along Thorndon Wharf bulkhead at approximately STA 240. Approximately 600 mm of ground settlement measured relative to pile-supported wharf. (S41.278250° E174.789205°, taken at 1124 hrs on 21NOV16)

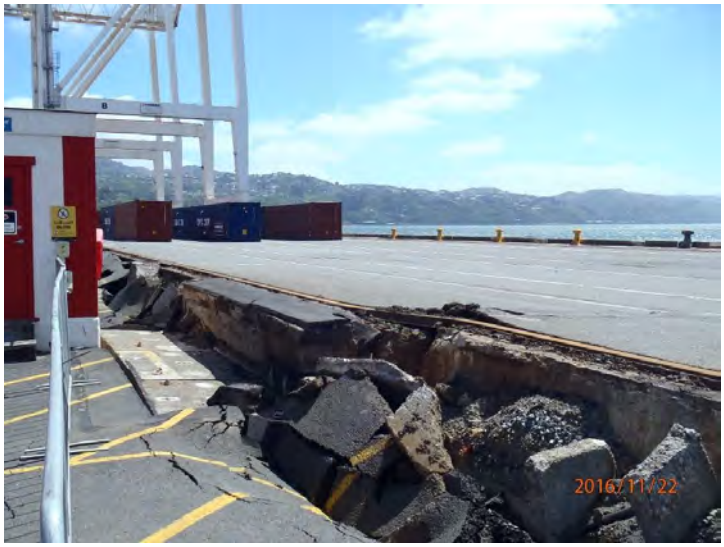

Figure 5.36: Looking north along Thorndon Wharf bulkhead at approximately STA 280. Approximately 600 mm of ground settlement measured relative to pile-supported wharf. (S41.277743° E174.789236°, taken on 22NOV16)

(a)

(b)

Figure 5.37: (a) Looking north towards the southern end of Thorndon Wharf. The vertical bulkhead pile is sheared just below the pile cap. QuakeCoRE-GEER team was informed that many piles in this area were sheared near the pile cap (from a boat survey by others; T+T (2016) private communication) (S41.280219° E174.789974°, taken at 1152 hrs on 22NOV16) (b) Looking north under the Thorndon Wharf bulkhead toward damaged plumb and battered bulkhead piles. (S41.277312° E174.789081°, taken at 13:38 hrs on 08MAY17)

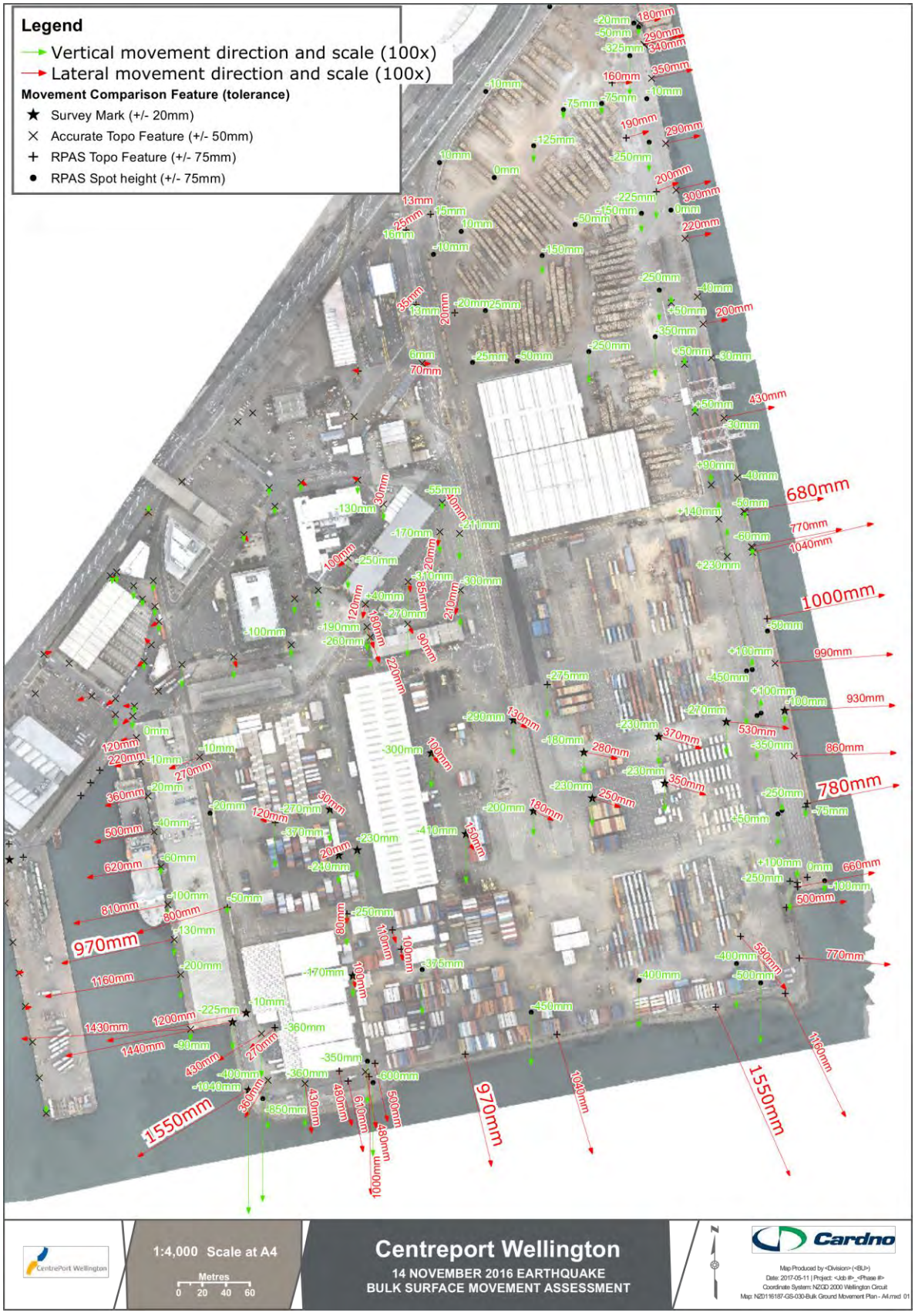

Figure 5.38: Aerial survey of Thorndon Reclamation and Wharf (performed by Cardno).

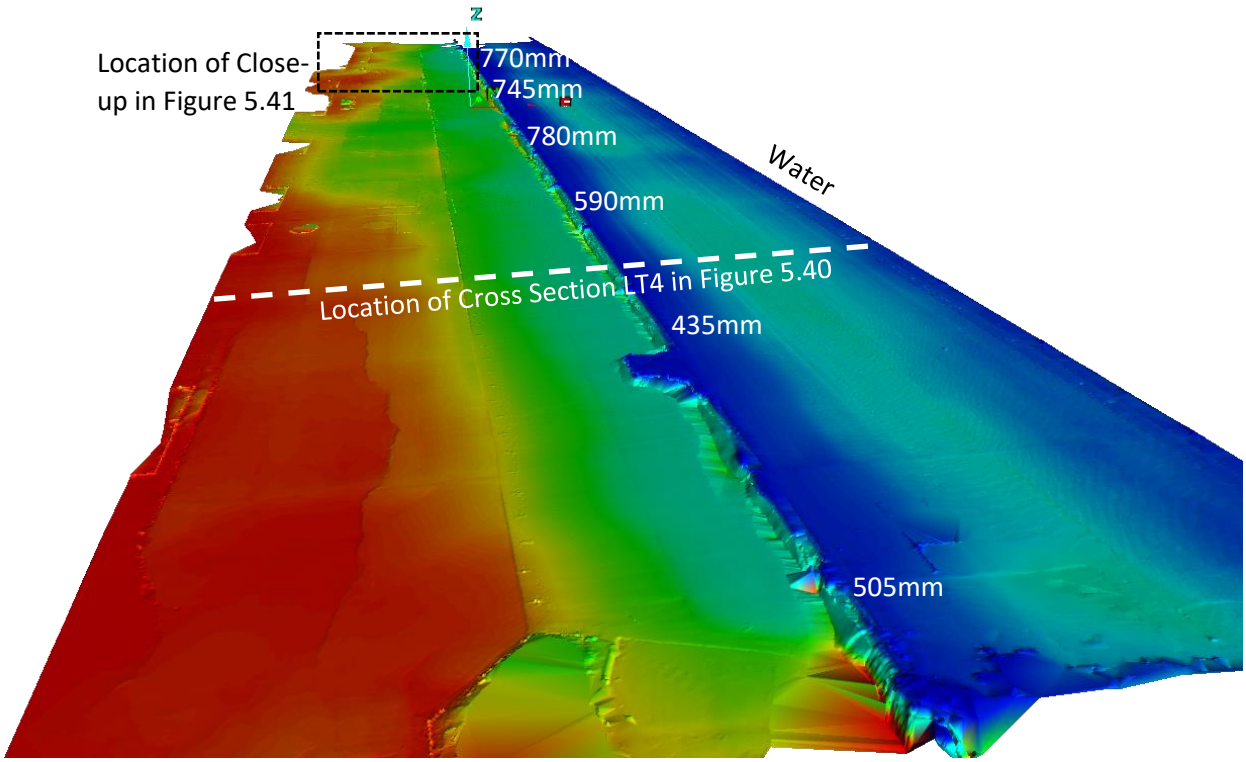

Figure 5.39: Perspective view of the LiDAR DEM of the eastern section of the port looking northward including the Thorndon Wharf and surrounding area colored by elevation to highlight discontinuities from cracks. Elevation ranges from approximately 2.60 m (red) to 3.60 m (dark blue). Differential settlements between the Wharf and Port are identified.

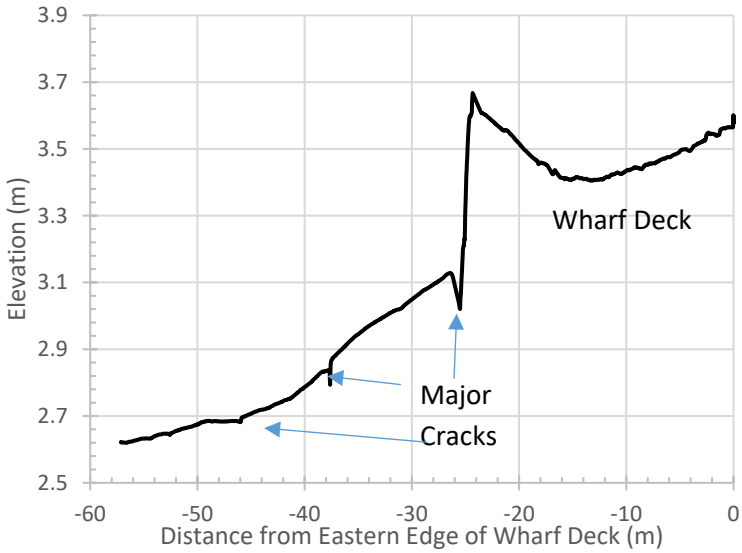

Figure 5.40: Elevation profile for cross section LT4 across Thorndon Wharf and inland fill. The location of the cross section is shown in Figure 5.39.

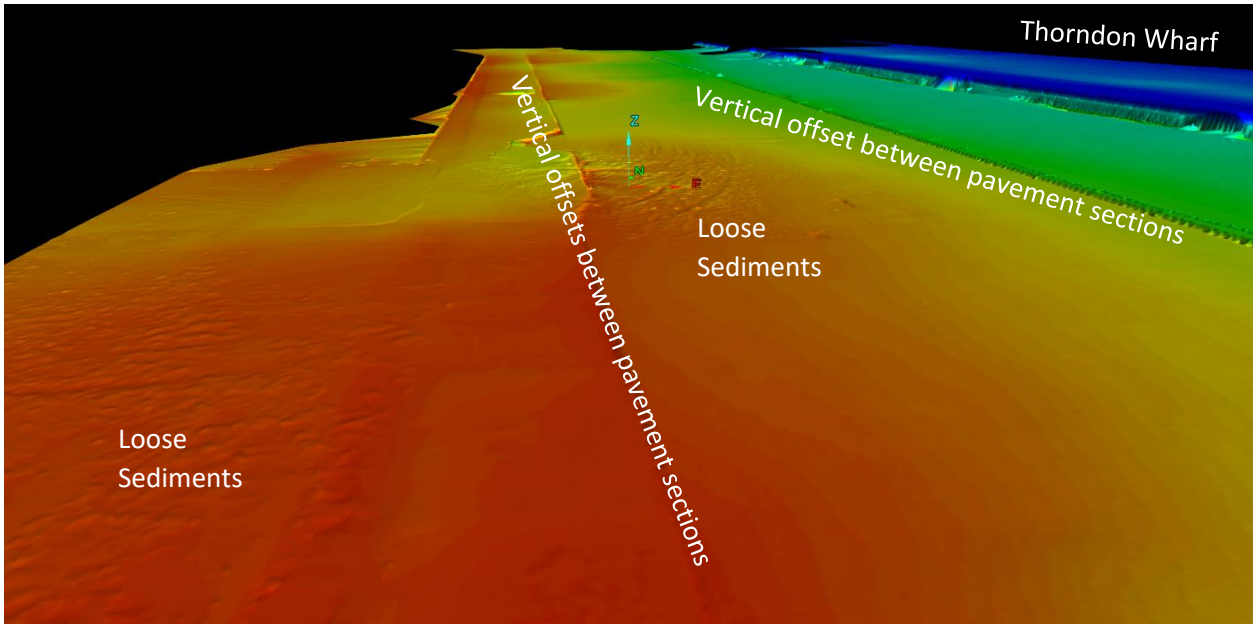

Figure 5.41: Close-up of the port surface highlighting cracking and separation between asphalt sections as well as loose sediments from ejecta (rougher sections of DEM) in the vicinity of Thorndon Wharf (see Figure 5.39).

5.6.3 King's Wharf

King's Wharf is supported on driven timber piles. The fill behind the wharf liquefied and moved laterally towards the wharf (sea) displacing King's Wharf to the west. The spreading displacement was the largest at the south end of the wharf where based on our lateral spreading measurements the lateral movement of soils behind the wharf exceeded 1.1 m. The ground along the edge of the reclamation displaced westward (towards the wharf) and downwards (beneath the wharf deck) as illustrated in Figure 5.42 (and Figure 5.54). The ground settlement relative to the deck of the wharf was approximately 560 mm at the southeast corner of the wharf (Figure 5.42) and 530 mm at the northwest corner of the CS building (Figure 5.54). Ground movements in the vicinity of the CS building (S41.28105° E174.78483°) near the southern end of King's Wharf were measured and are listed in Table 5.8 for Transects CS-1, CS-2, and CS-6, which will be presented and discussed later in the report. Note that the magnitude of spreading displacements generally decreased towards the north section of the wharf.

The inland timber piles split due to seaward (westward) lateral movement of the deck relative to the piles (Figure 5.43). Westward movement of the structure is visible in Figure 5.44, in which the southern row of piles is shown leaning to the west. Some vertical curvature of the wharf deck can be observed in the LiDAR DEM (Figure 5.45) and associated cross section in Figure 5.46. Differential settlement between the wharf and adjacent ground range from 475 mm to 630 mm as measured from the LiDAR-derived DEM. The wharf deck exhibits significant concavity (downward) as observed in the cross section plotted on Figure 5.46.

Figure 5.42: Looking North along bulkhead of King's Wharf. Approximately 560 mm of ground settlement relative to deck at southeast corner of King's Wharf. The west wall of the Cold Store shed is visible to the right of the photograph. (S41.281142° W174.784444°, taken at 1416 hrs on 21NOV16)

Figure 5.43: Looking under King's Wharf at an inland bulkhead pile. Timber pile is split from lateral movement (seaward/westward) of the deck relative to the pile. (S41.280900° E174.784375°, taken at 1412 hrs on 21NOV16)

Figure 5.44: Looking west along southern end of King's Wharf. Westward tilt of piles is visible. (S41.281281° W174.784097°, taken on 17NOV16)

5.7 Effects on buildings

5.7.1 General

Several engineered structures located on or adjacent to CentrePort Wellington were affected by the liquefaction-induced ground movements at the port. A few buildings were supported on shallow foundations. Most buildings were supported on pile foundations. Detailed reconnaissance observations for each building are presented in the following sections. Buildings are identified in Figure 5.47.

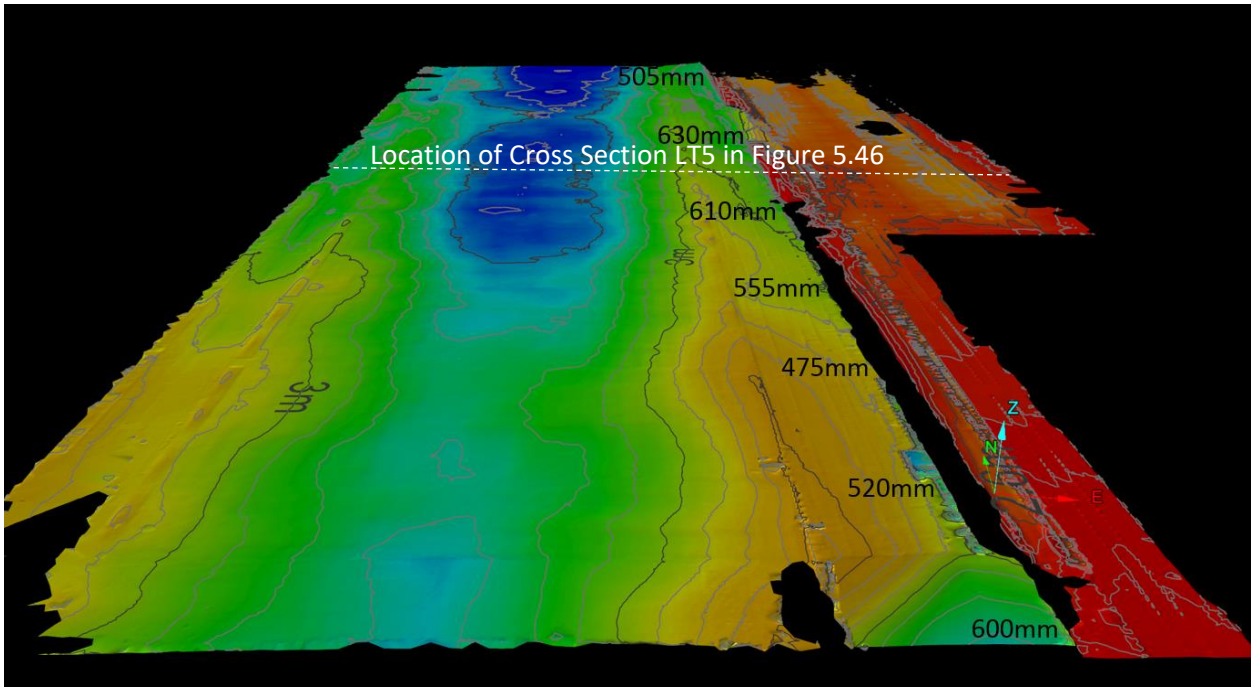

Figure 5.45: Perspective view of the LiDAR derived DEM (looking northward) of the pile supported King's Wharf showing measurements of differential settlement the adjacent ground. Elevation ranges from approximately 2.50 m (red) to 3.30 m (dark blue)

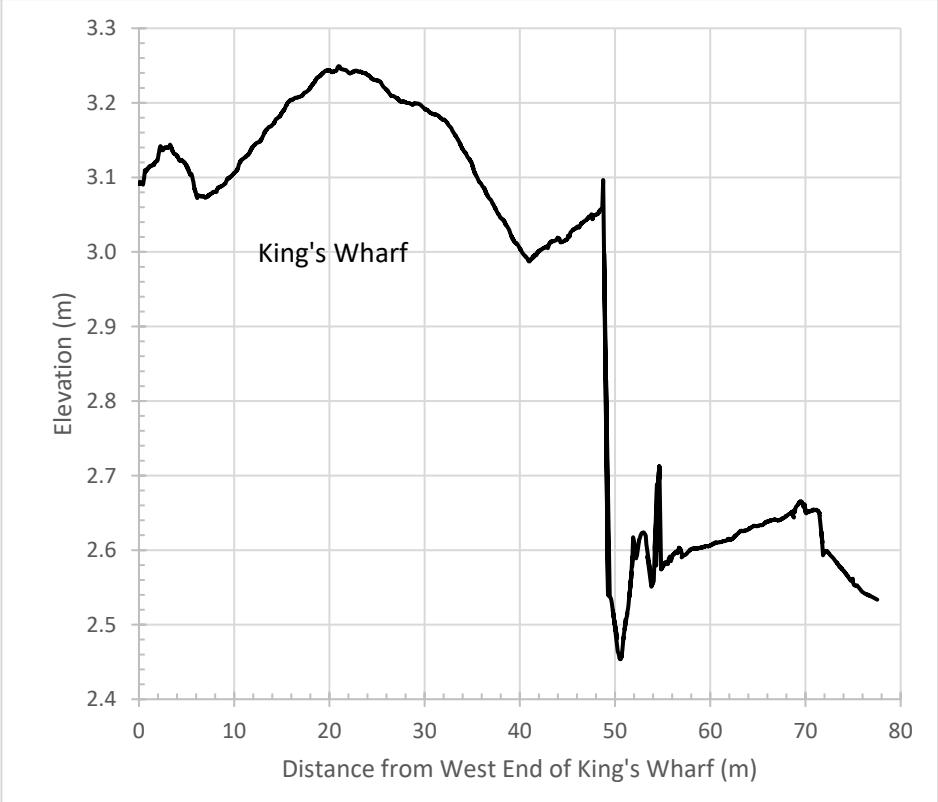

Figure 5.46: Cross section LT5 taken across King's Wharf and the adjacent ground based on LiDAR data shown in Figure 5.45.

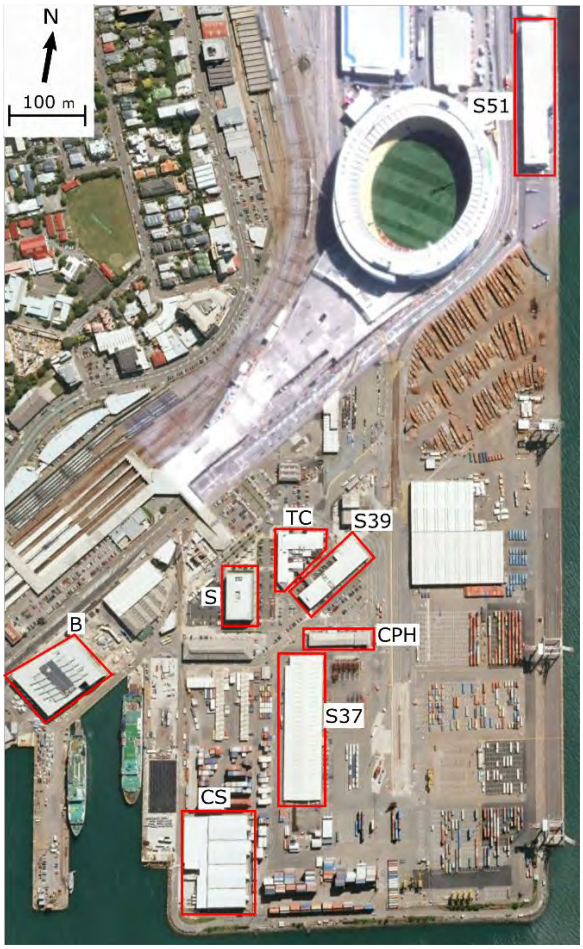

Figure 5.47: CentrePort Wellington map identifying buildings studied in this reconnaissance. (Base image from Google Earth™)

5.7.2 Buildings on Shallow Foundations

5.7.2.1 CPH Building

The CPH building (S41.27829° E174.78618°) is founded on reinforced concrete (RC) spread footings connected with RC grade beams (Figure 5.48). There were no apparent signs of structural distress, and the building was operational at the time of the reconnaissance in late November 2016. The building and surrounding fill settled relatively uniformly, however, ground a few meters to the west of the CPH building did not appear to settle significantly as it was elevated relative to the surrounding ground and the floor level of the CPH building. The elevated ground was likely supported by the old bulkhead piles of the demolished Pipitea Wharf (see Figure 5.2), which minimized liquefaction-induced settlement of the ground and pavement above it. The building and fill settled approximately 230 to 260 mm relative to the ground supported on piles, as shown in Figure 5.49. Settlement appeared to be more or less uniform across the building footprint, as there were no apparent signs of relative movement or tilt of the ground floor of the CPH building from the visual investigation. However, a preliminary analysis of the LiDAR scans indicate a slight tilt (i.e., of 0.105 degrees) in the large operations room on the east end of the building.

Figure 5.48: Uniform settlement of CPH building which is founded on shallow foundations that apparently displaced downward the same amount as the surrounding fill. This photo is looking northeast at the southwest corner of the building. (S41.278395° E174.785639°, taken at 1230 hrs on 21NOV16)

Figure 5.49: Uniform settlement (230-260 mm) of the building relative to ground supported on old bulkhead piles of Pipitea Wharf. Looking north along western wall of CPH building. The perimeter walkway slopes down towards the building at 11 degrees over 1.35 meters. (S41.278395° E174.785639°, taken at 1225 hrs on 22NOV16)

5.7.2.2 CS Building

The CS building (S41.28105° E174.78483°) is supported on a composite shallow foundation with RC spread footings and mats. The building consists of an irregular-shaped single-story open loading bay in its western part (herein called the Shed) and a rectangular-shaped large cold storage facility on its eastern part (herein called the Freezers). The structural frames and supporting foundations of these two parts of the building appear to be independent. From observation, the structural system of the Shed is composed of concentrically-braced steel frames. The QuakeCoRE-GEER team members were given access to the Shed (i.e., the western part of the building) but not to the Freezers (i.e., the eastern part of the building). We did have access to the ground surrounding the building.

The differential ground movements across the building footprint induced structural deformation in the CS building. Seaward lateral ground movements on the order of 1 m occurred towards the western and southern slopes in the southwest corner the CentrePort reclaimed land. Figure 5.50 shows the location of six transects along which the location and width of lateral ground cracks in the pavement surrounding the CS building were recorded. Superimposed on this figure are plots of cumulative lateral ground displacement as a function of distance from the crest of the waterfront slopes for each transect. They show that, at the south side of the building, the fill moved towards the sea (southward) approximately 0.8 to 1.3 m. Similarly, the fill moved 0.8 to 1.1 m to the west direction. The top plot in Figure 5.50 indicates that the foundations of the building were subjected to a lateral stretch of approximately 200 mm. This stretch occurred over a column span of approximately 8.8 m, which corresponds to a lateral strain of about 2.3 percent. Tables 5.8 and 5.9 provide the measured crack widths and distances from the transect reference point for the east-to-west (CS-1, CS-2, and CS-6) and north-to-south (CS-3, CS-4, and CS-5) transects, respectively. Data for all six transects are plotted in Figure 5.51.

Significant separation between the CS building foundation and pavement slab were observed on the south side of the building (as well as settlement and spreading of the surrounding pavement). Figure 5.52 shows a LiDAR scan documenting this separation, which ranges from 30 mm (west) to 230 mm (east).

Gravelly liquefaction ejecta was observed around the building (Figure 5.53). Figure 5.54 shows lateral ground movements and partial collapse of the slope at the reclamation edge along the western wall of the Shed of the CS building (which is parallel and adjacent to King's Wharf), where the ground settled approximately 530 mm relative to the King's Wharf. This part of the building is closest to the crest of the slope and it underwent the largest lateral movement. Figure 5.55 shows lateral movements near the crest of the western slope, and Figures 5.56 and Figure 5.57 show lateral spreading towards the southern slope with a vertical offset of approximately 1.1 m. In these large cracks and vertical offsets, shallow soils beneath the pavement were visible and consist of gravelly quarry rock reclamation fill. Crack widths and locations along the bottom of the outside walls of the CS building were also measured. Figure 5.58 shows results of this survey, which are consistent with the previously described lateral spreading measurements and indicate a lateral stretch of the shallow foundation of the Shed of approximately 200 mm in the westward direction.

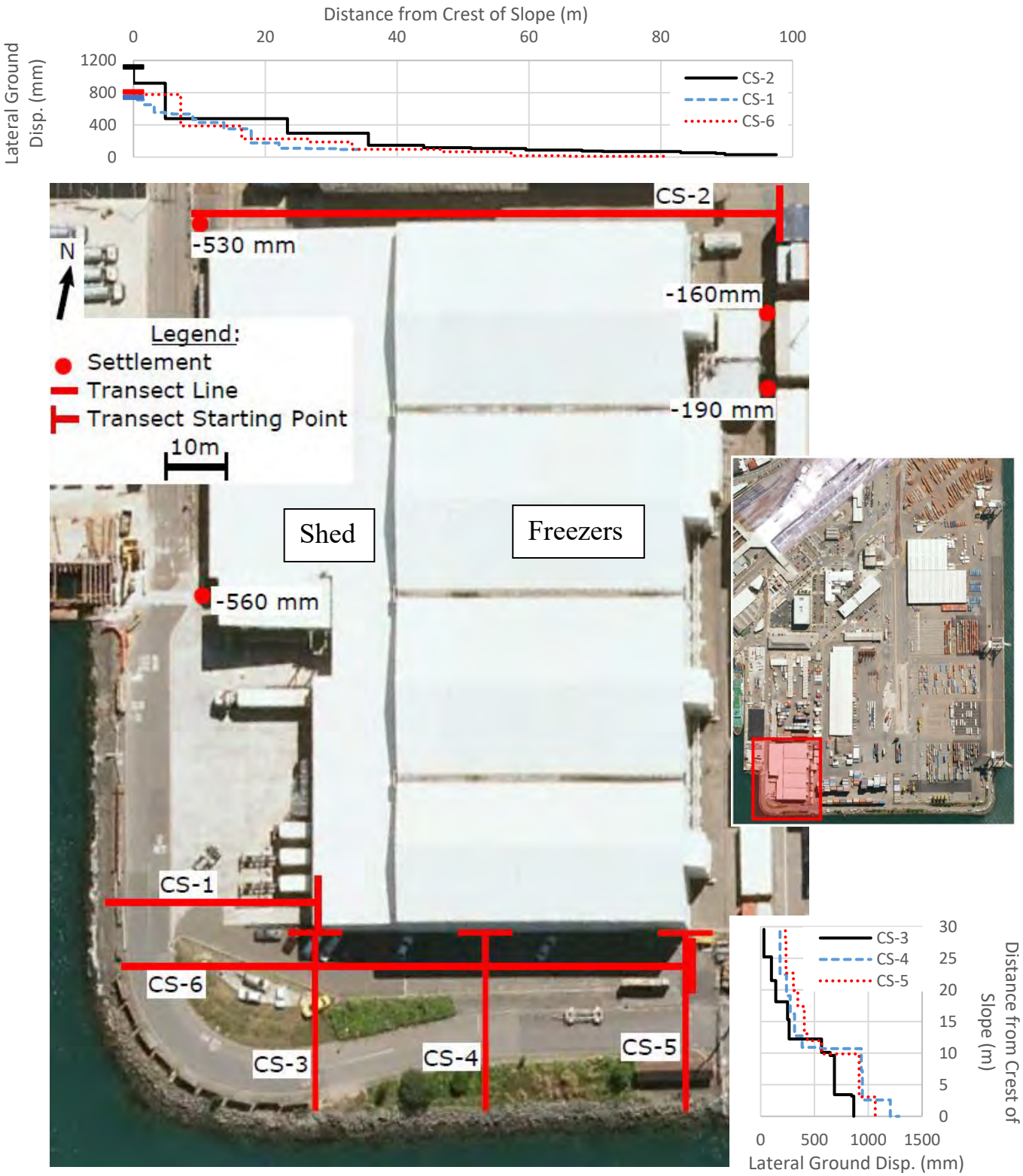

Figure 5.50: CS building lateral ground movement transects and vertical settlement measurement locations. Cumulative ground displacement versus distance from crest of slope are provided. Note that the crest of slope is further east at CS-2 than at CS-1 and CS-6, therefore, displacement plots do not perfectly align with satellite image for CS-2. Settlement measurements to the northeast are relative to the building which also settled.

Table 5.8: CS Building east-to-west lateral ground movement transects.

CS-1		CS-2		CS-6		
Horizontal Distance from Reference Point (m)	**Crack Width (mm)**	**Horizontal Distance from Reference Point (m)**	**Crack Width (mm)**	**Horizontal Distance from Reference Point (m)**	**Crack Width (mm)**	**Vertical Offset (mm)**
1.06	95	0.00	30	14.43	10	0
4.21	10	7.80	15	28.60	7	0
9.03	5	9.20	10	37.56	50	0
13.17	65	14.50	15	48.16	30	-5
17.40	175	26.30	5	61.69	90	0
21.55	80	29.50	12	68.11	40	-2
25.60	35	38.00	20	78.42	160	-30
26.26	70	46.30	10	87.68	390	-210
29.42	5	53.50	30	94.84	30	-5
30.42	15	61.90	150	–	–	–
32.10	95	74.17	180	–	–	–
33.75	60	92.70	440	–	–	–
35.25	30	97.53	200	–	–	–
Total:	740	Total:	1,117	Total:	807	-252

Table 5.9: CS Building north-to-south lateral ground movement transects.

CS-3			CS-4			CS-5		
Horizontal Distance from Reference Point (m)	**Crack Width (mm)**	**Vertical Offset (mm)**	**Horizontal Distance from Reference Point (m)**	**Crack Width (mm)**	**Vertical Offset (mm)**	**Horizontal Distance from Reference Point (m)**	**Crack Width (mm)**	**Vertical Offset (mm)**
0.05	30	0	0.00	180	-30	0.33	230	0
4.40	70	0	6.80	60	0	2.02	5	0
8.15	40	0	10.15	35	0	7.02	70	-45
11.50	110	-10	13.00	40	-30	9.80	40	0
14.30	15	0	16.50	70	-150	12.30	60	60
17.40	300	-250	18.30	170	-25	16.64	30	-65
19.50	80	90	18.52	380	-770	17.72	130	90
20.00	40	10	21.98	10	0	19.82	350	-470
26.20	160	50	26.64	260	0	26.62	150	0
26.43	20	0	29.22	80	-105	29.68	35	0
29.62	0	-360	–	–	–	–	–	–
Total:	865	-470	Total:	1,285	-1110	Total:	1,100	-430

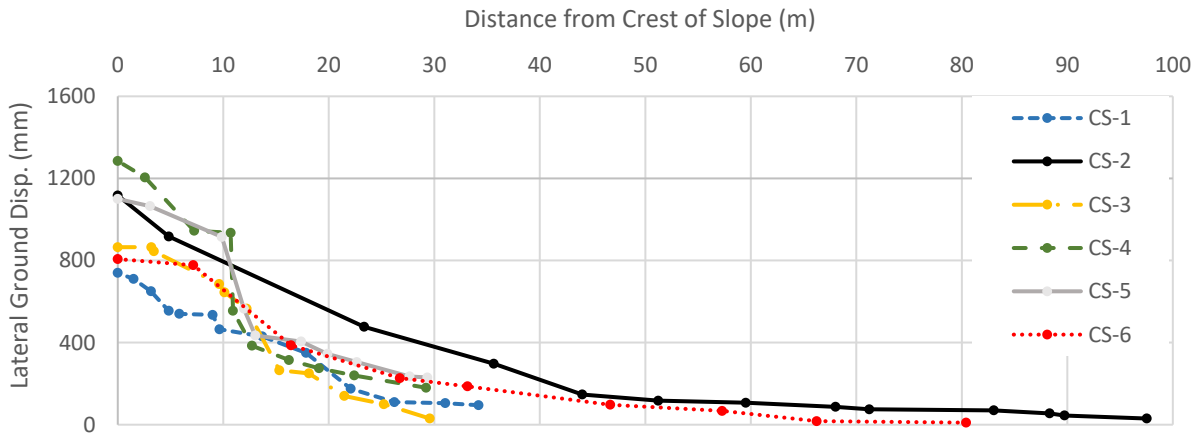

Figure 5.51: Cumulative lateral ground displacement versus distance from the crest of the waterfront slope for Cold Store lateral spread transects.

Figure 5.52: Perspective view of LiDAR scan looking westward showing the horizontal separation from building foundation and settlement of pavement observed on the south side of the CS building looking west (colored indicates intensity). The separation varies from 0.23 m wide to 0.03 m wide horizontally from the building's eastern side to its western side.

Figure 5.53: Gravelly liquefaction ejecta looking east along the northern wall of the CS building. (S41.280528° E174.784984°, taken at 1651 hrs on 22NOV16)

Figure 5.54: Looking north along the west wall of the CS building. The ground settled approximately 530 mm relative to the pile-supported bulkhead of King's Wharf, which is shown at the left side of the photograph. (S41.280923° E174.784389°, at 1411 hrs on 21NOV16)

Figure 5.55: Ground cracks in area west of the CS building and along the southwestern slopes of CentrePort (looking south). The CS building can be partially seen on the upper left corner of the photograph. (S41.281478° E174.784430°, taken at 1418 hrs on 21NOV16)

Figure 5.56: Approximately 1.1 m of vertical offset resulting from the southward lateral movement of the southern edge of CentrePort reclaimed land near its western side. Looking west near the southern wall of the CS building. (S41.281701° E174.785268°, taken at 1427 hrs on 21NOV16)

Figure 5.57: LiDAR scan of damage to the asphalt pavement and concrete curbs on the access road located south of the CS building. The vertical offset is approximately 1.1 m. This view is looking to the northeast.

Figure 5.59 documents significant cracking resulting in exposure of rebar in the foundation of the CS building on the north side from a LiDAR scan. Figure 5.59(a) looks south at the north wall of the CS building while Figure 5.59(b) shows the same crack running northward. The width of this crack is fairly consistent at 200 mm for much of the length as was observed in the LiDAR scan; however, it widens to 500 mm at some locations in the north and narrows to approximately 180 mm closer to the building (minimum width is 150 mm).

The western part of the CS building (i.e., the Shed) is a steel-frame, single-story structure with an open bay. As can be seen on the satellite image of the crack map shown in Figure 5.58, the total span of the Shed on its north end is about twice as wide as its span width on its south end. The northwest part of the Shed is closest to the free-face of the slope (Figure 5.54), and consequently experienced the largest lateral ground movement. Thus, the northern part of the Shed displacement laterally westward more than its southern end. The westward lateral movement of the north end of the building separated the Shed from the Freezers along the northern half of the building (Figure 5.60a). The differential lateral ground movements across the north-south length of the Shed produced deformations, cracks, and openings in the overlying foundation and structure. This deformation pattern was apparent by comparing the magnitude of building cracks along the north wall to those on the south wall, as well as separation of construction joints in the interior floating slab of the Shed. Measurements of construction joint separation in the slab are shown schematically in Figures 5.61 and 5.62 for the northern and southern parts of the Shed, respectively. Figure 5.63 was taken inside the Shed part of the CS building and shows construction joint separations. Figure 5.64 shows panoramic imagery co-acquired with the LiDAR data that can also be utilized for measurements. The maximum separation between slabs was measured to be 230 mm.

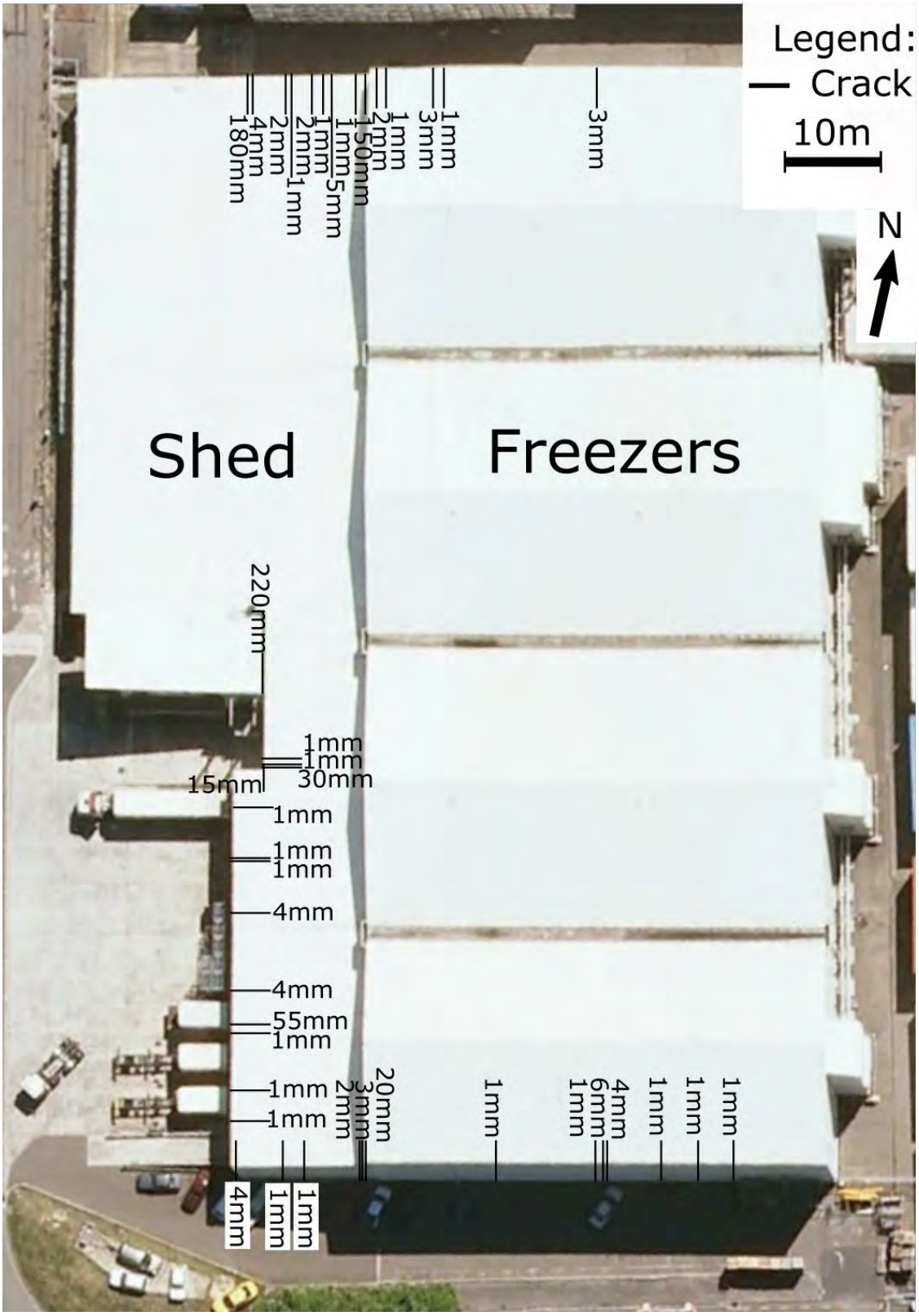

Figure 5.58: Location and width of lateral ground movement-induced cracks in the RC concrete walls at the base of the exterior building walls of the CS building. Crack openings are parallel to each wall.

(a)

(b)

Figure 5.59: (a) Significant damage and cracking observed in the LiDAR scan data at the north end of the CS building. (b) The same crack extending northward across the port.

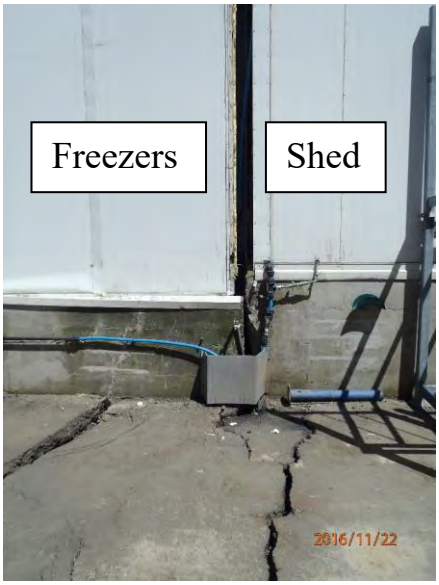

(a)

(b)

Figure 5.60: Cracks along the exterior north wall of CS building: (a) 150 mm of separation between Shed and Freezers (i.e., westward/seaward movement of the Shed relative to the Freezers), (S41.280584° E174.784705°, taken at 1445 hrs on 22NOV16), and (b) 180 mm crack in the shed from westward lateral spreading (also shown in Figure 5.59b). (S41.280607° E174.784533°, taken at 1444 hrs on 22NOV16)

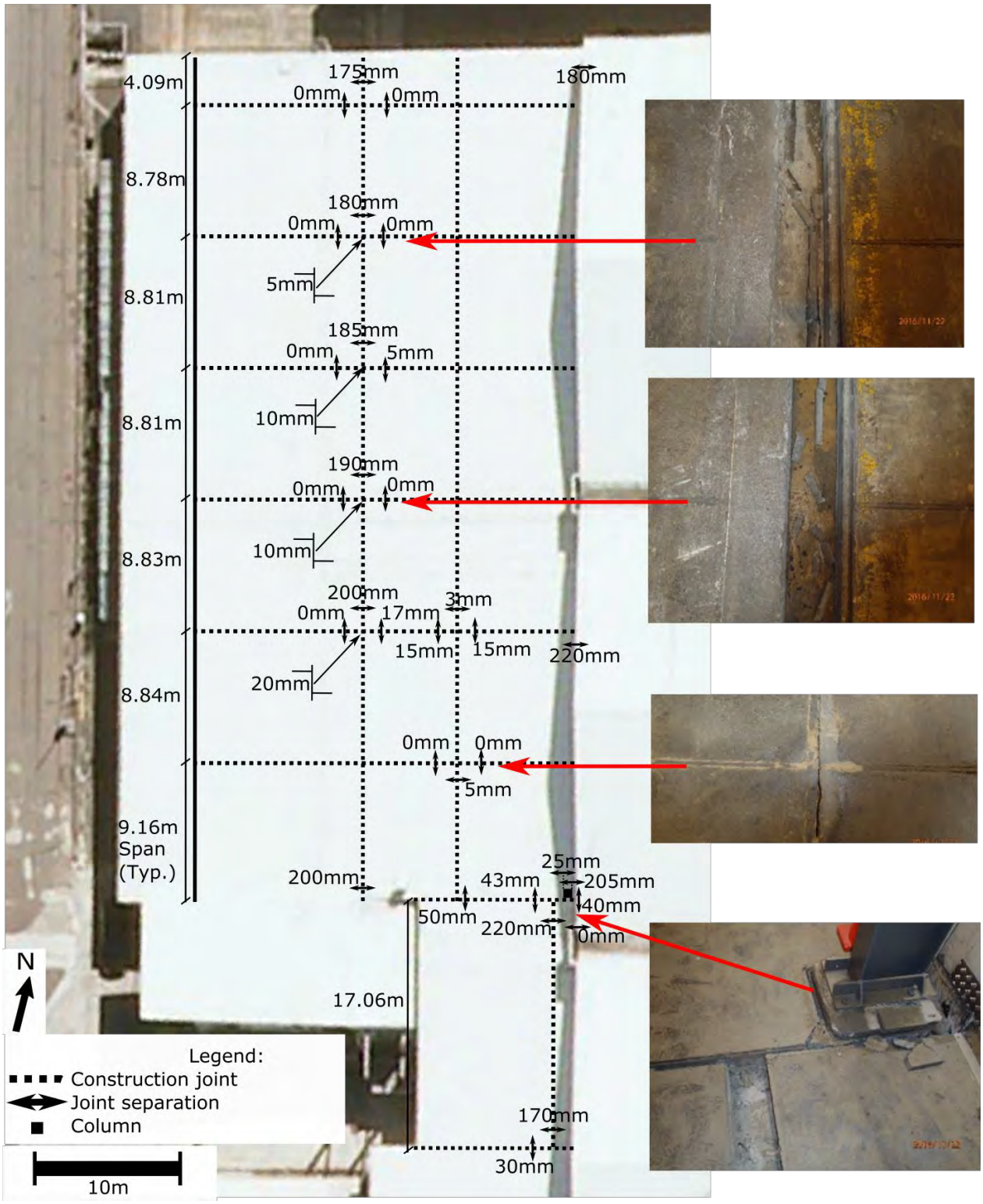

Figure 5.61: Northern part of Shed floor slab contraction joint separation measurements. Photographs along right side of figure are of contraction joints at which measurements were taken and are aligned vertically with each depicted joint. (Taken 22NOV16)

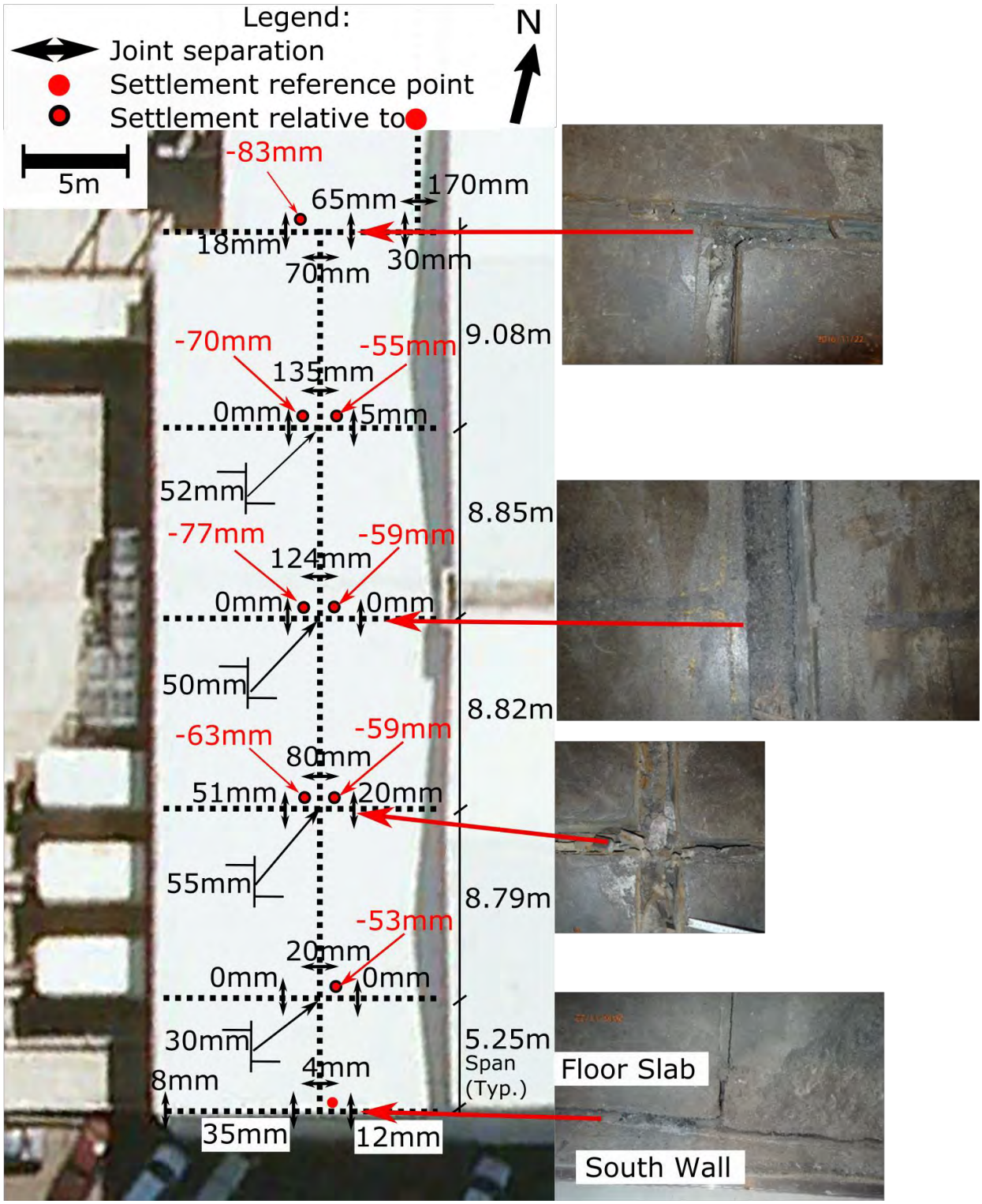

Figure 5.62: Southern part of Shed floor slab contraction joint separation measurements. Photographs along right side of figure are of contraction joints at which measurements were taken and are aligned vertically with each depicted joint. (Taken 22NOV16)

Figure 5.63: Contraction joint separation of ground floor slab inside the Shed of CS building looking south. As shown in photo, joint separations occurred in two orthogonal directions. (S41.281255° E174.784797°, taken at 1520 hrs on 22NOV16)

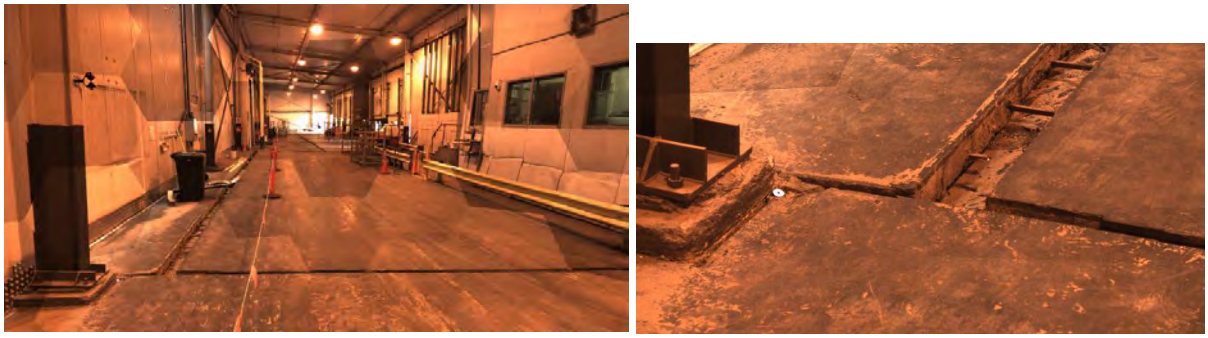

(a) (b)

Figure 5.64: Example panoramic imagery co-acquired with the laser scans: (a) overview, and (b) close-up of floor separation in the CS building. The larger crack measures 230 mm in width and the smaller crack measures 75 mm in width.

The differential lateral ground movements across the footprint of the Shed part of the CS building were also manifested in the deformation pattern of its steel framing. This deformation pattern is shown in Figures 5.65 and 5.66. Figure 5.65 is a photograph of the second frame from west to east along the north wall (i.e., the third, easternmost, bay is not shown in this sketch). Figure 5.66 is a schematic of the three west-most columns along the north wall looking north from the interior. The western-most column span along the north wall was measured as 8.663 m from column centerline to centerline at a height of 1.5 m above the floor slab. The next span to the east was measured as 8.789 m in the same way. In addition to the tilting of these columns along the north wall, at least two columns along the east wall of the shed were rotated at the base, causing buckling of the concentric bracing between columns (Figure 5.67).

Figure 5.65: Internal north wall of Shed of CS building showing 1.5° clockwise tilt of the left column (2nd column from the west along north wall), and 2° counterclockwise tilt of the right column (3rd column from the west along north wall). This deformation was caused by a 180 mm opening in the RC base wall, which is visible in the bottom middle of the photograph where light is entering building. This column span is 8.789 m from centerline of column to centerline at a height of 1.5 m above the floor slab. (S41.280626° W174.784450°, taken at 1452 hrs on 21NOV16)

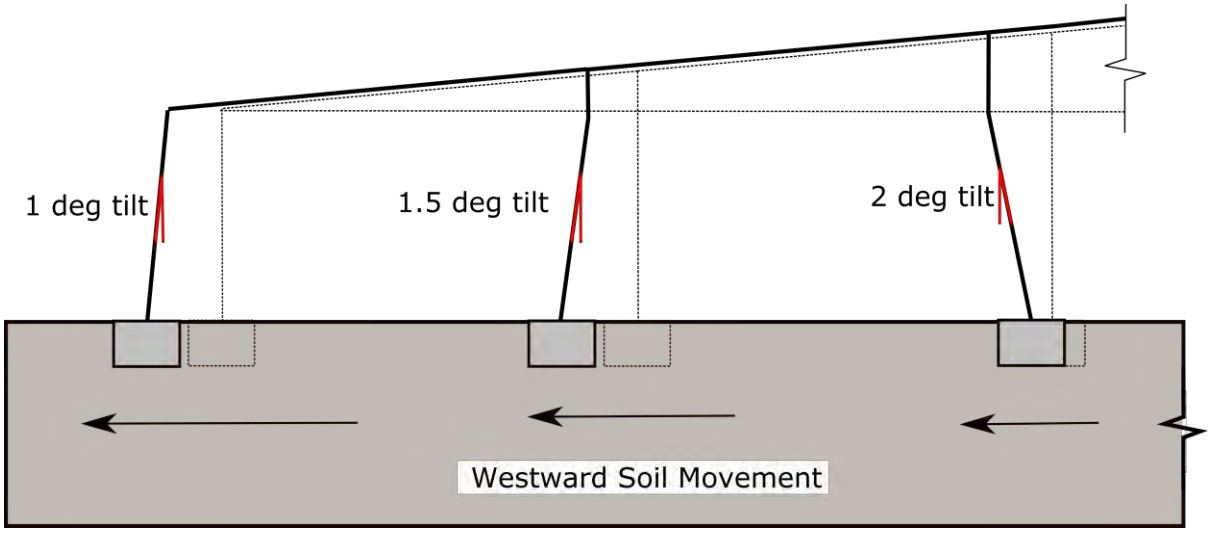

Figure 5.66: Schematic of deformation pattern of steel frame along the north wall of CS building (3 west-most columns of the Shed; looking north from interior).

Figure 5.67: Internal east wall in northern part of the Shed, which shows column-pedestal connection failure due to rotation of the base of the column and buckling of concentric bracing. (Approx. at S41.280939° E174.784778°, taken at 1615 hrs on 22NOV16)

5.7.3 Buildings on deep foundations

5.7.3.1 S39 building

The S39 building is supported on Frankie piles. The old buried mass concrete seawall (i.e., Old Seawall) runs parallel and adjacent to the southeast wall of the building. Additionally, along the southeast wall, a segment of the historic Fryatt Quay Wharf deck (Figure 5.2) was left intact. The ground to the south of the seawall and wharf settled 220 mm relative to the top of the wharf deck and the pile-supported building (Figure 5.68). Approximately 100 to 190 mm of settlement was observed along the south west wall of the building (Figure 5.69). On the northwest side of the building, the ground adjacent the building settled approximately 50-100 mm relative to the building (Figure 5.70). The QuakeCoRE-GEER team was informed that the ground floor slab dropped 150 mm inside the building (T+T (2016), private communication).

Figure 5.68: Southeast side of Building S39 and a buried segment of the Fryatt Quay Wharf deck parallel to the building. Fill to the south of the buried mass concrete seawall/wharf settled 220 mm relative to the pile-supported building and wharf deck. (S41.277984°, E174.785776°, taken at 1230 hrs on 22NOV16)

Figure 5.69: Looking southeast along southwest wall of S39. Fill settled approximately 190 mm relative to pile-supported building at the northwest corner of the building (shown on lower left corner of photo), and magnitude of settlement decreased south-eastward along this wall. (S41.277994°, E174.785467°, taken on 17NOV16)

Figure 5.70: Looking southwest along northwest wall of S39. Fill settled 50-100 mm relative to pile-supported building. (S41.277882°, E174.785371°, taken on 17NOV16)

5.7.3.2 TC building

The TC building is immediately to the northwest of the S39 building, and is supported on driven RC piles. Liquefaction ejecta was observed along the short southwest wall of the building, and 150 mm of ground settlement relative to the building was measured (Figure 5.71).

Figure 5.71: Southwest wall of TC building with liquefaction ejecta and 150 mm of ground settlement relative to building. (S41.277858°, E174.785081°, taken at 1246 hrs on 22NOV16)

5.7.3.3 S37 building

The western half of the S37 building is founded on the deck of the buried, partially demolished pile-supported old Pipitea Wharf, and the east wall of the building is supported on piles. The precast seawall that formerly ran along the bulkhead of the Pipitea Wharf is now buried and runs south-to-north through about the centerline of the building. The ground floor slab not supported either on piles, the old wharf deck, or the precast seawall settled up to 550 mm relative to these structures (Figures 5.72, 5.74, and 5.75; from LiDAR scan). The ground settled approximately 375 mm relative to the building along the exterior of the east wall of the S37 building (Figure 5.76). Figure 5.74 plots elevations from transect LT6 (see Figure 5.27 for transect location) through the S37 Building, and Figure 5.75 provides a 3D view of the building interior from a LiDAR scan. Approximately 16 m west of the western wall of the S37 building, a buried row of piles from the old Pipitea Wharf protruded from the ground as the surrounding fill settled approximately 300 mm relative to the piles (Figure 5.77).

Figure 5.72: Looking west across inside of the S37 building. Approximately 400-550 mm of differential settlement between the ground and the buried precast concrete seawall that runs south-to-north through the center of the building. (S41.279065°, E174.785787°, taken at 1220 hrs on 21NOV16)

Figure 5.73: Looking west across north wall of Building S37. Approximately 400mm of differential settlement between ground and deck of buried, pile-supported Pipitea Wharf that supports the western side of the shed. (S41.278571°, E174.785632°, taken at 1227 hrs on 21NOV16)

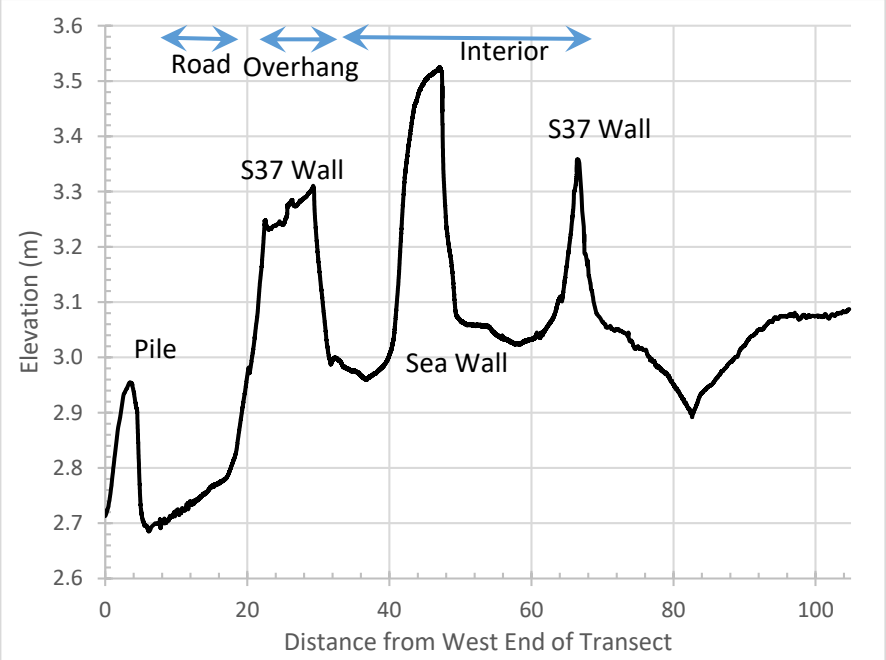

Figure 5.74: East-west cross-section (LT6) through the northern part of Building S37. Note the significant vertical exaggeration.

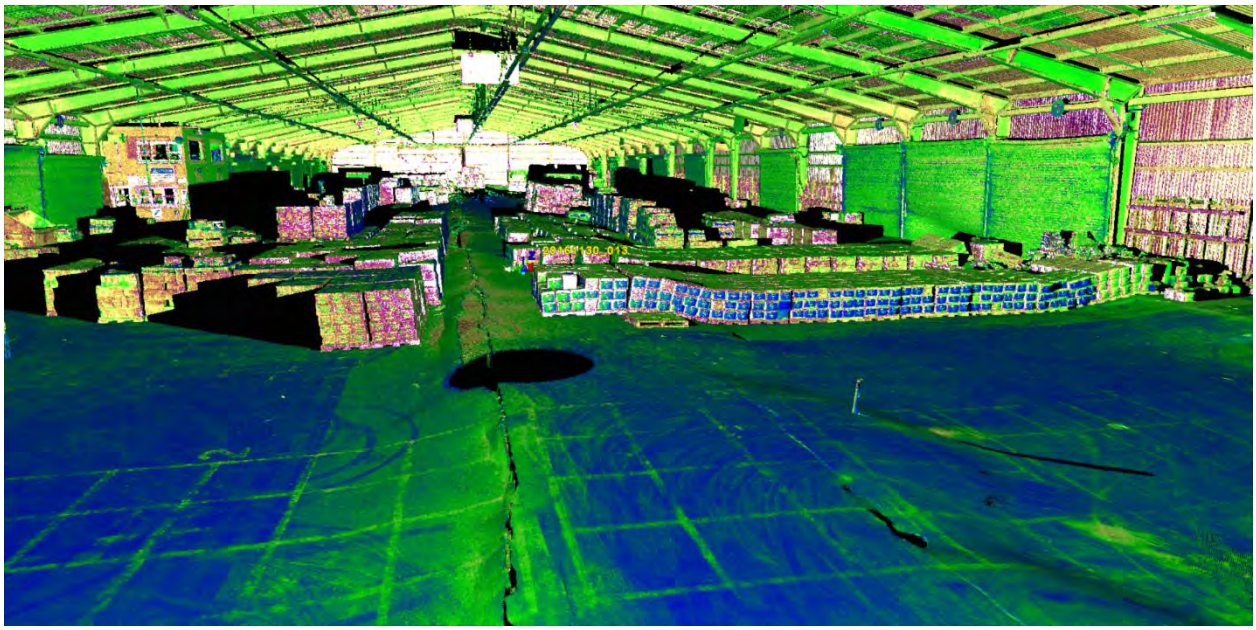

Figure 5.75: LiDAR scan obtained inside Building S37 showing cracking and settlement of the pavement around the buried precast concrete seawall (up to 550 mm of differential settlement occurred).

Figure 5.76: Looking south along east wall of Building S37, which shows approximately 375 mm of differential settlement between fill and pile-supported east wall of the building. (S41.279065°, E174.785787°, taken at 1220 hrs on 21NOV16)

Figure 5.77: Looking south along western-most row of piles from partially demolished and buried Pipitea Wharf, which is approximately 16 m west of Building S37. Fill settled 300 mm relative to embedded piles (S41.278798°, E174.785186°, taken on 17NOV16). A cross section (LT1) is shown in Figure 5.29.

5.7.3.4 S51 building

The S51 building is in the northeastern reclaimed land of CentrePort Wellington. This area of the port was reclaimed using hydraulically-placed dredged fill. The eastern wall of the building is founded on the pile-supported wharf, and the remainder of the building is founded on piles. The ground south of the building settled 230 mm relative to the wharf deck (Figure 5.78). Settlement magnitudes decreased from south to north, and only 10 to 20 mm of ground settlement was observed relative to the wharf in the surrounding ground north of the building. The wharf that supports the eastern wall moved laterally eastward approximately 85mm (35 mm crack at bulkhead and 50 mm crack 14.6 m west of bulkhead), which resulted in cracking of the southern wall near the wharf bulkhead (Figure 5.78). This equates to 85 mm of lateral movement over 14.6 m corresponding to a lateral strain of approximately 0.58 percent. Additionally, several vertical cracks were observed in the western exterior walls of the building (Figure 5.79).

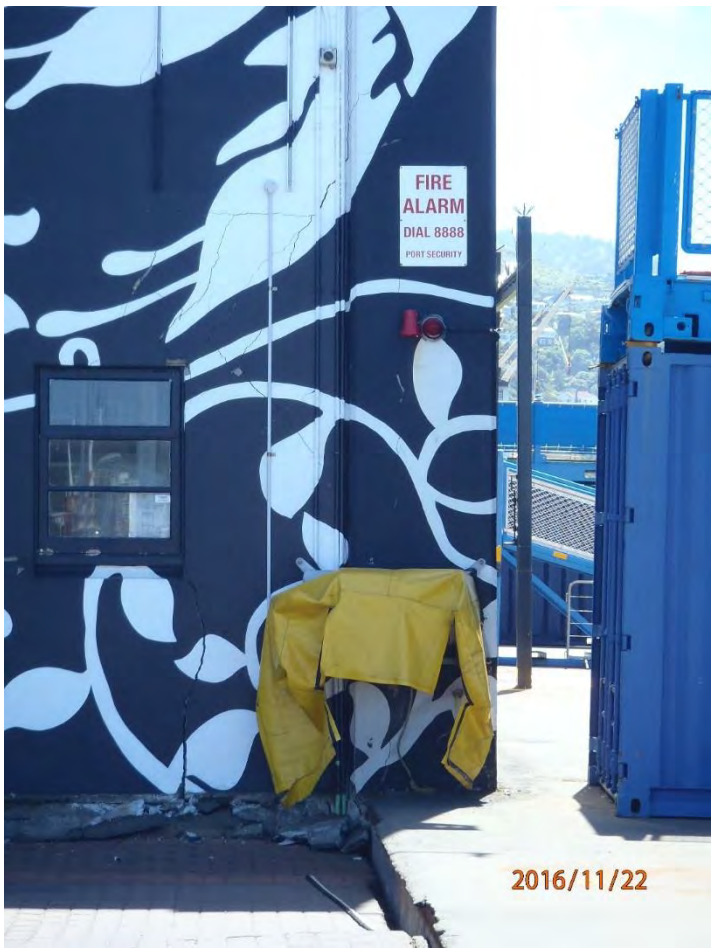

Figure 5.78: Southeast corner of Building S51 looking north, which shows 230 mm of differential settlement between wharf that supports its east wall and the inland fill. Also visible is 35 mm crack from seaward movement of wharf relative to adjacent ground. (S41.272404°, E174.787815°, taken at 1303 hrs on 22NOV16)

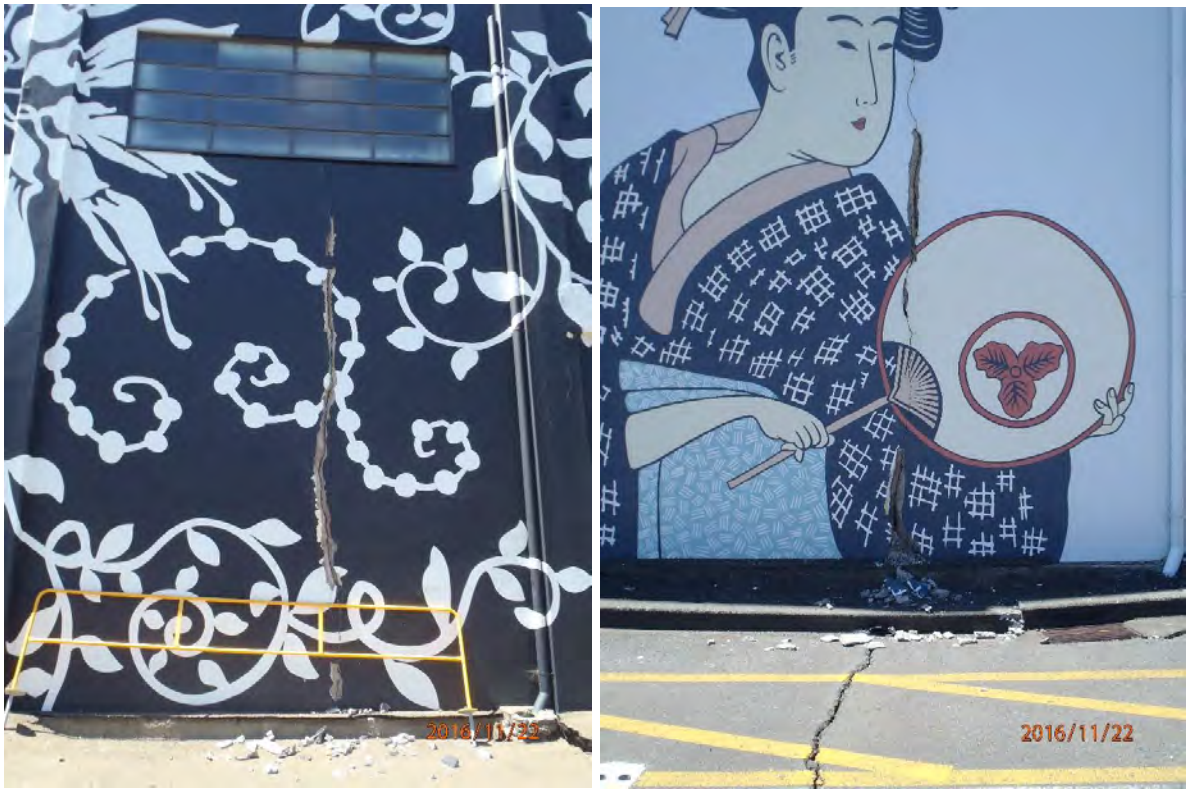

Figure 5.79: Vertical cracks along exterior west wall of S51 located at approximately 25 meters (left photo), and 60 meters (right photo) north of the southwest building corner. (Left: S41.272224°, E174.787391°, taken at 1316 hrs on 22NOV16. Right: S41.271906°, E174.787307°, taken at 1312 hrs on 22NOV16)

5.7.3.5 S building

The S building is a relatively new (i.e., constructed in 2006) 5-storey reinforced concrete building founded on piles. The corners are on driven reinforced concrete piles while the interior columns are founded on cast-in-place concrete piles. No ground improvement was performed under the building. The building suffered structural damage, and is being investigated thoroughly by CentrePort. The interested reader is referred to publications that will be forthcoming by others. No signs of foundation damage were visible at the ground surface during the QuakeCoRE-GEER team visit though some level of distress in the ground adjacent to the building was evident. The ground settled 100 to 200 mm relative to the pile-supported building (Figure 5.80), in a relatively uniform fashion though some deviations from this pattern were also evident. Ground floor infill walls along the perimeter of the building were cracked in places (Figure 5.81), and the Level 1 floor slab pulled out and partially collapsed (Figure 5.82).

Figure 5.80: Looking west at southeast corner of the S building at which fill settled approximately 100 to 200 mm relative to pile-supported building. (S41.278285°, E174.784757°, taken at 1243 hrs on 21NOV16)

Figure 5.81: Damage to ground floor infill wall on the east side of the S building (S41.278114°, E174.784715°, 1241 hrs on 21NOV16)

Figure 5.82: Pull-out and partial collapse of Level 1 floor slab in the S building taken along the west wall of the building. (S41.277982°, E174.784255°, taken at 1246 hrs on 21NOV16)

5.7.3.6 B Building

The B building is supported on piles with stone column ground improvement performed over the southeastern (seaward) half of the building footprint. The surrounding ground settled approximately 50 to 90 mm uniformly relative to the building (Figure 5.83). No other significant movements were observed.

(a) (b)

Figure 5.83: Ground settlement relative to the pile-supported B building at: (a) the southwest corner of the building with ground improvement (S41.279767°, E174.782100°), and (b) northwest corner of the building without ground improvement (S41.279419°, E174.781443°). (taken at 1350 hrs on 21NOV16)

CentrePort Wellington Acknowledgements

Special thanks for the collaboration provided by the CentrePort Ltd. especially for allowing access to our team and making special arrangements for our multiple visits. We would like to acknowledge the great support and collaboration from Stuart Palmer, Mike Jacka, and Sjoerd van Ballegooy, from Tonkin + Taylor, who as engineers for the CentrePort provided critical input and support in various phases of these efforts. Site access assistance through Hugh Cowan of the Earthquake Commission is sincerely appreciated. Use of results from aerial survey of Thorndon Reclamation and Wharf performed by Cardno is gratefully acknowledged.

The NZ team was principally supported by EQC Capability Grant at the University of Canterbury, and MBIE support provided for the 2016 Kaikoura Earthquake Reconnaissance. The US GEER team contributors were supported by the National Science Foundation (NSF) through the Geotechnical Engineering Program under Grants CMMI-1266418 and CMMI-1724866. Any opinions, findings, and conclusions or recommendations expressed in this material are those of the authors and do not necessarily reflect the views of the NSF. For more information visit the GEER website: www.geerassociation.org.

The NZ-US QuakeCoRE-GEER team performed on-site reconnaissance on November 17, 20, 21, 22, 23 and 30, and December 1 and 2, 2016. Profs. Misko Cubrinovski, University of Canterbury, and Jonathan Bray, University of California, Berkeley, led these QuakeCoRE-GEER efforts and participated in the inspections on multiple occasions. Christopher de la Torre (UC) contributed to most of these inspections and compilation of the gathered data. Prof. Brendon Bradley (UC), Dr. Gabriele Chiaro (UC) and Dr. Liam Wotherspoon (UA) also were members of the early reconnaissance teams. All LiDAR scanning at CentrePort was performed and processed by Prof. Michael Olsen, a U.S. GEER team member from Oregon State University, with his student, Matthew O'Banion. Leica Geosystems, David Evans and Associates, and Maptek I-Site provided equipment and/or software utilized in this study. Particle-size analyses on the ejected soils were performed in the Geotechnical Laboratory of the University of Canterbury.

References

Anderson, G. (1984). *Fresh about the Cook Strait – An appreciation of Wellington Harbour*. Methuen Publications, p.215.

Boulanger, R.W. and Idriss, I.M. (2012). Probabilistic Standard Penetration Test-Based Liquefaction-Triggering Procedure. *J. of Geotech. Geoenviron. Eng*., 138, 1185-1195

Boulanger, R.W. and Idriss, I.M. (2014). CPT and SPT Based Liquefaction Triggering Procedures. Report No. UCD/CGM-14/01, Center for Geotechical Modeling, Department of Civil and Environmental Engineering, University of California, Davis, April 2014.

Bradley, B. A., H. N. T. Razafindrakoto, and V. Polak (2017). Ground motion observations from the 14 November 2016 Mw7.8 Kaikoura, New Zealand earthquake and insights from broadband simulations, Seismological Research Letters, 88(3): 740-756.

Hutchison, A. J. H. (1973). Reclamations in Wellington Harbour with special reference to recent developments. New Zealand Engineering. 15 August 1973, 217-224.

Idriss, I.M., and Boulanger, R.W. (2008) Soil Liquefaction during Earthquakes. Earthquake Engineering Research Institute, Monograph-12, Oakland, California, USA.

Olsen, M.J., & Kayen, R. (2012). "Post-earthquake and tsunami 3D laser scanning forensic investigations," ASCE Forensics Conference 2012, San Francisco, California. CD-ROM.

Olsen, M.J., Wartman, J., McAlister, M.*, Mahmoudabadhi, H.*, O'Banion, M.S.*, Dunham, L., and Cunningham, K., (2015). "To fill or not to fill: Sensitivity analysis of the influence of resolution and hole filling on point cloud surface modeling and individual rockfall event detection." Remote Sensing, Special Issue- Use of LiDAR and 3D point clouds in geohazards, 79(9),12103-12134. doi:10.3390/rs70912103

Semmens, S., Dellow, G. D., and Perrin, N.D. (2010). It's Our Fault – Geological and Geotechnical Characterisation of the Wellington Central Business District. *GNS Science Consultancy Report* 2010/176. 52p.

Tonkin & Taylor Ltd. (1998). Proposed Coldstore Geotechnical Report. Prepared for CentrePort Limited. Ref No. 82363.

Tonkin & Taylor Ltd. (2000). CentrePort Shed R Geotechnical Report. Prepared for CentrePort Limited. Ref No. 82787-01.

Tonkin & Taylor Ltd. (2006). Harbour Quays Development Factual Geotechnical Report, Revision 2. Prepared for CentrePort Wellington Limited. Ref No. 83725.004

Tonkin & Taylor Ltd. (2012). Thorndon Container Wharf Seismic Assessment Geotechnical Factual Report. Prepared for CentrePort Limited. Ref No. 85369.001.

Tonkin & Taylor Ltd. (2014). Thorndon Container Wharf Seismic Assessment Geotechnical Interpretive Report. Prepared for CentrePort Limited. Ref No. 85369.001.

6 GEOTECHNICAL EFFECTS ON SOUTH ISLAND BRIDGES AND INFRASTRUCTURE

The transportation network in the northeast part of the South Island was significantly affected by ground shaking and ground deformation due to the Kaikoura event. The Hurunui, Marlborough, and Kaikoura council districts are located in this affected zone and were the focus of post-earthquake reconnaissance efforts. There are 268 state highway bridge structures (primarily reinforced concrete) and 636 local road bridge structures within these three districts (Palermo et al., 2017). Many of these were only minimally affected by the earthquake or not affected at all, however, moderate to significant damage was observed. The key bridges of interest within each district are discussed in detail in subsequent sections.

6.1 Hurunui District

Reconnaissance efforts in the Hurunui District of North Canterbury were primarily centred around Waiau and the surrounding towns, bridges, and roads. Figure 6.1 shows an overview of the surveyed area in the Hurunui District, indicating the bridges and other infrastructure sites that were visited. A total of 15 bridges were surveyed in this district, including 10 highway bridges and 5 rural road bridges. Of these, 6 were found to have no damage or only minor indications of damage. These sites are indicated using green markers in Figure 6.1. The observations made at key sites in this district are summarised individually below.

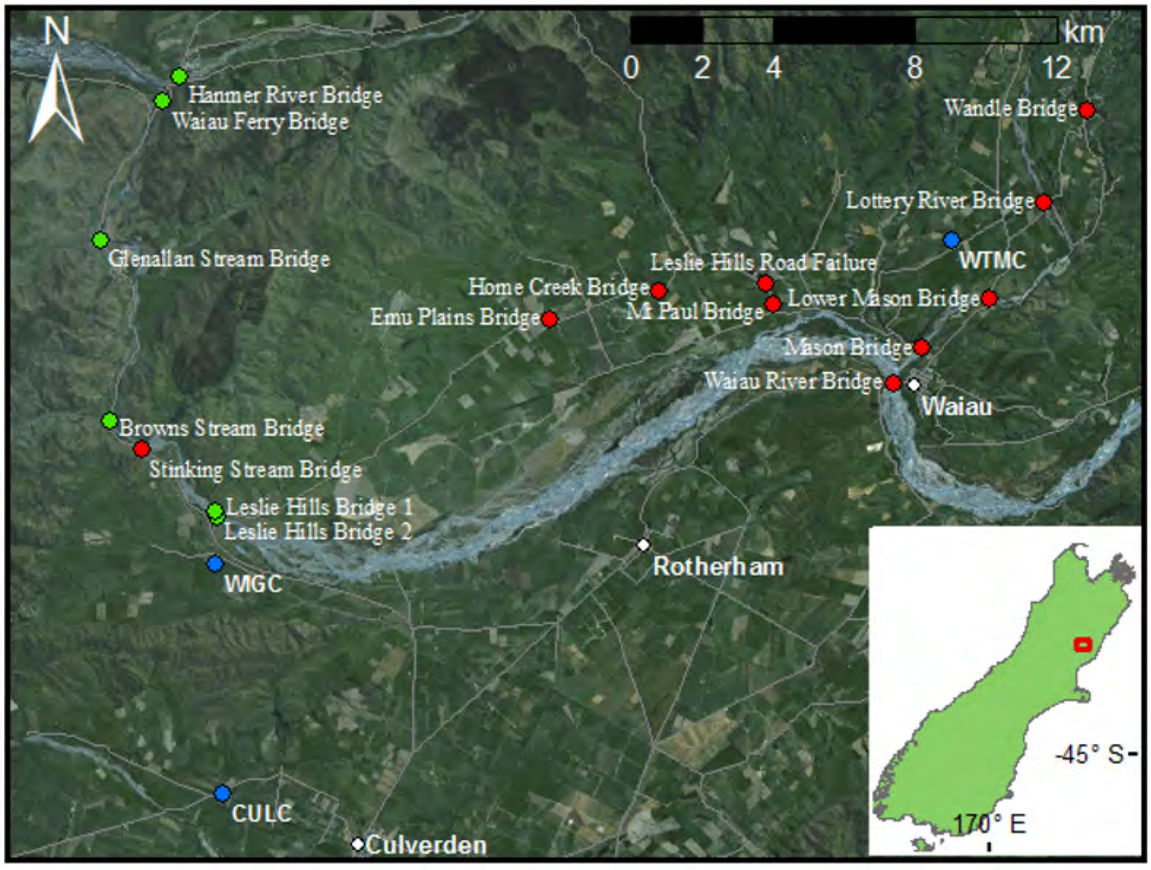

Figure 6.1: Bridge sites surveyed in the Hurunui District. Green markers indicate bridges with minor or no damage observations. Red markers indicate sites with moderate to severe damage observations. Blue markers indicate strong motion stations.

6.1.1 Waiau River Bridge [-42.6555, 173.0334]

The Waiau River Bridge is a simply-supported, precast reinforced concrete beam bridge built in 1965. The superstructure of the bridge is comprised of 33 spans with five I-beams across each of the 17 m long spans. The superstructure is supported by seat abutments and 32 wall piers. The piers are typically 4 m wide, but 7.25 m wide at the passing bays. The deck sits on 12-mm thick neoprene strip bearings at each support and is transversely restrained by dowels that secure the end diaphragms of the deck at the piers and abutments (Palermo et al., 2017). The overall structural damage to the Waiau River Bridge was moderate, and the bridge was passable with speed restrictions during the survey period of 17-18 November 2016. Gravel fill was added to the approaches on both ends of the bridge to account for the settlement and allow vehicles to smoothly pass over the bridge.

Figure 6.2 shows a general layout of the western approach to the Waiau Bridge. The abutment is located where the green polygon is placed, and the bridge deck is elevated over the river bank for about 100 m before encountering the river proper. The river was running higher than depicted in the photo, but the edge of the water was in about the same location. Clear evidence of liquefaction and lateral spreading was observed at this site, with corresponding damage to the approach embankment and bridge abutment. There was settlement of the approach embankment relative to the bridge deck, and there were cracks parallel to the roadway in the embankment crest and along sides of the road as shown in Figure 6.3 and Figure 6.4. The lateral cracks were approximately 4-5 cm wide and up to 10-12 cm wide in places. It is likely that the gravel spread over the roadway obscured further cracking and the damage in the embankment.

Figure 6.2: Site layout for western approach to Waiau River Bridge [-42.65555, 173.0302].

The magnitude of the settlement and outward movement at the western abutment was indicated by the relative movement of the various structural members. As shown in Figure 6.4(b), a concrete wingwall on the south side of the abutment (with the person standing on it) moved outwards by 10-20 cm and settled relative to the abutment wall by about 40-50 cm (pre-earthquake photos indicate that all of the concrete bodies on this side of the approach were originally flush and level). The outward movement was greater further away from the abutment (i.e., 10 cm at the abutment wall, 20 cm further back). Similar settlement of 40-50 cm was observed at the abutment wall on the north side (not shown here). The construction detailing is different on the north side, so there was not a direct way to measure the outward movement, but the outward deformation appeared to be similar in magnitude.

Figure 6.3: Lateral cracking on road side in western approach embankment of Waiau River Bridge. Photos taken looking east towards bridge [-42.6556, 173.0294]: (a) North side; (b) South side.

Figure 6.4: South side of western approach embankment to Waiau River Bridge [-42.6556, 173.03]: (a) Lateral cracks in embankment side; (b) Settlement and outward movement at abutment wall.

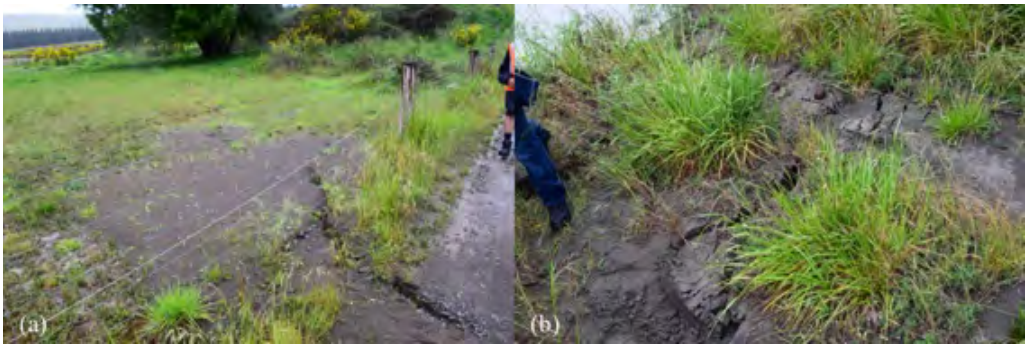

Figure 6.5: Surficial evidence of liquefaction at western approach to Waiau River Bridge: (a) Ejecta and cracking adjacent to southern toe of approach embankment [-42.6558, 173.0297]; (b) Lateral spreading cracks near river bank [-42.6556, 173.0312].

Sediment ejecta were observed on the near the toe of the southern side of the embankment (in the approximate vicinity of the blue polygon shown in Figure 6.2). The ejected material was spread over an approximately 5 m diameter area as shown in Figure 6.5(a). The particle size distribution for this ejecta material (as well as samples recovered from other bridge sites in the Hurunui district) is provided in Figure 6.6. Lateral spreading cracks parallel to river were also observed closer to the river bank, with a representative example shown in Figure 6.5(b). Ejected material was also observed in the vicinity of these cracks, but with a lesser volume of material than was found at the toe of the approach embankment. The observed lateral spreading cracks were relatively minor, with widths typically less than 5 cm. The cumulative deformation of the river bank indicated by the cracks was also relatively minor, on the order of 20-30 cm.

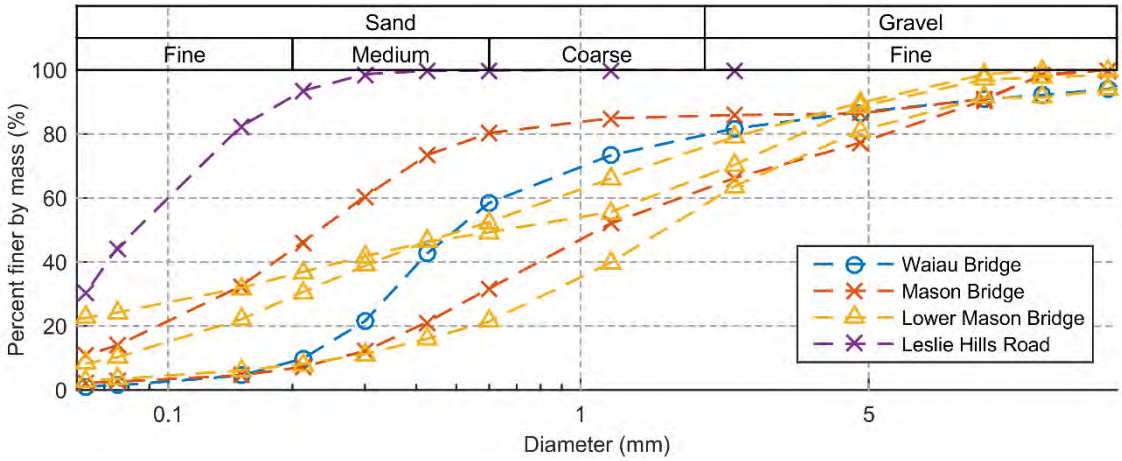

Figure 6.6: Particle size distributions of ejecta samples recovered at bridge sties in the Hurunui district

Structural damage indicative of liquefaction and lateral soil deformation was also observed. The riverward face of the western abutment wall had significant cracks and had potentially undergone some back rotation (i.e., lower portion moved closer to river than top portion). The cracking is indicated in Figure 6.7(a), where it appears that a chunk of the concrete has completely broken free from the main body of the wall. The soil subsidence on the abutment side is also visible in Figure 6.7(a) as the difference between the current ground surface and the markings on the abutment wall and through the exposure of the underside of the abutment.

Further deformation was observed at the bridge piers, most significantly in the form of differential settlement and twisting of the second pier from the western abutment, resulting in the rotation of the bridge deck shown in Figure 6.7(b). The settlement was larger on the north side of the pier, resulting in the dip in the roadway shown in Figure 6.7(b). The evidence of twisting was further indicated by the expansion gap in the bridge deck above this pier, which had widened on the south side, and had been compressed on the north side. This settlement may be liquefaction-related, but no ejected material was observed near the second pier. Most of the bridge piers showed cracks at the interface with the pile caps with some minor spalling of cover concrete, with a representative example shown in Figure 6.8(a). At some of the piers near the waterway, this damage mode was more severe, with longitudinal bar exposure and buckling as shown in Figure 6.8(b). It is likely that this damage at the base of the wall piers is due primarily to inertial loads during strong shaking.

Figure 6.7: Structural damage at western approach area to Waiau River Bridge [-42.6556, 173.0302]: (a) Severe cracking in the abutment wall (looking west from under the bridge deck); (b) Differential settlement at second pier (looking east).

Figure 6.8: Structural damage to base of piers for Waiau River Bridge [-42.6553, 173.0351]: (a) Cracking at pile cap interface; (b) Exposure and buckling of longitudinal bars.

The surveyed area and some features of interest at the eastern approach of the Waiau Bridge are shown in Figure 6.9. The damage at this approach was nominally similar to that observed at the western side. There was clear evidence of liquefaction and lateral spreading, as well as lateral cracking, settlement, and outward deformation of the approach embankment relative to the abutment wall. As with the western approach, gravel was added to the roadway to accommodate the settlement of the approach.

Figure 6.9: Site layout eastern approach to Waiau River Bridge [-42.6552, 173.037].

Representative photos of the liquefaction ejecta observed near the eastern approach are shown in Figure 6.10. There were various smaller sand boils, such as that shown in Figure 6.10(a), in the paddock north of the bridge (gold polygon in Figure 6.9). Samples could not be obtained without jumping a fence and entering the paddock, but the ejected material appeared to be visually similar to the material collected on the western side. Lateral spreading cracks were also observed on the eastern river bank, with some representative examples shown in Figure 6.11. As shown, the cracks are relatively minor. Based on observations from the bridge deck, it is possible that some of the piers have moved slightly, the cracked area could not be accessed to obtain a direct measurement. A cumulative deformation of perhaps 20 cm across the river bank was indicated by the cracks based on the deck-based survey.

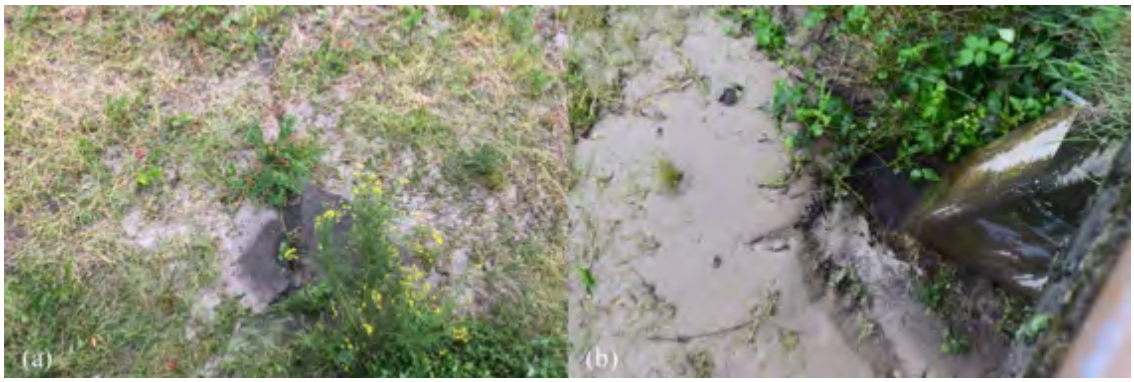

Figure 6.10: Liquefaction ejecta near the eastern approach to Waiau River Bridge [-42.6552, 173.037]: (a) Ejecta in paddock on north side of bridge; (b) Ejecta directly adjacent to bridge pier on south side.

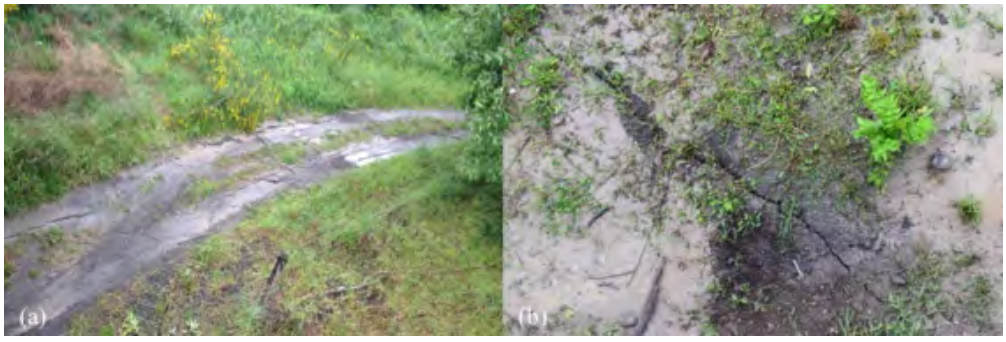

Figure 6.11: Lateral spreading cracks with ejecta near the eastern approach to Waiau River Bridge [-42.65525, 173.036].

Figure 6.12: Lateral cracking on both sides of roadway in eastern approach embankment to Waiau River Bridge [-42.6551, 173.0380]: (a) Northern side (looking east away from bridge); (b) Southern side (looking east).

Figure 6.13: Settlement and outward movement at north side of eastern abutment to Waiau River Bridge as indicated by offset of concrete members [-42.6552, 173.037].

Representative photos of the cracks parallel to the roadway observed in the eastern approach embankment are shown in Figure 6.12 These cracks essentially extend over the full 40-50 m length of the embankment and are up to 10 cm wide. There were additional lateral cracks on the outside of the guard rails of similar scope, as well as a few minor 1-2 cm wide cracks in the roadway itself (not shown here).

As with the western side, the settlement and outward movement of the eastern approach embankment relative to the abutment wall is well indicated by the relative movement of structural members as shown in Figure 6.13. The settlement on the northern side (that shown in Figure 6.13) was 18-20 cm, with larger settlement with increasing distance from the centre of the road. The relative lateral movement of the concrete members shown indicates 10 cm of outward deformation in the approach. The settlement and outward movement on the south side of the road were similar in form to that shown for the north side, but slightly lesser in magnitude, with about 14-16 cm of settlement and 5-6 cm of outward movement indicated by the relative movement of the various concrete members. The outward movement of the embankment is greater further back from the abutment, as the lateral cracks in the embankment (e.g., Figure 6.12) indicate at least 20 cm of outward deformation. Unlike the western side, no significant damage was observed in the eastern abutment wall; however, evidence of subsidence in the fill in front of the abutment was observed, with some pile exposure below the abutment wall.

6.1.2 Mason Bridge [-42.6469, 173.0431]

The Mason Bridge is a 197 m long, 3.73 m wide reinforced concrete bridge built in the 1980s to span the Mason River on River Road. The deck is supported on 16-18 m long precast double hollow core units supported on single column bents with hammerhead pier caps over 12 spans. The lateral load resisting system at this bridge consists of transverse shear keys at the abutments and internal shear keys at all of the piers (Palermo et al., 2017). Figure 6.14 shows a general layout of the surveyed site at the Mason Bridge, indicating the locations of some of the geotechnical features of interest described in the following discussion.

Figure 6.14: Surveyed area and features of interest for Mason Bridge [-42.6469, 173.0431].

Cracks were present in the western approach embankment parallel to roadway as shown in Figure 6.15, indicating outward spreading of the embankment. The cracks were about 5-10 cm wide and there were more on the southern side than on the northern side. No surficial evidence of liquefaction was observed near the western approach, and it is not clear if this damage is liquefaction-related. The settlement and relative movement at the western abutment was minor, with evidence suggesting a maximum of 2 cm of relative movement between the abutment and deck. No cracks or ground deformation occurred in the fill in front of the abutment as would be expected for significant abutment movement.

Figure 6.15: Cracks along edges of the western approach embankment for Mason Bridge (looking east towards bridge) [-42.6464, 173.04196]: (a) North side; (b) South side – inset shows close-up of cracks as indicated.

The southern edge of the roadway on the eastern approach to the Mason Bridge was cracked parallel to the road axis. Smaller cracks were observed on the northern side of the eastern approach, with a representative example shown in Figure 6.16(b). A power pole located at the crest of a second embankment directly adjacent to the approach is askew and has clearly moved towards the bridge and towards the river as shown in Figure 6.16(a). The power lines were pulled out of alignment, and there was more movement at the base of the pole than at the top (back rotation). The settlement of the embankment at the abutment wall was very minor, and only minor cracks were apparent in the approach roadway. No evidence of surficial liquefaction was visible on either side of the eastern approach embankment, though ejected material was found on the eastern river banks near the approach.

All of the piers for the Mason Bridge had significant damage at the connection to the footings, indicative of plastic hinging during shaking. Figure 6.17 shows some of the worst examples. In some cases, only the cover concrete was involved, while in others, the spiral reinforcement was exposed. On the piers shown in Figure 6.17, the longitudinal reinforcement is exposed and has buckled. The significance of the plastic hinging damage increased towards the centre of the bridge. Near the abutments, the spalling was concentrated towards the longitudinal direction. Near the centre, the spalling damage was concentrated on the on the southern side of the piers, indicative of strong shaking perpendicular to the main axis of the bridge. It is not clear if the piers have undergone permanent deformation due to soil failure, as only small (2-3 cm) gaps were observed between some of the footings and surrounding soil.

Figure 6.16: Northern side of eastern approach to Mason Bridge (looking west) [-42.6475, 173.04465]: (a) Power pole has moved down the slope of an embankment directly adjacent to bridge approach embankment; (b) Cracks parallel to roadway in embankment fill.

Figure 6.17: Severe examples of plastic hinging at base of Mason Bridge piers (looking north) [-42.6469, 173.0432].

Figure 6.18: Ejecta near bridge piers and footings at Mason Bridge [-42.647, 173.043]: (a) Looking east; (b) Looking north; (c) Looking west; (d) Looking north.

Liquefaction ejecta was present at nearly all of the piers on the eastern river bank, with larger volumes of ejected material for the piers closer to the river. Some characteristic examples are shown in Figure 6.18. A sample was obtained from the ejecta surrounding the fourth pier from the western abutment, and the particle size distribution is presented in Figure 6.6. Ejecta was also prevalent all over the eastern river bank, with particularly large volumes of ejected material where there was no vegetation and smaller volumes in the grassy areas. The ejecta typically had a tan-brownish film of silty fines on top, then a greyish coarser sand below this, grading coarser with depth. The ejecta on the river bank was quite weathered by the survey date of 17-18 November 2016.

6.1.3 Lower Mason Bridge [-42.6343, 173.0664]

The Lower Mason Bridge is a single-lane, 8-span reinforced concrete bridge, supported by 7 single-column piers located on Inland Road north of Waiau. The general layout of this bridge site is shown in Figure 6.19. The bridge is about 165 m long from abutment to abutment (each span is 20.7 m long based on measurements taken on the deck). The deck is supported by two 150 cm tall concrete I-girders that sit about 3 m apart centre-to-centre. The bridge girders are simply-supported and seated on elastomeric bearing pads at both abutments and at all internal piers. Transverse shear keys are present at all piers excepting the central pier, however, there is a gap built-in between the deck girders and the shear keys such that there is a degree of seismic isolation for transverse shaking (Palermo et al., 2017). No shear keys are present at the abutments. Expansion joints are located at the centre of the bridge and at either abutment, and the embankment slopes on all four sides were roughly 2:1 (horizontal to vertical).

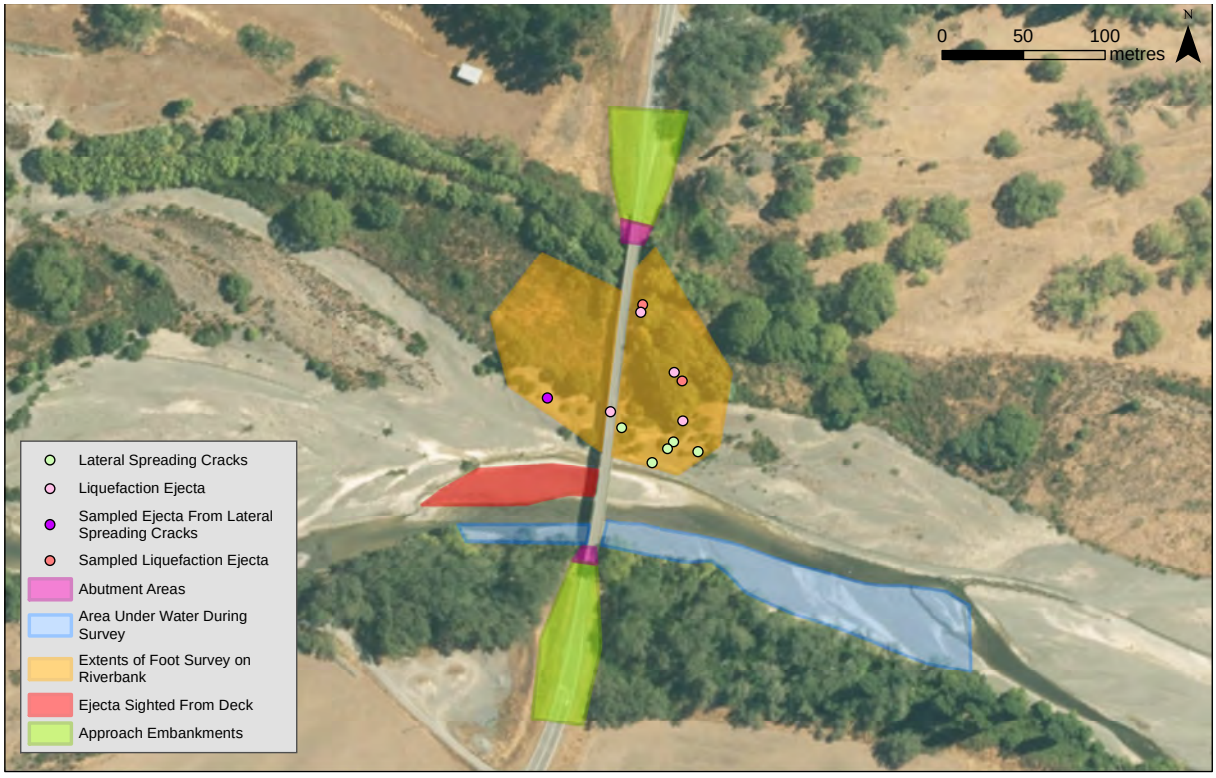

Figure 6.19: Overview of Lower Mason Bridge site indicating areas surveyed and some key features of interest [-42.6343, 173.0664].

Cracking, settlement, and outward movement (i.e. away from longitudinal bridge axis) were observed in both the southern and northern approach embankments. Some representative cracking on the roadway is shown in Figure 6.20, and some representative cracking on the embankment sides is shown in Figure 6.21. The cracks in the roadway were concentrated at the edges of the pavement, but there were a few more centrally located as well as a few sporadic transverse cracks oriented perpendicular to the axis of the road. The cracks in the roadway were generally fairly narrow in width, with most about 3-4 cm wide, but there were areas with cracks up to 30 cm wide.

Figure 6.20: Cracking in approach roadways at Lower Mason Bridge: (a) Western side of south approach looking north [-42.6353, 173.0662]; (b) Eastern side of south approach looking north [-42.6353, 173.0662]; (c) North approach looking northwest across road [-42.6330, 173.0666].

At the southern approach, the cracks adjacent to the roadway extended back about 41 m from the abutment on the east side and 28 m on the west side. At the northern approach, the lateral cracking on the road side extended back about 33 m and 20 m on the west and east sides, respectively. There may have been more cracks in the centre of the roadway, but the gravel

placed on the roadway for both approaches to accommodate the settlement likely obscured some deformation features. The gravel on the south approach extended back about 73 m from the abutment, though not over the full width of the road past about 30 m. On the north side, the gravel extended back about 15 m from the abutment wall over the full width of the road.

Figure 6.21: Cracking in sides of approach embankments at Lower Mason Bridge. (a) West side of south approach looking north [-42.6353, 173.0662]; (b) East side of south approach looking north [-42.6353, 173.0662]; (c) and (d) West side of north approach looking north and south, respectively [-42.6330, 173.0666].

The cracks in the sides of the embankments generally extended over lesser lengths than those in the roadway, and were more severe on the western sides of both approach embankments. The cracks in the western side of the southern approach embankment were about 26 m long, extending back from the outside corner of the abutment wall, and up to 30 cm wide. On the western side of the northern approach embankment, the zone of cracking was not one continuous crack, but instead a series of discrete cracks. These were about 5 cm in width, and individually about 5 m long. On the east side of the northern approach, some rip-rap material had evidently moved out perpendicular to the road axis by at least 10 cm. The cracks in at the edge of the roadway and in the sides of the embankments indicate up to about 40 cm of cumulative outward deformation of the embankment fill in both directions.

The guard rails and posts in both approach embankments were damaged as indicated in Figure 6.20(c), This damage was most likely primarily due to shaking, and the damage at the northern approach was more severe than at the southern approach. The posts have been pulled out of the ground and sheared in pieces in some places, and cracks in the soil propagate out way from most of the posts.

Figure 6.22: Settlement and outward movement at west side of north abutment to Lower Mason Bridge [-42.6334, 173.0666]: (a) Edge of abutment wall looking east; (b) Abutment wall looking north; (c) Edge of abutment wall looking north; (d) Embankment side of abutment wall near deck connection looking south.

The settlement and outward deformation of the embankment soils was clearly evident at the abutment walls, as there were marks on the abutment walls indicating the original position of the soil as shown in Figure 6.22. Though the western side of the northern abutment is shown here, the photos are typical of all four sides; however, a trench for a replacement water line dug at the western side of the southern approach embankment obscured the position of the settled native soils. Settlements on the bridge side of the abutment walls were on the order of 50-60 cm at both abutments. On the approach side of the north abutment (see Figure 6.22(d)), the settlements are approximately 35 cm, though there is newly-placed gravel fill obscuring the full extents of the settlement here. The outward bulging of the soil at the abutments was approximately 10-15 cm on the three sides where it could be measured (all except western side of the south abutment where utilities work erased evidence), with a typical example shown in Figure 6.22(c). This is less than is suggested by the cracks in the roadway and embankment sides, but not excessively.

Figure 6.23: Cracking and gapping in fill below bridge deck at northern abutment to Lower Mason Bridge indicating riverward movement of the fill [-42.6334, 173.0666]: (a) Looking north; (b) 60 cm gap between wall and fill.

Figure 6.24: Damage to abutment-deck connection at Lower Mason Bridge due to relative movement of abutment wall and deck. The breakaway member to the left was pushed back away from the deck and rotated 180° such that the connection point for the expansion joint faces away from the deck [-42.6334, 173.0666].

The soil and fill on the bridge side of the abutments (beneath the bridge deck) also display damage indicators consistent with riverward movement. Figure 6.23 shows some representative cracking in this fill material as well as the approximately 60 cm gap that has been formed by the fill soils moving away from the abutment wall. The cracks in this area on both sides of the bridge were up to 20 cm in width, and indicated a cumulative deformation of at least 1 m. It was also evident that the rip-rap (visible in the lower left corner of Figure 6.23) had undergone riverward deformation at both abutments. There were newly exposed areas where rocks had moved away from each other or from the soil. It is unclear whether or not this movement is due solely to shaking, due solely to lateral spreading, or to some combination of the two.

Some of the structural damage at the bridge is further indicative of the deformations that have occurred at the site. Figure 6.24 shows the northern abutment-to-deck connection. The breakaway concrete member indicated has been pushed back away from the bridge and flipped over such that the metal and rubber material that formed the expansion joint is now on the abutment side. This type of damage to the breakaway member was found at both abutments, and in both cases the distance between the abutment wall and deck was less than as designed. Further evidence of the riverward movement of the abutments at each side is found by the buckled guard rails at the central expansion joint connecting the two main spans of the bridge as shown in Figure 6.25. It is likely that shaking-related deformation accounts for some of this, but the deck spans are at least 10 cm closer together than normal at the centre of the bridge.

Figure 6.25: Buckling of guard rails at centre expansion joint of Lower Mason Bridge indicating that the two main deck sections have undergone permanent inward deformation. Photo facing south [-42.6343, 173.0664].

Figure 6.26: Cracks in northern river bank on eastern side of bridge. Photo taken from bridge deck. Riverward direction is down for this orientation [-42.6342, 173.0665].

Liquefaction ejecta and lateral spreading cracks were observed throughout the northern river bank area near the bridge as indicated in Figure 6.19. These features were observed both from the bridge deck and via a foot survey of the riverbank area. Figure 6.26 shows some of the

lateral spreading cracks visible on the eastern side of the bridge, and Figure 6.27 shows some of liquefaction ejecta visible from the bridge deck located in some small islands in the middle of the main flow of the river. The remaining evidence of liquefaction and lateral spreading was only visible when down on the northern river bank around and below the bridge. Some representative examples of the cracking and sediment ejecta found in this area are shown in Figure 6.28, while particle size distributions are shown in Figure 6.6. The sediment ejecta features are mostly less than 1 m in diameter, though there are some larger more spread out areas of ejecta. Based on the lateral spreading cracks observed, the magnitude of cumulative deformation in the soil was at least 50-80 cm.

Figure 6.27: Liquefaction ejecta on west side of bridge (looking west). [-42.6345, 173.0657].

Figure 6.28: Representative photos of the lateral spreading cracking and liquefaction ejecta observed on the Northern river bank near the bridge in the areas indicated by Figure 6.19.

In addition to the permanent deformation of the bridge embankments, abutment walls, and bridge decks likely due to the evident liquefaction and lateral spreading at this site, the structural damage of Figure 6.29 indicates that shaking-related damage was a major factor in the response of this bridge. Damage consistent with plastic hinge formation was observed at

the base of all the bridge piers aside from the central pier; some typical examples are shown in Figure 6.29(a) and (b). These hinge zones displayed extensive cover spalling and a significant number of buckled and fractured bars. Further shaking damage is shown in Figure 6.29(c) and (d), with a closer view of the guardrail buckling at mid-span. The girders have also become unseated from the bearing pads at both abutments. Figure 6.29(d) shows this at the western side of the south abutment. On the eastern side of the south abutment, the girder is still atop the bearing pad, but only half of the pad is below the girder. At the north abutment (not shown here), the eastern girder is unseated and the bearing pad for the western girder is askew.

Figure 6.29: Structural damage at Lower Mason Bridge [-42.6343, 173.0664]. (a) Damage at base of piers looking south; (b) Base of southern-most pier looking north; (c) Deformation at central expansion joint looking southeast; (d) Girder unseated from bearing pad.

6.1.4 Wandle Bridge [-42.5864, 173.1003]

Wandle Bridge is a 35 m long, 3 span, precast concrete bridge spanning a portion of the Mason River on Inland Road. The Wandle Bridge had to be closed due to the severe structural damage shown in Figure 6.30, and a bailey bridge was put in place to allow vehicles to cross the river. Significant plastic hinging occurred at the base of the bridge piers, which are no longer standing vertically, significant diaphragm damage occurred in the bridge deck, and the bridge is only marginally stable. This structural damage is almost certainly shaking-related and the spalling associated with the hinging is located on the eastern side of the piers. The

geotechnical damage at this site was minor. A series of cracks were observed near the river adjacent to the toe of the southern approach embankment. These cracks are only a few centimetres wide. No surficial evidence of liquefaction was observed.

Figure 6.30: Structural damage to Wandle Bridge [-42.5864, 173.1003]: (a) South approach from under bridge; (b) Plastic hinging on pier near south approach; (c) Deck at southern end; (d) South abutment; (e) North approach from under bridge; (f) Minor hinging on pier near north abutment.

6.1.5 Lottery River Bridge [-42.6097, 173.0854]

The Lottery River Bridge is a single-lane, 6-span reinforced concrete bridge supported by single-column piers located on Inland Road about 3.5 km north from the Lower Mason Bridge. The structural design of this bridge is nominally identical to the Lower Mason Bridge, just adapted for a shorter overall span (Palermo et al., 2017). Figure 6.31(a) shows the transverse shear key at one of the interior piers and the lack of a shear key at the central pier. The observed structural damage at the Lottery River Bridge was similar in nature to the

Lower Mason Bridge, with compression failure of the expansion joint over the central pier, residual displacements and unseating over some of the elastomeric bearing pads, and uneven residual spacing of the expansion joints. The base of the piers at the Lottery River Bridge also displayed damage consistent with full plastic hinge formation, with a typical example shown in Figure 6.31(b).

Figure 6.31: Lottery River Bridge [-42.6097, 173.0854]: (a) General layout; (b) Plastic hinge damage at base of pier.

Settlement and transverse deformation of the approaches was observed at both abutments, with a similar scope to that detailed for the Lower Mason Bridge. Approximately 40 cm of settlement was observed in the fill ahead of both abutments. Figure 6.32(a) shows the northeast approach, but any cracks are obscured by the gravel fill used to accommodate the settlement. There was residual relative displacement between the deck and abutments on both sides of the bridge, with the deck moving north relative to the abutments on both sides. Figure 6.32(b) shows the residual transverse displacement at the northeast side, and Figure 6.32(c) shows the residual longitudinal displacement at the southwest abutment, as well as the residual movement of the bearing pad for this beam.

Figure 6.32: Damage at Lottery River Bridge [-42.6097, 173.0854]: (a) Gravel in-fill due to settlement and guardrail damage at northeast approach looking northeast; (b) Residual transverse offset of deck and abutment at northeast abutment looking southwest; (c) Residual displacement of bearing pad at southwest abutment looking west.

6.1.6 Stinking Stream Bridge [-42.6724, 172.7748]

Visual surveys along Highway 7 between Culverden and the turn-off for Hanmer Springs indicated two primary areas of interest. The locations of these sites are shown in Figure 6.33(a) with close-up site layouts provided in Figure 6.33(b) and (c). Their location relative to the wider survey area is shown in Figure 6.1. The Stinking Stream Bridge is a 12.2 m long, 7.3 m wide single-span, two-lane bridge that was surveyed by two reconnaissance teams, first on 14 November and then again on 17 November 2016.

Figure 6.33: Highway 7 area: (a) Site locations for areas of interest; (b) Road crack site layout [-42.6310, 172.7718]; (c) Stinking Stream Bridge site layout [-42.6724, 172.7748].

There were roadway settlements at the abutments of about 5-10 cm, with corresponding transverse cracks as shown in Figure 6.34. There were also longitudinal cracks in the roadway indicative of outward movement of the approach soils. The magnitude of the outward movement and settlement increased with distance away from the road centreline. At the northern corner, the settlement appeared to be about 20-40 cm as shown in Figure 6.35(d), while at the other corners the settlement is less (about 5-10 cm). Longitudinal cracking was also present in the soils adjacent to the road way at the east, north, and west corners of the bridge as shown in Figure 6.34(d), Figure 6.35(b), and Figure 6.36(d), respectively. These cracks have a maximum width of about 5 cm. The rip-rap below the abutments has moved

towards the stream and down away from the abutment, exposing the base of the abutment. This is shown for the western corner in Figure 6.36(b) and (c). No surficial evidence of liquefaction was noted at this site and no mechanism for the damage has been identified.

Figure 6.34: Stinking Stream Bridge [-42.6724, 172.7748]: (a) Looking north on 14 November; (b) Southern corner on 14 November; (c) and (d) Eastern corner on 17 November.

Figure 6.35: Northern corner of Stinking Stream Bridge [-42.6724, 172.7748]. (a) Looking south on 14 November; (b) Looking south on 17 November; (c) Hole in roadway; (d) Settlement on 17 November.

One interesting feature at the Stinking Stream Bridge is given by Figure 6.35(a) and (b), which show essentially the same view of the northern corner of the bridge on 14 and 17 November, respectively. The visual damage on 17 November is more severe than it was on the day following the main shock. The longitudinal cracking is more extensive, and an

approximately 50 cm diameter hole has opened up in the road surface. This suggests four possibilities: (1) ground deformation did not change, but pavement damage only occurred after traffic was reopened; (2) additional time-dependent ground deformation occurred; (3) additional ground deformation occurred due to aftershocks; or (4) some combination of the three possibilities.

Figure 6.36: West corner of Stinking Stream Bridge [-42.672427, 172.774764]: (a) Settlement and cracking at abutment; (b) Settlement looking east; (c) Rip-rap movement away from the abutment base; (d) Cracking in approach.

Figure 6.37: Cracks on free-face side of roadway on Highway 7 looking south [-42.6310, 172.7718]. Location and site layout shown in Figure 6.33.

The other site of note along the surveyed stretch of Highway 7 are the roadside cracks shown in Figure 6.37. The location and layout of this site are provided in Figure 6.33(a) and (b), respectively. The cracking shown in Figure 6.37 is approximately 50 m long and up to 30 cm

wide and involved the free face of a section of road that passes along a slope. The Waiau River flows off to the left of the photos shown in Figure 6.37. No evidence of liquefaction was observed near the cracks, but possible evidence of liquefaction, in the form of pooling water, was observed closer to the river bank in the general area of this ground deformation.

6.1.7 Home Creek Bridge [-42.6323, 172.9528]

Visual surveys in the Emu Plains area located northwest of Waiau Township identified a number of sites of interest along Leslie Hills and River Roads, particularly at a series of rural bridges on Leslie Hills Road. The locations of these sites are shown in Figure 6.1. Home Creek Bridge is an 8 m long, 3.67 m wide single-span and single lane precast and pre-tensioned concrete bridge spanning a section of Home Creek on Leslie Hills Rd. Visual surveys at the Home Creek Bridge site indicated 15-20 cm wide transverse roadway cracks in the western approach to the bridge. As shown in Figure 6.38(a), there were 3 or 4 of these cracks in the approach, indicating an accumulated extension towards the bridge/stream of at least 45 cm. There was about 25-30 cm of settlement at the western abutment and wingwalls as shown in Figure 6.38(b), (c), and (d). For context, the callipers resting against the abutment wall in Figure 6.38(b) are 20 cm long. There were also a few transverse cracks in the approach near the abutment, but it appears that the wingwalls held the soil back sufficiently without any notable structural damage indications.

Figure 6.38: Home Creek Bridge [-42.6323, 172.9528]: (a) Roadway cracks in western approach; (b), (c), and (d) Settlement at western abutment.

6.1.8 Leslie Hills Road Failure [-42.6306,172.9895]

As Leslie Hills Road turns southeast towards River Road (see Figure 6.1), extreme damage was encountered in the roadway. As shown in Figure 6.39, a section of road adjacent to an escarpment has completely failed, breaking up into several chunks with a total vertical offset of 1.5 to 2 m. It is likely that some portion of the failed material was man-made fill given the difference between the topography to the right of the road in Figure 6.39(a) and the former topography of the road. Evidence indicates that this road failure is related to surface faulting, however, there was also evidence of excess pore water pressure build-up or liquefaction, as some minor liquefaction ejecta was sighted nearby.

There is also significant damage to the road to the west and east of the major failure zone. Figure 6.39(c) and Figure 6.40 show some representative photos of the damage observed to the west of the major road failure, indicating some significant transverse and longitudinal cracks in the road, a somewhat smaller road failure area adjacent to a side slope, and some cracking through a paddock next to the roadway. On the east side of the major failure zone on Leslie Hills Road, the damage is characterised by compression of the roadway material as evidenced by the compression ridging shown in Figure 6.41(a) and (b). The damage to the roadway on the east side of the large failure zone is essentially continuous up to the Mt Paul Bridge discussed in the next section.

Figure 6.39: Failure and severe cracking on Leslie Hills Road (photos all taken looking west) [-42.6306,172.9895]: (a) Overview of major failure area; (b) Closer view of failure area; (c) Cracking to west of failure area.

Figure 6.40: Damage west of failure area on Leslie Hills Road (both photos taken looking west) [-42.6306,172.9895]: (a) Cracking and failure of the road on free face of embankment; (b) Adjacent cracking through paddock.

Figure 6.41: Damage observations east of Leslie Hills Road failure area [-42.6306,172.9895]: (a) Compression ridging in pavement material; (b) Side view of compression ridge; (c) Minor liquefaction ejecta.

The small sand boil on the edge of the road surface shown in Figure 6.41(c) was the only surficial evidence of liquefaction (particle size distribution shown in Figure 6.6) observed in the vicinity of the major roadway failure on Leslie Hills Rd. Despite the lack of significant evidence of liquefaction at the site, excess pore pressure build-up or liquefaction of some underlying material still seems to be a possible cause for some of the ground deformation and damage observed in this area.

6.1.9 Mt Paul Bridge [-42.6355, 172.9923]

The Mt Paul Bridge is an 18.9 m long, 4.34 m wide precast concrete bridge spanning a stream on Leslie Hills Road just a few hundred metres southeast from the major failure area discussed in the previous section. The damage at this bridge site was characterised by severe cracking in the roadway and settlement of the approaches relative to the abutments and deck. Figure 6.42 shows some indications of the roadway cracking located between the Leslie Hills Road failure site and the Mt Paul Bridge. As shown, the general cracking pattern of Figure 6.42(a) found further away from the bridge gradually becomes dominated by the wider longitudinal cracks of Figure 6.42(c) found closer on to the bridge. These longitudinal cracks are approximately 20-30 cm wide and are located all across the roadway, not just at the edges. No surficial evidence of liquefaction was observed at this site, but the ejecta sited closer to the major road failure site is only a few hundred metres away.

At the immediate bridge approaches, the damage is even more severe. As shown in Figure 6.43, the soil and rip-rap below the bridge also appears to have settled and moved towards the stream, completely exposing the underside of the bridge abutments. As shown in Figure 6.44, there is significant cracking and outward movement of the approach soils, with outward deformations on the order of 40-50 cm. There is also significant settlement of the approach roadway and approach soils relative to the deck on both sides of the bridge with magnitudes on the order of 40-50 cm. For approximate reference, the elevation of the original ground surface can be discerned by the markings on the guardrail posts.

Figure 6.42: Cracking in roadway approaching Mt Paul Bridge from the north along Leslie Hills Road [-42.6355, 172.9924].

Figure 6.43: Settlement below abutment at Mt Paul Bridge [-42.6355, 172.9923].

Figure 6.44: Settlement and cracking in approaches to Mt Paul Bridge [-42.6355, 172.9924]: (a) Southwest corner; (b) Southeast corner; (c) Northeast corner; (d) Northwest corner.

6.1.10 Emu Plains Bridge [-42.6394, 172.9149]

The Emu Plains Bridge is a 20.5 m long, 4 m wide timber bridge on Leslie Hills Road at the location indicated in Figure 6.1. The damage at this bridge site was similar to that observed at all of the other surveyed rural bridges. Figure 6.45 shows some representative photos from this site. There was significant cracking in the roadway, particularly on the east side of the bridge, where the longitudinal cracks were up to 30 cm wide and the transverse cracks were about 10 cm wide with up to 20 cm of vertical offset in places. The settlement of the eastern approach ranged from about 10-20 cm with the largest settlements on the southeast corner of the bridge as shown in Figure 6.45(b). No surficial evidence of liquefaction was observed at this site, and the mechanisms for this deformation have not been identified.

Figure 6.45: Damage at Emu Plains Bridge [-42.6394, 172.9149]: (a) Roadway damage looking west towards bridge; (b) Settlement at eastern abutment; (c) and (d) Significant cracking in roadway on eastern side of bridge (photos taken facing east away from bridge).

6.2 Marlborough district

The bridge reconnaissance in the Marlborough district was based in Blenheim. Surveys were completed within Blenheim, as well as along SH63 heading west from Blenheim into the Wairau Valley, and along SH1 heading south from Blenheim towards Kaikoura. A total of 12 bridges were surveyed in the Marlborough district as shown in Figure 6.46. The bridges on SH63 and two of the rural bridges north of Blenheim did not show any signs of earthquake damage. These sites are indicated using green markers in Figure 6.46. In contrast, earthquake-induced damage was observed at all of the surveyed bridges on SH1 south of Blenheim. The key observations made at these bridge sites are discussed individually in the following subsections. Three additional SH1 bridges south of Ward were surveyed, however these sites technically fall within the Kaikoura District and are discussed in the following section along with the rest of the Kaikoura District sites.

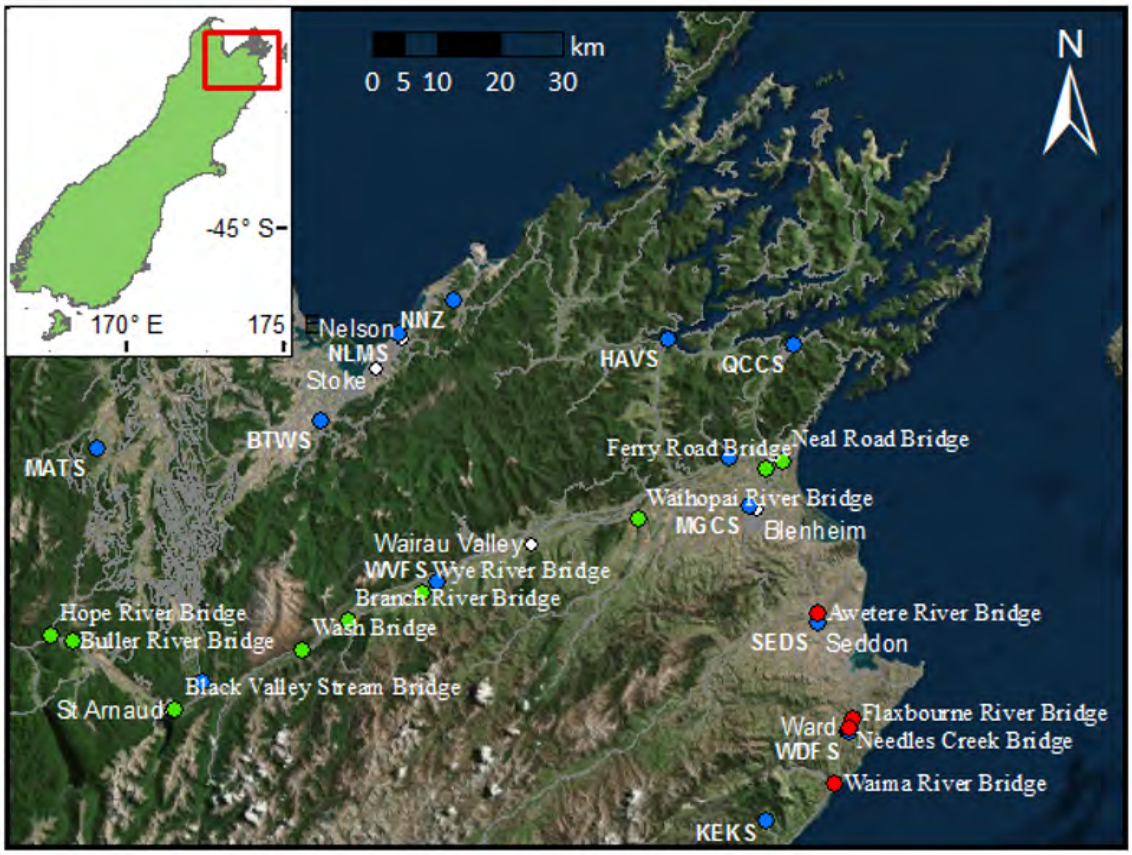

Figure 6.46: Bridge sites surveyed in the Marlborough District. Green markers indicate bridges with minor or no damage observations. Red markers indicate sites with moderate to severe damage observations. Blue markers indicate strong motion stations.

6.2.1 Flaxbourne River Bridge [-41.8085, 174.1458]

The Flaxbourne River Bridge is a 5-span reinforced concrete bridge built in the 1950s to span the Flaxbourne river north of Ward on SH1. The deck is monolithic with beams and is supported on four wall piers with abutments at either end. The superstructure is not integral to the piers, and the only lateral connection to the piers and abutments is via a series of vertical reinforcing bars working in dowel action, with two bars per beam. There are no expansion joints over the bridge span (Palermo et al., 2017).

Damage was observed in both the superstructure and substructure for the Flaxbourne River Bridge. The deck was separated from the piers and abutments, as the bars connecting the superstructure and substructure did not provide sufficient shear capacity for the lateral seismic demands. The dowel action of the bars was clearly observed, however, as the surrounding cover concrete was broken and the confining transverse reinforcement was bent and even fractured in some cases as shown in Figure 6.47(a). The severity of this damage varied along the length of the bridge, with the worst damage observed in the two southernmost piers, where the deck had been displaced southwest from the original position. The residual transverse deck displacement is shown in Figure 6.47(b) as the girder is offset from its original position. The damage to the piers themselves was more severe at the two northernmost piers where the deck-pier connection was less damaged.

Plastic hinging occurred at both abutments with exposed and buckled reinforcement, and cracking was observed at the base of some of the piers. At the southern abutment, the plastic hinging occurred at the top of the abutment columns, fully exposing the longitudinal reinforcement of the columns as shown in Figure 6.47(c). The cast-in-place soil retaining beam at this abutment had moved towards the river by approximately 200 mm and there were clear signs of longitudinal movement of the beam diaphragm atop the abutment seat as shown in Figure 6.47(d). At the northern abutment, the plastic hinging was observed at the top of the piles. Cracking was observed across the pile depth, with concrete spalling on both the front and back faces of the piles.

Figure 6.47: Damage at Flaxbourne River Bridge [-41.8085, 174.1458]: (a) Damage at deck-pier connection; (b) Residual transverse deck displacement; (c) Exposed and buckled reinforcement in abutment columns; (d) Residual longitudinal deck displacement.

An inspection of the interface between the piers and pile caps at the accessible piers (all but the southernmost pier) indicated cracking at the pier base extending through the entire interface as shown in Figure 6.48(b), (c) and (d). These piers were tilted in the longitudinal direction such that the tops of the piers had moved south, with a typical example shown in Figure 6.48(a). Exposed and buckled longitudinal reinforcing bars were observed at the northern bridge piers, and there was clear evidence of 10 mm of relative movement towards the river channel between the base of the northernmost pier and its pile cap. Moderate settlement of the approaches was observed at the Flaxbourne River Bridge with longitudinal cracking in the roadway indicative of outward spreading in the approach. No surficial evidence of liquefaction was observed at the bridge site.

Figure 6.48: Substructure damage at Flaxbourne River Bridge [-41.8085, 174.1458]: (a) Tilted pier; (b) Cracking at pier base; (c) and (d) Cracking and exposed reinforcement at base of piers.

6.2.2 Needles Creek Bridge [-41.8217, 174.1370]

The Needles Creek Bridge is a 5-span concrete bridge built in the 1950s with a structural design that is nominally identical to the Flaxbourne River Bridge. The primary difference between these two bridges is that where the Flaxbourne River Bridge is linked to the wall piers by dowels, the superstructure of the Needles Creek Bridge is integral to the piers (Palermo et al., 2017). The Needles Creek Bridge is located about 1.7 km south along SH1 from the Flaxbourne River Bridge, and is sited approximately 640 m away from the Ward fire station strong motion station (WDFS). Figure 6.49 shows an elevation view of the bridge and provides a reference numbering system for the piers and abutments. Figure 6.50 shows a plan layout of the Needles Creek Bridge site with a summary of the observed geotechnical damage and ground failures mapped in the area.

Figure 6.49: Layout of Needles Creek Bridge in elevation view.

Figure 6.50: Overview of Needles Creek Bridge site with indications of ground damage. Orange area is the bridge deck, red lines indicate cracks, and the green markers indicate sand boils. The blue line indicates the creek bed.

Liquefaction ejecta was observed under the Needles Creek Bridge between piers 2 and 3 and between piers 3 and 4, as well as in the free field on the west side of the bridge as indicated in Figure 6.50. Some typical liquefaction evidence is shown in Figure 6.51. Lateral spreading cracks were also observed along the free-face of the river, extending up to the edges of the piers as shown in the site layout of Figure 6.50 and the photos of Figure 6.52. Settlement of at least 15 cm was observed at both abutment walls, completely exposing the underside of the abutments as shown in Figure 6.53. Cracks were present in nearly all of the piles visible beneath the exposed abutment bases, varying in width from 1-5 mm. Figure 6.54(a) shows a representative example of this damage. A gap of 25-30 cm was observed between the abutment piles and the surrounding soil, indicative of relative movement of the soils and foundations. Similar soil-structure gapping of 10-25 cm was observed at the base of piers 1, 3, and 4. Figure 6.54(b) shows this gapping at the base of pier 3.

Figure 6.51: Liquefaction ejecta at Needles Creek Bridge site [-41.8217, 174.1370]: (a) Ejecta between piers 1 and 2; (b) Ejecta between piers 3 and 4; (c) Ejecta in free field west of bridge.

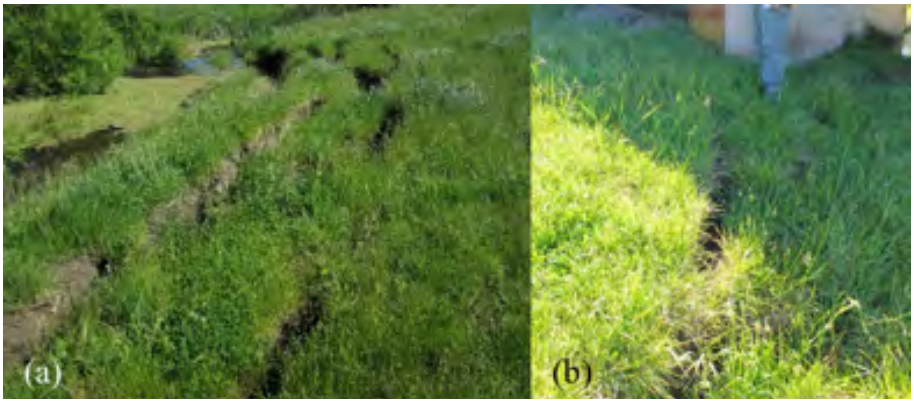

Figure 6.52: Free field lateral spreading cracks at Needles Creek Bridge site [-41.8217, 174.1370]: (a) Cracks along free face of the river; (b) Cracking near bridge pier.

Figure 6.53: Soil subsidence below abutments at Needles Creek Bridge [-41.8217, 174.1370]: (a) North abutment wall looking northwest; (b) South abutment wall looking south.

Figure 6.54: Pile and footing damage at Needles Creek Bridge [-41.8217, 174.1370]: (a) Crack in pile for south abutment; (b) Soil-footing gapping at pier 3.

Significant plastic hinging was observed at the top and bottom of the piers for the Needles Creek Bridge. As shown in Figure 6.55(a), there was a tendency for the formation of single cracks rather than distributed cracking, and for these single cracks to extend over the full width of the wall piers, which indicates that the bridge was more heavily loaded in the longitudinal direction. This inference is also supported by the observation that the bridge deck had clearly sheared off of abutment 1 on the north end as shown in Figure 6.55(b). The pier cracking was particularly severe at piers 1 and 2. Exposure and buckling of the longitudinal reinforcement was observed at the top of pier 1 as shown in Figure 6.55(c), and this pier had a measured residual tilt of about 3° from vertical as shown in Figure 6.55(d). It appeared that this tilting was due to the base of the pier moving towards the river, likely due to the lateral spreading that occurred on the banks of the creek.

Figure 6.55: Structural damage at Needles Creek Bridge [-41.8217, 174.1370]: (a) Cracking across length of pier 1 looking south; (b) Deck sheared off of abutment 1 facing west; (c) Cracking at pier 1 facing east; (d) Tilting of pier 1 facing east.

6.2.3 Waima River Bridge [-41.9021, 174.1122]

The Waima River Bridge is an 8-span bridge on SH1 constructed in 1975. The Waima River Bridge has simple spans with two precast, prestressed I-beams seated on circular monopile piers with hammerhead bents. Seismic retrofit was carried out at this bridge in 2003 to reduce the likelihood of deck unseating during earthquake shaking (Palermo et al., 2017). Figure 6.56(a) and (b) show some of the retrofitting measures. The Waima River Bridge displayed noticeable residual transverse deck displacement, with two components: a rigid body component towards the sea (eastward), and a deformation component directed primarily westward. The deformation pattern was curved between the abutments, with the largest transverse displacement at the centre of the overall bridge span. The deck was also twisted

about the longitudinal axis such that the southern edge is now higher than the northern edge. Cracking and spalling of concrete was observed around the retrofitted steel brackets attached to the deck beams, with a representative example shown in Figure 6.56(b). Cracking was also observed at both abutments and at the tops of the exposed abutment piles as shown in Figure 6.56(c). The piers near the southern abutment had a noticeable tilt with the top of the pier translated to the west. The tilt at the southernmost pier is shown in Figure 6.56(d). Minor flexural cracking was also observed around the base of some piers.

Figure 6.56: Damage at Waima River Bridge [-41.9021, 174.1122]: (a) South abutment facing south; (b) Damage to concrete beams around retrofit brackets; (c) Cracking at top of abutment pile; (d) Tilt of southernmost pier facing north.

Figure 6.57: Geotechnical damage at Waima River Bridge site [-41.9021, 174.1122]; (a) Ejecta at piers of railroad bridge 50 m upstream; (b) Settlement at south approach looking north.

Liquefaction ejecta was observed around a few of the piers of a railroad bridge running parallel to the Waima River Bridge approximately 50 m upstream as shown in Figure 6.57(a), but nothing was evident closer to the Waima Bridge itself. Settlement was observed in front of the abutment walls as shown in Figure 6.56(a), exposing the piles beneath the abutment, and approach settlement greater than 10 cm was observed at the south side of the bridge as shown in Figure 6.57(b). Relatively minor longitudinal cracks at the edge of the approach roadway were observed, indicative of a modest amount of outward spreading in the approach material.

6.2.4 Awatere River Bridge [-41.6585, 174.077]

The Awatere River Bridge is a 10-span reinforced concrete bridge constructed in 2007. The bridge superstructure consists of 1.2-m deep precast, prestressed U-beams that are integral with the piers and seated on bearings at the abutments. The deck is continuous over the length of the bridge. The interior piers consist of 5.5 m long 1.0 m diameter circular columns supported on single 1.2-m diameter steel-cased drilled shafts (Palermo et al., 2017). Flexural damage was observed in the Awatere River Bridge piers, with flexural cracking at the tops of the pier columns near the abutments, and spalling of concrete at the top and bottom of the pier columns near the middle of the bridge as shown in Figure 6.58(a) and (b). Residual displacement of the deck was evident at the southern abutment, as the bearings shown in Figure 6.58(c) indicate a residual movement in to the southeast. It is unknown if all of this residual displacement is due to the Kaikoura event or due in part to a previous seismic event such as the 2013 Lake Grassmere earthquake.

Figure 6.58: Damage at Awatere River Bridge [-41.6585, 174.077]: (a) Flexural damage at top and bottom of pier column near middle of bridge facing west; (b) Spalling of concrete at base of pier column; (c) Residual displacement in bearing pad at southern abutment; (d) Damage to previously grouted area.

It is interesting to note that all of the observed cracking and spalling had occurred in areas that had been previously repaired with grout. A typical example of this is shown in Figure 6.58(d). No surficial evidence of liquefaction was noted at the Awatere River Bridge site, and there was no significant settlement in the approaches. Settlement was observed in the fill below the bridge and in front of the abutment walls, exposing the base of the abutments, but no obvious or large transverse cracks were observed in this fill material.

6.3 Kaikoura District

Significant non-ground faulting and non-landslide damage was observed at six bridges within the Kaikoura District as shown in Figure 6.59. Three of these bridges are located on SH1 north of Kaikoura township (and north of the landslides at Okiwi Bay that are blocking access to Kaikoura from the north on SH1). Two are located just north of Oaro, a few kilometres south of Kaikoura; one is a highway bridge on SHI and the other is a railway bridge over the Oaro River. The remaining bridge is a smaller local road bridge over Lyell Creek within Kaikoura. The Clarence Valley Road Bridge (not shown in Figure 6.59), which experienced complete collapse is also briefly discussed. In addition to these larger bridges, several smaller bridges and culverts within the Kaikoura township are discussed in this section.

Figure 6.59: Bridge sites in the Kaikoura District with observations of moderate to severe damage. Red markers indicate bridge sites. Blue markers indicate strong motion stations.

6.3.1 Mororimu Stream Bridge [-42.2173, 173.8673]

The Mororimu Stream Bridge is a 3-span cast in-situ integral reinforced concrete structure built in 1951. The spans are supported on wall piers that are founded on strip footings. The Mororimu Stream Bridge is curved horizontally and has a vertical slope, with the north side sitting higher than the south side, and is oriented essentially directly in-line with an east-west plane (Palermo et al., 2017).

The structural damage to the bridge was primarily confined to the substructure with the exception of one minor transverse crack found in the underside of the deck near the western pier. Extensive cracking was observed in both abutments, in the abutment columns, and at the tops of the piers as shown in Figure 6.60(a)-(c). Settlement was observed in both approaches, with approximately 10 cm of settlement at the eastern abutment shown in Figure 6.60(d). Settlement and outward spreading was observed in the fill ahead of both abutments, and soil gapping of several centimetres was observed around the base of some piers. No surficial evidence of liquefaction was noted anywhere in the vicinity of the bridge site.

Figure 6.60: Damage observed at Mororimu Stream Bridge [-42.2173, 173.8673]: (a) Cracking in eastern abutment looking south; (b) Abutment column cracking; (c) Cracking at top of pier; (d) Settlement of eastern approach looking west.

6.3.2 Mororimu Overbridge [-42.2166, 173.8686]

The Mororimu Overbridge is a 4-span reinforced concrete bridge also constructed in 1951 located about 100 m northwest along SH1 from the Mororimu Stream Bridge. The spans are supported on multi-column bents, with four columns for the outer piers and a two-column portal frame at the central pier to accommodate trains. All three piers are founded on strip footings. The Mororimu Overbridge is flat and straight (i.e., no tilt or curvature).

Cracking was observed at the top of the abutment and pier columns as shown in Figure 6.61(a) and (b). There was extensive cracking below the knee joints of the portal frame at the central pier, with the damage to the northern column shown in Figure 6.61(c). The damage at each pier was most severe at the top of the shortest column, with concrete spalling and some exposed reinforcement as shown in Figure 6.61(d). The geotechnical damage was similar to that observed at the Mororimu Stream bridge, with settlement in the approaches, settlement of the fill ahead of the abutments, and soil gapping around the base of the piers. No surficial evidence of liquefaction was observed at the Mororimu Overbridge site.

Figure 6.61: Structural damage observations at the Mororimu Overbridge [-42.2166, 173.8686]: (a) Abutment column cracking; (b) Damage to pier columns; (c) Cracking below knee joint of central pier column; (d) Exposed reinforcement at top of pier column.

6.3.3 Clarence River Bridge [-42.1592, 173.9103]

The Clarence River Bridge is a 6-span balanced cantilever, single cell box girder bridge built in 1975 and seismically retrofit in 2007. The superstructure is supported on wall piers, and is monolithic with the piers. The piers are supported by two concrete piles each, and the abutments are supported on steel H-piles. The box girder supporting the deck is seated at the abutments on three elastomeric bearings, and is anchored to the abutments by a row of hold-down rods to prevent uplift during live loading. The Clarence River Bridge is sloped vertically, with the north side higher than the south side, and is moderately curved in the horizontal direction, with the concave side to the east (Palermo et al., 2017).

The structural damage at the Clarence River Bridge was primarily confined to the substructure, and the damage patterns are indicative of primarily of transverse movement during shaking. As shown in Figure 6.62(a), cracking was observed where a vertical member providing transverse resistance to the deck frames into the abutment wall. This cracking is indicative of transverse deck movement during shaking. The hold-down rods tying the deck beams to the abutment seat display corresponding damage, with residual displacements evident in the transverse direction as shown in Figure 6.62(b). Settlement of the deck relative to the abutment seat was also evident as shown in Figure 6.62(c). Further evidence of transverse movement was observed at the pier footings, where as shown in Figure 6.62(d) and Figure 6.63(a), there was concrete spalling and cracking at the pier-footing interface and in the top surface of the footing.

Figure 6.62: Structural damage at Clarence River Bridge [-42.1592, 173.9103]: (a) Cracking in transverse abutment wall; (b) Residual deformation in hold down rod securing deck to abutment; (c) Deck settlement at abutment; (d) Concrete spalling at base of pier.

Figure 6.63: Damage at Clarence River Bridge [-42.1592, 173.9103]: (a) Cracking in top of footing; (b) Settlement of fill ahead of abutment; (c) Soil gapping at base of pier; (d) Spreading cracks in roadway at southern approach looking south.

Settlement was observed in both approaches, but the magnitude was limited by the presence of an approach slab. The settlement at the northern approach opened an approximately 25 mm wide gap between the abutment and slab. Settlement of the fill ahead of the abutment wall was also observed as shown in Figure 6.63(b), and soil gapping was noted at the base of several piers. Figure 6.63(c) shows a representative example of this gapping. Roadway cracks indicative of transverse approach spreading were observed on both sides of the bridge, and were particularly severe in the southern approach as shown in Figure 6.63(d).

6.3.4 Lyell Creek Bridge [-42.3892, 173.6773]

The bridge crossing Lyell Creek on Hawthorne Road is an east-west oriented single-span bridge with a total deck length of 7.15 m. The bridge crossing is slightly skewed relative to the river, making an angle of approximately 65 degrees to the river. The deck consists of wooden planking supported by two longitudinal I-beams. The I-beams appear to be tied together at two locations by U-sections. At both ends, the deck is supported on concrete abutments. This bridge was rendered unusable after the earthquake on account of the large movements of the abutments and deck slab. Figure 6.64 shows an overview of the Lyell Creek Bridge site.

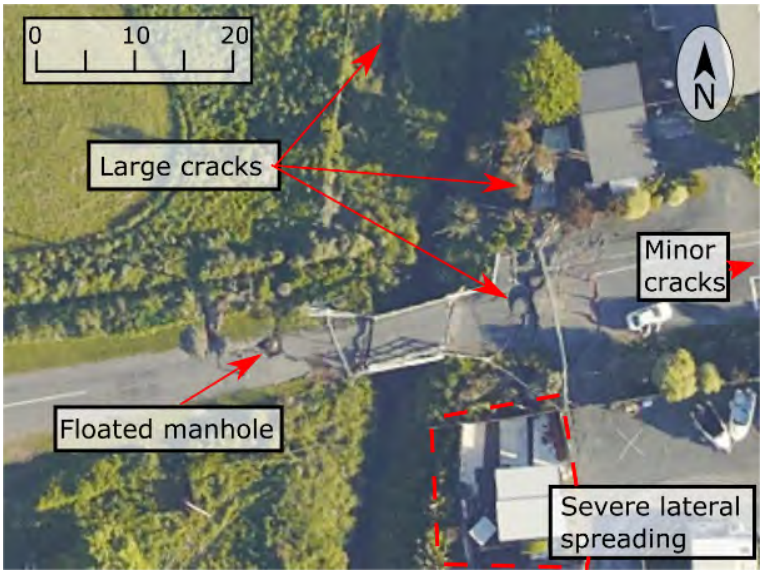

Figure 6.64: Site layout and features of interest at Lyell Creek Bridge [-42.3892, 173.6773].

On the eastern side of the bridge, cracks around 4 cm wide began on the south side of the road, (approximately 1.7 m from the end of the deck), running parallel to the road, becoming oriented at 45° to the road approximately 5 m from the end of the deck. This crack became approximately 20 cm wide at the centre of the road. One major crack 50 cm in width and parallel to the river was observed 9 m from the end of the deck. The crack to the east of the bridge was located a distance of 15.5 m from the end of the deck, was perpendicular to the road, and approximately 5 cm wide. The road appears to drop 15 cm to the river side of this crack. At the south of the road, the crack rotated 45° in plan and continued towards the river. Along the road, there were a number of cracks approximately 2 cm wide between 5 m and 19 m from the river. Figure 6.65(a) shows some of these features in the eastern approach.

Figure 6.65: Approach cracking at Lyell Creek Bridge [-42.3892, 173.6773]: (a) Eastern approach looking east; Note: crack at 9, from the bridge abutment (location of field member) was 50 cm wide, and had a vertical offset of 30 cm. (b) Western approach looking east.

Some earthwork had been carried out on the western side of the bridge as shown in Figure 6.65(b), and at the time of the visit, there were no obvious lateral spreading cracks crossing through the road to the west of the bridge. Heavy cracking was apparent around a manhole located on the north side of the road, 10 m west of the bridge abutment. Aerial photography taken on 14 November shows that there were three large cracks spreading out from the

manhole to the west, north (roughly parallel to the river), and to the southeast. At the time of the survey, the relative vertical offset between the manhole cover and the road surface was approximately 520 mm, of which a large part appears to be composed of settlement of the backfill. The lines of the cracks suggest that they could be associated with buried services. Close inspection of aerial photography shows that there were large lateral spreading cracks in the on the grassy banks both to the north and south of the bridge, though these were not observed on foot.

Figure 6.66: Back rotation of east and west abutments at Lyell Creek Bridge [-42.3892, 173.6773]: (a) Looking south at bridge; (b) Looking north at bridge.

Both the east and west abutments experienced large rotations, with the base of the abutment moving inwards toward the waterway as shown in Figure 6.66. At the northeast corner of the bridge, the deck slab and deck beam appear to have remained connected together, but have displaced approximately 630 mm northwards relative to their original anchor point on the abutment. As shown on the left side of Figure 6.67, to accommodate the lateral movement, the north deck beam was forced to override the lateral guide lug. The vertical displacement of the deck at the location of the deck-beam was 400 mm relative to the top of the abutment. In addition to these translational movements, the deck and beam have rotated 12° anticlockwise in plan. The deck beams appear to have been anchored to the abutment using single steel bars. The movement at this abutment has pulled the bar out of the abutment, and the lateral movement has created two 90° bends in the bars as shown in Figure 6.68(b).

Figure 6.67: Eastern side of Lyell Creek Bridge [-42.3892, 173.6773]. Photo facing west.

Figure 6.68: Damage at Lyell Creek Bridge [-42.3892, 173.6773]: (a) Eastern end of bridge looking north; (b) Bent anchor bars at east abutment-deck connection; (c) Gap between deck and west abutment looking south; (d) Twisting of deck beams.

At the southeast corner of the bridge, the deck slab has separated from the deck beam and overridden the abutment, resulting in a vertical offset of 200 mm between the top of the deck slab and the abutment as shown on the right side of Figure 6.67 and in Figure 6.68(a). The deck slab appears to have translated northwards approximately 600 mm. The position of the deck beam relative to the abutment at the southeast corner was not inspected, but is assumed to have displaced northwards by around 600 mm (similar to the deck beam at the northeast corner). A large shear crack is present in the abutment where the southern deck beam meets the east abutment. Additional cracks outboard of the deck beam are also apparent on the eastern abutment.

On the west side of the bridge, the abutment has rotated such that the base moved inwards toward the river. Additionally, as shown in Figure 6.68(c), a gap has opened consistent with the rotation (in plan) of the deck slab observed at the east end of the bridge. The southern deck beam translated laterally to the south by 100 mm, where it was restrained by the lateral guide lug. As a result of the abutment rotation, the base of the southern deck beam is in contact with the western abutment, while there is a 180-200 mm horizontal gap between the top of the beam and the abutment. It is estimated that the rotation of the abutment in the vertical plane is around 16°. At the northwest corner, the bottom of the deck beam has remained in contact with the abutment, however, the rotation of the deck slab has bent the end flange plate at the top of the deck beam and twisted the deck beam structure as shown in Figure 6.68(d). The deck beam does not appear to have translated in plan relative to the abutment.

6.3.5 Other Bridges and Culverts in Kaikoura Township

6.3.5.1 Middle Creek Railway Bridge

The railway crosses Middle Creek just southwest of the oxidation ponds at the location marked on Figure 4.126. The concrete bridge deck is supported by two piers which are supported by 4 × 2 pile groups (Figure 6.69). As shown in Figure 6.70, ejected material was observed on the east side of the bridge, close to the north pier and abutment. The settlement of the approach fills left the railway unsupported at both ends of the bridge as shown in Figure 6.71, while Figure 6.72 captures the failure in the concrete abutment at the north end of the bridge due to the passive soil loads.

Figure 6.69: Middle Creek Railway Bridge (facing northwest) [-42.3672, 173.6862].

Figure 6.70: Liquefaction close to the north pier and abutment of Middle Creek Railway Bridge (facing southeast) [-42.3670, 173.6861].

(a) (b)

Figure 6.71: View along the tracks of Middle Creek Railway Bridge. Settlement of the approaches to the bridge left the rails unsupported: (a) Looking north [-42.3672, 173.6860]; (b) View looking south [-42.3670, 173.6861].

Figure 6.72: Damage to the north abutment of the Middle Creek Railway Bridge facing northwest [-42.3670, 173.6861].

6.3.5.2 Middle Creek Bridge – Mt Fyffe Rd

An ~9.5-m long, single lane bridge that crosses Middle Creek on Mt Fyffe Road also experienced damage, as shown in Figure 6.73 through Figure 6.76. As shown in Figure 6.73(b), fill was placed to compensate for subsidence of the both the north and south approaches and the barriers on the northern approach rotated outward. Also, both the reinforced concrete north and south abutments to the bridge experienced cracking (Figure 6.74-Figure 6.76).

(a)

(b)

Figure 6.73: Bridge crossing Middle Creek on Mt Fyffe Road (8 Dec 2016): (a) Cracking of concrete on south abutment (facing southwest) [-42.3692, 173.6548]; (b) Outward rotation of barriers on approach (facing south) [-42.3691, 173.6547].

Figure 6.74: Damage to the south abutment on the east side of the bridge (8 Dec 2016, facing south) [-42.3692, 173.6547].

Figure 6.75: Damage to the north abutment on the east side of the bridge (8 Dec 2016, facing north) [-42.3692, 173.6549].

Figure 6.76: Damage to the north abutment on the west side of the bridge (8 Dec 2016, facing north) [-42.3692, 173.6547].

6.3.5.3 Culverts

Lateral spreading was observed in the area of the Waimagarara culvert on State Highway 1 (Athelney Road). To the north of the culvert, lateral spreading cracks were parallel to the road, with the spreading occurring towards small drainage ditches. Lateral spreading displacements on the east side of the road, north of the culvert, were of the order of 30-50 cm wide and typically 60 cm deep. These cracks were offset from the road, by approximately 2 m (Figure 6.77 and Figure 6.78). Cracks in the road and ejecta on the south side of the Waimagarara culvert are shown in Figure 6.79 and Figure 6.80. Damage was also noted on culverts located on the smaller roads west of Kaikoura on Hawthorne Road (Figure 6.81) and Mill Road (Figure 6.82), often with cracking in the wingwalls.

Figure 6.77: Lateral spreading cracks at the side of Athelney Road (9 Dec 2016, facing north) [-42.3598, 173.6765]. Note the drainage ditch to the right of the photo.

Figure 6.78: Cracking on the north-side of the Waimagarara culvert on Athelney Road (9 Dec 2016, facing south) [-42.3599, 173.6765].

Figure 6.79: Cracking on the south side of the Waimagarara culvert on Athelney Road (9 Dec 2016, facing north) [-42.3606, 173.6765].

(a)

(b)

Figure 6.80: Ejecta on the south of Waimagarara Culvert on Athelney Road, approximately 10 m from the creek (9 Dec 2016): (a) East side of the road facing east [-42.3603, 173.6766]; (b) West side of the road facing north [-42.3603, E173.6765].

Figure 6.81: Cracking in the concrete at Hawthorne Road culvert (8 Dec 2016, facing northwest) [-42.3900, 173.6675].

Figure 6.82: Failure of the northwest wingwall of the Lyell Creek culvert on Mill Road (8 Dec 2016, facing west) [-42.3765, 173.6788].

6.3.6 Oaro Overbridge [-42.5121, 173.5063]

The Oaro Overbridge is a 5-span reinforced concrete bridge spanning railroad tracks on SH1 just north of Oaro. The middle piers (adjacent to railroad tracks) are single-column hammerhead bents, and the outer piers are four-column bents. It appears that the superstructure is integral to the piers and abutments at either end (unconfirmed). The Oaro Overbridge is curved, with the concave side to the west, and tilted such that the eastern side is higher than the western side. Significant settlement of at least 1.0 m was observed at the southern approach as shown in Figure 6.83. This settlement was slightly larger on the eastern side and large spreading cracks are apparent throughout the approach roadway. It appears that the approach fill has spread primarily towards the west (to the left in Figure 6.83). Direct photographic evidence is not currently available for the northern side, but it is apparent from the bent guardrails on the far side of the bridge in Figure 6.83(a) that some settlement occurred there as well. No surficial evidence of liquefaction or cracking consistent with spreading in the longitudinal direction was reported at the Oaro Overbridge site, but at the time of reporting only rapid reconnaissance results were available for this location.

Figure 6.83: Settlement and severe approach roadway cracking at southern abutment to Oaro Overbridge [-42.5121, 173.5063] looking north. Photos by D. Dizhur and M. Giaretton.

The observed structural damage was primarily to the bridge substructure, and was particularly concentrated in the abutments and the pier columns closest to the abutments. At the southern end, shown in Figure 6.84(a), moderate flexural cracking was observed at the top of all four pier columns just below the knee of the joint with the superstructure. Figure 6.84(a) also shows the settlement of the fill ahead of the south abutment, resulting in exposed piles. Based on the markings evidenced on the abutment wall, this fill has subsided at least 50 cm. Figure 6.84(b) shows a corresponding view of the northern end of the bridge. On this side, the damage at the top of the pier columns was much more severe, with concrete spalling, significant cracks passing all the way through the columns, and exposure of longitudinal reinforcement. Figure 6.84(c) provides a closer view of the tops of the two westernmost columns of the northern pier. Figure 6.84(b) also shows the more moderate flexural cracks near the base of the pier columns on the northern end. The slope ahead of the northern abutment is much less abrupt than at the south side, and settlements in this area appear to be less than observed on the southern end. A severe crack was observed over the entire length of the north abutment wall as shown in Figure 6.84(d). This crack is just below where the beams connect to the abutment, and the attendant spalling and bent reinforcing steel are indicative of significant pounding at this end.

Figure 6.84: Damage at Oaro Overbridge [-42.5121, 173.5063]: (a) Settlement of fill ahead of southern abutment and cracking at top of pier columns looking south; (b) Cracking in fill ahead of northern abutment and plastic hinging at top of pier columns looking north; (c) Closer view of damage at top of pier columns in northernmost pier looking north; (d) Cracking across face of northern abutment wall, just below deck beams looking north. Photos courtesy of D. Dizhur and M. Giaretton.

The central hammerhead piers were much less damaged than the four-column piers closer to the abutments. As shown in Figure 6.85(a), these piers are both longer and more substantial than those nearer the ends. Some relatively minor cracking in the horizontal member just below the deck beams was observed in the eastern side of the northern face of the northern hammerhead pier (upper left in Figure 6.85(a)). Minor flexural cracking was also observed at the base of this pier column as shown in Figure 6.85(b).

Figure 6.85: Damage at Oaro Overbridge [-42.512089, 173.506345]: (a) Northernmost central hammerhead pier looking south; (b) Flexural cracking at base of northernmost hammerhead pier. Photos courtesy of D. Dizhur and M. Giaretton.

6.3.7 Oaro River Rail Bridge [-42.514025, 173.50682]

Significant damage was observed at a railroad bridge crossing the Oaro river about 100 m due south of the Oaro Overbridge. This is an 8-span reinforced concrete bridge with integral wall piers and abutments located less than 30 m from the ocean. Significant residual lateral deformation was observed at this bridge, resulting in the bent rails shown in Figure 6.86(a). It appears that the bridge has rotated as a rigid body such that the northern end has moved eastwards by about 25-50 cm while the southern end has stayed essentially in place. No cracks are evident in the northern approach as would be expected for movement of the fill material, supporting the hypothesis of structural movement. Figure 6.86(b) indicates that regardless of the source of the movement, the entire bridge structure has remained intact. Settlement of the approach fill was also evident at both sides of the bridge.

Figure 6.86: Damage at Oaro River Rail Bridge [-42.514025, 173.50682]: (a) Residual lateral deformation towards the east at the northern abutment has bent the tracks (photo looking south); (b) Northern abutment looking north. Photos courtesy of D. Dizhur and M. Giaretton.

6.3.8 Bridge on Clarence Valley Road [-42.11066, 173.84156]

The bridge crossing the Clarence River on the Clarence Valley Road in an area of surface faulting and severe flooding experienced complete collapse. This bridge is located approximately 10 km west from SH1 northwest of Clarence and Waipapa Bay, and in contrast to some of the rural bridges discussed from the Hurunui District in earlier sections of this report, the Clarence Valley Road Bridge was a relatively newly built structure spanning a reasonably significant distance. Figure 6.87 shows a view of the collapsed bridge site from the western side of the Clarence River taken at some point in the week following the 14 November. As shown, the superstructure of the bridge has completely collapsed. Severe surface faulting was present in this area in addition to the flooding shown in Figure 6.87.

Figure 6.87: Collapse of Clarence Valley Road Bridge [-42.11066, 173.84156]. Photo taken from western side looking east (stuff.co.nz, 2016).

References

Dizhur, D. and Giaretton, M. (2016). Personal communication. November 2016.

Palermo, A., Liu, R., Rais, A., McHaffie, B., Andisheh, K., Pampanin, S., Gentile, R., Nuzzo, I., Granerio, M., Loporcaro, G., McGann, C.R. and Wotherspoon, L.M. (2017). "Performance of road bridges during the 14 November 2016 Kaikōura earthquake". *Bulletin of the New Zealand Society for Earthquake Engineering*, **50**(2): 253-270.

stuff.co.nz (2016) Quake shuts off Clarence Valley access, isolates farmers and residents. http://www.stuff.co.nz/business/farming/86674297/Quake-shuts-off-Clarence-Valley-access-isolates-farmers-and-residents. Last accessed 08 June 2017.